

3D Printed Optics for Widefield and Super-Resolution Optical Microscopy

A thesis submitted in partial fulfilment of the
requirements for the degree of Doctor of Philosophy

Jay Christopher

Centre of Microsystems and Photonics
Electronic & Electrical Engineering Department
University of Strathclyde, Glasgow
December 2024

Declaration of Authorship

This thesis is the result of the author's original research. It has been composed by the author and has not been previously submitted for examination which has led to the award of a degree.

The copyright of this thesis belongs to the author under the terms of the United Kingdom Copyright Acts as qualified by University of Strathclyde Regulation 3.50. Due acknowledgement must always be made of the use of any material contained in, or derived from, this thesis.

Signed:

A handwritten signature in black ink, appearing to read "Jay Christ", with a long horizontal flourish extending to the right.

Date: 16/12/2024

Abstract

Biological imaging research is fundamental to the development of both science and healthcare. One important factor within this development is 3D printing technology, which has become lower cost yet higher quality with each passing year. The technology has therefore seen success in its application to biological research and in-the-field healthcare diagnostics. Some biomedical imaging systems have yet to be developed at lower costs due to the requirement for specific optical elements. These unique constraints of optical elements can often create a premium in their price due to their bespoke manufacturing processes, and this in turn imposes a barrier to entry that constrains the array of available biological and diagnostic optical imaging in low-resource settings. When considering prototype, non-standard and free-form lens geometries within optical imaging research, the costs in manufacturing each optic increases further still. It is these costs especially which are passed onto the consumer, which itself slows or even halts completely the participation of biomedical research within low resource settings.

The research within this body of work has shown the use of resin-based 3D printing of optical quality elements at low costs. A method for post-processing 3D printed parts into optical quality components was developed, with the 3D printed optics quantified in terms of their transmissivity, form and surface roughness in comparison to similar commercial optical elements. Until now, 3D printed optical elements have only shown success in standard chrome lithography test target imaging. Using two custom objective designs, 3D printed optics were used in brightfield and fluorescence microscopy to image sub-cellular biological features, showing that 3D printed optics can be a useful tool for biomedical research and healthcare diagnostics in high and low resource settings. From the shown success in imaging using 3D printed optics within biological research, other optical microscopy methods are automatically available to test the low cost, custom elements. One key area of interest is therefore optical microscopy beyond the diffraction limit, with the super-resolution technique multifocal image scanning microscopy a key contender for optical element comparison due to its use of microlens arrays. Therefore, a custom lenslet array was designed and manufactured using 3D printing techniques and integrated into an image scanning microscope. This integration showed comparable improvements to the contrast obtained using a commercial microlens array when examining mitochondria within a fixed BPAE cell sample. These results act as a key indicator to the successes which 3D printed optics can have within super-resolution microscopy techniques.

Acknowledgements

First and foremost, I would like to express my utmost gratitude to my supervisor Dr. Ralf Bauer for his consistent support throughout my research during a globally difficult time. From him I have learned many skills essential to a career as an academic and scientist, though perhaps more importantly I have learned from his kindness, generosity and patience.

I would like to thank my examiners Dr Caroline Müllenbroich and Prof. James Windmill for their detailed, fair and to-the-point examination of my thesis.

I also want to thank the members of my research group in the Centre of Microsystems and Photonics for their continuous encouragement and, despite starting my research in the middle of a pandemic, ensuring I could still make the most of my experience working alongside researchers at different stages of their studentships and careers.

A huge thank you also to the Centre for Biophotonics group, for always making me feel welcome. Some of my favourite moments from my PhD have been from your organised chaos, especially at conferences. I especially want to thank Becca & (Dr/Landlord) Megan, for sticking with me since 2015, as well as Liam and Gail, for their mentorship and guidance.

I could not have succeeded so without the consistent and unfaltering support of my family who, in countless different ways, shaped me to become the person I am now. I will always be grateful for the gifts they have given me. Especially my wonderful nieces.

This thesis could not be complete without acknowledging my tight-knit friend group I have had the pleasure of knowing since my undergraduate years. Thank you for your constant encouragement, and for ensuring that I was able to relax a while whenever I got out of the lab. From cozy pubs, LOTR marathons and Hogmanay parties, thank you for taking my mind off work.

Finally, I want to thank my partner Rosie who I have been fortunate enough to have at my side for over a decade now. Your consistent care, encouragement, guidance and patience has helped me surpass even my highest aspirations. I hope I can pay your kindness back in full.

Contents

Declaration of Authorship	i
Abstract	ii
Acknowledgements	iii
Contents	iv
List of Figures	vi
Chapter 1 – Introduction	1
Aims & Novelty	1
Outline	1
Publications	2
Chapter 2 – Background	5
2.1 Optical Microscopy	5
2.2 Super-Resolution Microscopy	10
2.3 Additive Manufacturing	21
2.4 3D Printed Optics	27
2.5 Discussion	34
Chapter 3 - Optical Quality 3D Printing	35
3.1 Manufacturing Optical Quality 3D Prints	36
3.2 Evaluation Methods of Printed Parts	57
3.3 Discussion	68
Chapter 4 – Imaging using 3D Printed Objectives	70
4.1 Microscope Construction & Characterisation	70
4.2 Brightfield Imaging using a Single 3D Printed Lens	82
4.3 Brightfield Imaging using Multiple 3D Printed Lenses	88
4.4 Fluorescence Imaging using a Single 3D Printed Lens	94
4.5 Fluorescence Imaging using Multiple 3D Printed Lenses	100
4.6 Discussion	104

Chapter 5 – Multifocal Image Scanning Microscopy using 3D Printed Optics	107
5.1 Lenslet Arrays	108
5.2 Application in Multifocal Image Scanning Microscopy	113
5.3 Image Scanning Microscopy Results	118
5.4 Discussion	131
Chapter 6 – Conclusion	133
6.1 Research Achievements	133
6.2 Future Work	137
6.3 References	139
Appendix A	157
Appendix B	158
Appendix C	160
Appendix D	161
Appendix E	166

List of Figures

- Figure 1.** Widefield imaging vs Point-Scanning Confocal _____ Page 6
- Figure 2.** Rayleigh and Abbe resolution limits as Gaussian Point-Spread Functions ____ Page 7
- Figure 3.** PALM principal example _____ Page 12
- Figure 4.** STED Microscopy example. Scale bars = 3 μm _____ Page 13
- Figure 5.** Example of the Moiré effect _____ Page 15
- Figure 6.** Line plot showing the excitation illumination point \mathbf{x}_1 (blue) and detection point \mathbf{x}_2 (red) for ISM imaging with the resultant combined PSF signal \mathbf{x} (black). _____ Page 17
- Figure 7.** Image scanning microscopy schematic of PSF processing with biological image output. (A) ROI of extracted fluorescent spots. (B) Convolution of captured fluorescence with Gaussian filter. (C) Pixel resampling of the processed fluorescence. (D) Resolution enhanced resulting image. Figure (A-C) adapted from Ward and Pal and (D) from York *et al.* Scale bars = 5 μm . _____ Page 18
- Figure 8.** Multifocal image scanning microscopy technique. (A) Multifocal excitation. (B) Optical pinholing. (C) Contraction of pinholed spots using second microlens array. (D) Optical image summation onto camera. Figure adapted from York *et al.* _____ Page 19
- Figure 9.** The essential steps from design to final printed part _____ Page 21
- Figure 10.** SLA printing schematic. _____ Page 23
- Figure 11.** Two-Photon polymerisation example. _____ Page 25
- Figure 12.** Schematic showing the staircase effect equal to z-height in the final print against the initial design _____ Page 28
- Figure 13.** 3D printed optics examples. (A) 2PP 3D printed half-ball lenses; (B) SEM images of 2PP manufactured micro-objectives at different FOVs and cross-sectional images of micro-objective lens at different FOVs; (C) Colour changing Fresnel lens printed by SLA method; (D) Intraocular lens printed using DLP method; (E) multi-material contact lenses printed by DLP method. _____ Page 30
- Figure 14.** SEM images of 2PP manufactured microlenses for imaging applications. (A) – SEM images of the 2PP manufactured microlenses; (B) – Zoom in of the SEM individual lenslet; (C) – Image acquired using 3D printed optic within an optical microscope. _____ Page 32
- Figure 15.** Imaging performance of 2PP manufactured optics. (A) – Ray-tracing of printed triplet system; (B) –1951 USAF target imaged using 3D printed triplet system; (C) – SEM image of the triplet system. Scale bars = 20 μm _____ Page 33
- Figure 16.** Photograph of missing layers from the Form 3 printer. _____ Page 37
- Figure 17.** Chitubox sliced STL file with supporting structures for successful printing (A) and axial

slices (B). Highland cow file unaltered and obtained from <https://www.thingiverse.com/thing:5417799> _____ Page 39

Figure 18. Example photographs of under (A) and over exposed (B) printed targets with digitally zoomed ROIs _____ Page 41

Figure 19. Images of the difference in resultant prints from two different commercial clear resins. (A) Target print from Resin 1 for curvature evaluation. (B) Target print from Resin 2 for curvature evaluation. (C) Transparency comparison between two printed targets using different resins. (D) Feature precision using Resin 2. (E) Feature precision using Resin 1. _____ Page 44

Figure 20. Comparison of different resin yellowing both immediately after printing and after some post-curing. (Top) – Anycubic High Clear resin printed cuboids with different thicknesses and differing timescales of post-curing. (Bottom) – Elegoo Translucent ABS-like resin printed cuboids with different thicknesses and differing timescales of post-curing _____ Page 45

Figure 21. 3D printed optic before (left) and after (right) spin-coating procedure. Before coating the optic the print layers create a staircase toward the centre axis of the lens. After spin-coating, the lens surface is smoothed across the staircase surface _____ Page 47

Figure 22. Exaggerated diagram of 3D printed optic refractive index interfaces after spin-coating procedure, with arrows to indicate the path of collimated light through the optic. _____ Page 50

Figure 23. Schematic of 3D printed optics spin-coating manufacturing process. (A)-(D) Manufacturing an optically clear non-planar surface; (E)-(G) Manufacturing an optically clear planar surface; (A) 3D printing schematic showing the layer-by-layer technique using incident UV light; (B) Cleaning stage using isopropyl alcohol (IPA) to remove residual resin; (C) spin coating non-planar surface by pipetting resin onto surface prior to spinning; (D) non-planar spin coated surface cured with UV light; (E) resin pipetted onto glass slide for spin coating; (F) resin-coated glass slide and 3D printed planar surface placed in contact and vacuumed together; (G) UV curing of resin coated slide and planar 3D printed surface; (H) schematic of resultant optically clear 3D printed part, shown here as a plano-convex lens _____ Page 51

Figure 24. Visual differences in the obtained transparency of a 3D printed optic using the described optical post-processing methods. From left to right they introduce a lens with no optical post-processing; a lens where only its planar side has been optically post-processed; a lens where only its convex surface has been post-processed; and a lens with both surfaces optically post-processed _____ Page 53

Figure 25. Schematic of 3D printed optics moulding manufacturing process. (A)-(D) Manufacturing an optically clear non-planar surface; (E)-(G) Creation of a mould and optically clear final optic; (A) 3D printing schematic showing the layer-by-layer technique using incident UV light; (B) Cleaning stage using isopropyl alcohol (IPA) to remove residual resin; (C) spin

coating non-planar surface by pipetting resin onto surface prior to spinning; (D) non-planar spin coated surface cured with UV light; (E) outgassing of coated 3D print; (F) mould mixture is used to create a master mould from the processed print; (G) a transparent UV curing resin fills the mould; (H) the moulded optic is obtained by UV curing the resin within the mould. ___ Page 54

Figure 26. Photograph examples of key moulding process stages with commercial MLA for comparison. Scale bars = 15 mm _____ Page 56

Figure 27. Photograph of processed and unprocessed cuboids of various thicknesses for optical transparency evaluation. The processed cuboids show higher optical transparency on the gridlines beneath across all cuboid thicknesses compared to the unprocessed cuboids __ Page 57

Figure 28. Transmission results from multi-mode laser light through optically clear 3D printed blocks of increasing thicknesses (left) and the schematic of the measurement setup (right). _____ Page 58

Figure 29. Optical profiler results from a commercial glass microscope slide and a planar surface post-processed using a commercial glass microscope slide. (Left) – 2.5x magnified optical profile image of the glass slide surface with a colourbar legend to show height differences. (Right) – 2.5x magnified optical profile image of the 3D printed post-processed planar surface with a colourbar legend to show height differences _____ Page 59

Figure 30. Surface roughness measurements acquired using the optical profiler of the commercial glass microscope slide and the 3D printed planar surface manufactured using a glass microscope slide. (Left) – Commercial glass slide x and y surface roughness line profiles generated using the optical profile results. (Right) – 3D printed optically post-processed planar x and y surface roughness generated using the optical profile results _____ Page 61

Figure 31. Non-contact results of commercial and 3D printed lenslets. (A) – Optical profile of commercial lenslet showing form across the surface. (B) – Optical profile of 3D printed lenslet showing form across the surface _____ Page 62

Figure 32. Surface roughness measurements acquired using the optical profiler of the commercial microlens array and the 3D printed lenslet array. (Left) – Commercial microlens array x and y surface roughness line profiles generated using the optical profile results. (Right) – 3D printed optically post-processed lenslet array x and y surface roughness generated using the optical profile results _____ Page 63

Figure 33. Stylus data from an uncoated convex surface of a 20 mm focal length, 12.7 mm diameter 3D printed lens _____ Page 64

Figure 34. Geometrical characteristics of the 3D printed lenses with a commercial comparison. (A) Surface profile of a commercial 20 mm focal length, 12.7 mm diameter lens; (B) Surface profile of a 3D printed version of a 20 mm focal length, 12.7 mm diameter lens; (C) Surface profile of a

3D printed 10 mm focal length, 6 mm diameter lens; (D) Surface profile of a 3D printed plano-concave lens with a -6 mm focal length and 6 mm diameter _____ Page 66

Figure 35. Geometrical characteristics of the commercial and 3D printed lenslet arrays. (A) Surface profile of the commercial version of the microlens array; (B) Surface profile of the 3D printed lenslet array _____ Page 67

Figure 36. Microscope setup for brightfield and fluorescence imaging comparison of 3D printed and commercial single and 4-lens objectives. (A) Schematic optical path of the microscope setup using either a group of 4 singlet lenses or a single plano-convex lens as the primary objective, shown as (B) and (C) respectively. 3DPL – 3D Printed objectives under test; DM – dichroic mirror; EF – emission filter. (B) Schematic and image of multi-lens objective with 4 singlet lenses. #2 Commercial aspherical $f = +6$ mm lens; #3 $f = +10$ mm plano-convex lens; #4 $f = -6$ mm plano-concave lens; #5 $f = +15$ mm plano-convex lens. (C) Photograph of single lens objective with 12.7 mm diameter, 3D printed $f = +20$ mm plano-convex lens and commercial counterpart with identical specifications. For both objective types, Numbers #1, #3 and #4 indicate which lenses are used to test 3D printed lenses in imaging. Scale bars = 10 mm. Page 71

Figure 37. Example of critical illumination and confirmation marker of Köhler illumination. (A) – Photograph of critical illumination from LED source. (B) - In-focus image of Aperture Diaphragm edges, exemplifying correct axial distance for Köhler _____ Page 72

Figure 38. Photographs of resultant illumination patterns using single mode excitation through optically clear spin-coated 3D printed optic. (A) Collimated illumination through a spin-coated 3D printed optic. (B) Collimated illumination through a commercial equivalent optic. (C) Defocused illumination through a spin-coated 3D printed optic. (D) Defocused illumination through a commercial equivalent optic. Scale bars = 50 mm _____ Page 73

Figure 39. Photographs of resultant illumination patterns using multimode excitation through optically clear spin-coated 3D printed optic. (A) Collimated illumination through a spin-coated 3D printed optic. (B) Collimated illumination through a commercial equivalent optic. (C) Defocused illumination through a spin-coated 3D printed optic. (D) Defocused illumination through a commercial equivalent optic. Scale bars = 50 mm _____ Page 74

Figure 40. Photographs of resultant illumination patterns using single mode excitation through optically clear moulded 3D printed optic. (A) Collimated illumination through a moulded 3D printed optic. (B) Collimated illumination through a commercial equivalent optic. (C) Defocused illumination through a moulded 3D printed optic. (D) Defocused illumination through a commercial equivalent optic. Scale bars = 50 mm _____ Page 76

Figure 41. Raytrace diagram, modulation transfer function (MTF) and 3D assembly schematics for single lens objective. Single lens objective with entrance aperture of 8 mm diameter at 1 mm

distance from the plano-convex lens; the MTF shows clear image deterioration due to the basic spherical lens design; the 3D assembly shows the 3D printed support to house the lens in a 25.4 mm cage plate _____ Page 78

Figure 42. Raytrace diagram, modulation transfer function (MTF) and 3D assembly schematics for the multi-lens objective. (A) Multi-lens objective with two plano-convex, one plano-concave and one aspheric lens and entrance aperture of 2 mm diameter at 1mm distance from the proximal end lens; the MTF shows an almost diffraction limited performance; the 3D assembly highlights the multiple spacers for axial alignment of the lenses _____ Page 80

Figure 43. Strehl ratio plot against lateral offset of individual lenses with respect to the optical axis, with supporting lens figure as plot legend _____ Page 81

Figure 44. Brightfield USAF Target images using lens #1 as a single-lens 8x objective. (A) left - Full FOV 1951 USAF target using commercial lens #1 as objective; middle – central cropped ROI from commercial lens image on left; right – line graph taken through group 7 elements 1-6; (B) left – Full FOV 1951 USAF target using 3D printed lens #1 as objective; middle - central cropped ROI from 3D printed lens image on left; right - line graph taken through group 6 elements 5-6 and group 7 elements 1-2 _____ Page 83

Figure 45. Brightfield variegated *Hosta* images using lens #1 as an 8x objective. (A) Top – Full FOV of the *Hosta* cellular network and stomata using the commercial 8x objective. Bottom Left – Digitally zoomed ROI showing multiple cells and stomata. Bottom Right – Digitally zoomed ROI of a single stoma surrounded by plant cells. (B) Top – Full FOV of the *Hosta* cellular network and stomata using the 3D printed 8x objective. Bottom Left – Digitally zoomed ROI showing multiple cells and stomata. Bottom Right – Digitally zoomed ROI of a single stoma surrounded by plant cells _____ Page 84

Figure 46. Brightfield cyanobacteria images using lens #1 as an 8x objective. (A) Top – Full FOV of an individual cyanobacteria filament using the commercial 8x objective. Bottom Left – Digitally zoomed ROI showing multiple cells within the filament. Bottom Right – Digitally zoomed ROI the chloroplast containing cells. (B) Top – Full FOV of an individual cyanobacteria filament using the 3D printed 8x objective. Bottom Left – Digitally zoomed ROI showing multiple cells within the filament. Bottom Right – Digitally zoomed ROI the chloroplast containing cells _____ Page 85

Figure 47. Brightfield onion images using lens #1 as an 8x objective. (A) Top – Full FOV of the iodine-stained onion cells using the commercial 8x objective. Bottom Left – Digitally zoomed ROI showing multiple cells and nuclei. Bottom Right – Digitally zoomed ROI of the onion nuclei. (B) Top – Full FOV of the iodine-stained onion cells using the 3D printed 8x objective. Bottom Left – Digitally zoomed ROI showing multiple cells and nuclei. Bottom Right – Digitally

Figure 48. Brightfield images using the 4-lens objective. (A-D) 1951 USAF Group 7 target images with line plot profiles underneath using commercial 4-lens objective configuration. (A) Fully commercial 4-lens objective; (B) lens #4 replaced with a 3D printed version; (C) lenses #3 and #4 replaced with 3D printed versions; (D) lenses #3, #4 and #5 replaced with 3D printed versions _____ Page 88

Figure 49. Brightfield images using three identically processed lenses of 3D printed lens #3 in the 4-lens objective configuration. (A-C) 1951 USAF Group 7 target images with line plot profiles underneath using commercial 4-lens objective configuration _____ Page 90

Figure 50. Brightfield variegated *Hosta* images using the 4-lens objective. (A) Commercial (left) and 3D printed (right) lens #4 objective images of the *Hosta* cells and stoma, with nuclei visible within the guard cells. (B) Commercial (left) and 3D printed (right) lens #3 and #4 objective images of the *Hosta* cells and stoma, with nuclei visible within the guard cells. Page 91

Figure 51. Brightfield cyanobacteria images using the 4-lens objective. (A) Commercial (left) and 3D printed (right) lens #4 objective images of the cyanobacteria filament with individual cells distinct from one another. (B) Commercial (left) and 3D printed (right) lens #3 and #4 objective images of the cyanobacteria filament _____ Page 92

Figure 52. Brightfield onion images using the 4-lens objective. (A) Commercial (left) and 3D printed (right) lens #4 objective images of the onion cells and nucleus. (B) Commercial (left) and 3D printed (right) lens #3 and #4 objective images of the onion cells and nucleus _____ Page 93

Figure 53. Fluorescent slide images taken using commercial and 3D printed 8x objectives. (Left) Thorlabs fluorescent slide imaged with the commercial 8X objective. (Right) Thorlabs fluorescent slide imaged with the 3D printed 8x objective _____ Page 95

Figure 54. Fluorescent bead images taken using commercial and 3D printed 8x objectives. (A) 500 nm fluorescent bead imaged with the 8x commercial objective. (B) 500 nm fluorescent bead imaged with the 8x 3D printed objective _____ Page 96

Figure 55. Fluorescence variegated *Hosta* images using lens #1 as an 8x objective. (A) Top – Full FOV of the fluorescing *Hosta* nuclei within the stomata guard cells using the commercial 8x objective. Bottom Left – Digitally zoomed ROI showing stomata nuclei. Bottom Right – Digitally zoomed ROI of a single stoma showing individually fluorescing nuclei. (B) Top – Full FOV of the fluorescing *Hosta* nuclei within the stomata guard cells using the commercial 8x objective. Bottom Left – Digitally zoomed ROI showing stomata nuclei. Bottom Right – Digitally zoomed ROI of a single stoma showing individually fluorescing nuclei _____ Page 98

Figure 56. Fluorescent cyanobacteria images using lens #1 as an 8x objective. (A) Top – Full FOV of an individual fluorescing cyanobacteria filament using the commercial 8x objective. Bottom

Left – Digitally zoomed ROI showing multiple cells within the filament. Bottom Right – Digitally zoomed ROI of the chloroplast containing cells. (B) Top – Full FOV of an individual fluorescent cyanobacteria filament using the 3D printed 8x objective. Bottom Left – Digitally zoomed ROI showing multiple cells within the filament. Bottom Right – Digitally zoomed ROI of the chloroplast containing cells _____ Page 99

Figure 57. Uniform fluorescent target images captured using 4-lens commercial and 3D printed lens combinations with respective line plots underneath. (A) – Fluorescent slide captured using the commercial objective. (B) – Fluorescent slide captured using the lens #3 combination of the 3D printed objective. (C) – Fluorescent slide captured using lenses #2 and #3 in the 3D printed objective _____ Page 100

Figure 58. Fluorescent bead images taken using commercial and 3D printed 4-lens objectives. (A) 500 nm fluorescent bead imaged with the 4-lens commercial objective. (B) 500 nm fluorescent bead imaged with the 4-lens objective with 3D printed lens #3. (C) 500 nm fluorescent bead imaged with the 4-lens objective with 3D printed lens #3 and #4 _____ Page 101

Figure 59. Fluorescent variegated *Hosta* images using the 4-lens objective. (A) Commercial (left) and 3D printed (right) lens #4 objective images of the *Hosta* stoma, with fluorescing nuclei visible within the guard cells. (B) Commercial (left) and 3D printed (right) lens #3 and #4 objective images of the *Hosta* stoma, featuring significant blurring in the 3D printed case _____ Page 102

Figure 60. Fluorescent cyanobacteria images using the 4-lens objective. (A) Commercial (left) and 3D printed (right) lens #4 objective images of the individually fluorescing cyanobacteria cells. (B) Commercial (left) and 3D printed (right) lens #3 and #4 objective images of the individually fluorescing cyanobacteria cells _____ Page 103

Figure 61. Designs of lenslet arrays showing two different geometries and the corresponding lenslet pitch. (A) – Honeycomb design showing minimised pitch displacement. (B) – Square lenslet array design showing a higher pitch displacement. (C) – Moulding fabrication schematic showing silicone moulding and UV resin casting. (D) – Moulded versions of each design. (E) The absorptive honeycomb mask _____ Page 110

Figure 62. Chitubox figure showing master copy (A) and pinhole array (B) at 90° to the build plate with supporting features _____ Page 112

Figure 63. Microscope setup for multifocal ISM comparison of 3D printed and commercial lenslet arrays. EX – 488 nm single-mode fibre-coupled excitation. SV – silver mirror. MLA – lenslet array under investigation, either the commercial microlens array or the 3D printed lenslet array. MEMS – 2 mm diameter 2D MEMS micromirror. DIC - dichroic mirror; EF – emission filter. CM – IDS-3060 CMOS camera _____ Page 113

Figure 64. Schematic for the ISM processing script in Python. (Left to Right) – Image stack is loaded into Python; each maximum intensity coordinate location is saved as a variable; each maxima at each coordinate location is cropped to an ROI; each of the cropped maxima are individually convolved with a Gaussian Blur; each convolved maxima is shrunk to by a factor of two by doubling the spatial region around the maxima information; each resulting maxima is added into one image with original spatial dimensions but double the lateral pixel numbers _____ Page 116

Figure 65. Fluorescence excitation on a uniform slide from the commercial and 3D printed lenslet arrays with individual spot line profiled below. (A) – Commercial microlens array with associated digitally zoomed in lenslet excitation ROI and line profile. (B) – 3D Printed lenslet array without background removing mask. (C) – 3D Printed lenslet array using background removing mask with associated digitally zoomed in lenslet excitation ROI and line profile _____ Page 118

Figure 66. Analysis of processing ROI and Gaussian Blur on resulting 165 nm bead, with widefield FOV for bead reference. (A) – Summed laser-scanning image showing each fluorescent bead in the dataset. (B-D) – Different results of ISM processing from pixel ROI windows of the fluorescent maxima. (E-G) – Different results of ISM processing from Gaussian Blur standard deviation values from a 7x7 fluorescence maxima ROI _____ Page 122

Figure 67. Resolution measurements from diffraction-limited and ISM configurations using 165 nm beads. (A) – Widefield image of 165 nm bead with resulting line-plot below. (B) – Summated image from the commercial MLA multifocal laser scanned implementation with respective line-plot below. (C) – optimised ISM on the 165 nm bead sample with respective line-plot below _____ Page 123

Figure 68. Widefield image of BPAE cell with fluorescent labelled mitochondria, including a digital zoom in of a ROI and cross-section through a mitochondria strand _____ Page 125

Figure 69. Laser scanned summed images from the commercial and 3D printed lenslet arrays without pixel re-assignment. (A) – The mitochondria in a BPAE cell with corresponding digital zoomed ROI and respective ROI line plot for a mitochondria strand using the commercial lenslet array. (B) – The same BPAE cell with labelled mitochondria with corresponding digital zoomed ROI and respective ROI line plot for the mitochondria strand cross-section using the 3D printed lenslet array _____ Page 128

Figure 70. Commercial and 3D Printed ISM results. (A) – Commercial microlens array ISM processed image, with corresponding digital zoomed ROI and respective line profile to show the cross section of a mitochondria strand. (B) – 3D Printed lenslet array ISM processed image, with corresponding digital zoomed ROI and respective line profile to show identical mitochondria

Figure 71. Geometrical characteristics of the lenses within section 3.x.x with 90° rotational variants in the measurement axis. (A) Surface profile of a commercial 20 mm focal length, 12.7 mm diameter lens; (A90) Surface profile of A rotated by 90°; (B) Surface profile of a 3D printed version of a 20 mm focal length, 12.7 mm diameter lens; (B90) Surface profile of B rotated by 90°; (C) Surface profile of a 3D printed 10 mm focal length, 6 mm diameter lens; (C90) Surface profile of C rotated by 90°; (D) Surface profile of a 3D printed plano-concave lens with a -6 mm focal length and 6 mm diameter; (D90) Surface profile of D rotated by 90°;

Page 155

“NO ADMITTANCE EXCEPT ON PARTY BUSINESS”

- J. R. R. Tolkien, *The Lord of The Rings*

Chapter 1. Introduction

Biomedical research maintains its fundamental position within the scope of global research, with COVID acting as a prominent and obvious example to its necessity. This essential field of research is predicated in part on the successful advancement of optical microscopy, to deepen our understanding of biological mechanisms at the cellular and sub-cellular level. However, a disproportionately large volume of biological and biomedical research currently exceeds the budget of researchers or healthcare clinic, especially in low resource settings. This wide economic availability gap is the motivation behind 3D printed optics within optical imaging, as a method of democratising microscopy and providing rapid, on the ground field diagnostics. Additionally, 3D printed optics offer new free-form design concepts for novel imaging applications.

1.1 Aims & Novelty

The overall aim of this research is to exemplify the current potential that low-cost desktop 3D printed optics has in the excitation or imaging arms of microscope imaging systems. The work is based on proof-of-principle work, predominantly by Vaidya¹ and later by Berglund², though it expands upon the current 3D printed optics research in development and application. Novel contributions have been made in this field within this body of work by manufacturing and utilising 3D printed lenses as objectives within brightfield and fluorescence biological imaging, and within super-resolution excitation of biological structures. The benefit is therefore a cost-effective method for customisable optics for use within biological imaging systems and super-resolution optical microscopy.

1.2 Outline

Chapter 1 provides a brief outline of the motivation behind the entailed research. Additionally, the aims of the PhD research and overall novelty is explained. Also highlighted in this chapter are peer-reviewed outcomes from the PhD including conference papers and journal papers.

Chapter 2 contextualises the work to follow by detailing the relevant microscopy methods for

Chapter 1. Introduction

biological imaging and 3D printing techniques for microscopy. The background concepts are covered to provide benchmarks and comparisons to justify the techniques used within this body of research.

Chapter 3 establishes the fundamental methods developed for low-cost optical quality 3D printing, as well as the quantification of these optics in characteristics such as form, surface roughness, and transmission. The shown results from the standard test targets and biological specimens were also part of a peer-reviewed journal publication and peer-reviewed conference papers/presentations.

Chapter 4 validates the performance of the 3D printed optics in comparison to their commercial counterparts within brightfield and fluorescence imaging. The microscope itself is detailed within this chapter and it is characterised using the commercial optics against standard test targets. The test target imaging is then compared against imaging using 3D printed objectives, as well as the comparative performance in resolving biological features using commercial or 3D printed objectives. The results from the standard test targets and biological specimens were again part of a peer-reviewed journal publication and peer-reviewed conference papers/presentations.

Chapter 5 details the developed super-resolution system and its application to biological structures. A comparison is then drawn on the performance of this system in its commercial form against using 3D printed optics in the fluorescence excitation of the biological structures and the microscopy information obtained is evaluated. Preliminary results from this chapter were included in a peer-reviewed conference paper/presentation.

Chapter 6 provides an overall evaluation and discussion of the outcomes and challenges of the full breadth of research detailed in the previous chapters. Additionally, potential future research is highlighted within this chapter.

1.3 Publications

1.3.1 Peer-reviewed Journals:

***Christopher, J.**, *Rooney, L. M. *et al.* “Low-cost 3D printed lenses for brightfield and fluorescence microscopy”, *Biomed. Opt. Express* 15, 2224-2237, 2024, <https://doi.org/10.1364/BOE.514653>

Chapter 1. Introduction

*Rooney, L. M., ***Christopher, J.** *et al.* “Printing, Characterising, and Assessing Transparent 3D Printed Lenses for Optical Imaging”, *Adv. Mater. Technol.* 2024, 2400043. <https://doi.org/10.1002/admt.202400043>

*Indicates co-first authors with equal contribution

Tinning, P., Donnachie, M., **Christopher, J.** *et al.* “Miniaturized structured illumination microscopy using two 3-axis MEMS micromirrors”, *Biomed. Opt. Express* 13, 2022, <https://doi.org/10.1364/BOE.475811>

1.3.2 Conference Papers & Presentations:

Christopher J., Donnachie, M. *et al.* “Using 3D printed optical elements for multifocal image scanning microscopy”, *Proc. SPIE* 12827 2024, <https://doi.org/10.1117/12.3002507>

Christopher, J., Rooney, L. *et al.* “Using 3D Printed Optics for Fluorescence Microscopy”, Royal Microscopical Society (RMS) conference Microscience Microscopy Conference (MMC), 2023, <https://doi.org/10.22443/rms.mmc2023.63>

Christopher, J., Tinning, P. W. *et al.* "3D printing optical components for microscopy using a desktop 3D printer," *Proc. SPIE* 12013 2022; <https://doi.org/10.1117/12.2608614>

Christopher, J., Donnachie, M. *et al.* “Increasing MEMS micromirror line-scan rates through 3D-printed micro-optics”, International Conference on Optical MEMS and Nanophotonics (OMN) and SBFoton International Optics and Photonics Conference (SBFoton IOPC), Campinas, Brazil, 2023, <https://doi.org/10.1109/OMN/SBFotonIOPC58971.2023.10230934>

Christopher, J., Rooney, L. *et al.* “Remote-refocus microscopy using a MEMS piston micromirror”, Royal Microscopical Society (RMS) Microscience Microscopy Conference (MMC) 2023, doi: [10.22443/rms.mmc2023.199](https://doi.org/10.22443/rms.mmc2023.199)

Christopher, J., Janin, P. *et al.* “22.3 kHz update rate Lissajous scanning using a single double resonant MEMS scanner”, International Conference on Optical MEMS and Nanophotonics (OMN) 2022

Chapter 1. Introduction

Tinning, P. W., Donnachie, M., **Christopher, J.** *et al.* "A structured illumination microscopy module using two micro-electromechanical system scanning micromirrors," Proc. SPIE 11967, Single Molecule Spectroscopy and Superresolution Imaging XV, 1196706 (2 March 2022); <https://doi.org/10.1117/12.2608564>

Chapter 2. Background

Optical microscopy has been studied, developed and employed for centuries, and has seen rapid development over the past few decades across a litany of techniques. Microscopy in its simplest form is used for a wide variety of purposes ranging from applications in biology and material science to quantum physics and climate change research. Specifically, high-resolution microscopy techniques are constantly being developed and are beginning to be used within biology more widely, though they often require more elaborate designs and therefore higher cost optics and control elements. Recently, 3D printing has been used to help develop budget-friendly optical microscopy with a prioritised focus on creating mechanical supports and parts. This chapter aims to explore and contextualise the high-level developments and trends in optical microscopy from the turn of the millennium and offers an in-depth analysis of the current state of 3D printing in microscopy, with a specific focus on 3D printing optical elements in microscopy.

2.1 Optical Microscopy

2.1.1 Microscopy Fundamentals

Optical microscopy has been an essential tool to solve biological questions since the 17th century^{3,4}. Since its origin, microscopy has been developed into evermore intricate methods to gain more and clearer information from a sample. In traditional brightfield widefield imaging, an image can be captured of a sample by collecting wavefronts emitted or scattered by the sample through a microscope objective which guides them toward the image plane, i.e. the specific axial position where the sample is in sharp focus^{5,6}. The sample can be illuminated using either white light, which creates contrast through transmission or scattering/reflection at the sample, or using specific excitation wavelengths to capture a fluorescence response created in the sample through extrinsic fluorescence labels or intrinsic sample fluorophores. The output is an image of the sample which has ideally been illuminated evenly across the full field of view (FOV), which allows e.g. biologists to obtain details about the morphology of their sample, tissue/cell information, including dynamic developmental process information. An alternative to widefield illumination is through point-scanning approaches, such as confocal microscopy. Instead of illuminating a wide area of a fluorescent sample (see Figure 1), confocal microscopy focuses a laser into the sample plane to create a small illumination spot.

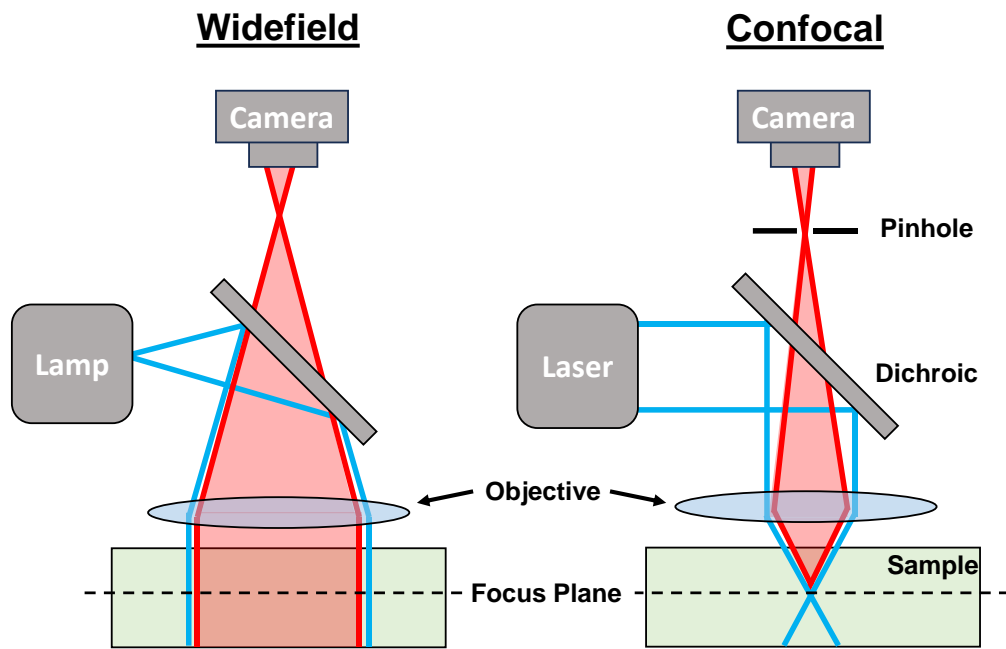


Figure 1. Widefield imaging vs Point-Scanning Confocal. Figure adapted from AxiomOptics ²³⁴

By passing the fluorescence emission from the sample through a dichroic mirror (a wavelength specific filter) and a pinhole, only sample information within the focal plane is detected, giving confocal microscopy the possibility to optically section samples and only allow information from the focus plane to reach a detector. However, only a small excitation area of the sample has been detected due to the focused illumination light, and for a complete sample image the excitation must be scanned across the entire FOV. Though extra complexity and work is required to obtain a complete sample image, the result is an image with less background noise through scattering in the regions outside of the sample focal plane, which is present in widefield illumination.

The details observed in an image of a sample are in both illumination cases limited by the diffractive nature of light, as found by both Abbe and Rayleigh⁷⁻⁹. The physical phenomenon limiting the ultimately achievable level of recoverable detail in the image of the sample is therefore called the optical diffraction limit, or the resolution limit of a microscope, shown visually in Figure 2. Specifically, the lateral depiction of the Abbe limit corresponds to the distance of two overlapping airy disks which are considered to be two perfect point-sources of light where the full-width at half maximum (FWHM) is distinguishable in each airy disk. The lateral Abbe resolution limit is therefore:

$$d_{xy} = \frac{\lambda}{2 \cdot NA} \quad (1)$$

where d_{xy} is the resolution of the system, which is dictated by the wavelength of light used, λ , and the numerical aperture NA which is the range of angles accepted in the imaging objective. It is also clear then from Abbe's limit that there is no dependency on magnification for the resolvable limitations of the microscope in question, as magnification and numerical aperture are not directly proportional to each other. A slightly different notation of the optical resolution limit originates from Rayleigh and this limit distinguishes two overlapping airy disks at a minimum distance where the central maximum of one airy disk overlaps with the first minimum of the other airy disk^{9,10}. This corresponds to a theoretical limit equation of:

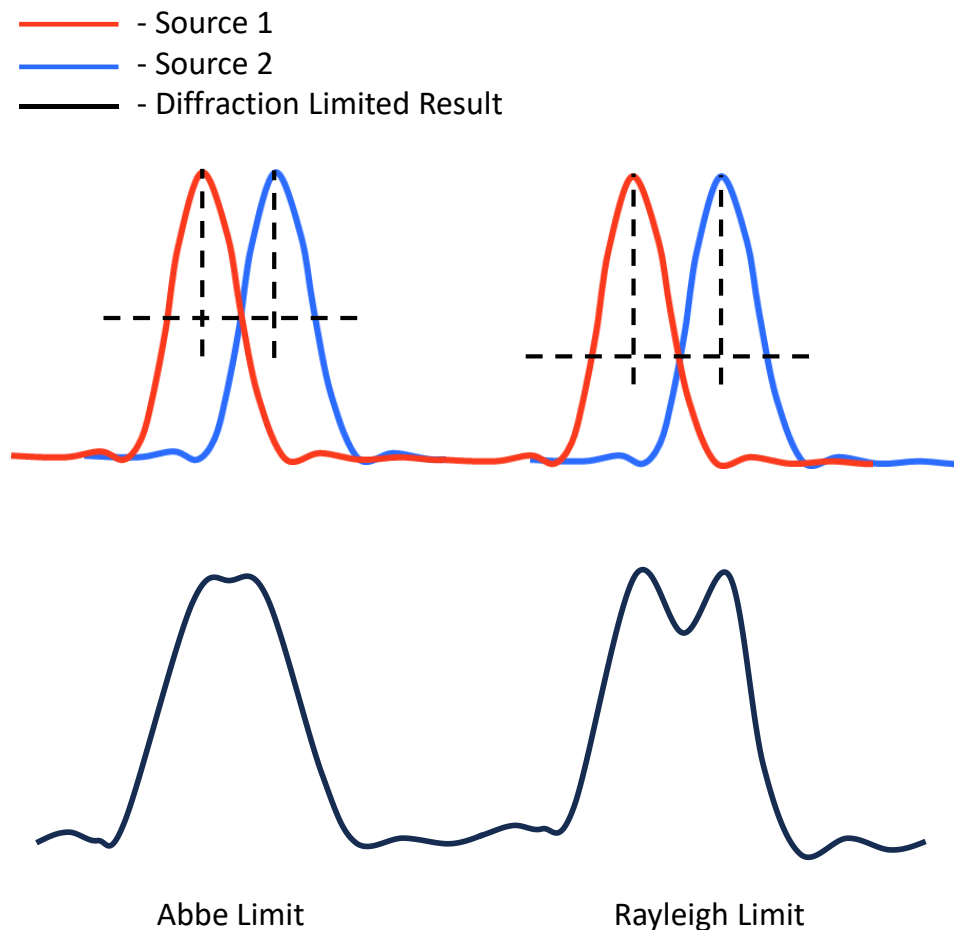


Figure 2. Rayleigh and Abbe resolution limits as Gaussian Point-Spread Functions. Figure adapted from Kaderuppan *et al.*^{2,35}

Chapter 2. Background

$$d_{xy} = \frac{0.61 \cdot \lambda}{NA} \quad (2)$$

Both equations are widely used in optical microscopy to evaluate the expected lateral resolution limits of the imaging system used¹¹⁻¹⁶. Even where an optical microscope is equipped with the highest quality optics with near perfect alignment and the highest obtainable NA, which currently is $\sim 1.7NA$, the resolution limit is still going to be limited to 150 – 200 nm in their best-case states. This theoretical limit, however, is virtually unattainable due a plethora of reasons including inhomogeneities in the specimen itself contributing scattering effects on the optical excitation, inhomogeneous refractive indices, and imperfect optics, all of which combine to slightly lower the resolution compared to the theoretical limit. A diffraction-limited image explicitly has its lateral and axial dimensions defined by the excitation wavelength used and NA of the objective, with the NA depending on the refractive index of the imaging media as well as the angular aperture of the imaging objective. The angular aperture of the objective limits the resolution as information is only collected from one side of the objective, meaning even if the information passed through the objective was kept perfect there still exists a fundamental limit due to the NA. When discussing resolution, microscopists are also not only limited to the lateral resolution but also the axial or z-resolution. This defines how well details can be resolved throughout axial sections of a specimen, i.e. the minimum distance through the focus of a sample at which two distinct objects can be distinguished. This was defined by Abbe as:

$$d_z = \frac{2 \cdot \lambda}{NA^2} \quad (3)$$

And using equation 3, the maximum diffraction limited axial resolution is ~ 360 nm. Therefore, if imaging a highly convolving structure such as cellular organelles for example, the diffraction-limited resolution appears not only as limitations of distinguishable features throughout the axial axis, but also as lower contrast in the imaging plane across the specimen due to out-of-focus light throughout the specimen.

2.1.2 Modern Microscopy

Optical microscopes have faced development in almost all parts of their manufacture since their uptake in research spaces and healthcare environments. Though as in the 18th century they still begin with an illumination source, which itself has seen significant developments across the past few decades. Older, expensive lamps and bulbs have mostly become dismissed

Chapter 2. Background

in favour of lower cost light-emitting diodes (LEDs)¹⁷⁻²¹. Lasers are additionally employed in many advanced imaging systems and themselves have become smaller and lower cost, allowing for more economic and efficient integration into smaller microscope systems^{22,23}. Additionally, to make full use of laser excitation in point-scanning microscopes, lateral mirror scanners have become more compact such as microelectromechanical systems (MEMS) micromirrors, which offer small diameter mirrors with over kHz range scanning speeds^{22,24-42}. And whilst eyepieces continue to be a useful tool especially in commercially available teaching microscopes, the digitisation of optical imaging through a variety of camera technologies, both low-cost and high-end, have made sharing results from an optical imaging system faster and simpler than ever. Optical microscopy has therefore transcended its origins, with lower cost and finer-tuned illumination manipulated by beam shaping devices and a sample imaged with low noise, fast and high sensitivity available through the latest camera generations.

One integral component, however, has not seen the same vivid level of development: the core element in all microscopes, the optics. Though the methods of optics production now have higher manufacturing accuracy, objective lenses now are virtually identical to objectives across the last century, aside from some key exceptions such as the Snouty objective^{43,44} which are used only in specific areas of optical microscopy. With specific integration also comes usually higher costs, as the volume of production and sales of Snouty objectives will be less compared to e.g. 40x oil-immersion objectives or glass plano-convex lenses. Throughout this, objective optics manufacture in general still utilises a glass grinding and polishing method which originated two centuries ago. Alternative fabrication approaches for large-scale optics manufacturing such as moulding or droplet techniques are available but only used for specific applications. It is the lack of development of fundamentally different optics fabrication approaches where new technologies could have a significant impact by enabling new approaches to be tested.

Regardless of the tools used in modern microscopy, fluorescent molecules are themselves beyond the optical diffraction barrier, at a scale of tens of nanometres in size. To distinguish details finer than the discussed diffraction limits, a plethora of physics phenomena have been used in recent history to surpass the optical diffraction barrier by two-fold or more, untangling further complex mysteries within biology. This specific area of optical microscopy is known as super-resolution microscopy.

2.2 Super-Resolution Microscopy

2.2.1 Overview

Through recent decades, numerous technological advancements have given way to faster and higher resolution imaging beyond the diffraction limit. The litany of developed techniques to surpass the resolution limit range from entirely optical methods, such as optical re-assignment of sample fluorescence, to computational techniques, such as localisation-based approaches, and an overview of some of the most prominent methods is given in Table 1. The foundations of going beyond the lateral resolution limit can be defined through either stochastic localisation approaches of individually fluorescing proteins, with techniques such as photoactivated localization microscopy (PALM) or minimal photon fluxes (MINIFLUX); or through structuring the illumination into defined patterns which vary in how they extract information beyond the resolution limit, such as in stimulated emission depletion (STED) compared to

	Technique	Method	Developments	Lateral Resolution	Merits	Limitations
Stochastic Techniques	SMLM	Stochastic Emission Separation	<ul style="list-style-type: none"> •PALM/STORM •PAINT 	10 – 20 nm	<ul style="list-style-type: none"> • Single-molecule sensitivity • High resolution 	<ul style="list-style-type: none"> • Usually 2-colour limited • Limited axial range • Low (≈ 30 s) imaging speed
	MINIFLUX	Stochastic PSF Engineering	Currently no new developments	1 – 3 nm	<ul style="list-style-type: none"> • Lower light doses to SMLM • Highest resolution 	<ul style="list-style-type: none"> • Similar imaging speed to SMLM • Small ($\approx 25 \times 25 \mu\text{m}$) FOV
Structuring Light	2D STED	PSF Engineering	<ul style="list-style-type: none"> •Time-Gated STED •Tau-STED 	Typically 40 – 60 nm	<ul style="list-style-type: none"> • No Post-processing • High penetration depth ($\approx 40+ \mu\text{m}$) 	<ul style="list-style-type: none"> • Phototoxicity • Low (≈ 0.2 s) imaging speed • Usually 2-colour limited
	SIM	Moiré Interference Shifting	<ul style="list-style-type: none"> •Lattice-SIM •PSIM •NL-SIM 	Typically 120 nm	<ul style="list-style-type: none"> • Volumetric live-cell imaging • Routine multi-colour imaging • Efficient optical sectioning 	<ul style="list-style-type: none"> • Sensitive to aberrations • Resolution improvements wavelength dependent
	ISM	Point-Scanning and Pixel Reassignment	<ul style="list-style-type: none"> • mSIM • iSIM • Re-Scan 	2-fold improvement on diffraction limit	<ul style="list-style-type: none"> • Easy to apply • Simple add-on to confocal microscope • Robust against artefacts and aberrations 	<ul style="list-style-type: none"> • Less efficient than SIM at high-frequency structures • Less contrast improvement to interference-based SIM

Table 1. Brief Super-Resolution Overview.

Chapter 2. Background

structured illumination microscopy (SIM). One caveat to note however is that MINFLUX also utilises structured excitation, so this technique can be considered as a middle-ground between the two ‘branches’ of super-resolution techniques. And it is the differences between the two overarching methods which intrinsically affect details such as the obtainable resolution, their applicability to biological samples, their FOV and 2D imaging speed, as well as the ways in which they can be developed further.

2.2.2 Super-Resolution Microscopy: Localisation Approaches

Single molecule localisation microscopy (SMLM) approaches are an effective way of obtaining exceptionally high resolutions beyond the optical diffraction limit. The techniques rely on the principle of selectively capturing fluorescing probes in the absence of other surrounding probes to construct a full image of the exact spatial location of the probes themselves, creating an image which is therefore beyond the optical diffraction limit. By utilising photoswitchable fluorescent probes as the fluorophores in the sample, the fluorescent molecules can switch between bright ‘on’ and dark ‘off’ states stochastically, allowing the creation of spatial areas where only single fluorophores are active at any given time and therefore satisfying the requirements to allow accurate localisation of the single fluorescent molecule⁴⁵. The locations of photoswitched molecules are acquired by stochastically controlling the activation of the fluorescent markers into their on state where they can be imaged, before bleaching into a permanent off state. This is then cycled repeatedly until the fluorescent markers have all bleached as indicated in Figure 3. Using this method, dense populations of fluorescent probes within diffraction-limited volumes can be individually distinguished from one another by separating their bright and dark states temporally. By

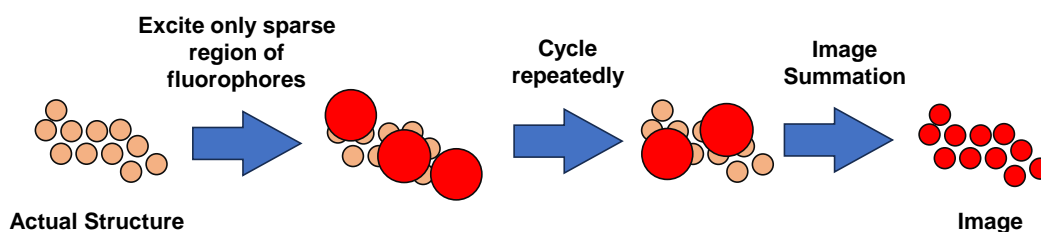
Conventional Fluorescence Microscopy**Single Molecule Localisation Microscopy**

Figure 3. PALM principle example. Figure adapted from Chiu *et al.*²³⁶

merging all the molecular positions into a single image, a super-resolved final image is created. From this principle, PALM⁴⁵⁻⁴⁷ and stochastic optical reconstruction microscopy (STORM)^{48,49} were developed as the main proponents of the approach, with different fluorescent probe chemistry distinguishing them. The theoretical localisation resolution for PALM/STORM is in the order of ≈ 20 nm, though in reality the resolution will be lower due to background contributions and noise⁵⁰. STORM has since been further developed into dSTORM^{51,52}. A key development withing SMLM has been Point accumulation in nanoscale topography (PAINT) where fluorophores switch between free diffusion and immobilisation by binding to a target of interest, instead of through photoswitching behaviour⁵³. Jungmann *et al.* then further developed PAINT through DNA-PAINT⁵⁴. SMLM techniques can be further improved by the application of total internal reflection fluorescence (TIRF)⁵⁵ or highly inclined and laminated optical sheet illumination (HILO)⁵⁶ microscopy as this limits the illumination to thin layers of a sample and improves the signal to noise ratio (SNR) and therefore the localisation precision/lateral resolution by reducing the out of focus background. However, the temporal resolution of many SMLM techniques can be very low (with 10,000s of images required for a high-resolution reconstruction), with complete image acquisition requiring a range of timescales between e.g. \approx thirty seconds and thirty minutes, depending on the sample and specific technique⁵⁷⁻⁶². Additionally, special fluorophores are often required to use this

style of technique, with again the non-trivial issue of phototoxic effects through cyclical photobleaching present^{63,64}.

2.2.3 Super-Resolution Microscopy: Structuring Illumination

Structuring illumination regularly relies on taking advantage of fundamental optical principles. Though some of these phenomena can be observed in everyday life, others are only possible using intricately designed and manufactured components to pattern illumination, such as lenslet arrays, or to change the phase of the input light, such as with phase masks. In principle the so far developed approaches can be sorted into two categories of structuring the illumination, based on point spread function engineering or full field light patterning.

2.2.3.1 Point Spread Function Engineering

Point spread function (PSF) engineering is a method of using physical phenomena to structure the fluorescence response of a sample. The method at its core is the practical origin of lateral super-resolution using structured illumination, which can be credited to Hell, Betzig and Moerner using reversibly switchable (or saturable) optical fluorescence transitions (RESOLFT)^{65–68}. Stimulated Emission Depletion (STED) exemplifies the RESOLFT concept to obtain super-resolution details, as shown in Figure 4. Succinctly, the process is based on synchronising two laser pulses: one which creates a fluorescence response in the sample, and

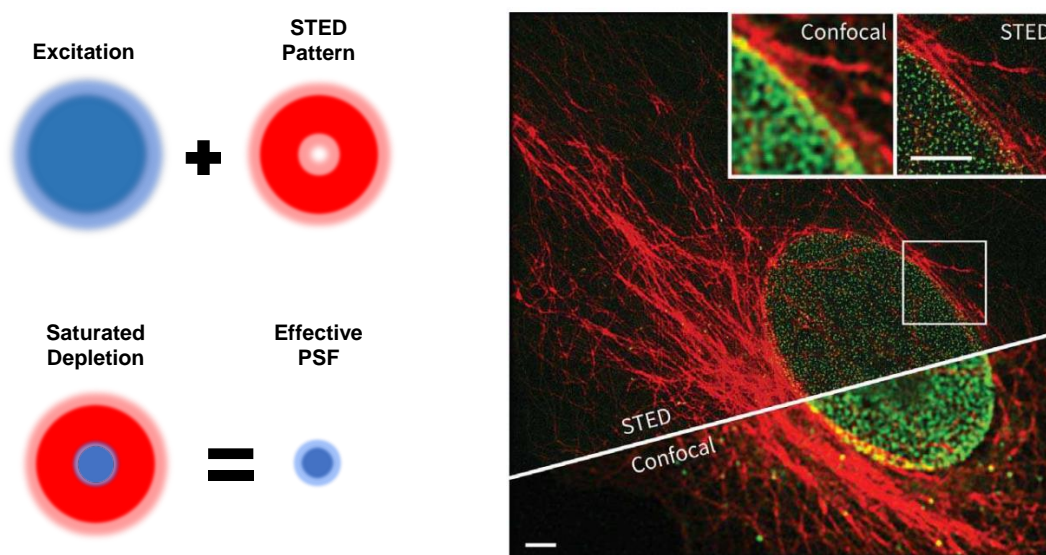


Figure 4. STED Microscopy example. Scale bars = 3 μm . Cellular image from Görnitz *et al.*²³⁷

Chapter 2. Background

a second one which suppresses or depletes part of the excited fluorescence. The initial excitation laser pulse results in a diffraction-limited area of fluorescing molecules, and by structuring the illumination of the second laser pulse with a wavelength that depletes the excited fluorescence (known as the depletion laser) with a phase plate into a toroidal pattern, only molecules within the extremely narrow centre of the toroid are capable of fluorescing after both pulses. Through the controlled engineering of the PSF to maximise the depletion area while still leaving a central gap, lateral resolutions in the sub-100 nm range can be acquired. This method of super-resolution also makes use of photoswitchable probes, though the process of STED requires extremely high incident energies to keep probes in their off state. This is one main issue with STED which is a non-trivial difficulty for imaging live-cell biology due to the high energy intensities incident on the organic structures, with phototoxicity and photobleaching being an integral problem in the sample in this case⁶⁹⁻⁷¹. Additionally, STED microscopy tends to contain higher instrument complexity compared to some other super-resolution methods despite having a relatively simple working principle, as well as having a generally limiting FOV. Since its experimental implementation, researchers have focused efforts on making the technique more applicable to live-cell biology and on minimizing the cost factor of the technique⁷²⁻⁷⁷.

One such development has been EasySTED, which mitigates issues surrounding the coalignment of the excitation and depletion beams' dependence on effective SNR by integrating both beams into a single source⁷⁸. This equally easily opens STED to multiple excitation wavelengths without complex alignment for each additional wavelength, as each excitation wavelength originates from the same source there is no complex optical alignment required for each wavelength. Ideally as the excitation with EasySTED has multiple and tuneable spectral regions, the depletion beam should also have this feature, for which STED microscopy can see q-plate integration to create the donut shaped beam profile for such purposes⁷⁹. Additionally, spatial light modulators also allow for easy co-alignment of the beams and simpler auto-alignment⁸⁰. STED microscopy has also seen further development through modern more economical laser architectures, for example in Time-Gated STED⁸¹⁻⁸⁵. A time delay is integrated into the collection of the fluorescence response after excitation, and provided that within that time delay the depletion beam is incident, substantially less intense depletion beam intensities are required. And equally this same principle applies in continuous wave STED (CW-STED), avoiding the need for expensive mode-locked or picosecond pulsed sources, though with some slightly differing integration⁸⁶. However, the benefits of these economical advancements also generally feature a reduction in the SNR. Other developments

Chapter 2. Background

include the RESCue⁸⁷ and MINFIELD⁸⁸ approaches which through similar mechanisms reduces the excessive photobleaching associated with STED microscopy, and both developments have since been integrated into the dyMIN technique⁸⁹. Within live-cell imaging, Tau-STED was developed as a method of integrating fluorescence lifetime imaging (FLIM) which improves the SNR of the system using the depletion laser to reduce the fluorophore lifetimes depending on their focal distance⁹⁰. STED's implementation is still contested in live-cell imaging⁶⁹⁻⁷¹, despite successes using different fluorescence markers having been reported⁷²⁻⁷⁷. However, there are still demands for direct differential interference contrast (DIC) integration to verify whether any morphological, cell dynamics, or growth rates have changed during *and* after STED illumination to exemplify the damage incurred.

2.2.3.2 Structured Illumination Microscopy

RESOLFT techniques became the initial practical confirmation of lateral super-resolution optical microscopy. Structuring the illumination has since also been developed in areas beyond PSF engineering, with special fluorophores no longer required due to the nature of the resolution enhancement process developments by Gustaffson *et al.*, labelled structured illumination microscopy (SIM)⁹¹⁻⁹³.

Structured illumination microscopy has pushed optical super-resolution further into dynamic live-cell research at lower excitation intensities and at higher FOVs. The SIM technique occupies itself an entire vein of the optical microscopy and super-resolution imaging techniques. A benchmark example in SIM uses two or more incident illumination beams to generate a sinusoidally varying illumination pattern⁹². This coupled with the high frequency information within a sample allows the visualisation of the high-frequency sample content

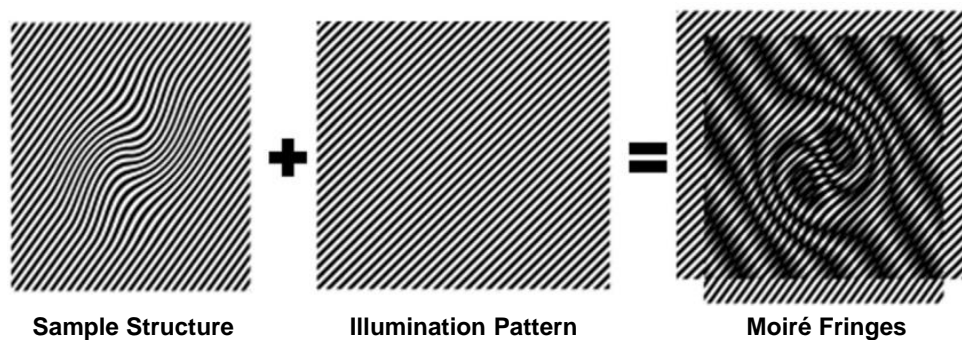


Figure 5. Example of the Moiré effect. Figure from Zhao *et al.*²³⁸

Chapter 2. Background

through the Moiré effect⁹⁴ which is shown in Figure 5. The Moiré effect itself therefore only occurs when one high spatial frequency pattern overlaps with another high spatial frequency pattern, and the optical interference between both patterns causes a third, lower spatial frequency pattern to emerge. The resultant image is therefore the effect of the sinusoidally-varying patterned illumination interfering with the pattern from the sample's fluorescence (which will contain fine structural details beyond the diffraction limit), and this overlap itself forms the Moiré effect. The acquired image contains the information about the higher frequency patterns used in its construction, and the information is recoverable by capturing multiple angles and phase patterns of the illumination frequency pattern²². This interference effect therefore holds additional information about the sample in frequency space, and by capturing images of varied phase and illuminated angle, this additional frequency space information can be extracted using Fast Fourier Transforms to generate a complete super-resolved image of the sample²². Additionally, if three excitation beams are used to generate the illumination pattern (3D-SIM) instead of two-beams (2D-SIM), the resolution enhancement can be extended into the axial direction, with the interference pattern between the beams having an axial component^{95,96}. Since the principles of SIM were developed, numerous additions to the technique have been presented such as nonlinear SIM (NL-SIM), which aims to introduce a nonlinear illumination intensity frequency to bypass the linear SIM systems resolution-limited illumination. By introducing the non-linear fluorescence response due to the near saturation limits of the excitation, the NL-SIM system is not limited by the optical microscope's NA⁹⁷⁻⁹⁹. Such implementations of NL-SIM include: plasmonic SIM (PSIM) which utilises tuneable surface plasmon interferometry¹⁰⁰; patterned activation of photoswitchable fluorophores (PA NL-SIM) which uses reversible photoswitching to obtain ~ 40 nm resolutions¹⁰¹; and saturated SIM, which uses fluorescence saturation as the nonlinear process to relate emission to excitation⁹⁹.

One approach to highlight within the wider SIM category is image scanning microscopy (ISM), which was experimentally introduced by Müller and Enderlein¹⁰², though the diffraction-limited principles date back to at least Shepherd in 1988^{103,104}. As basic principle, ISM works in a similar capacity to a confocal microscope but using a detector array¹⁰³. A single focused excitation spot is raster-scanned across a fluorescent sample in Nyquist-sampled steps (i.e. approximately two data points per resolution unit in unchanged spatial coordinates) where the fluorescence response is collected using the detector array. Each detector element itself collects information from all points on the sample, instead of solely the area of excitation as hypothesised in previous research¹⁰⁵. The recorded signal, shown as the

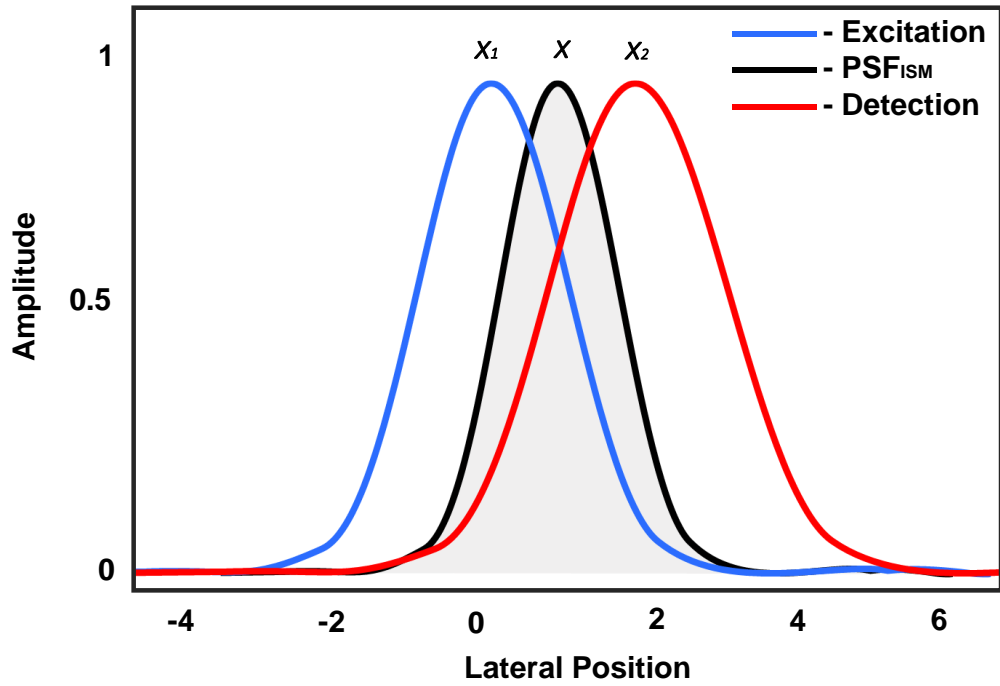


Figure 6. Line plot showing the excitation illumination point x_1 (blue) and detection point x_2 (red) for ISM imaging with the resultant combined PSF signal x (black). Figure adapted from Gregor *et al.*¹⁰⁶

black line in Figure 6, is therefore a *combination* of the illumination point in the sample, the blue excitation line in Figure 6, and the detection point in the sample which is the red line from Figure 6¹⁰⁶. Thus, the signal from the detector point of the sample must be equivalent to the peak of a confocal PSF, and is defined as the point:

$$x = \frac{(x_1 + x_2)}{2} \quad (4)$$

With x_1 and x_2 defined as the illumination point and detection point respectively. Image reconstruction, $I(x)$, can therefore be achieved through pixel reassignment where the signal is shifted to point x and through summation over all detector elements via:

$$I(x) = \int S(2x - x_2, x_2) dx_2 \quad (5)$$

This results in an image with confocal microscopy comparable resolution, though with a significant improvement to the signal to noise ratio (SNR). It was also found by Castello *et al.* that of the detector elements in ISM, only a small number of them recorded a significant

Chapter 2. Background

signal¹⁰⁷. The proposal was to therefore use a quadrant avalanche photodiode detector array of as little as four pixels, which results in resolutions close to confocal microscopy with a 1.5-fold improvement in SNR due to the re-assignment of photons into the central peak of the PSF. Later, Koho and Castello *et al.* found that by using a 5x5 single-pixel avalanche detector (SPAD), the benefits of ISM could be leveraged to provide a straightforward upgrade to existing confocal microscopes to allow fluorescence lifetime imaging and spectroscopic approach applications¹⁰⁸.

The ISM theory was then developed into a super-resolution technique through the work of Müller and Enderlein^{102,106} using a CCD detector, where the image of the fluorescent signal PSF is convolved with a fitted Gaussian distribution function before the pixel reassignment process, as exemplified in Figure 7. The result is then a super-resolved PSF and following image summation a complete super-resolution image is generated with up to a $\sqrt{2}$ resolution improvement, as exemplified in Figure 7. By following a linear deconvolution process on the resulting image, a final resolution doubling improvement can be observed. From this came multiple developments in ISM, including the development of confocal spinning disk ISM from

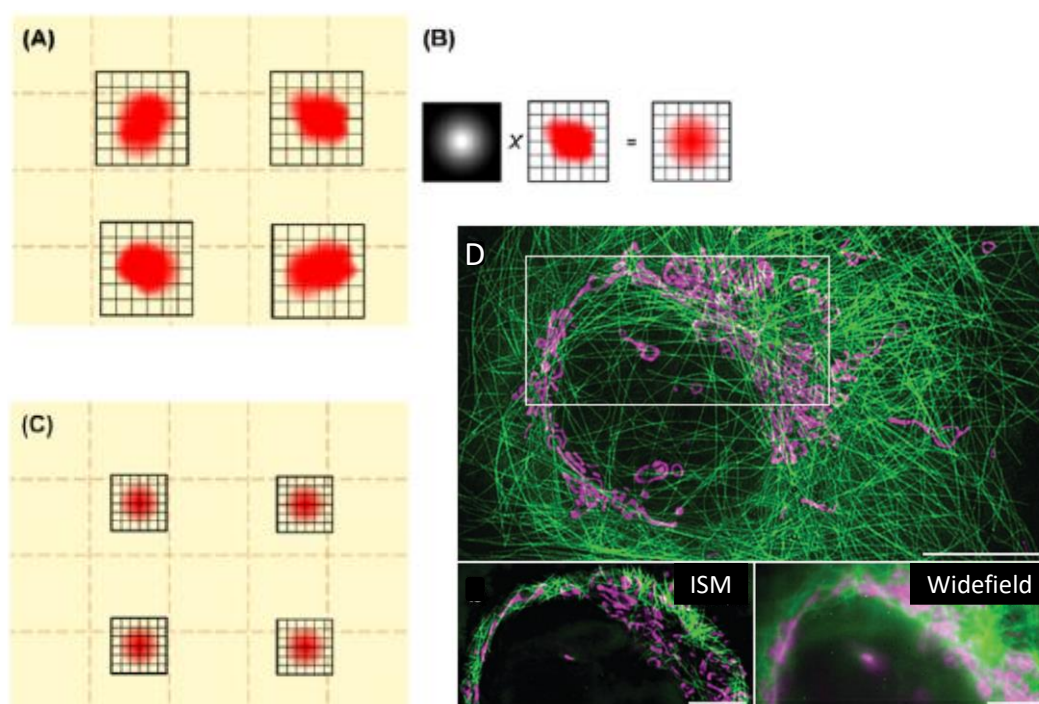


Figure 7. Image scanning microscopy schematic of PSF processing with biological image output. (A) ROI of extracted fluorescent spots. (B) Convolution of captured fluorescence with Gaussian filter. (C) Pixel resampling of the processed fluorescence. (D) Resolution enhanced resulting image. Figure (A-C) adapted from Ward and Pal²³⁹ and (D) from York *et al.*²⁴⁰. Scale bars = 5 μm .

Chapter 2. Background

Schultz *et al.* where the CCD detector images a region around the centre of each fluorescing spot¹⁰⁹.

One main problem surrounding ISM is that laterally raster scanning a single excitation spot in Nyquist criterion steps across the full FOV is a slow process, especially if axial sections are also required in the dataset. As a method of accelerating the imaging process, multifocal SIM (mSIM) was developed by York *et al.* which introduces a microlens array element in the illumination path, exciting up to hundreds of focused spots across the sample plane¹¹⁰. The ISM process is followed identically as before, as shown in Figure 7, though instead of a single illumination spot the process is applied to many excited regions simultaneously. Their developed method saw multiple improvements, including sample thicknesses eightfold thicker than previously seen in SIM. The benefit of their technique however is that a complete lateral scan is only required to move from the initial position of one fluorescent region to its nearest neighbour in both x and y directions, drastically decreasing the number of images and therefore time required, with speeds demonstrated at one 2D image per second. However, a considerable drawback is that computationally each of these spots must then accurately be processed, which is less trivial than processing a single excited spot in the image, though this is balanced well with the benefits in time saved per scanned sample. As a method of mitigating this problem while increasing imaging speed, York *et al.* developed an all-optical image reconstruction method for mSIM, which pushed their imaging speed as high as 100 fps¹¹¹.

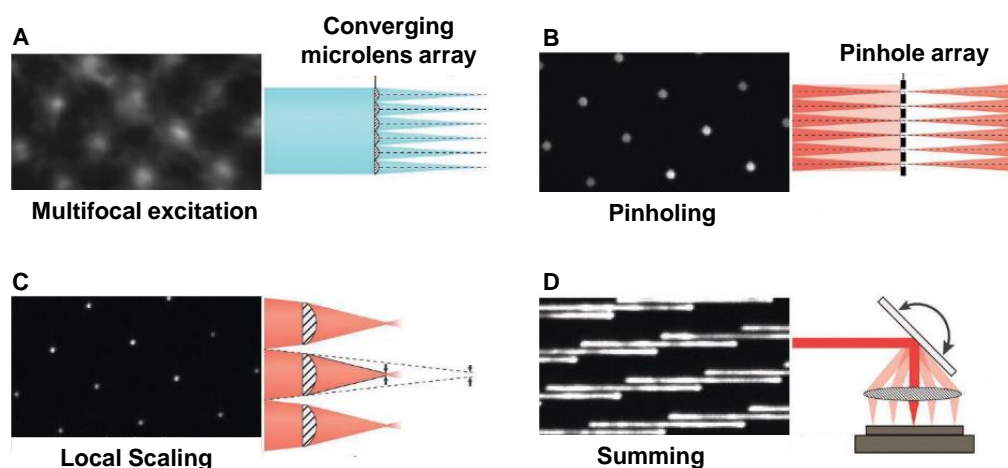


Figure 8. Multifocal image scanning microscopy technique. (A) Multifocal excitation. (B) Optical pinholing. (C) Contraction of pinholed spots using second microlens array. (D) Optical image summation onto camera. Figure adapted from York *et al.*¹¹¹

Chapter 2. Background

As shown in Figure 8, by using a microlens array (Figure 8A) for multifocal excitation, each emission is pinholed to reject out-of-focus light (Figure 8B) and optically locally contracted using a second microlens array (Figure 8C). These locally scaled fluorescent points are then summed directly on the camera (Figure 8D), resulting in a faster and significantly less computationally intensive version of mSIM. The progression of an all-optical ISM implementation has since been taken further by Ingaramo *et al.* who applied the approach with two-photon excitation, providing deeper penetration depths in thick scattering samples while improving contrast and optical sectioning¹¹². Later, Koho *et al.* utilised the two-photon ISM approach with a SPAD array detector to show further effective resolution enhancement¹⁰⁸, similarly to Gregor *et al.* who demonstrated a two-photon version of the ISM method including second-harmonic generation with resolution improvements to both techniques observed¹¹³. Alternatively, Tzang *et al.* showed two-photon ISM using holographic engineered excitation and detection PSFs to enable 3D imaging within a single 2D scan¹¹⁴.

Since these developments, other implementations of ISM have been presented under alternative naming conventions, such as rescan confocal microscopy by De Luca *et al.* which utilises a galvanometric mirror to perform the pixel reassignment and rescaling compared to digital micromirror devices (DMDs) used previously¹¹⁵. Following on from this work Breedijk *et al.* made use of annular illumination (a ring of illumination compared to a more conventional central gaussian spot) within De Luca's developments to obtain similar optical sectioning as in confocal microscopy with lateral resolutions equally similar to SIM¹¹⁶. One crucial realisation found in ISM and other pixel reassignment techniques by Roth *et al.* is that though the physical concentration of light is Lagrange invariance limited (meaning, the limit to the maximum achievable irradiance of an imaging system), these techniques circumvent this classical light concentration limit, in comparison to other super-resolution techniques¹¹⁷. This phenomenon is so far exclusive to pixel reassignment and is termed superconcentration. As the detected signal per unit sample area is increased compared to other resolution limited or super-resolution techniques, a higher SNR can be obtained as the PSF can be narrowed without the loss of photons, meaning lower input energies could be achievable for samples more delicate to higher excitation energies.

To construct the fast and all-optical version of the ISM implementations, microlens arrays are a fundamental component. These are relatively expensive optical components due to the high-precision machining or advanced technologies required to produce a glass optic with sub-millimetre lenslets, and this does limit the potential that the technique can have in reaching a

wider audience. A larger limiting factor with commercial microlens arrays is also the alignment tolerances of the optic contributing more significant aberrations. This is one area which 3D printing technologies could potentially address, as the benefits of designed free-form geometries can be integrated into custom microlens arrays. This offers the flexibility of user-defined patterns, shapes and sizes and with custom absorptive 3D printed pinholes matched to the printed array, mitigating the precision required with alignment tolerances.

2.3 Additive Manufacturing

2.3.1 3D Printing Essentials

3D printing is an additive manufacturing method encompassing a variety of different techniques. Mostly consisting of low-cost hardware with equally low-cost materials for the consumer, the short manufacturing adaptation times have made the rapid prototyping of 3D printed parts easily integrated into microscopy labs globally. 3D printers have become tools for creating mechanical and optomechanical supporting structures, as well as for creating custom alignment tools, which allow for faster and easier system creation and testing. Not only does this allow for complete integration of 3D printed components into optical imaging platforms, but they can also act as a tool to test the functionality of a design before purchasing precision machined parts, saving system designers time and money in their research.

In general, the process of 3D printing, exemplified in Figure 9, begins in a design software such as Autodesk Inventor, where a design ready for print is exported as Stereolithography

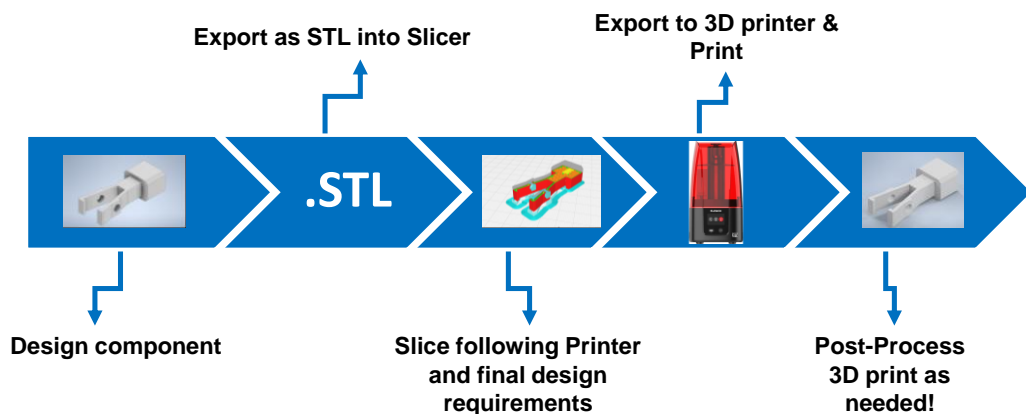


Figure 9. The essential steps from design to final printed part.

Chapter 2. Background

(STL) file format. This allows commercial printers to read and process the design via their own or third-party slicing software, such as Ultimaker Cura or Chitubox, which axially segments the design into layers required for the layer-by-layer fabrication process of the current generation of 3D printers. At this point, a user will usually be given the freedom to adjust the thickness of the layers, otherwise known as the z-resolution of the print, within a range of supported printing resolutions. This axial as well as the lateral achievable print resolution is one of the most fundamental differences between 3D printing technologies, defined by how they approach the layer-by-layer manufacturing of the design. For example, one of the simplest and lowest cost methods of additive manufacturing is Fused Deposition Modelling (FDM) which extrudes a melted filament onto a platform in layers until the model is complete. With FDM, axial print resolution is often in the order of 100 – 300 μm and the time taken to print a model is dependent on both the lateral and axial complexity and dimensions of the designed model. Additionally, despite the surface finish being often relatively coarse there is minimal to no post-processing required after the print aside from structural support removal when required. Though higher levels of precision are possible using alternative printing methods, FDM offers difficult to compete with low upfront costs and direct useable print parts. As a result, FDM 3D printing has started to be integrated into a wide variety of research and applications globally, with low-cost healthcare and diagnostics device design even possible using the technology¹¹⁸⁻¹²². However, in a growing number of cases higher resolution 3D prints are preferred, which can be achieved using amongst others photopolymerizing resin printing methods.

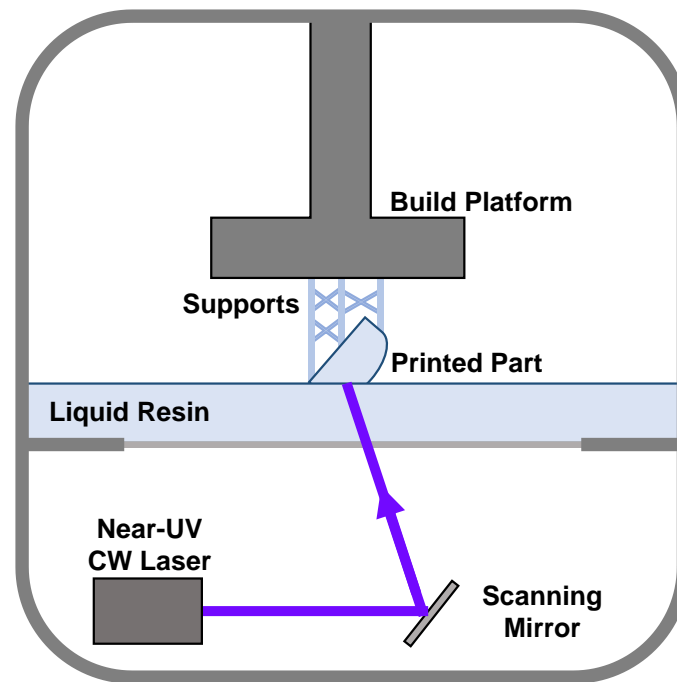


Figure 10. SLA printing schematic.

Stereolithography (SLA) in its laser-scanning implementation creates printed parts in a similar style to FDM, where parts are manufactured in a lateral scan across each layer though using a near-UV laser to cause photopolymerisation within a liquid resin instead of heating and extruding filament. The methacrylate-based resin is a transparent or opaque liquid mixture consisting of monomers with cross-linkers and photoinitiators, and it is the photoinitiators which start the polymerisation process under near-UV radiation¹²³⁻¹²⁹. As shown in Figure 10, the basic process to create a part focuses on a printing platform being immersed in the resin mixture and a near-UV laser controlling the spatial specific polymerisation of the resin depending on the lateral pattern/shape of uploaded design.

The result is a 3D print with axial resolutions typically around 25 - 100 μm , though its lateral resolution depends more on the size of the laser spot in conjunction with how incrementally fine the laser spot can be controlled. Predominantly due to the requirement of a laser, this method of 3D printing is often more expensive than FDM printing and has further post-processing requirements as excess resin needs to be cleaned away from the 3D print. The resulting print has however a significantly higher surface finish, with smaller layer step sizes and reduced roughness within a layer. The SLA manufacturing method being fundamentally

Chapter 2. Background

a laser spot-scanning approach, the technique holds some similarities to FDM approaches as one point at a time is created. Therefore, this technique can take longer to manufacture a printed component compared to print processes using array illumination to create entire layers at one time. One key development in SLA is micro-SLA (μ SLA) which overcomes the Gaussian excitation-induced surface defects and improves the lateral resolution down to 5 μm through sub-micron printing stage movement during layer polymerisation¹³⁰⁻¹³⁵.

On a more budget-friendly side of high-resolution 3D printing, digital light processing (DLP) or LCD screen printers utilise much of the same method as SLA printing, though without the laser requirement. Instead, near-UV LEDs project a layer design at a time into the liquid resin tank, using a DMD (for the DLP approach) or an LCD to create the required print patterns¹³⁶⁻¹⁴⁰. The axial component of the print works identically to SLA manufacturing. This creates a pixel-limited lateral resolution, typically in the order of 20 – 50 μm and with axial resolutions as high as 10 μm without the inclusion of pulsed excitation sources. The result of this method is an extremely affordable 3D print process, taking into account its possibility to achieve high level surface details. In addition, third-party resins are more commonly usable in DLP/LCD printer compared to SLA printers, as more often DLP/LCD printer have open software formats that allow customisable print settings, such as exposure times per printed layer, leaving the printing variables in the user's control.

On the higher-end of 3D printing, Two-Photon Polymerisation (2PP) is a highly accurate version of SLA to 3D print parts with sub-micron detail using a focused laser beam to cure photopolymerising resin at a 150 nm resolution¹⁴¹⁻¹⁴⁸. Compared to lower cost methods, instead of causing polymerisation through the molecular absorption of one near-UV photon, pulses of two near-IR photons are absorbed as shown in Figure 11¹⁴⁸. The difference between these methods is therefore that instead of molecules being excited to a high energy state using one photon within a small volume, the molecules are only excited into a high energy state

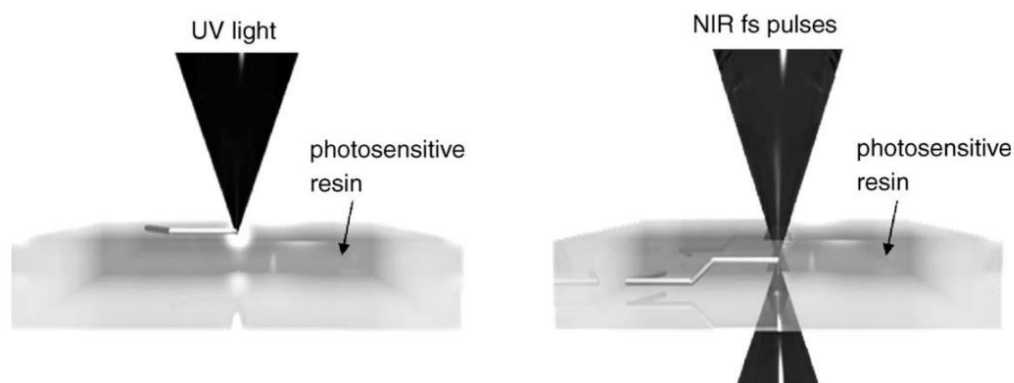


Figure 11. Two-Photon polymerisation example. Figure adapted from Wu *et al.*¹⁴⁶

when the second IR pulse is incident on them. The method has been further developed to improve the resolution up to 10 nm using STED-like approaches^{149–151}. As the resolution is beyond the visible spectrum of light, post-processing beyond part washing is often unnecessary. However, though the printing resolution is superior to other 3D printing methods, the maximum scale of a part is currently up to ≈ 1 cm volume with long print times on the order of days required, depending on the print scale. Some holography methods have been employed recently in an effort to reduce manufacturing times while maximising printing volumes beyond the layer-by-layer approach^{152–154}.

2.3.2 3D Printing for Optical Applications

Additive manufacturing within optical imaging and microscopy has supported not only researchers, but also education and healthcare settings. The inexpensive and rapidly replaceable parts achievable with 3D printed approaches offer unique potential for these fields. Systems like the FlyPi¹⁵⁵ and OpenFlexure¹⁵⁶ project expose optical microscopy to a wide audience, and both educate on simple zebrafish or fruit fly samples, as well as in diagnostic applications. The broad range of applications at low costs encapsulates the solid foundation 3D printing has built itself within the area of optical imaging system development.

One early-stage example in the implementation of 3D printed optomechanics in optical microscopy is the OpenFlexure project^{156–160}. Through the combination of inexpensive optics and Raspberry Pi equipment with a fully FDM 3D printed microscope chassis, sub-cellular resolution has been obtained in brightfield imaging, which has provided e.g. rapid field

Chapter 2. Background

diagnostics of blood-based diseases at minimised costs or setup¹⁶¹. As a result, this imaging technique has been taken on by researchers and healthcare practitioners across the globe¹⁶²⁻¹⁶⁷. This underlined one of the other main benefits of 3D printing within imaging research, which is the relative ease of making open-source software and hardware in enabling replicability or validation of the 3D printed optomechanics and their results. In addition, by integrating 3D printed components into the optomechanics of a microscope, there exists further inexpensive microscope development in rudimentary redesigning where extra optical components, alternative sources of illumination, and additional cameras all can be integrated into the designed project. Outside of complete microscope chassis, individual parts for microscopy systems can integrate 3D printing, including microscope bases¹⁶⁸⁻¹⁷⁰, the body¹⁶⁹⁻¹⁷¹, filter holders^{168,169}, and pinholes¹⁷¹, which all improve the customisation of a microscope system. And outside of the microscope itself, a variety of sample manipulation options, such as syringe pump systems, have integrated 3D printed components for repeatable low-cost assembly¹⁷².

Modular designs have been a particular favourite in FDM 3D printing, such as the UC2¹⁷³ and miCube¹⁷⁰ systems which allow for precise optical microscopy manufacturing with customisation due to their modular designs. Developments such as these highlight that optical microscopy is progressively opening to and embracing of open-source technologies, with lower cost components becoming ever more compact and powerful. Similarly, the M4ALL microscope development allows a user to manufacture cost-effective cube structures to create optical cage mounting systems¹⁷⁴. This not only minimises the costs involved in an optical imaging system, but it also opens the potential for preliminary proof of concept data before purchasing commercially produced optomechanics, where or if necessary. Optical microscopy combined with 3D printed components used in this way highlights the support 3D printing can offer in developing optical imaging systems while maintaining impressive precision in data acquisition and analysis^{155,156,165,167,173,174}.

Each of the examples of 3D printing within optical imaging microscopy leverage the rapid prototyping capabilities of 3D printers with customisation potential across a broad range of applications. Each of the examples integrally support the mechanical basis of a microscope, with optical components left as commercially available glass optics. However, 3D printing methods have developed significantly over recent decades, making integration into microscopy systems cheaper and easier than ever with custom designs available to the researcher, as with mechanical 3D printing.

2.4 3D Printed Optics

2.4.1 Optics Manufacturing Methods

For centuries glass lens manufacturing processes have been employed that traditionally require grinding and polishing steps, which are time-consuming and costly¹⁷⁵⁻¹⁷⁷. Modern approaches to creating optical lenses have created alternative lower cost and time-saving methods such as injection moulding lenses, with the costs minimized through mass-scale lens production. To create the injection moulded lenses and optics, however, high precision moulds have to be manufactured first before the high-quality optics themselves can be created. This itself can be both expensive and time-consuming¹⁷⁸⁻¹⁸⁰. When considering the more recent developments of prototype, non-standard and free-form lens geometries employed within imaging research¹⁸¹⁻¹⁸³, the costs in manufacturing each lens or lens mould increases further still. In all cases, the higher initial costs are passed onto the consumer, which can slow or even stop the participation of researchers within optical imaging who have minimal resources. Optical components have continued to be glass or injection moulded plastic lenses, with minimal scope for lens customisation as per the needs of the researcher.

To try out alternative routes, researchers have investigated FDM techniques to manufacture glass components in a molten state, though due to the high surface roughness the applications have so far been limited to elements for microwave and THz range usage¹⁸⁴⁻¹⁸⁷, as well as some reflective components¹⁸⁸⁻¹⁹⁰. However, some researchers have observed successful application of FDM 3D printed glass components as flat optics^{188,189} as well as with optical fibres¹⁹¹⁻¹⁹⁴.

Some commercial contenders for customisable lens designs with sub-micron detail utilise highly precise 2PP methods. One of the key benefits of two-photon optical printing approaches, like direct laser writing (DLW), is its high printing resolution with minimal-to-no post-processing. As the technique can manufacture optical components with sub-micron precision, it can be an extremely useful tool for precision manufacturing of optical parts, including patterning onto the tip of an optical fibre¹⁹⁵⁻¹⁹⁹; microlenses²⁰⁰; multifocal lenses²⁰¹; ring resonators²⁰²; and numerous other complex lenses²⁰³⁻²⁰⁷. However, although two-photon printing techniques can provide optical quality details without further post-processing steps, the method is still inaccessible to many research groups due to the expensive pulsed laser excitation source required for fabrication. Equally, a large spatial footprint is required for this optical manufacturing method, despite only producing up to single centimetre-scale

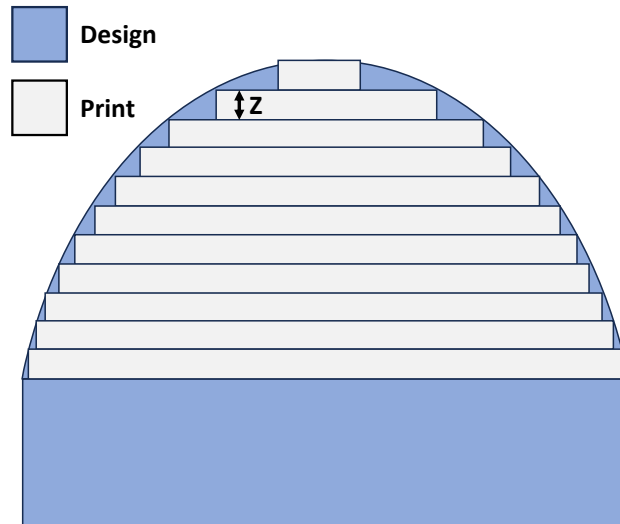


Figure 12. Schematic showing the staircase effect equal to z -height in the final print against the initial design.

components, which itself takes long periods of time to manufacture due to the high surface quality printing method. The technique therefore lends itself to high-budget research with nano-scale optical quality components.

When attempting to produce optical quality lenses using lower cost SLA or DLP style technology and budget friendly clear resins, one key issue presents itself immediately after printing. Once the design, for example a plano-convex lens, has been cleaned of excess resin the well-documented ‘staircase’ effect can be observed^{208,209}, as exemplified in Figure 12. As the printing platform moves e.g. $10\ \mu\text{m}$ axially between each layer of the lens design, a staircase of concentric layers is created across the designed lens.

The resulting rough lens surface therefore does not transmit light well enough in this state to be optical quality as the scattering effects at the surface dominate. To counteract the effects of the staircase effect, numerous smoothing methods have been developed to obtain a low surface roughness transparent final optical element. Perhaps the simplest concept is to subtract away material from the surface by sanding and polishing the surface with progressively finer grit abrasives^{210,211}. Whilst this does result in a transparent optical element which could be usable for some consumer grade purposes, both the presence of microscopic scratches from the abrasive processing and the lack of homogeneity of polishing across the surface make it an incompatible method for optical microscopy. Generally, additive post-processing may be preferable to smooth the staircase effect, as more control can be offered in homogeneously

Chapter 2. Background

smoothing a curved or flat surface. It has been shown that due to matching refractive indices, adding extra liquid clear resin to the printed surfaces increases the optical clarity of the 3D print significantly. The easiest way to do this, conceptually, is by dip-coating the 3D print in a vat of liquid clear resin²¹⁰. When removing the print from the clear resin, the print becomes observably transparent, and when cured using a near-UV light source the coating will preserve this optical clarity of the part, as any printing resolution-limited features have been smoothed. The main reason this method is in general not preferred, however, is that the user lacks complete control over important variables such as the thickness or the homogeneity of the applied coating across the surface. Again, for some consumer grade purposes this may be good enough, however when attempting to manufacture lenses with specific focal lengths the unpredictable coating thickness can create issues in acquiring optical quality lenses featuring geometries which match the original design. One critical development was therefore the homogeneous addition of extra resin onto a 3D printed lens surface by using a spin-coating procedure after the resin was deposited^{1,2,23,210-212}. This method has the most promising outcome of the ones described so far as coating homogeneity, thickness and therefore surface quality and focal length are within a higher degree of the user's control. Through this post-process step the SLA and DLP methods can obtain the required surface roughness for optical quality parts as shown by Vaidya and Solgaard first¹, and then by Berglund and Tkaczyk². The DLP printing process itself can be useful for additional internal patterning of optical components, such as diffraction gratings, prisms and lenses as shown by Vallejo *et al.*²¹³. By adjusting parameters such as the volume of resin used and the spin-coating speed and time, the technique offers direct control, albeit with some surface imperfections or inhomogeneities still present. Re-moulding of the 3D printed optic has also been shown as a promising approach². However, this again requires the creation of a high-quality master mould which itself has practical and economic drawbacks. Additionally, methods of improving the printing quality were developed including an iterative grayscale pixel intensity method through Xu *et al.*²⁰⁹ which introduces machine learning to produce smoother printed surfaces. In a similar vein, Yuan *et al.* demonstrated that optical quality microlens arrays could be fabricated using DLP technology through oscillations in the printing axis from a linear vibration generator²¹⁴. More recently, techniques based on the DLP method include high-resolution projection μ SLA (P μ SLA)²¹⁵⁻²¹⁷; fast and large volume high area rapid printing (HARP)²¹⁸; and continuous liquid interface production (CLIP) for fast 3D printing²¹⁹ have all been developed.

An alternative volumetric method, developed by Elgarisi *et al.* uses buoyancy equations to create a precise mixture medium of e.g. Glycerol and De-ionised water, and through the

computed boundary conditions a ring can be manufactured for 3D printing custom optics²²⁰. By then immersing a specific volume of rapidly curing resin into the medium around the edge of the boundary ring and illuminating with near-UV light, an entire printed optic can be simultaneously manufactured with optical quality surface roughness. However, though an impressive and fast method, the technique relies on complex mathematics and non-trivial issues with experimental accuracy, though its free-form manufacturing is impressive.

An overview of some of the current 3D printed lens research progression is shown in Figure 13. which exemplifies the vast array of 3D printed lens manufacture already developed. Figure 13A and B show the wide array of optical quality lens manufacturing across a range of printing dimensions, with optical quality half-ball lenses on the millimetre scale compared to micro-objectives at the hundreds of micrometre volume. Equally, the diversity of optical lens 3D prints is shown in Figure 13C through E, which show the lower-cost manufacturing of temperature variable optics, freeform lens geometries and multi-material contact lenses

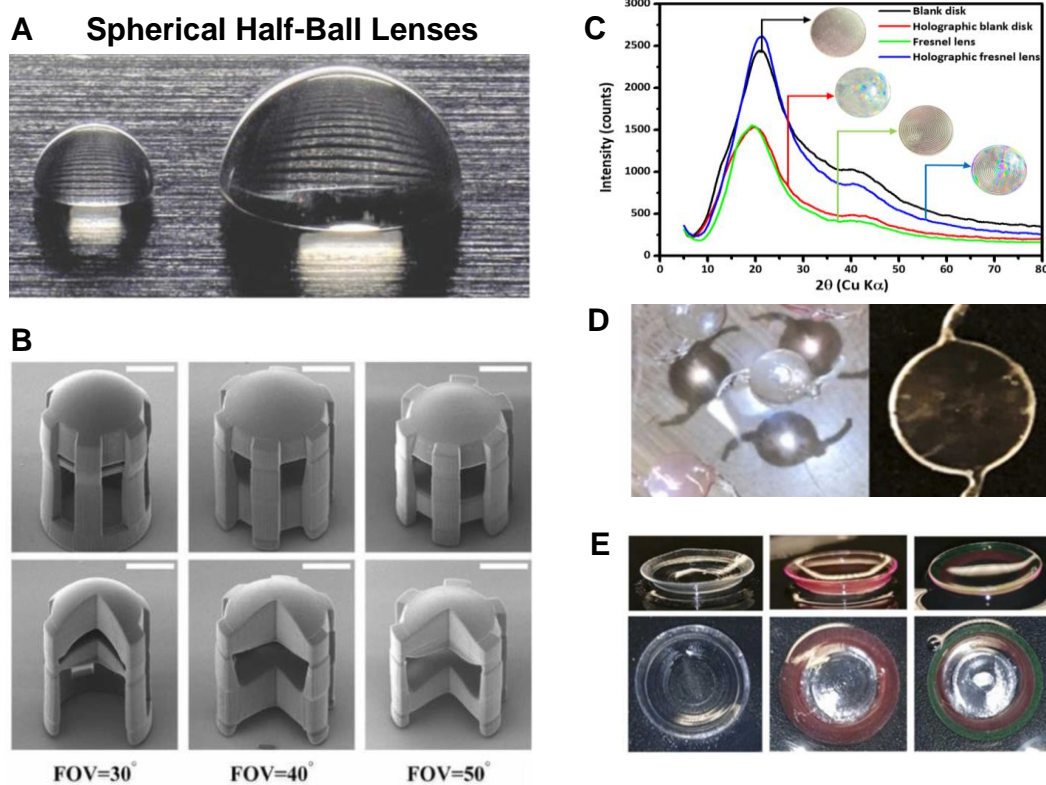


Figure 13. 3D printed optics examples. (A) 2PP 3D printed half-ball lenses²⁴¹; (B) SEM images of 2PP manufactured micro-objectives at different FOVs and cross-sectional images of micro-objective lens at different FOVs²⁴²; (C) Colour changing Fresnel lens printed by SLA method²⁴³; (D) Intraocular lens printed using DLP method²⁴⁴; (E) multi-material contact lenses printed by DLP method²⁴⁵.

Chapter 2. Background

respectively. Overall, SLA techniques have recently helped to address the economic gap between optical 3D printing technologies without sacrificing optical quality as seen with DLP printing. The unique ability of 3D printing techniques to manufacture free-form optical geometries in custom configurations allows for rapid, low-cost and in-house optics construction, and therefore microscope objective construction. The development of specifically the lower cost optics manufacturing methods are already resulting in optics which are capable of rivalling fully commercial microscopy results^{1,221–223} and through continuous development it may become a major optical manufacturing method for researchers and healthcare services globally. By exemplifying the current state of low-cost optics manufacture for expensive imaging techniques, 3D printed optics could become a powerful tool in rapidly developing biomedical research across the globe.

2.4.2 3D Printed Optics in Imaging

A variety of different optical components and geometries have been replicated or newly designed using a range of 3D printing technologies. The capability of 3D printing techniques to manufacture custom, free-form optical components is well suited for applications in imaging and microscopy, where research-specific developments in optical techniques can often require special optics which are difficult to manufacture using traditional methods. The new degrees of freedom which 3D printing offers the field of optics now allow for completely novel exploration of microscopy and imaging approaches. So far within optical imaging and microscopy research, the most commonly used 3D printed optics are via high-precision two-photon polymerisation methods, though lower cost desktop 3D printers have seen significant advancements in recent years.

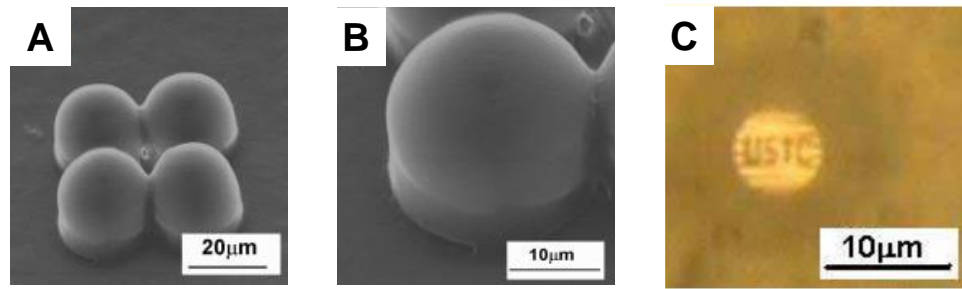


Figure 14. SEM images of 2PP manufactured microlenses for imaging applications. (A) – SEM images of the 2PP manufactured microlenses²⁰⁰; (B) – Zoom in of the SEM individual lenslet²⁰⁰; (C) – Image acquired using 3D printed optic within an optical microscope²⁰⁰.

Within imaging using 3D printed optics, shown in Figure 14 is the first image obtained using a printed microlens from Guo *et al.* using two-photon polymerisation methods²⁰⁰. This work characterised the printed optic and exemplified that a 3D printed optic could transmit light well-enough to obtain an image of a sample, which in this case was a centimetre-scale target, with interferometry results supporting the conclusions from their imaging. However, the resolution of the imaging system using a printed optic is not included in the discussion, leaving room for further work in evaluating 3D printed optics in imaging systems based on this proof of principle. Building on this development was Malinauskas *et al.* who further investigate the DLW process in imaging by integrating the printed element onto a fibreoptic tip²⁰⁶. Their work builds heavily on the characterisation of printed lenses and their associated roughness' as well as with the integration of diffractive optical elements. And while some integration of the optic imaging performance is shown, this again is not heavily focused on in contrast to the overall quality evaluation of the printed optic. Building once more on the foundations of micro-optics printed onto optical fibre tips was Liberale *et al.* who detail the light propagation using the manufactured optic²²⁴. Their imaging results of airy disks produced through their printed optic demonstrate the quality that two-photon fabrication methods can obtain in beam-shaping and custom excitation potentials. However, the application of 3D printed optics in imaging still misses integral details of how a printed optic collects light from a sample within an imaging system. This gap was filled by Gissibl *et al.* who show a complete image characterisation of 3D printed micro-objectives manufactured using two-photon technology onto an optical fibre¹⁹⁸. The results from this work, as well as in their later papers on the subject^{195,225,226}, demonstrate the impressive customisation of optical components that 3D printing technologies possess. Gissibl *et al.* have demonstrated in their literature a complete overview of two-photon

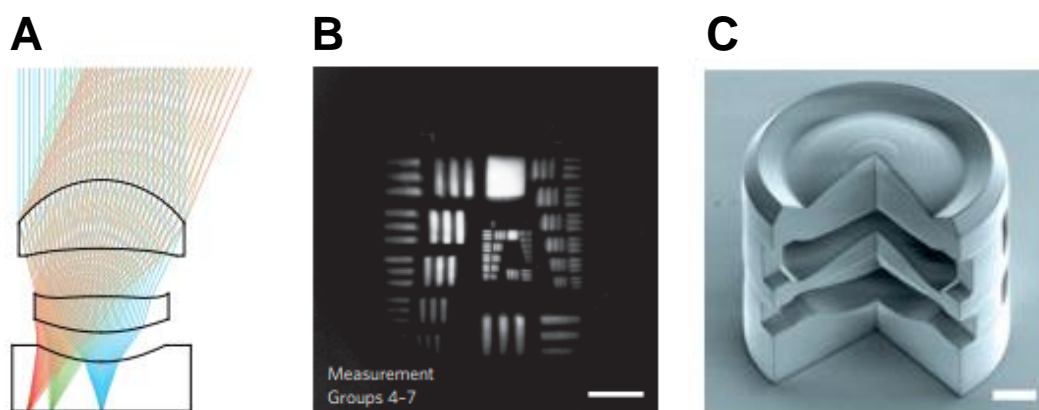


Figure 15. Imaging performance of 2PP manufactured optics, adapted from Gissibl *et al.*¹⁹⁸ (A) – Ray-tracing of printed triplet system; (B) –1951 USAF target imaged using 3D printed triplet system; (C) – SEM image of the triplet system. Scale bars = 20 μm .

lithography produced optics as shown in Figure 15, including images of 1951 USAF targets collected using their printed optics with resolvable details on the scale of 500 lpmm^{-1} which was previously unprecedented. Additionally, they exemplify the presence of optical aberrations throughout the 3D printed optic, as well as inhomogeneities in beam profiling and uniformity across the researcher's other works^{198,225–229}. Recently, glass-like micro-optical fabrication using DLW (or so-termed LDW) methods and imaging was shown by Gonzalez-Hernandez, showing the progression of materials for optical free-form fabrication methods²³⁰. Shown is therefore the ability to image fine details using a 3D printed optic, provided that the surface roughness and transparency of the lens is sufficient as per two-photon techniques. However, two-photon technology, though offering exceptionally fine customisable printed optics, still requires high budgets to obtain the image quality optical element.

In an effort to obtain similar free-form optical freedom at the lower-budget scale and building on the SLA characterisation of Vaidya and Solgaard¹, lower cost optical quality 3D printed lenses were used in imaging applications through the work of Berglund and Tkaczyk². Multiple low-cost optics production and processing methods were introduced, and optical characteristics such as flatness and form error, surface roughness, radius of curvature and wavelength specific transmittance were all detailed. Additionally, a comparison of image quality was shown using a standard chrome lithography target in a simple imaging system using commercial, moulded, and spin-coated lenses. The results from lower costing free-form optics manufacturing were benchmarked for imaging system integration specifically.

Chapter 2. Background

However, on the lower costing scale, minimal published work in imaging has been shown in comparison to the higher-budget research or principal characterisations. This creates a crucial gap within low-cost 3D printed lenses for free-form optical performance within biological brightfield and fluorescence imaging.

2.5 Discussion

Contextualised within this chapter has been the fundamental information required to evaluate the data results to follow. A litany of microscopy terminology and methods have been described, including localisation and structured illumination techniques. As such, active follow-on applications of these background optical microscopy techniques can be shown within the next few chapters. Additionally, details of 3D printing technologies have been investigated as has 3D printing's current role within optical microscope been explored. With this, the potential for further advancements in both 3D printing and optical microscopy can be explored in further detail through the results within the next chapters. Specifically, miniaturised and economic methods of structured illumination will be investigated further in conjunction with the advancement of 3D printed optical quality components within optical microscopy.

Chapter 3. Optical Quality 3D Printing

When manufacturing in-house optical components, careful selection of the 3D printer and clear resin are essential in obtaining optical quality 3D prints. This chapter aims to detail the underlying work on evaluating low-cost 3D printers and resins and where the developed low-cost additive manufacturing approach has shown experimental success or comparative drawbacks to commercial optics. One consideration to note is that many of the below detailed current limitations of low-cost 3D printed optics made for microscopy may be reduced or disappear completely as budget-friendly 3D printing technology advances. Documented below is the fabrication and characterisation processes for the low-cost optical quality 3D printed optics used in the microscopy chapters of this thesis, including planar-surface cuboid elements of various thicknesses, spherical lenses with different prescriptions and lens arrays. Following the description of their manufacture, the characterisation of each optical element including transmissivity, surface roughness and form evaluation is shown, with comparisons drawn to their commercial optical counterparts of similar or identical geometries and prescriptions.

3.1 Manufacturing Optical Quality 3D Prints

3.1.1 3D Printer Selection

The first step to optical quality 3D printing is choosing an appropriate printer. These days a large variety of resin-based desktop 3D printers can output an element ready for optical post-processing. They can roughly be classified by their illumination approaches into SLA, mSLA and LCD, where the first printer used within the research was the Formlabs Form 3 (~£3k retail price, 2019 release date). This SLA style printer was chosen due to its 25 μm x, y and z resolution from its 85 μm laser-spot size, as well as its high-quality clear resin. Though convenience was offered by providing the user Formlabs resins with their respective variables (exposure times, lift speed etc) all pre-set, the user is locked into exclusively using Formlabs resins which can be costly, as well as limiting the degrees of freedom in the use of the printer and resin. At the time, lower cost printers and good clear resins were only beginning to emerge and with a goal of 3D printed lenses integrated into optical microscopy systems, printer and material reliability was paramount to the success of the research aims. Additionally, this printer was chosen based on preliminary work performed by a previous PhD student within the group who showed some success in optical quality custom prisms. It was later found however that printed parts from the Form 3 were prone to underdeveloped (i.e. ‘missing’ or ‘undercured’) layer lines within the bulk print as shown in Figure 16. Additionally, inhomogeneity in the form of curved surfaces between prints when using the Form 3 led to the investigation of other printers for their optics manufacturing potential.

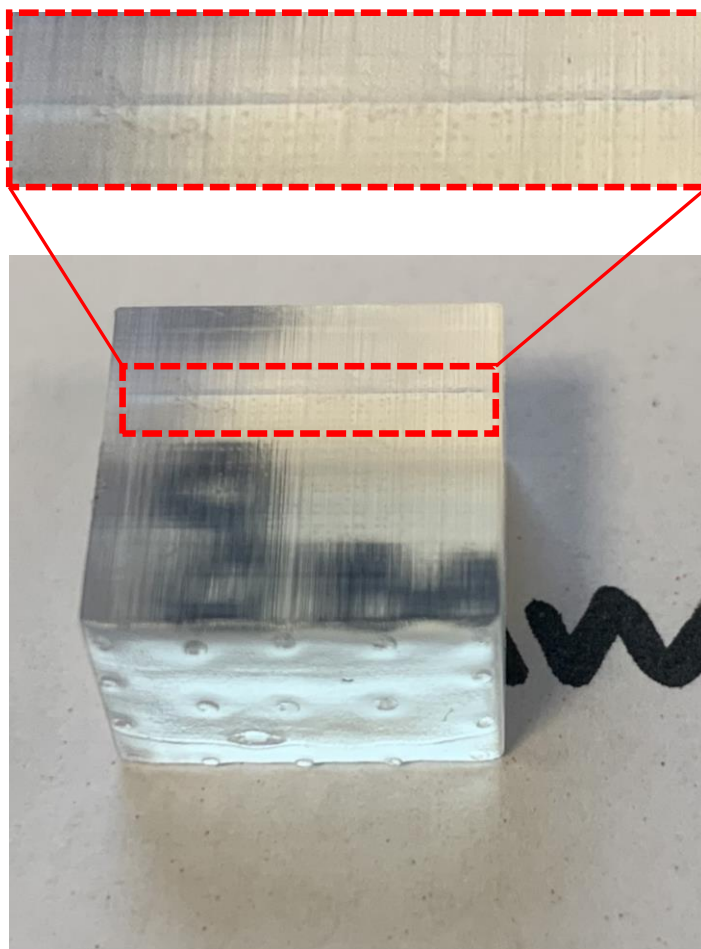


Figure 16. Photograph of missing layers from the Form 3 printer.

One 3D printer which became available at the start of the PhD at significantly lower cost compared to the Form 3 was the LCD mSLA based Anycubic Photon S printer (£450 retail price, 2020 release date). A user was offered the freedom to customise variables using this printer, though at the expense of having to dial in the printing settings to a window of success, which itself takes extra time, energy and money. This printer had a lower lateral resolution at $50\ \mu\text{m}$, though it allowed for a higher axial resolution of $10\ \mu\text{m}$ to be utilised. Using this style of printer also permitted user-control over variables such as the exposure times, granting customisation and an open resin system compared to the locked system in the Formlabs printer. As the Formlabs Clear resin produced optical prints with high transparency compared to cheaper clear resins available at the start of the PhD, this resin was used in the Photon S to

Chapter 3. Optical Quality 3D Printing

manufacture lens components. Additionally, the Formlabs Clear resin had a refractive index of ~ 1.5 ²³¹ which meant any mismatches between lenses manufactured with this resin and commercial glass optics was understood during experimental design. This printer worked reliably and well for the cost and specifications at the time. Throughout the PhD even higher resolution budget resin-printers came onto the market, with monochrome LCD displays enabling significant advances in print-time and resolution. Through adaptation to latest affordable print technology, most of the experimental results in the thesis were achieved using the Elegoo Mars 2 printer (£300 retail price, late 2021 release date), featuring similar $49\ \mu\text{m}$ printing resolution at similarly low costs, though with faster print times. The printer was calibrated to use Formlabs Clear resin as budget transparent resins were still lower quality in comparison. This printer and resin combination was used as the foundation for the body of research within optical characterisation and imaging using 3D printed optics as shown in this chapter and within the published work within Chapter 4, unless otherwise noted.

As thesis research progressed toward smaller diameter lenses in the form of lenslet arrays for ISM applications, the Mars 2 did not have a high enough lateral resolution to produce a miniature lens with the required curvature detail. The printer used for the body of work in Chapter 5 was therefore a further upgrade that became available in 2023, the Phrozen Sonic Mini S, with 8K pixels and lateral resolution of $23\ \mu\text{m}$ (\$360 retail price, 2023). This low-cost printer provided high enough resolution, combined with grayscale in the slicing software, to manufacture lenslet arrays with high enough precision for acceptable excitation beam profiles for ISM.

Chapter 3. Optical Quality 3D Printing

3.1.2 Design and Print Preparation

To 3D print any structure, a 3D model has to first be obtained, which can be designed by the user using their preferred computer aided design (CAD) program, e.g. Autodesk Inventor. Alternatively, a stereolithography file (.STL) can be downloaded from open-source sites such as Thingiverse. Additionally, .STEP files can be downloaded from a host of component suppliers, e.g. Thorlabs, which can be translated into .STL files ready for 3D printing. For either a user's own models or downloaded models, one of the considerations for printing any curved structure includes ensuring a high mesh quality in the export settings when translating the file into the .STL format, as this will effectively translate into curved surfaces of the 3D print being smoother compared to lower mesh qualities. Additionally, ensuring no hollow parts are present in the design can minimise errors in the print through avoiding vacuum forces during printing or encapsulating liquid resin within the finished print, which will eventually cause cracking due to outgassing if not vented. Before being able to print the model, the .STL has to be imported into a slicing software, such as Chitubox Basic or Ultimaker Cura, to translate the file into a printer-ready format by segmenting the 3D design into 2D layers (slices) to be printed one on top of the next as shown in Figure 17. where the required supporting structure and axial slices are exemplified by A and B respectively.

In this body of work Chitubox was the chosen software for 3D printing optical components. Its print preparation starts by selecting the specific chosen 3D printer to ensure variables such as build plate dimensions; LCD screen size and pixel sizes are correct. For each print,

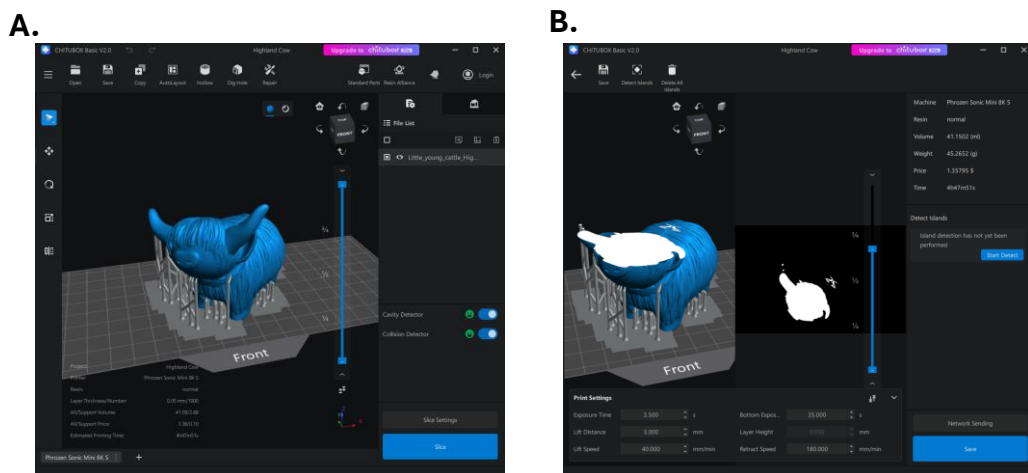


Figure 17. Chitubox sliced STL file with supporting structures for successful printing (A) and axial slices (B). Highland cow file unaltered and obtained from <https://www.thingiverse.com/thing:5417799>

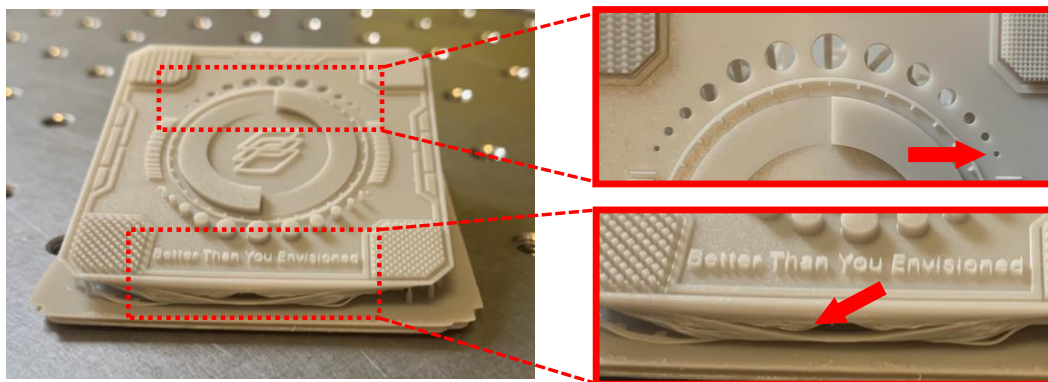
Chapter 3. Optical Quality 3D Printing

parameters related to the chosen resin and layer thickness can be adapted, with main layer exposure times, bottom layer number and exposure time, z-stage movement speed and z-layer height being intrinsically linked for optimal printing. The z-layer height has additionally a limitation based on the accuracy of the 3D printer axial resolution. The chosen printing variables can affect multiple parameters of the completed print; for example, a higher resolution print made of 10 μm layers will take proportionally longer than a lower resolution print made from 50 μm layers, though vertical details in the print will have higher smoothing at 10 μm compared to 50 μm . Depending on the print geometry, supports can also be necessary to ensure the printed part does not have feature failure during printing, as too high an overhang angle of the print can result in sagging print features, or completely missing parts of the finished design. If the print includes internal hollow features which have not been dealt with in the CAD stage, this can be adjusted by either manually drilling at discrete locations on the print to vent the liquid resin out of the hollow location, or most slicing software will usually provide the option to include a software generated hole to allow liquid resin to drain. Equally, the design orientation in the slicing software can be a non-trivial optimisation problem, as areas where resin can pool may result in overcuring, sagging, or print failure depending on the weight of liquid resin pooled.

Chapter 3. Optical Quality 3D Printing

In addition to the numerous features and considerations mentioned already, one of the most important to consider and optimise for 3D printed optics is the exposure time, which the user can fine-tune (usually down to tenths of a second) to give the best feature precision of the printed parts with minimal overcuring or undercuring, both of which are shown in Figure 18. Undercuring exemplifies itself through incomplete parts of the final print as seen in Figure 18A. Though the holes on the test print are well-defined as seen in the top ROI red arrow in Figure A, the supporting sections exhibit missing printed layers shown at the red arrow in the bottom ROI of Figure 18A. For 3D printed optics this could result in curvature differences to the original design due to a loss in precision per printed layer, with incomplete voxels affecting the surface structure. Additionally, though a complete print may be observed at an undercured layer exposure, any supporting structures within more complex structured 3D prints will exhibit considerable malleability and softness. This could pose a problem to the uniformity

A Under Exposed



B Over Exposed

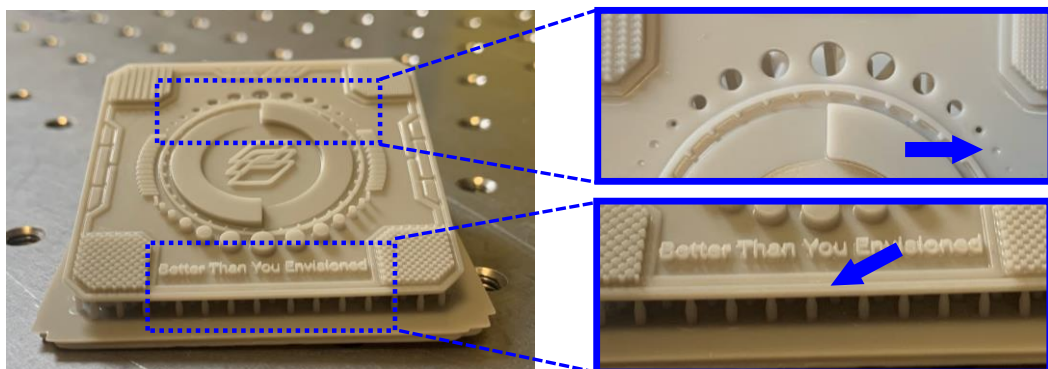


Figure 18. Example photographs of under (A) and over exposed (B) printed targets with digitally zoomed ROIs.

Chapter 3. Optical Quality 3D Printing

across the 3D print as low-density structural supports may lack in their ability to keep the 3D printed part stable during the printing process. Overcuring on the other hand will be visible by a loss in feature precision as excess illumination is smoothing out any precise features, shown in Figure 18B. Though the supporting structures and edges look well-matched to the design seen at the blue arrow of Figure 18B's bottom ROI, the finest feature holes have not been printed through the whole part and are fully or partially closed (shown by the blue arrow in the top ROI of Figure 18B). In the case of 3D printed optics, this may present itself instead as increased thicknesses around the curvature and height of the optical component and therefore a difference in the radius of curvature and focal length from the designed part. This change in thickness is due to a higher total absorption in the liquid resin at each layer due to the longer exposure time causing polymerisation in areas which would have been unaffected at lower light doses. For transparent resins even further overcuring can be present in comparison to opaque resins due to the higher optical transmissivity of the resin and therefore deeper absorption into resin beyond the targeted layer.

The exposure time variable itself is broken into two parts in most standard slicer software: the base or bottom exposure time, and the layer exposure time. The former is usually only for the first 5-10 printed layers to ensure secure adhesion to the build plate for the rest of the print and is usually on the order of multiple 10s of seconds. The layer exposure time will usually be approximately 10x smaller than the base exposure, depending on the resin used, and tweaking the exposure time by one-tenth of a second can vary a print from overcured or undercured to optimised for the desired print features. Both the resin and printer choice will also impact on the exposure time through the illumination power available with the printer and the layer curing times originating from the resin material properties. Overall, this will impact on the full model print time together with the choice of printing directly on the build plate or using supports to print the parts. The advantage of mSLA printing is that its simultaneous layer exposure means only the overall height of the tallest part to print determines the full print time, instead of a combination of print heights and quantity of designs as is the case in FDM or SLA printing.

With each of the identified variables calibrated, or in the first instance set to within limits where a complete print will be produced with reasonable feature resolution, the print can be sliced, and the resulting printer file can be added to the mSLA printer ready for printing.

3.1.3 Printing and Post-Processing

Before printing, the printer needs to be calibrated axially to ensure level printing and that the initial distance between the LCD screen and print head is optimised. This is usually performed by removing the resin vat, loosening the print head and using the zeroing function that comes with the printer's UI. A piece of paper between the print head and the LCD screen is utilised to effectively mimic the thickness of the resin vat film in order to obtain a zero location for the print head to limit itself to. An additional step for successful printing is to gently mix the liquid resin to ensure homogenous distribution of photoinitiators throughout the resin mixture. If printed immediately after mixing, bubbles from the mixing process may be present in the print, which for 3D printed optics causes random scattering of light which is undesirable for optics. These macroscopic bubbles can be eliminated before printing by waiting for most bubbles to dissipate after mixing, which should be completed in a short (10 – 30 minute) timescale depending on the viscosity of the resin. By decreasing the print head retraction and lowering speed and increasing wait times before and after illumination, bubble generation can also be mitigated during the printing process. Microscopic bubbles may still be present within a 3D printed optical quality component, though these will be virtually impossible to eliminate as the print head moves in and out of the resin filled vat after printing each layer. Additionally, these bubbles are hypothetical as they have not been observed within any of the resultant work in 3D printed optics to follow. With resin prepared as described above, the sliced design loaded onto the printer, and the printer calibrated, optical quality 3D printing can now be initiated using the printer's user interface.

Following the minutes to multi-hours printing, the 3D print will be left suspended on the print head and, given enough time, will drip most excess resin back into the vat below. To make the printed design safe to handle and remove excess uncured resin, it must be washed well with a compatible cleaning agent, usually through complete immersion within the cleaning medium. This cleaning agent can be water, if a water-washable resin is used, though in most cases isopropyl-alcohol (IPA) will be more suitable to clean off excess resin through either vortexing the printed part (plus the print-head if possible, which otherwise can be wiped clean) or utilising an ultrasonic bath. Once the part has been cleaned and left to either air-dry or has been blow dried using compressed air, any used supports should be removed as they are at their weakest at this point. If required, the part can then be cured further in a curing station to solidify any remaining uncured resin as well as toughening the solid resin further. This post-print curing increases the hardness of the part overall which can be desirable if higher impact resilience and lower fragility are required, especially in thinner printed sections. This curing

Chapter 3. Optical Quality 3D Printing

stage can also slightly change the surface finish on the 3D print, including the potential of yellowing of the surface and bulk material or flexing of thin parts depending on the resin used. These features, which can be inherent to the resin chemistry, will be discussed later. Finally, the result is a completed print, ready for use or form evaluation to iteratively improve the design or fabrication variables.

When manufacturing 3D printed optics, resin choice and 3D printer resolution are paramount. To exemplify this point, two different resins were used to print test targets which were evaluated on their feature quality, bulk-print quality, and overcuring signs (see Figure 19). For the bulk print quality, one evaluation is based on any resulting stress within the print, shown by significant deformation in the flatness of the print as seen in the difference in curvature (highlighted using the added dotted line) between Figure 19A and B's printed parts using two

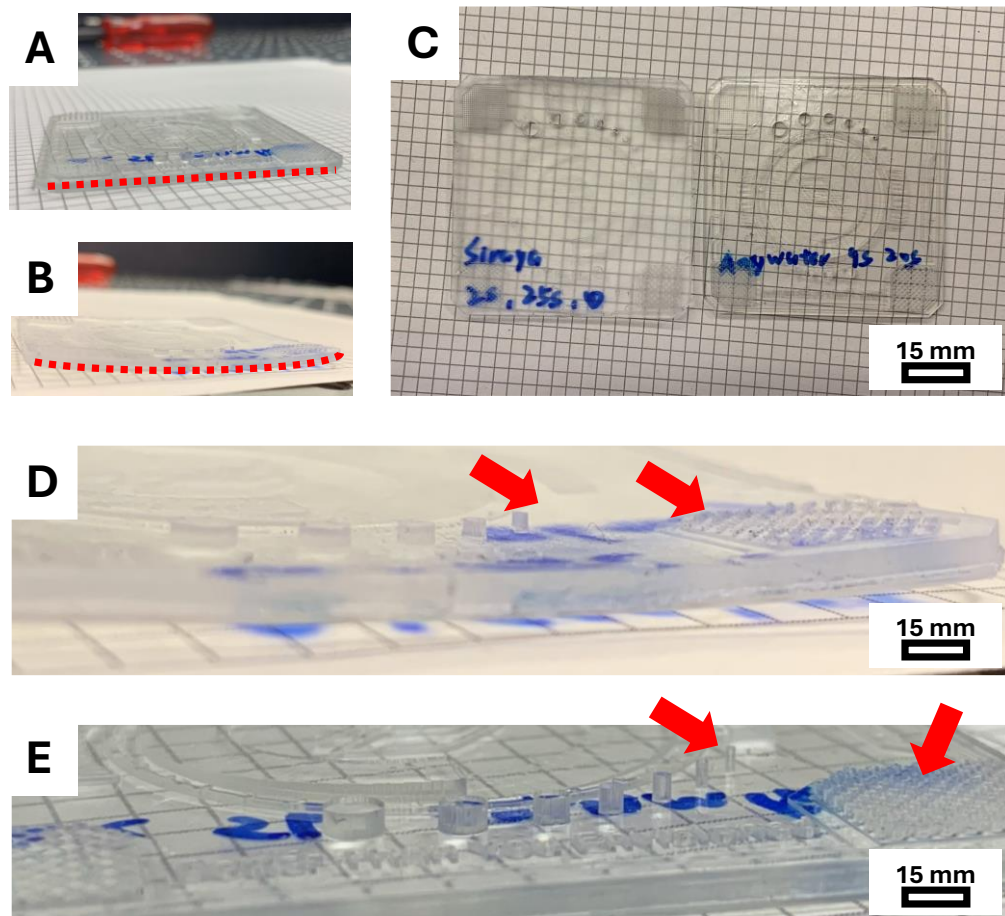


Figure 19. Images of the difference in resultant prints from two different commercial clear resins. (A) Target print from Resin 1 for curvature evaluation. (B) Target print from Resin 2 for curvature evaluation. (C) Transparency comparison between two printed targets using different resins. (D) Feature precision using Resin 2. (E) Feature precision using Resin 1.

Chapter 3. Optical Quality 3D Printing

different resins. Other variables which can be observed for bulk print quality for 3D printed optics resins are scattering effects within the resin reducing the transmission of the 3D print before coatings are even applied, as seen Figure 19C. The previously mentioned ‘quality of the features’ is in reference to the precision with which test targets are printed compared to other resins using their respective optimal exposure times, shown as the fine feature details in Fig 19D and E at the highlighted arrow regions. At the highlighted regions, the details from the 3D print in D are inferior in their fine details to those in E, with some of the finest cylinders missing from the print in D. Even at the optimal exposure time poor quality features can still be present, shown by a loss in feature detail which is purely dependent on the resin chemistry itself. The most visually obvious characterisation in transparent resin is yellowing in the

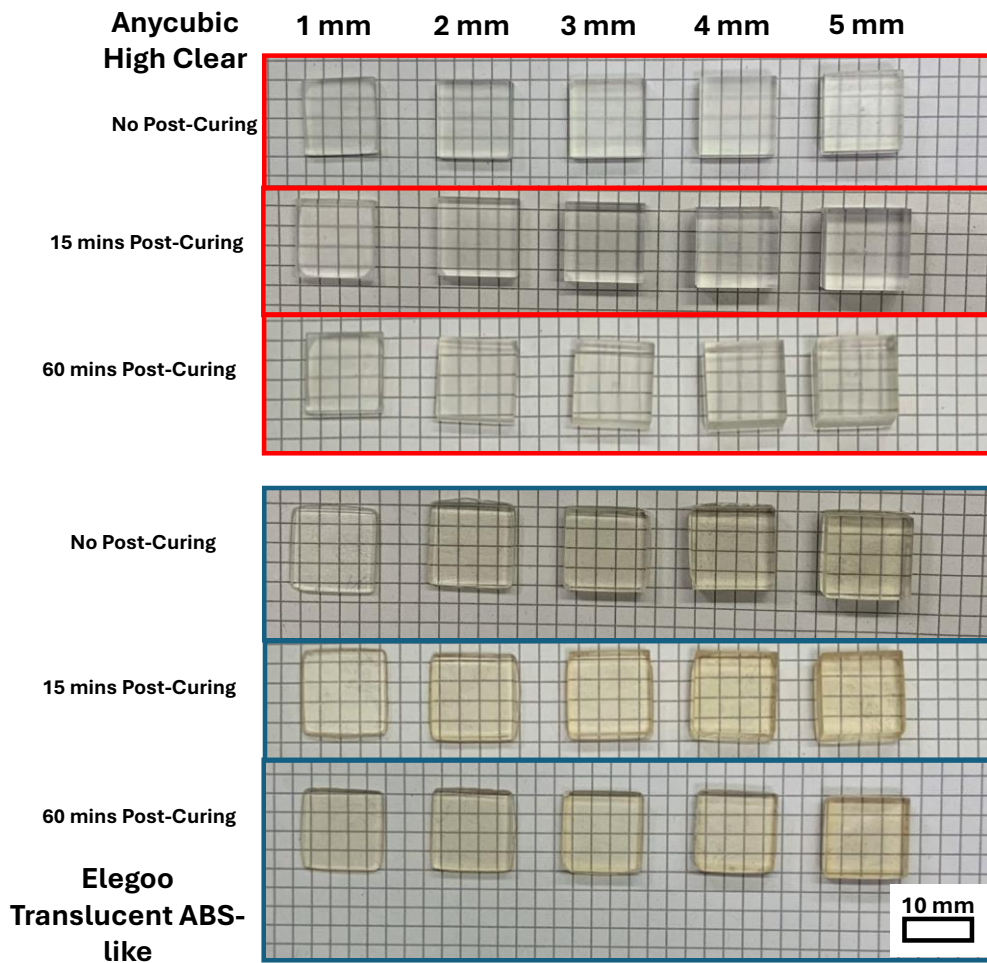


Figure 20. Comparison of different resin yellowing both immediately after printing and after some post-curing. (Top) – Anycubic High Clear resin printed cuboids with different thicknesses and differing timescales of post-curing. (Bottom) – Elegoo Translucent ABS-like resin printed cuboids with different thicknesses and differing timescales of post-curing

Chapter 3. Optical Quality 3D Printing

printed part which is exemplified in Figure 20. using two different transparent resins. The yellow colour is due to the unique chemical recipe of the resin itself, where resins with unique photoinitiators, or unique ratios of photoinitiators in the resin mixture will have differing degrees of discoloration compared to other clear resin formulae. In addition, the yellowing cannot be simply remedied by minimising or reducing the exposure time per printed layer, as even at their minimum necessary exposure time to ensure sufficient hardening of the bulk print and features, yellowing can still be a by-product due to the resin chemistry itself. It can therefore be observed that the yellowing is compounded through the UV curing post-processing steps essential for obtaining optical quality printed parts which is shown in Figure 20. Evident from the Anycubic High Clear results in the top of Figure 20 in red is minimal discolouration, both immediately after printing and at different post-curing times across all thicknesses of cuboids. This is especially evident in comparison to the like-for-like results using the Elegoo Translucent ABS-like resin on the bottom of Figure 20 shown in blue.

The yellowing in a bulk printed optic could itself be an issue when the optic is integrated into the excitation or collection arms of an imaging system, as higher yellowing can mean higher absorption within certain visible wavelengths. For applications in microscopy this could mean higher sample illumination input powers may be necessary to obtain a similar SNR compared to parts with a non-yellowing resin, as well as making the print itself prone to damage or heat generation through light absorption when using laser excitation.

3.1.4 Optical Quality Processing

To obtain optically transparent 3D prints with optical quality surfaces they must first be post-processed. Described within this section are the specific methods used to obtain optical quality printed parts for the data collected over the remaining chapters of this text.

Whether the 3D printed element is planar or not, the finished print will in general not be of optical quality. For the non-planar case, this is due to the well-documented ‘staircase effect’ which is created due to the layer-by-layer printing technique and shown in Figure 21. However, despite the absence of this effect when printing planar structures, the printed surfaces will still be at best translucent and are not yet optical quality due to the surface roughness of the printed faces. This surface roughness is predominantly a result of the lateral illumination profile of each LCD pixel from the 3D printer, as each 2D pixel at the surface of the print has a gradient of intensity. This leads to a non-uniform surface at the micron-scale, and this micron-scale surface roughness therefore reduces the optical clarity of the 3D printed

Chapter 3. Optical Quality 3D Printing

planar surface. A smaller part of this is due to the pixel illumination not being sub-wavelength, as this would result in illumination homogenous to provide optical quality prints.

In the case of non-planar surfaces there is the requirement to smooth over the staircase effect as shown in Figure 21(left). A consistent coating method is necessary to ensure the coating is applied with symmetry across the designed surface, and in the case of a spherical surface radially symmetric coating methods are crucial for homogenous optical transmission. Of the additive coating methods, spin-coating was the most attractive for the work in this thesis as dip-coating the 3D printed optic can result in a difficult to manage symmetrical increase in surface thickness. By lacking radially symmetric control across the surface and the coating thickness, a change in the radius of curvature occurs in difficult to replicate ways. It also creates a non-homogenous coating across the surface resulting in stronger optical aberrations, though still with an achieved transparent end-product. Spin-coating itself has numerous factors to consider, not limited to: the viscosity of the resin; the volume of resin dispensed onto the 3D print surface; the application of resin statically (stationary 3D print) or dynamically (as the print spins); the diameter of the lens; the radius of curvature; the spin-time for lens coating and the spin-speed; and whether or not to coat in stages e.g. 1000 RPM for 10 s then 2000 RPM for 5 s. Each of these variables individually will contribute toward changes in the offset from the designed component, which could also contribute to the type and intensity of any induced optical aberrations, and honing each variable for each optical design will result in an optimally

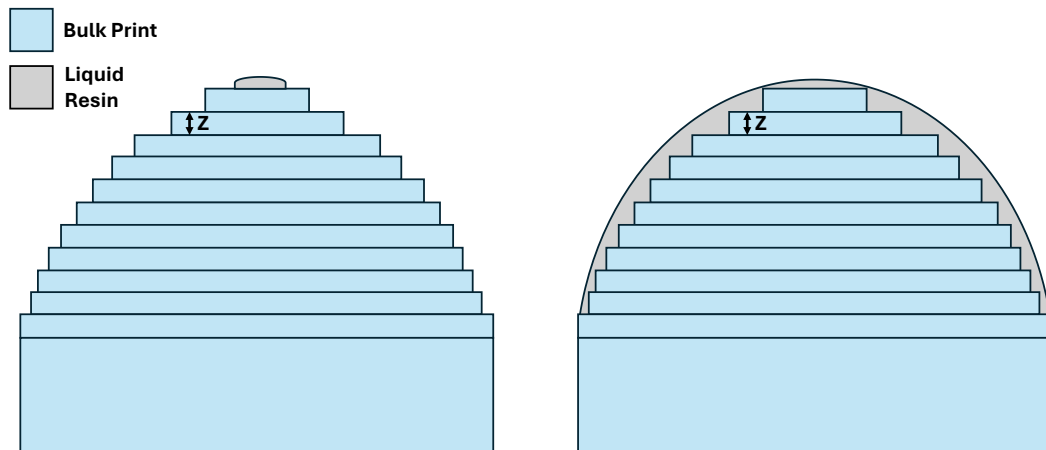


Figure 21. 3D printed optic before (left) and after (right) spin-coating procedure. Before coating the optic, the print layers create a staircase toward the centre axis of the lens. After spin-coating, the lens surface is smoothed across the staircase surface.

Chapter 3. Optical Quality 3D Printing

produced optical element using 3D printing. Other evaluations on the spin-coating protocols for staircase effect smoothing have been shown^{1,2,211} which created a foundation for the optimisation of the variables contained within this chapter. Where possible and practical, the impacts of each variable were quantitatively investigated on curved surfaces with commercial glass counterparts for points of comparison.

To achieve nanometre scale surface roughness for flat printed surfaces, post-process spin-coating approaches or free-form moulding with flat and polished optical quality glass elements as master moulds can be used. This can be done by using for example a glass microscope slide, coated with the same or similar clear resin used in the construction of the printed part. After coating the slide, it can be gently pressed flat against the 3D printed planar face with a curing process ensuring adhesion and replication of the flat surface to the 3D print. Prior to curing an extra step is required to remove any trapped air bubbles in the liquid resin between the glass microscope slide and 3D printed part. This can be done through vacuuming the slide/optic combination to remove microscopic bubbles which without removal will contribute to a diminished optical quality of the finished part. Following removal of bubbles and once cured and removed from the glass slide, the printed component has effectively taken on the transmission properties of the glass slide by mimicking its surface roughness. The specific methods on how prints are processed to obtain optical quality characteristics will be further expanded on later in this chapter, and using these principles, optically transparent flat surfaces can be manufactured with relative ease and low-cost resources. It should be noted that researchers have shown that a glass microscope slide can be fixed to the print head and, following axial recalibration to ensure the thickness of the glass slide has been accounted for, directly printing planar surfaces onto this glass slide can result in an optical quality surface without further optical post-processing on this surface²³².

Chapter 3. Optical Quality 3D Printing

For the optical elements utilised within the optical setups in chapters 4 and 5, two transparent resins were used for 3D printing, with their optimised print parameters shown in Table 2. These resins were used across two different 3D printers, subject to availability at the time of the respective imaging experiments: the Elegoo Mars 2, and the Phrozen Sonic Mini S. The Anycubic High Clear resin was not tested on the Elegoo Mars 2 as chronologically the optical experiments involving the Mars 2 printer had already been completed before the Anycubic High Clear resin and Phrozen Sonic Mini S printer had been purchased. The higher lateral resolution of the Phrozen printer made it the optimal choice for the experiments within Chapter 5, and therefore optimal variables for the Mars 2 and the Anycubic High Clear were not required. However, the Formlabs Clear resin (RS-F2-GPCL-04) and Anycubic High Clear resins were compared for their exposure times and feature quality using the Phrozen printer as this would determine which resin was best used for the results in Chapter 5.

Resin	3D Printer	Base Exposure Time	Layer Exposure Time
Formlabs Clear	Elegoo Mars 2	60 s	9 s
Formlabs Clear	Phrozen Sonic Mini S	45 s	8 s
Anycubic High Clear	Phrozen Sonic Mini S	35 s	4.2 s

Table 2. Printing details required for the resins and printers used within optical characterisation and imaging experiments. All printing was performed at 10 μm layer heights for 3D printed optics.

Chapter 3. Optical Quality 3D Printing

Additive post-processing also contributes the non-trivial consideration of refractive index differences, if different materials are used for coating compared to the bulk material. Shown in Figure 22 is an exaggerated schematic of a post-processed lens and the follow-on effects from different materials used for lens manufacturing. The refractive index boundaries provide different amounts of refraction of light, indicated by the arrows in the figure, where the angle light refracts at in θ_1 will be unequal to the angle of refraction for θ_2 assuming that the two different resins of feature two different refractive indices. The boundary toward the planar surface for a refractive index n_3 should contribute no alternative diffraction due to the refractive index being the same across the boundary shown within the figure. As such, these boundaries can contribute toward optical aberrations from the 3D printed optic due to the refractive index mismatches at each interface.

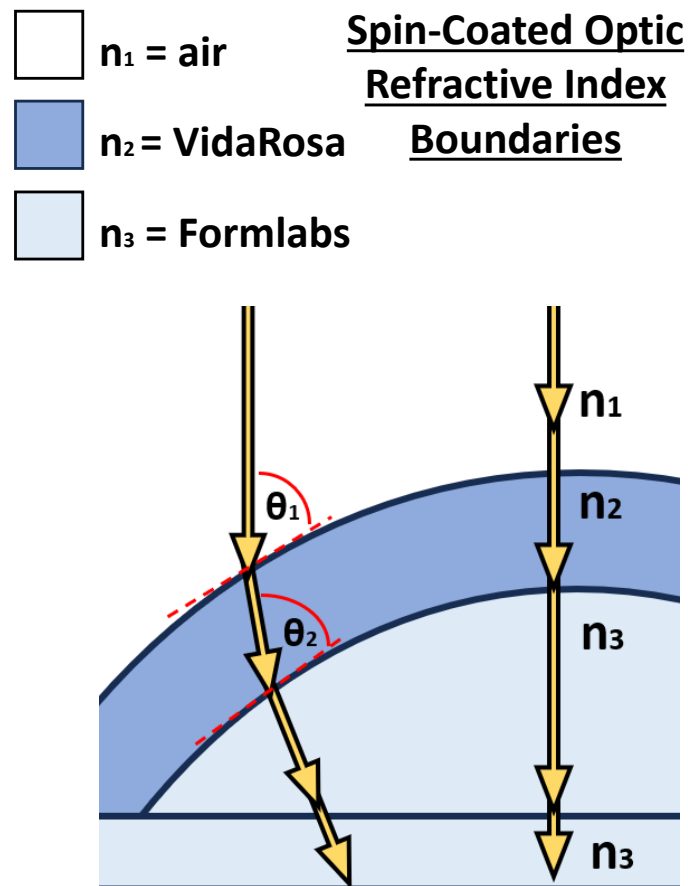


Figure 22. Exaggerated diagram of 3D printed optic refractive index interfaces after spin-coating procedure, with arrows to indicate the path of collimated light through the optic.

3.1.5 Spin-Coated 3D Printed Optics Methodology

As mentioned previously, lens geometries for 3D printed lenses were created in a mechanical CAD software (Autodesk Inventor Professional 2023), with identical geometry to off-the-shelf components for cross-comparison. The design files were translated to printer-readable file formats using a free slicer software (Chitubox basic) and printed using a consumer grade 3D printer with 10 μm layer step size. Detailed fabrication characteristics for each optic manufactured are shown in Table 3 in Appendix A.

The fabrication process to obtain optical quality non-planar components is shown in Figure 23A-D and should be invariable of the clear resin used, unless otherwise stated. This shows the initial 3D printing step in A which results in a print with a staircase effect equal to the chosen z-resolution. It is followed by a cleaning step B where the completed print was cleaned with 100% isopropyl alcohol (IPA) for a maximum of 10 minutes and blow-dried with compressed nitrogen. In step C the curved surface was spin-coated with a secondary clear resin (UV resin “Crystal clear”, Vida Rosa) using a friction-only affordable (~£2000) spin coater (Ossila L2001A3-E463-UK) at e.g. 1800 RPM for 12 seconds for a 20 mm focal length. The secondary resin is used in this case as curing times for a 20 mm focal length lens convex

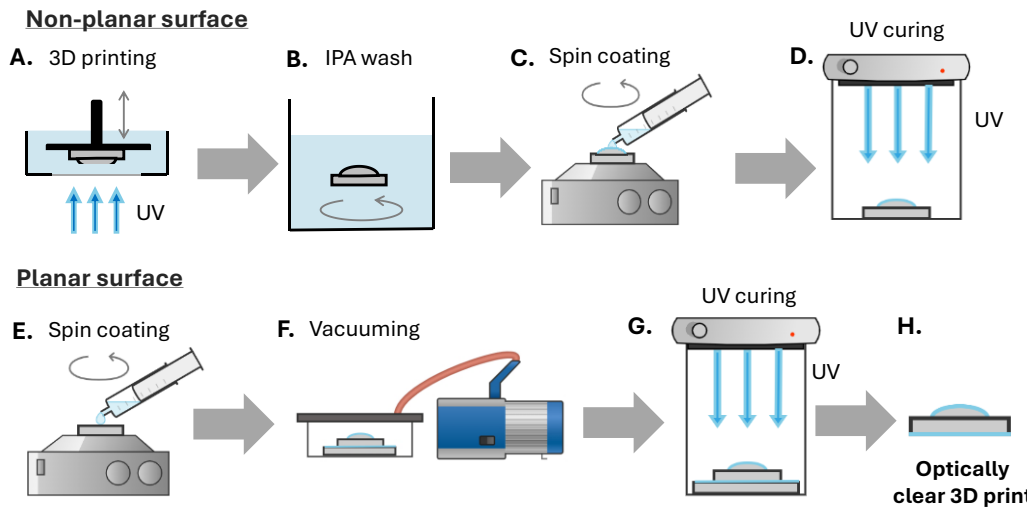


Figure 23. Schematic of 3D printed optics spin-coating manufacturing process. (A)-(D) Manufacturing an optically clear non-planar surface; (E)-(G) Manufacturing an optically clear planar surface; (A) 3D printing schematic showing the layer-by-layer technique using incident UV light; (B) Cleaning stage using isopropyl alcohol (IPA) to remove residual resin; (C) spin coating non-planar surface by pipetting resin onto surface prior to spinning; (D) non-planar spin coated surface cured with UV light; (E) resin pipetted onto glass slide for spin coating; (F) resin-coated glass slide and 3D printed planar surface placed in contact and vacuumed together; (G) UV curing of resin coated slide and planar 3D printed surface; (H) schematic of resultant optically clear 3D printed part, shown here as a plano-convex lens.

Chapter 3. Optical Quality 3D Printing

surface, with similar coating thicknesses and identical curing conditions, is mere minutes using Vida Rosa compared to over 3 hours using Formlabs Clear Resin. This extended time would add both impracticality to the technique as well as inhomogeneity in ensuring radially uniform curing across the lens surface, particularly for short focal length convex lenses where resin can pool toward the diameter of the lens resulting in non-uniform thicknesses across the surface. The resin was dispensed onto the centre of the static, curved surface using a 1000 ml pipette at an angle of $\approx 40^\circ$ to ensure good wettability. Coating parameters such as spin speed and spin time, which again are intrinsically related to the printed lens dimensions, were independently optimized for each lens type used. As per step D a UV curing step for 12 minutes was performed using 405 nm and 385 nm LED excitation (Elegoo Mercury Plus 2-in-1 wash and cure station). After curing the curved surface, the lens was spray-washed with a small (< 50 ml) amount of IPA and blow-dried with compressed nitrogen, partially to remove surface dust from the lens post-curing, though more-so to prepare the planar surface for coating in a plano-convex lens design.

The planar surface coating (Figure 23E-H) is created by spin-coating a glass microscope slide with liquid resin (RS-F2-GPCL-04, Formlabs for the Mars 2 prints, Vida Rosa for Phrozen prints) at 1400 RPM for 10 seconds shown as stage E, and then placing the cleaned planar surface onto the slide to enable best planar surface quality². It should be noted that lenses with a smaller diameter can have better flatness to their normal axial position by increasing the spin speed to e.g. 1800 RPM, as these smaller diameter lenses require less resin to coat their planar surface. Additionally, larger diameter lenses may benefit from slower spin speeds as a thicker layer of resin will spread across the planar surface, which ensures a good ratio of resin to the bulk optic to ensure uniform coverage compared to smaller volumes of resin. To remove macroscopic and microscopic air bubbles formed within the resin between the printed lens and glass slide, the combination was left in a vacuum chamber of -0.9 bars for 30 minutes as per step F or until all bubbles had been removed. The lens-slide combination was then UV cured for 8 minutes using the same Mercury Plus wash and cure station as before, shown in G, which bonds the 3D printed part to the slide. The finished lens, shown in H, was removed from the glass slide using a freezer spray to leverage differential thermal expansion between the printed plastic and glass slide. Some manual leveraging with a scalpel at the 3D printed lens' edge was additionally required at times. To exemplify the optical clarity improvement from each step, the result of each lens processing step is shown in Figure 24 using 20 mm focal length lens designs. Each lens shown has a 12.7 mm diameter, though a 25.4 mm boundary ring

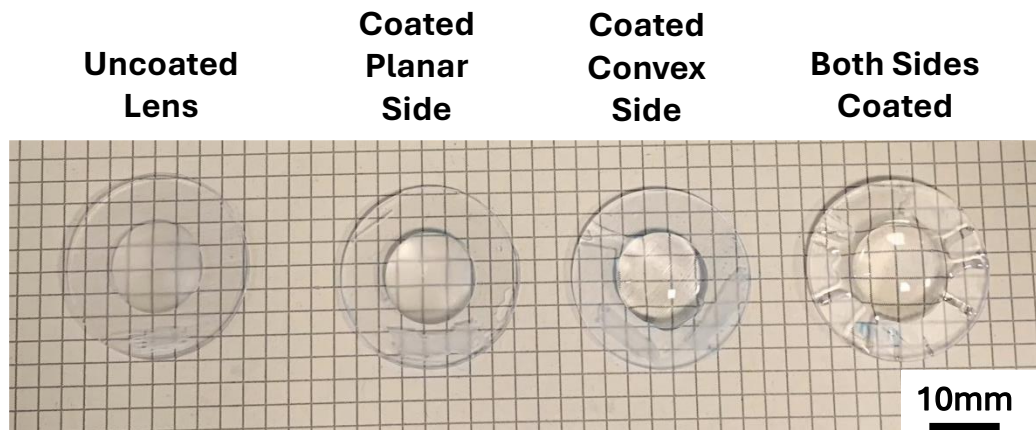


Figure 24. Visual differences in the obtained transparency of a 3D printed optic using the described optical post-processing methods. From left to right they introduce a lens with no optical post-processing; a lens where only its planar side has been optically post-processed; a lens where only its convex surface has been post-processed; and a lens with both surfaces optically post-processed.

surrounds each lens as an area for low-risk handling so as not to damage the lens surface and as a mounting support for 25.4 mm lens holders. To manufacture and process lenses using this spin-coating method the material costs were found to be under \$0.18 per lens, without considering the printer cost, curing station cost, or spin-coater.

3.1.6 Moulded 3D Printed Optics Methodology

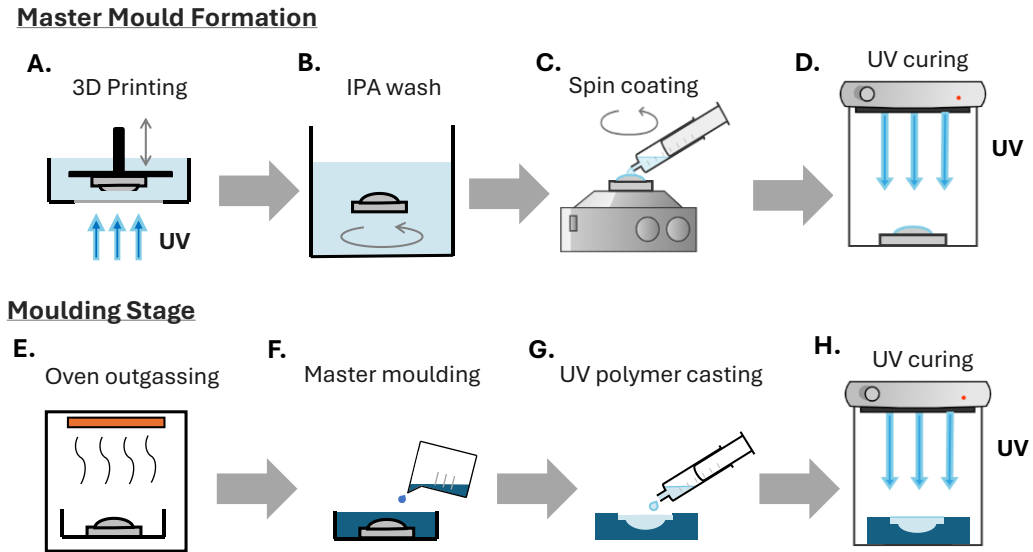


Figure 25. Schematic of 3D printed optics moulding manufacturing process. (A)-(D) Manufacturing an optically clear non-planar surface; (E)-(G) Creation of a mould and optically clear final optic; (A) 3D printing schematic showing the layer-by-layer technique using incident UV light; (B) Cleaning stage using isopropyl alcohol (IPA) to remove residual resin; (C) spin coating non-planar surface by pipetting resin onto surface prior to spinning; (D) non-planar spin coated surface cured with UV light; (E) outgassing of coated 3D print; (F) mould mixture is used to create a master mould from the processed print; (G) a transparent UV curing resin fills the mould; (H) the moulded optic is obtained by UV curing the resin within the mould.

An alternative method of optical quality lens manufacture utilises silicone moulding, which was the method used for lenslet array production for imaging in Chapter 5. Moulding was used for this case as the printers used throughout the optics development result in the occurrence of some diffraction-related aberrations originating from the non-uniform voxels in the direct printing process. This was not observed in a moulded lens fabrication process, which is explored in more detail in Chapter 4. Traditionally, as explained in Chapter 2, moulding utilises a high-quality master copy to obtain precise moulds which mimic the surface roughness and form of the master copy. This works well as a technique for optical quality additive manufacturing, though as previously stated the requirement of the master copy could minimise the economic benefits of manufacturing the optical element unless numerous copies are required. To maximise the economic benefits in conjunction with the freedom for custom lens design, the master mould was itself a post-processed 3D printed optic using the previously described spin-coating method due to the high-quality surface roughness obtained from spin-

Chapter 3. Optical Quality 3D Printing

coated 3D printed optics. For Chapter 5 specifically, the master copy was manufactured using Anycubic High Clear resin as material on the Phrozen Sonic Mini 8K S 3D printer, printed at a 90° angle to the print-bed with anti-aliasing features maximised (anti-aliasing level 2). Vida-Rosa resin was then used as the transparent resin for moulded optical components. The master copy used in Chapter 5 was a custom design array of millimetre scale lenslets. Once the optical quality master copy has been created, it must be outgassed as shown in step E, which was done using a 55° C oven for 48 hours to speed up the naturally occurring outgassing process. If the outgassing of the 3D printed part was not performed, the silicone moulding mixture would not bond to the master copy as it would stay in a semi-liquid state at the mixture-mould interface. The result of this is a mould with millimetre-scale surface roughness incapable of producing imaging quality 3D printed optics. Therefore, once the 3D print has been outgassed the master copy is ready to be used to create the master mould, from which numerous 3D printed moulded optics could be manufactured.

The mould itself is a low-cost commercially available two-part silicone mixture (e.g. Let's Resin Silicone Mould making kit, from Amazon) which when mixed and left at room temperature completely solidifies into a flexible mould. Once the two-part mixture was well-combined, it was poured over the master-copy as per step F and left to set for at least 48 hours at room temperature. The method of optics manufacture, shown at each stage in Figure 25 with commercial MLA for comparison, is evidently significantly slower than the direct fabrication process, however inhomogeneities in the bulk optic are virtually eradicated. The 48-hour mould making step allows the mould plenty of time to completely dry and solidify, resulting in a flexible mould with inverse optical geometry to the master copy, though with near-identical surface properties as shown later in this chapter. The master mould was then filled with Vida Rosa resin shown in step G with bubbles either pipetted away or left to pop over time under vacuum. Caution is necessary at this step however as under vacuum the liquid resin 'foams' with bubbles until completely degassed, which can result in the resin spilling over the mould and reducing the volume of resin for moulding leading to an inhomogeneous part thickness.

To ensure the planar side of the optic had the same clarity and surface roughness as those produced following Figure 24's methodology, a Vida Rosa spin-coated glass slide was gently applied to this surface, with the spin-coating step necessary to minimise bubble generation between the slide and resin within the mould. The mould could then be cured for 30 minutes, shown in stage H, to ensure complete curing throughout the bulk optic and to the edges of the

Chapter 3. Optical Quality 3D Printing

mould as well. One observation includes that thinner (e.g. < 4 mm thick) silicone moulds would deform during the curing process due to the expansion of the resin and from the heat by-product generated through curing the Vida Rosa resin, so thicker-walled moulds performed better for this stage. The master copy was therefore designed as shown in Figure 26 to incorporate a large well to provide ample room for the moulding mixture. Once curing is complete, the moulded lens can be easily removed from the silicone, the glass slide leveraged as previously described in section 3.1.5, and the result is a 3D print assisted lens with optical quality properties and without the influence of voxel patterning and inhomogeneities within the bulk optic. This manufacturing method isn't unlike the moulding technique developed by Elgarisi *et al.*²²⁰ in their differential media experiments. However, unlike their technique, honing of the media densities or designed boundary conditions are instead replaced with delay times while waiting for curing stages to complete.

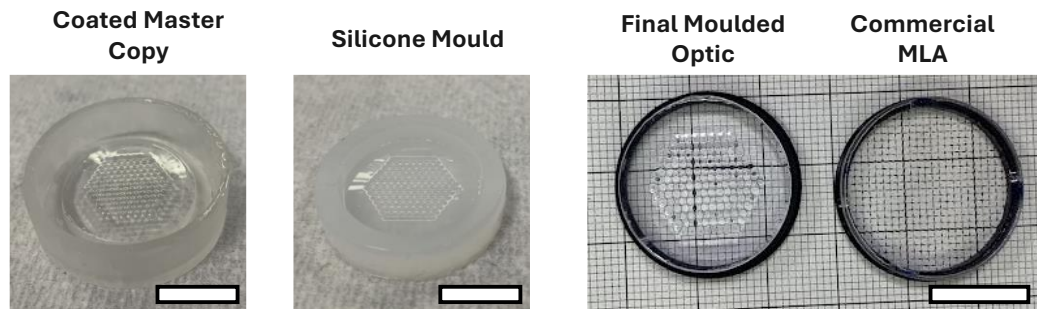


Figure 26. Photograph examples of key moulding process stages with commercial MLA for comparison. Scale bars = 15 mm.

3.2 Evaluation Methods of Printed Parts

3.2.1 Optical Transmission

Test cuboids with varying thickness as shown in Figure 27 were used to evaluate the optical transmission characteristics with respect to the 3D printed optical thickness and illumination wavelength. They were designed with 12.7 mm by 12.7 mm surfaces, thicknesses ranging from 1-5 mm in 1 mm increments, and printed and processed following the planar printing and processing steps in sections 3.1.5 and 3.1.6. The cuboid's processed and unprocessed versions are shown in Figure 27, however only processed cuboids were used to examine transmission results. A three colour multi-mode laser diode module (Odicforce OFL352-300) with wavelength outputs of 445 nm, 520 nm, and 638 nm was used as the illumination source for evaluating the wavelength dependent transmission, as shown in Figure 28. The input and transmitted power through the 3D printed cuboids was sequentially measured three times to obtain an average and standard deviation uncertainties at a single output power for each wavelength using a Thorlabs S121C optical power meter, with power fluctuations between measurements on the scale of 3% or less.

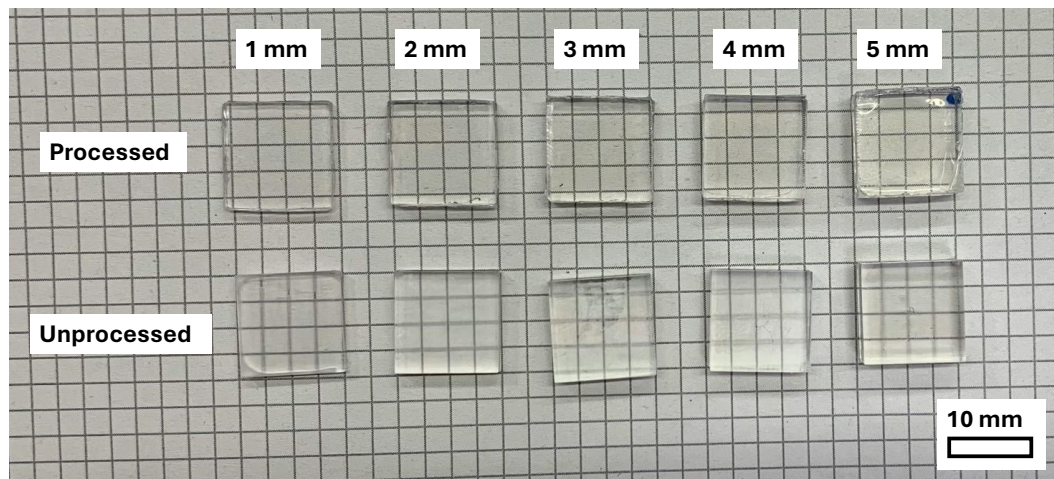


Figure 27. Photograph of processed and unprocessed cuboids of various thicknesses for optical transparency evaluation. The processed cuboids show higher optical transparency on the gridlines beneath across all cuboid thicknesses compared to the unprocessed cuboids.

Chapter 3. Optical Quality 3D Printing

Figure 28 shows the optical transmission of 3D printed test cuboids as a function of block thickness and wavelength. The blocks are separated into moulded components, following the moulding procedure using Vida-Rosa resin as the complete optic, and direct prints, following the spin-coating procedure using Formlabs Clear resin for the complete part. For the directly printed parts, for each wavelength the transmission decreases as the block thickness increases, which is expected to follow an exponential decay with further increasing thicknesses. Additionally, for each block thickness the transmission decreases as the wavelength of light decreases, for example at 3 mm block thickness the transmission decreases from 90 % at 638 nm to approximately 85 % at 445 nm. This is a logical outcome as the curing wavelengths for the 3D printing resin, and therefore the wavelengths with the highest absorption, are near UV so it is expected that the transmission will be lower for lower wavelengths of light. The transmission for the highest wavelength used, 638 nm, is initially 92% and drops by 1-2% with every 1 mm added to the block thickness. The moulded lenses do however not exemplify the same behaviour. Instead, their transmission is consistently within a maximum 4% loss range

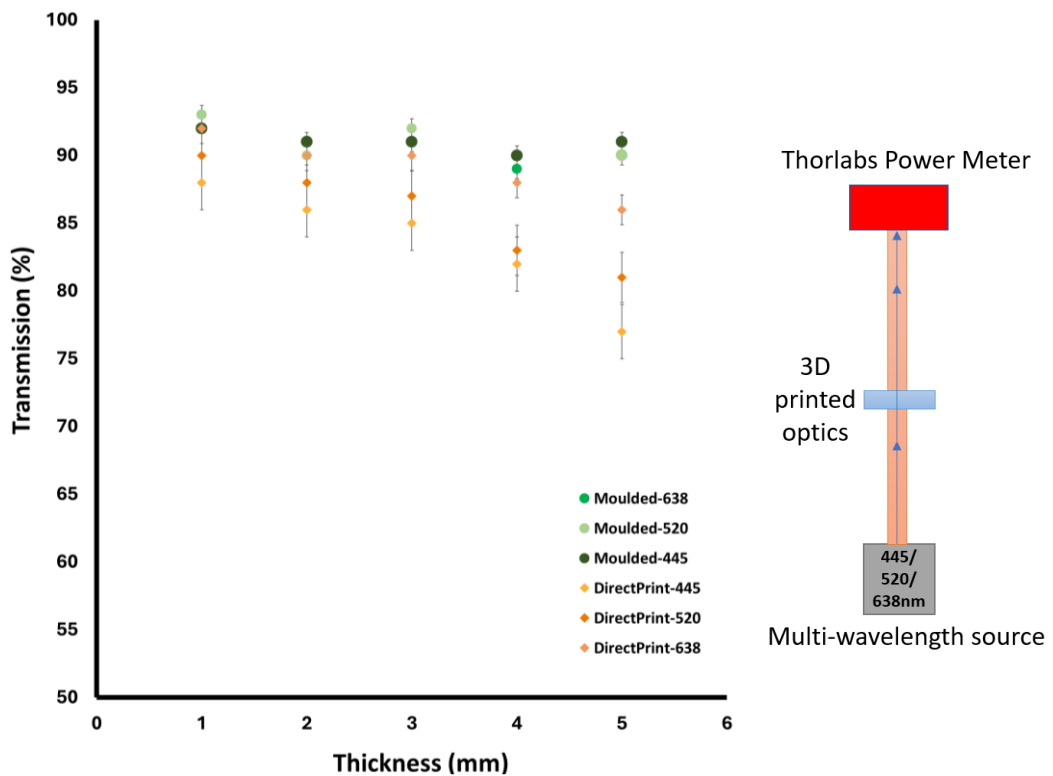


Figure 28. Transmission results from multi-mode laser light through optically clear 3D printed blocks of increasing thicknesses (left) and the schematic of the measurement setup (right).

Chapter 3. Optical Quality 3D Printing

across all wavelengths and thicknesses. This will be in part due to the difference in absorption between the two resins at each wavelength, as well as the minimisation of scattering in the moulded optic due to the lack of voxel-based manufacturing in comparison to the directly printed optic. In addition, some of the observed losses for both sets of optics are also in part due to Fresnel reflections from the incident laser light onto the flat surface. In comparison to the commercial data from Thorlabs bought parts across the three distinct wavelengths using an uncoated 10 mm thick NBK7 block, the moulded optics differ by only 1% on average compared to the Thorlabs block, though at half the measured thickness. As expected, the directly printed cuboids differ by 3 – 8% on average to the Thorlabs block.

3.2.2 Surface Quality: Non-Contact Measurement Approach

Quantitative information about the optical surfaces was obtained through a non-contact approach using the Veeco NT1100 White Light Optical Interferometer. The interference between a reference arm and the sample under test creates fringes on an optical surface and axially shifts them, through translating the reference arm, to obtain highly accurate (on the order of nanometre to sub-nanometre-scale) surface and roughness results. Using this approach, a glass slide used to manufacture optical quality 3D prints was measured as a benchmark for form uniformity and surface roughness, with a processed planar surface measured against this for comparison. The planar surface of the manufactured part can be seen to be comparable in form on average to a glass slide identical to one used in the coating

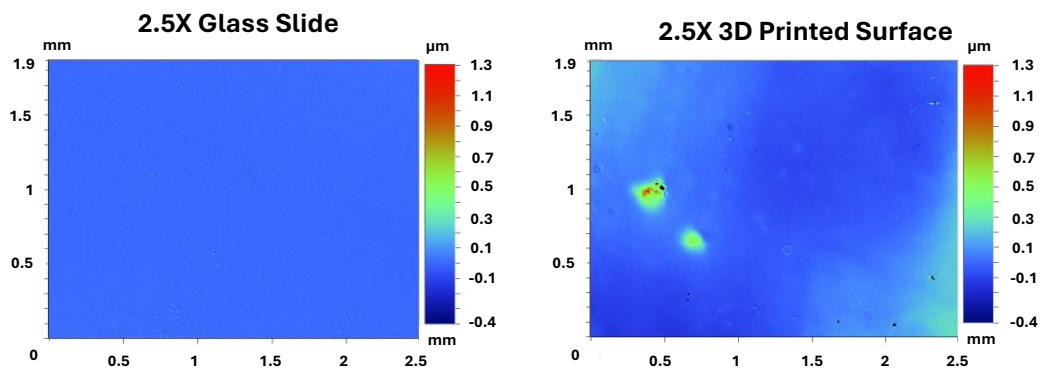


Figure 29. Optical profiler results from a commercial glass microscope slide and a planar surface post-processed using a commercial glass microscope slide. (Left) – 2.5x magnified optical profile image of the glass slide surface with a colourbar legend to show height differences. (Right) – 2.5x magnified optical profile image of the 3D printed post-processed planar surface with a colourbar legend to show height differences.

Chapter 3. Optical Quality 3D Printing

procedure of the printed planar surface (see Figure 29). There is a region on the processed 3D print surface with high malformation, though this is more likely to be microscopic dust or dirt during the spin-coating process as the post-processing is performed outside of cleanroom conditions. Aside from this region, which artificially increases the overall form height, most of the 3D printed surface lies within the blue defined region of the colour bar legend which corresponds to a mean roughness of 70 nm. For the commercial glass, the form is considerably more uniform despite the presence of microscopic dust particles, therefore exhibiting a mean roughness of 7 nm. Despite the 3D printed planar surface having an order of magnitude difference in average form across the surface, the processed 3D printed surface still exemplifies a mean roughness less than $\lambda/12$ which is beyond the requirement for optical clarity in reference to the flatness form of the surface.

1D form line plots can also be obtained from the optical profile results via x and y axis line-plots across the optical profile image as shown in Figure 30. This allows an average roughness value along single axes to be extracted from the optical profile image using the Vision software used in conjunction with the instrument. Note the form itself can vary from positive and negative values depending on the surface's deviation from an average 'zero' value. The glass slide 1D form plot results in an average roughness value below 100 nm across both x and y line-plots, which is to be expected from a glass microscope slide. This superior flatness is mostly impacted by dust particles present on the glass which impact the optical measurement, though even despite this the average flatness is still at the nanometre scale. Similarly, the 3D printed optic has copied the optical quality flatness well, however some higher discrepancies in the form of the flat surface below and above the averaged 'zero' value can be seen in the x and y plots. This will be due to some inhomogeneity in the thickness of the resin across the surface, resulting in regions of higher and lower optical quality surface roughness. Despite

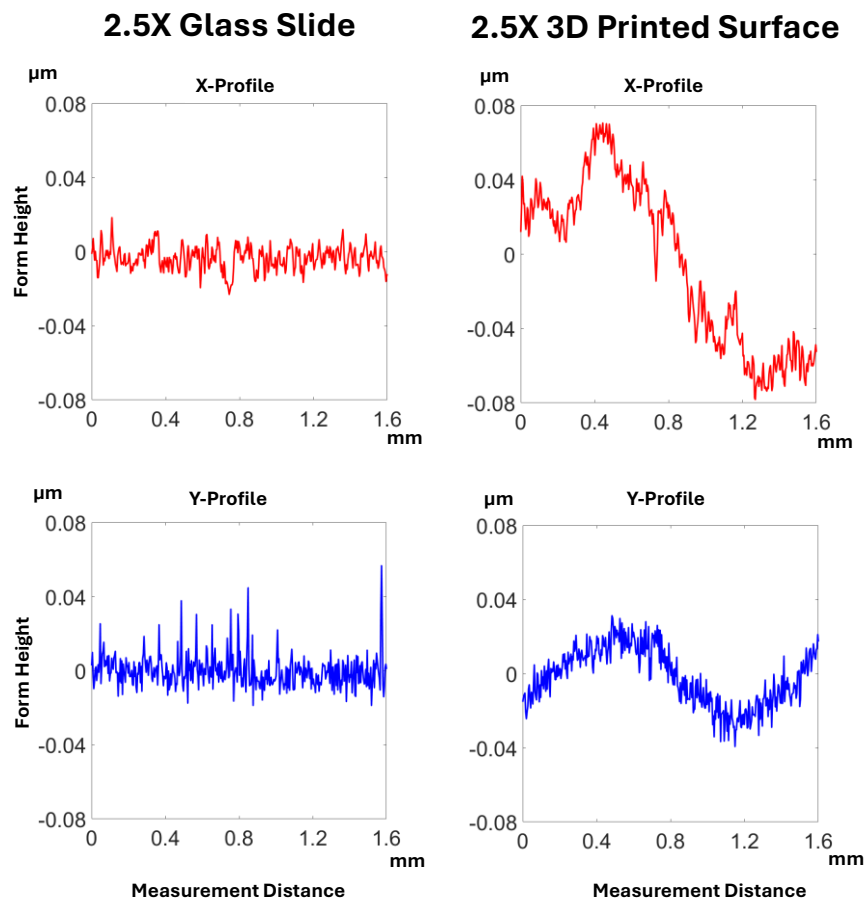


Figure 30. Surface roughness measurements acquired using the optical profiler of the commercial glass microscope slide and the 3D printed planar surface manufactured using a glass microscope slide. (Left) – Commercial glass slide x and y surface roughness line profiles generated using the optical profile results. (Right) – 3D printed optically post-processed planar x and y surface roughness generated using the optical profile results.

this, the extracted average roughness remains at the tens of nanometre scale across each axis, providing an optical quality surface for the 3D printed part. For the convex surface of a 20 mm focal length lens, the optical profiler was not able to obtain a complete signal across the FOV to obtain quantitative information to compare both a commercial and 3D printed optic. This optic was therefore evaluated using contact methods of surface quantification.

Chapter 3. Optical Quality 3D Printing

The commercial and 3D printed lenslet arrays were characterised using the same methods as the larger optics described in this section, using the Veeco NT1100 White Light Optical Interferometer. The optical profiles of the commercial and 3D printed lenslets are shown in Figure 31. The smaller pitch commercial lenslets exhibit some non-uniformity across the measured FOV, though this could be a result of measuring almost the entire lenslet compared to a significantly smaller region of the 3D printed lenslet. The form measurement covers a full $1.3\ \mu\text{m}$ measurement height, with a measured mean roughness of $227\ \text{nm}$ across the full FOV. The 3D printed lenslet shows good form and clarity across the optical profile measured area, though again this is only over a small ROI as is obtainable using the optical profiler at this accuracy range for comparison. The printed lenslet does include a higher mean roughness of $348\ \text{nm}$ across the measured FOV, though this is expected from the spin-coated convex optical surface.

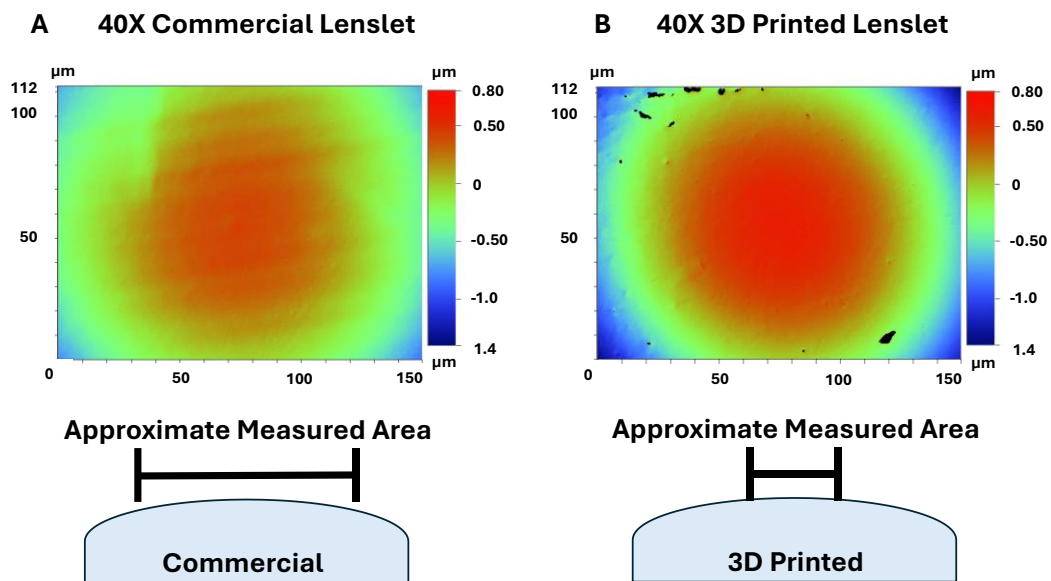


Figure 31. Non-contact results of commercial and 3D printed lenslets. (A) – Optical profile of commercial lenslet showing form across the surface. (B) – Optical profile of 3D printed lenslet showing form across the surface.

Chapter 3. Optical Quality 3D Printing

Shown in Figure 32 is the extracted 1D form line profiles from the optical profiler of the commercial and 3D printed lenslet arrays. The glass lenslet array x and y line profiles show a spherical surface, which is expected, by measuring across the full width of the individual lenslet. The mean roughness values extracted from the line-plot range from 100 - 200 nm across both x and y line-plots. This roughness is likely higher due to the inhomogeneous areas toward the 80 - 100 μm range of the y-profile in Figure 32. The 3D printed optical line profiles, though homogeneously spherical across the measurement range, do have a higher mean roughness of 170 - 320 nm across each axis. The higher roughness is an expected outcome as has been previously seen for 3D printed optical surfaces compared to commercial optics, though the mean roughness for the 3D printed optic surfaces are still within a high enough range for optical quality transparency.

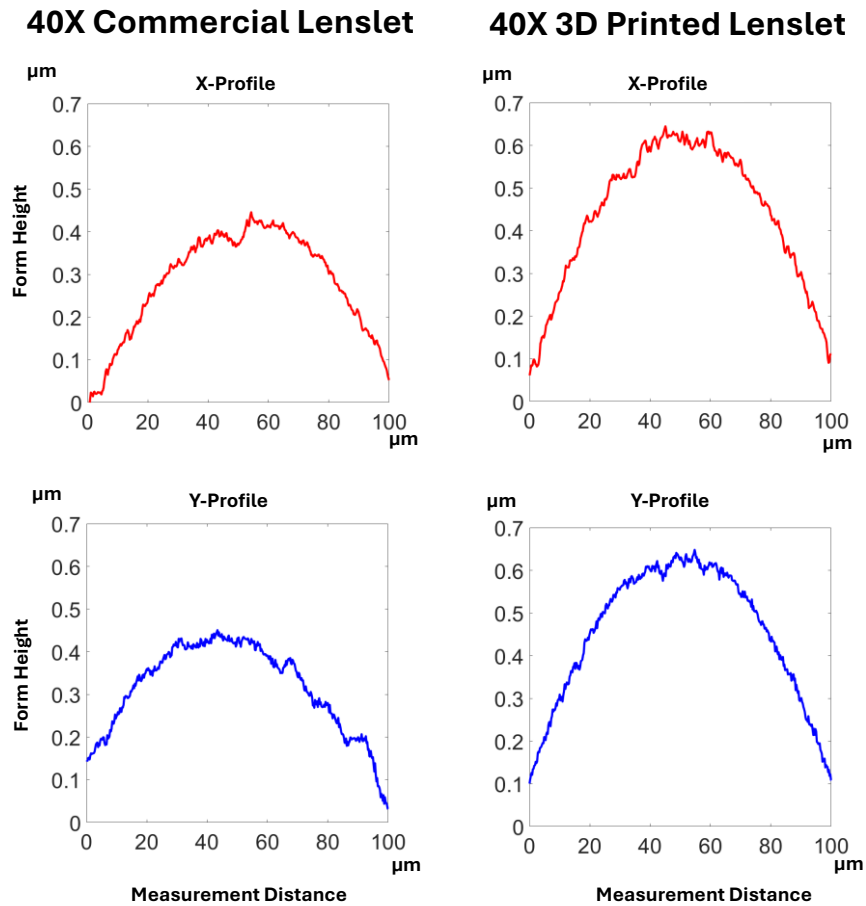


Figure 32. Surface roughness measurements acquired using the optical profiler of the commercial microlens array and the 3D printed lenslet array. (Left) – Commercial microlens array x and y surface roughness line profiles generated using the optical profile results. (Right) – 3D printed optically post-processed lenslet array x and y surface roughness generated using the optical profile results.

3.2.3 Surface Quality: Contact Measurement Approach

Following the manufacturing procedure described in section 3.1.5, curved surfaces of 3D printed optics were evaluated using the KLA Tencor Alpha-Step IQ stylus profiler within a cleanroom environment. This equipment covers a single axis roughness and form measurements through direct contact with a stylus featuring nanometre-scale precision. Using this, the profile of the 20 mm commercial glass polished lens was measured as comparison to a printed convex surface of matching design geometry. Plano-convex lenses were manufactured and used as a simple way to evaluate different prescriptions and how processing these prescriptions differs between each lens geometry. To exemplify the necessity for spin-coating to obtain optical quality surfaces, stylus results of an uncoated 3D printed lens are shown in Figure 33. From this figure, the 10 μm step height can be seen from the 3D printed layers. Some smoothing at the boundary between one layer and the next is seen in the figure, which is in part due to the stylus' inability to get directly into the corner of each step, as well as from some slight overprinting expected in the corner of each step of the staircase due to

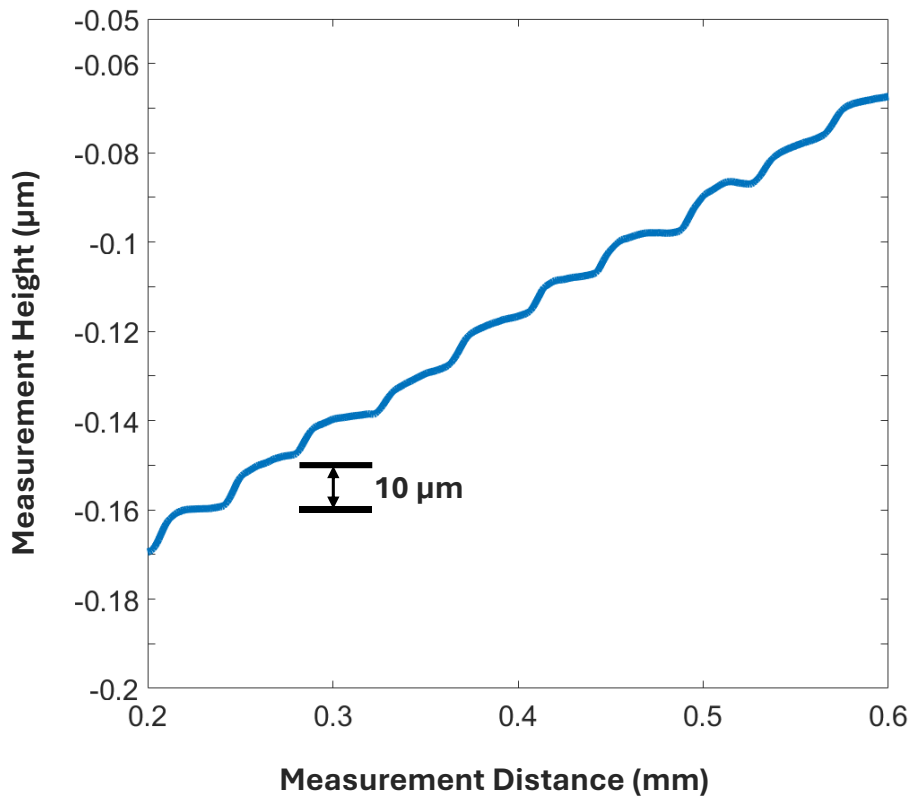


Figure 33. Stylus data from an uncoated convex surface of a 20 mm focal length, 12.7 mm diameter 3D printed lens.

Chapter 3. Optical Quality 3D Printing

slight overprinting from one layer onto the next. The stylus profiler results also allow for the quantification of one or multiple lenses as 3D printed objectives in custom imaging systems, which is investigated further in Chapter 4. Lenses were designed to match commercial Thorlabs plano-convex designs, making use of a ½” diameter 20 mm focal length plano-convex lens (LA1074), and three 6 mm diameter lenses consisting of a plano-convex $f = 10$ mm focal length lens (LA1116), a plano-convex $f = 15$ mm focal length lens (LA1222), and a plano-concave $f = -6$ mm focal length lens (LC2969). The results from the stylus profiler were processed in MATLAB in a custom circle fitting function (Appendix B) to evaluate the form adherence of the curved surfaces to an ideal spherical fit, as well as extracting radius of curvature measurements from the data. The stylus data fitted against an ideal circular fit allows for an absolute error to be produced between the data points and the perfect circle. Additionally, differences in the radius of curvature between the designed part and measured radius of curvature from the circle fitting function can be compared. These results can be seen

Chapter 3. Optical Quality 3D Printing

in Figure 34 for 3 printed lenses and 1 commercial glass lens as comparison. To show the effect of spin-coating processes on the 3D printed lens surfaces, stylus results were then taken as a point of comparison. For the 20 mm lenses in Figure 34, the resulting measured radii of curvature are 9.67 mm for the 3D printed lens and 9.93 mm for the commercial glass lens. The shape error for both lenses over a 1.6 mm central diameter is within 200 nm of an ideal spherical shape, with surface roughness below 70 nm RMS for both lenses. The < 2 mm measurement range was used as larger measurement distances either required less measurement accuracy in the stylus profiler or were out-of-bounds for the stylus profiler to

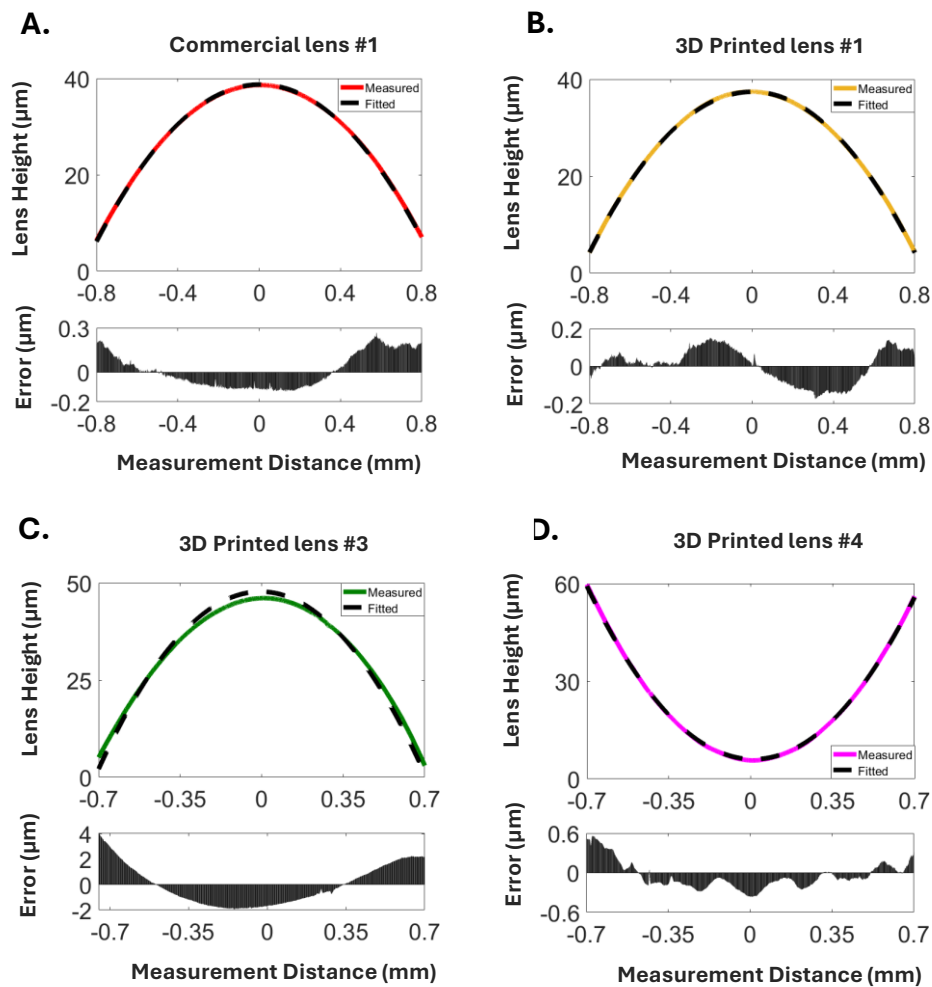


Figure 34. Geometrical characteristics of the 3D printed lenses with a commercial comparison. (A) Surface profile of a commercial 20 mm focal length, 12.7 mm diameter lens; (B) Surface profile of a 3D printed version of a 20 mm focal length, 12.7 mm diameter lens; (C) Surface profile of a 3D printed 10 mm focal length, 6 mm diameter lens; (D) Surface profile of a 3D printed plano-concave lens with a -6 mm focal length and 6 mm diameter.

Chapter 3. Optical Quality 3D Printing

obtain. For the 6 mm diameter spherical singlet lenses used in Chapter 4 to evaluate the performance and trade-offs of using multiple lenses for custom imaging objectives, the measured surface shapes are shown in Figure 34 C-D. The shape error for the 10 mm focal length plano-convex lens shows the highest error of almost 4 μm which could be due to its higher curvature compared to lens 4 in the multi-lens configuration (Figure 34). At the same time the error for the plano-concave lens is less than 500 nm. For all three cases the surface roughness is below 150 nm RMS. The measured radii of curvature are for all three cases within 94 % of the design specification based on the original Thorlabs design files. Additionally included in Appendix C are 90° rotations of each optic within the stylus profiler to evaluate the perpendicular measurement axis. The curvature radii deviates across this rotation by < 1 % for the commercial optic and at its highest < 7 % for the 3D printed optics, highlighting the source of astigmatism within the printed lens surfaces. The surface roughness of the flat sides of all lenses is identical to the results from section 3.2.2 where planar surfaces were evaluated. The stylus profiler was also used for line plot results (Figure 35) to evaluate the moulded optics for the lenslet arrays used in Chapter 4. The commercial lenslet conforms well to an ideal spherical fit, with an error as low as 300 nm present, though the majority of the spherical form data from the ideal circular fit lies within a sub-100nm range. Radius of curvature information could not be extracted from the manufacturer, though a measured value of 3.5 mm was obtained. In comparison, the 3D printed lenslet shows higher form errors of its spherical fit, as shown in the line plot in Figure 35B, though this is within the expectations from spin-coating optical elements. The printed lenslet still appears to have good adherence to a spherical

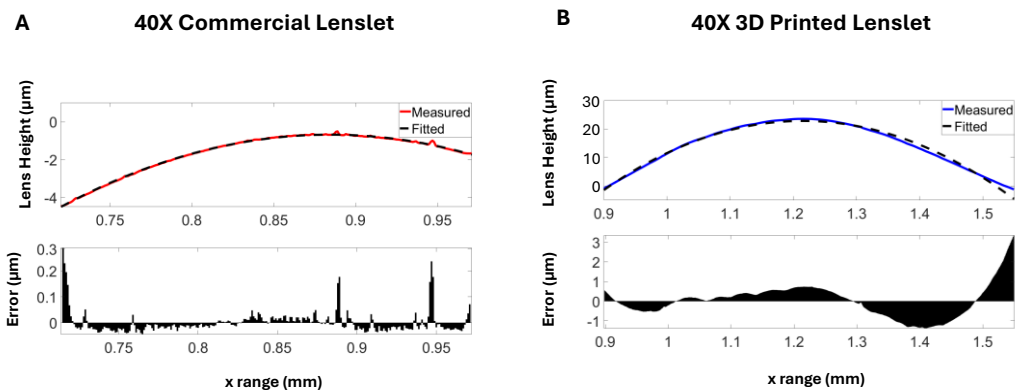


Figure 35. Geometrical characteristics of the commercial and 3D printed lenslet arrays. (A) Surface profile of the commercial version of the microlens array; (B) Surface profile of the 3D printed lenslet array.

Chapter 3. Optical Quality 3D Printing

geometry as with the other printed optical profiles of larger diameter lenses. The measured radius of curvature was 2.4 ± 0.08 mm compared to the designed 3 mm. This is a 20% difference from the design, though the expectation is that the significantly smaller diameter of lens contributes to higher discrepancies from the design as spin-coating inhomogeneities may be compounded at these low lens diameters. An additional note on this is that the lenslets themselves can have their complete pitch measured, which provides a complete insight into the lens curvature and roughness compared to the relatively small measurable area of 1-2 mm of a 6 mm or 12.7 mm diameter lens. Using the stylus to obtain roughness measurements, mean roughnesses in the range of 70-110 nm were obtained across the 3D printed lenslets, showing that they are therefore suitable in roughness for optical quality microscopy. Uniformity of the lenslet curvature is well-matched to the circular fit as with the other 3D printed optics shown previously. Despite the reduced quality of the printed lenslet array from the stylus data, the evidence of whether or not these inexpensive, rapid prototype, custom lenslet arrays can be useful for super-resolution microscopy will be within the biological data acquisition itself. Therefore, the lenslets documented in this section are used for image scanning microscopy in fluorescence biology.

3.3 Discussion

As post-processing methods evolve with new technologies becoming available, there is a clear potential to have low-cost optical quality 3D printed lenses rivalling the quality of commercial lenses. With the current generation of low-cost printing technology available it has been found that one of the optimal methods to reliably create imaging-quality lenses is through the spin-coating and moulding manufacturing techniques documented in this chapter. Lab-produced optics can vary from batch to batch due to difficult to account for human error, with the most destructive errors being visible by eye. However, by following the outlined manufacturing methods within this chapter an additively manufactured optical element can be created within the tolerances required for optical microscopy. Otherwise, by measuring the radius of curvature across multiple axis rotations on the same optic the radius of curvature can be honed to values on the order of single percentage differences away from the nominal value. Optical characteristics such as the transmissivity of the optical components, which has high averages above 90 % across block thicknesses and wavelengths for moulded optics, have been shown for the printers and resins used for the imaging involved in the next chapters. The transmissivity of directly printed cuboids was shown to fall significantly more across

Chapter 3. Optical Quality 3D Printing

wavelengths and increased thicknesses than the mould manufactured cuboids. Despite this, the method of manufacture is still used for optical lenses in optical microscopy research shown in Chapter 4. Additionally, the optical components were analysed using optical profilometry and stylus measurements, where their respective forms were found to be close to the ideal fits compared to commercial optics. For the optics used in Chapter 4 imaging, they complied well to the perfect spherical fit at >94 % adherence regarding their radii of curvature, and despite some form deviations and higher roughness's than the commercial components or spherical fits, the optics are promising for their use within biological imaging systems. The 3D printed optics showed surface roughness on the order of tens to low hundreds of nanometres, making them smooth enough for optical transparency and microscopic imaging. Additionally, the commercial microlens and 3D printed lenslet array were evaluated using the optical profiler and stylus, where enough signal was obtained using the optical profiler at high magnification to analyse the form of the optics. Both lenslet arrays showed wavelength range surface roughness on their convex surfaces, and though radius of curvature measurements were unable to be concluded for the commercial optic, the 3D printed optic showed 80 % similarity to its design specification, which should still be compliant with a quantitative comparison for imaging in Chapter 5 compared to the commercial optic. The comparative quantification of 3D printed lenses for microscope objective integration and 3D printed lenslet arrays for excitation beam shaping compared to their commercial equivalents has therefore been shown to be possible. The results from this quantification have significant promise for the current generation of low-cost 3D printed optics' integration into biological microscopy, where the investigation of their imaging performance is shown in Chapter 4, and the investigation of their beam shaping capabilities is shown in Chapter 5.

Chapter 4. Imaging using 3D Printed Objectives

To benchmark the optical quality 3D printed lenses can achieve using the technology and processes described in the previous chapter, the lenses are used as imaging optics in brightfield transmission and epi-fluorescence microscope configurations and compared to their commercial counterparts. Single and multi-lens configurations of 3D printed and commercial lenses will be used and compared as custom imaging objectives. This will include the evaluation of lateral resolution and contrast homogeneity using standard chrome-lithography resolution targets, as well as comparing identifiable details within more complex biological structures in brightfield transmission microscopy. Additionally, the performance comparison for exciting and collecting fluorescence signals from biological samples will be presented.

4.1 Microscope Construction & Characterisation

4.1.1 Microscope Design

A simple custom transmission and epifluorescence microscope was designed as an evaluation platform for two different imaging objectives (see Figure 36). The imaging objectives under test consisted of (A) a single $f = 20$ mm plano-convex lens with a theoretical magnification of 8x and NA of 0.1, and (B) a multi-lens higher magnification 50x objective with a theoretical NA of 0.35 which consisted of multiple $\varnothing = 6$ mm lenses. These objectives can be interchanged at the '3DPL' location in Figure 36A, where B and C within this figure show an image and schematic of the multi-lens objective and single lens objective to be used at this location. The figure shows the brightfield illumination arm in yellow, including all elements needed for a Köhler illumination, as well as the imaging arm in red, and the fluorescence excitation arm in blue.

For the brightfield illumination arm, Köhler illumination was set up to ensure homogenous illumination across the sample, with samples such as standard resolution test targets and fixed cell slides placed between the Köhler condenser lens and the imaging objective under test. Homogenous illumination was critical in ensuring a quantitative comparison between commercial and 3D printed imaging optics. The source for the Köhler illumination was a white light LED (Luxeon LST1-01H06-3088-01) collimated using a 5x objective (Beck 5x/0.12 Air) which acts as a collector lens. The collimated light was apertured through the field diaphragm

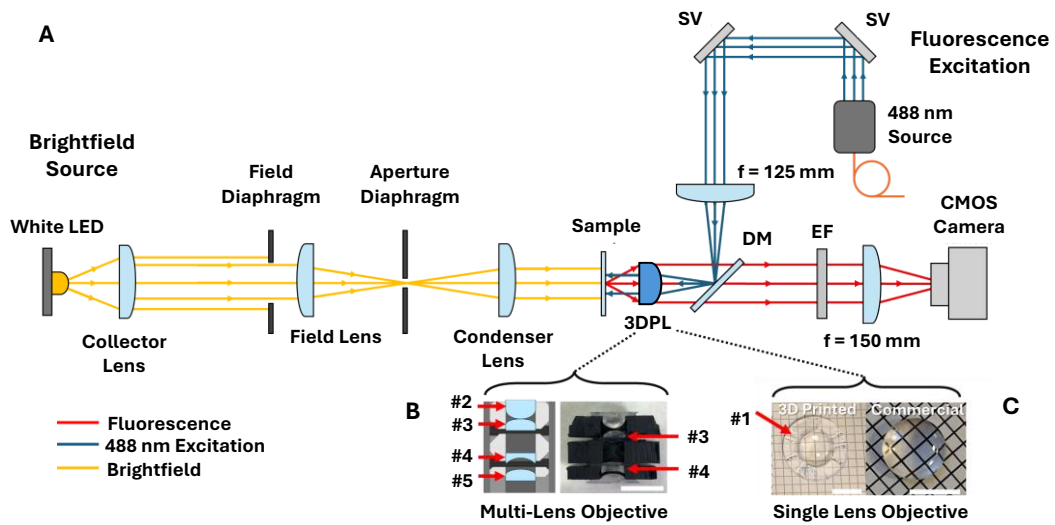


Figure 36. Microscope setup for brightfield and fluorescence imaging comparison of 3D printed and commercial single and 4-lens objectives. (A) Schematic optical path of the microscope setup using either a group of 4 singlet lenses or a single plano-convex lens as the primary objective, shown as (B) and (C) respectively. 3DPL – 3D Printed objectives under test; DM – dichroic mirror; EF – emission filter. (B) Schematic and image of multi-lens objective with 4 singlet lenses. #2 Commercial aspherical $f = +6$ mm lens; #3 $f = +10$ mm plano-convex lens; #4 $f = -6$ mm plano-concave lens; #5 $f = +15$ mm plano-convex lens. (C) Photograph of single lens objective with 12.7 mm diameter, 3D printed $f = +20$ mm plano-convex lens and commercial counterpart with identical specifications. For both objective types, Numbers #1, #3 and #4 indicate which lenses are used to test 3D printed lenses in imaging. Scale bars = 10 mm.

(Thorlabs ID20) and focused through the aperture diaphragm (Thorlabs ID20) using an $f = 60$ mm plano-convex field lens (Thorlabs LA1134-A). The light was then collimated onto the sample using an $f = 100$ mm plano-convex condenser lens (Thorlabs LA1509-A) to create uniform illumination over the field of view. When swapping imaging objectives, the illumination NA can be changed by adjusting the aperture diaphragm to ensure maximised illumination energy density while maintaining homogenous flat-fielded illumination.

The fluorescence epi-illumination was set up to use a single-mode 488 nm laser diode (Odicforce OFL-488) for illumination through the objectives under test. This coherent single mode illumination led to some diffraction phenomena through the 3D printed lenses which is discussed later. To mitigate this, the excitation source was fibre-coupled into a 5 m long multimode fibre (Thorlabs M43L05), which mitigated the appearance of diffraction effects by slightly defocusing the excitation onto the sample. The output light from the multimode fibre was reflected off two silver mirrors with tip-tilt adjustment (Newport U100-A-LH ULTIMA) for lateral beam-steering into a 30 mm cage system. The excitation was then partially

Chapter 4. Imaging using 3D Printed Objectives

collimated towards the objectives under test using a commercial $f = +125$ mm achromatic lens (Thorlabs AC254-125-A) and a dichroic mirror (Chroma ZT405/488/561/640rpcv2) which are also within a 30 mm cage system. By using a cage system, the $f = +125$ mm lens can be repositioned as needed relative to the objective under test without inducing significant aberrations. For fluorescence imaging, two 500 nm long pass emission filters (Thorlabs FELH0500) were placed in the infinity space before the $f = 150$ mm achromatic lens acting as tube lens (Thorlabs AC254-150-A). An industrial grade CMOS camera (IDS U3-3060CP) was used to capture the microscope images. The 3D printed objectives were axially aligned to create a telecentric imaging setup for each configuration.

4.1.2 Microscope Calibration

A simple way to confirm that the axial alignment of the brightfield illumination setup was acting in Köhler illumination was through observation of critical illumination onto the aperture diaphragm. Critical illumination is a directly observable form of illumination where an image of the illumination source itself is imaged onto the sample. Using an LED as the source, an image of the LED emitter itself could be seen (as the illumination image shown in Figure 37A) at the location of the aperture diaphragm, which corresponds to the image plane of the field lens. This is an important outcome as it exemplifies that the image plane from the light source is no longer in the sample plane. By aligning a condenser lens after this location the sample

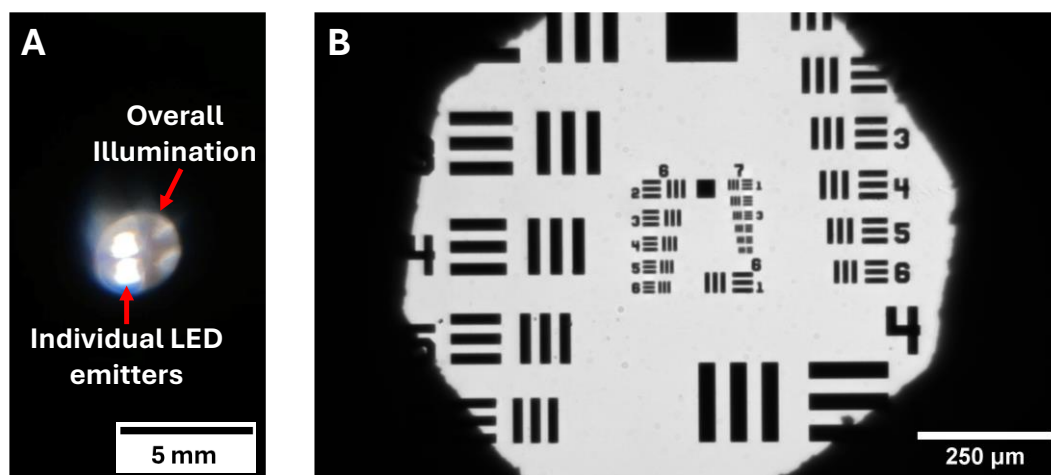


Figure 37. Example of critical illumination and confirmation marker of Köhler illumination. (A) – Photograph of critical illumination from LED source. (B) - In-focus image of Aperture Diaphragm edges, exemplifying correct axial distance for Köhler.

illumination can therefore be flat-fielded. Additional confirmation of Köhler illumination was observed through in focus imaging of the aperture diaphragm onto the camera when restricting the FOV as shown in Figure 37B.

For the fluorescence excitation the 488nm laser source was initially fibre coupled through a single mode fibre and after collimation through the 3D printed single lens objective showed significant diffraction and speckle patterning as shown in Figure 38. The diffraction effects in Figure 38A compared to the single-collimated spot from a complementary glass lens in Figure 38B are presumed to be a result of a voxel-based patterning throughout the bulk optic. The cause of this is likely due to the 3D printing process, where inhomogeneous illumination in each pixel across each printed layer has the potential to create regularly patterned refractive

Single-Mode

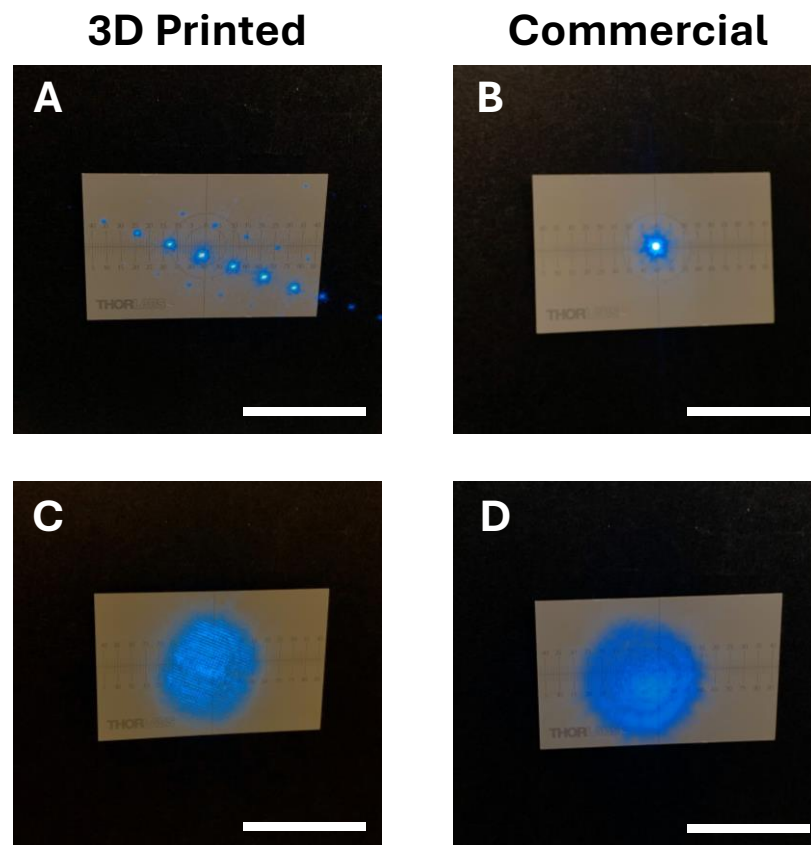


Figure 38. Photographs of resultant illumination patterns using single mode excitation through optically clear spin-coated 3D printed optic. (A) Collimated illumination through a spin-coated 3D printed optic. (B) Collimated illumination through a commercial equivalent optic. (C) Defocused illumination through a spin-coated 3D printed optic. (D) Defocused illumination through a commercial equivalent optic. Scale bars = 50 mm.

index changes through the print which act as a volume grating. When defocusing the illumination, the single-mode output still exemplified the voxel-based patterning throughout the 3D printed optic shown in Figure 38C, despite its surface roughness being sub-optical wavelength. This is opposed to the more homogenous defocused image created using a glass optic in Figure 38D. Homogenous excitation across a fluorescent sample was vital to quantitatively characterise the performance of a 3D printed optic in comparison to a commercial glass optic, and therefore the excitation was switched from single to multi-mode laser illumination in an effort to minimise the diffraction effects.

Figure 39 uses the same experimental setup and printed lens geometry as Figure 38, but with the multi-mode excitation. It can be seen from Figure 39A that diffraction effects are still

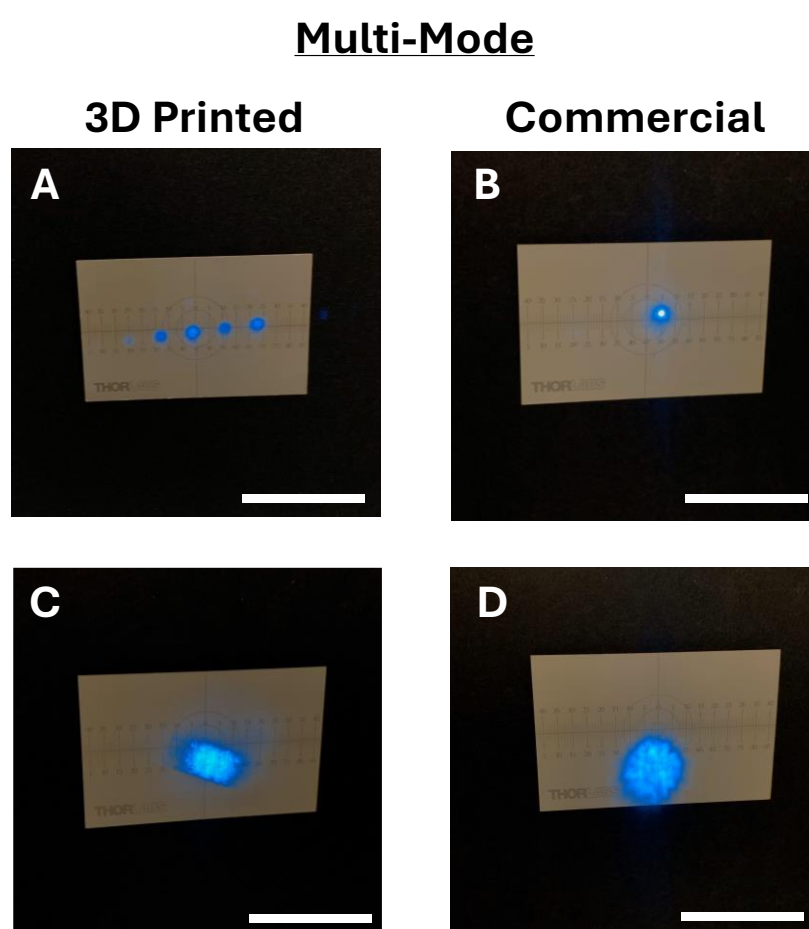


Figure 39. Photographs of resultant illumination patterns using multimode excitation through optically clear spin-coated 3D printed optic. (A) Collimated illumination through a spin-coated 3D printed optic. (B) Collimated illumination through a commercial equivalent optic. (C) Defocused illumination through a spin-coated 3D printed optic. (D) Defocused illumination through a commercial equivalent optic. Scale bars = 50 mm.

Chapter 4. Imaging using 3D Printed Objectives

observable under multi-mode collimation similar to those in Figure 39A under single-mode excitation. This can be expected as though higher spatial modes are present, temporal coherence is still present in both different fibre-coupled inputs. The diffraction pattern spots have not been removed by switching to higher spatial modes, however the voxel-based patterning has been reduced in comparison to single-mode illumination, which can be seen in Figure 39C. This shows that higher illumination homogeneity is possible through defocusing the excitation, effectively blurring the illumination into one pattern in comparison to Figure 39C, which exemplified the voxels within the 3D printed optic. The spatial uniformity under multi-mode excitation is additionally not dissimilar to the commercial optic shown in Figure 39D. As a result, the 3D printed optics could therefore be used in quantitative comparisons to the commercial optics during their operation as fluorescence excitation and collection

microscope objectives. An additional note on the topic of laser excitation through the 3D printed lenses is that moulded optics do not exhibit the same behaviour as directly printed optics, shown in Figure 40. When creating collimated illumination using a moulded optic, no diffraction patterns are visible under single-mode excitation and Figure 40A shows considerably comparable homogeneity to the commercial optic performance when creating collimated illumination in Figure 40B. There is however the addition of extra background/speckle, likely due to lower ideal surface characteristics of the moulded lens compared to the polished glass optic. When defocusing through both optics, similar homogeneity is observed through the moulded lens as seen in Figure 40C in comparison the commercial counterpart of Figure 40D.

Single-Mode

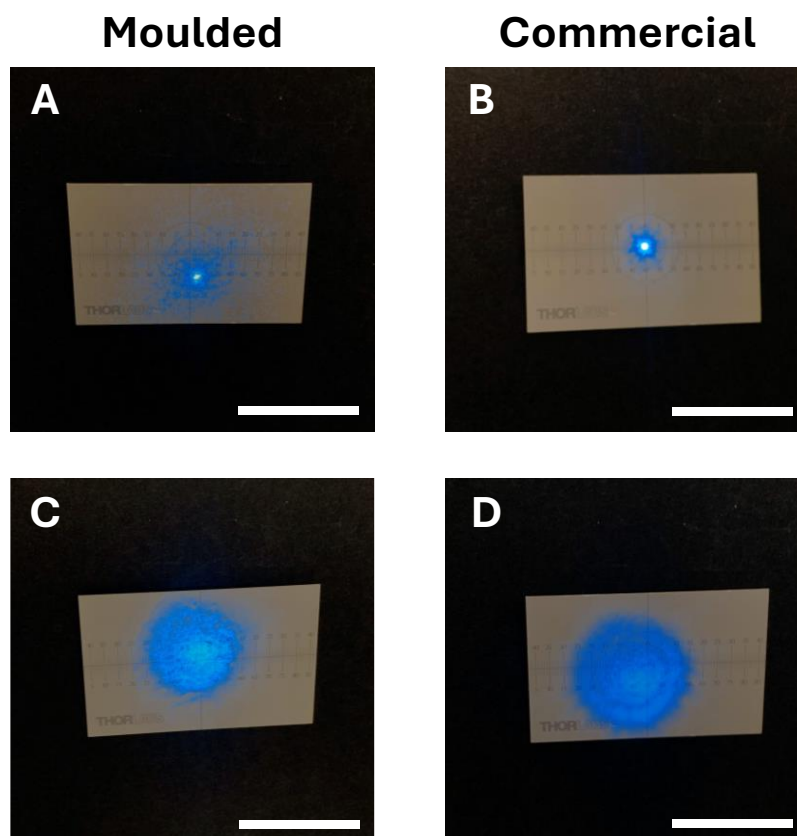


Figure 40. Photographs of resultant illumination patterns using single mode excitation through optically clear moulded 3D printed optic. (A) Collimated illumination through a moulded 3D printed optic. (B) Collimated illumination through a commercial equivalent optic. (C) Defocused illumination through a moulded 3D printed optic. (D) Defocused illumination through a commercial equivalent optic. Scale bars = 50 mm.

Chapter 4. Imaging using 3D Printed Objectives

The moulding approach was only used after the imaging experiments within this chapter had been performed, though it was used for the 3D printed microlens arrays used in Chapter 5. The moulding results therefore exemplify that the diffraction-based effect is a direct result of the Elegoo Mars 2 LCD printing process, which should be taken into consideration when using 3D printed optics within excitation or imaging applications. Additionally, newer generation printers may have improved pixel illumination homogeneity and therefore lower refractive index variation. Direct printing with the Mars 2 was nevertheless the method used for 3D printed optics included as imaging objectives due to the availability at the time of experimentation, showcasing the performance that is available even with the effect observed with collimated illumination.

4.1.3 Objective Design

The two types of primary microscope objectives using 3D printed elements were designed using the raytracing software Optalix to determine optimal lens placements and configurations. Design constraints include that plano-convex lenses were used due to their easy printability, i.e. the flat surface can adhere to the build plate without supporting structures contributing to any lens face deformation. Additionally, the focal length of 20 mm was chosen as higher focal length lenses reduce the curvature of the lens and therefore the number of layers available to form the curved surface and base surface for the following coating process, reducing an accurate curvature replication. For the multi-lens objective, 6 mm diameters were chosen in an effort to create a small-scale, classical objective lens-scale package, with plano-convex and plano-concave lenses chosen to increase the NA and enable some spherical aberration reduction.

Chapter 4. Imaging using 3D Printed Objectives

A simplistic approach of a single plano-convex 12.7 mm diameter $f = 20\text{mm}$ lens (Thorlabs LA1074) was used as single element objective (see Figure 36C for a comparison of the 3D printed and commercial glass lens). The resulting theoretical performance of this objective lens was evaluated in Optalix as shown in Figure 41 with the ray-tracing diagram, modulation transfer function (MTF) and schematic. The MTF effectively details the optical performance of a lens or series of lenses and effectively defines the theoretical measured contrast of the optics across a range of spatial frequencies. Values of an MTF below 0.2 exhibit too poor contrasting features which is then considered to be the diffraction limited performance of the optical input in question. Comparisons were able to be drawn between a theoretical maximum and the measured objective both for centrally focused results and for results at a lateral displacement on the lens, which for the measured lenses was $\pm 3.5\text{ mm}$ with the laterally displaced MTF profiles indicated where appropriate. As a result, the MTF matches well at $\approx 245\text{ lp/mm}$ for an MTF of 0.2 between the theoretical maximum (blue) and the centrally

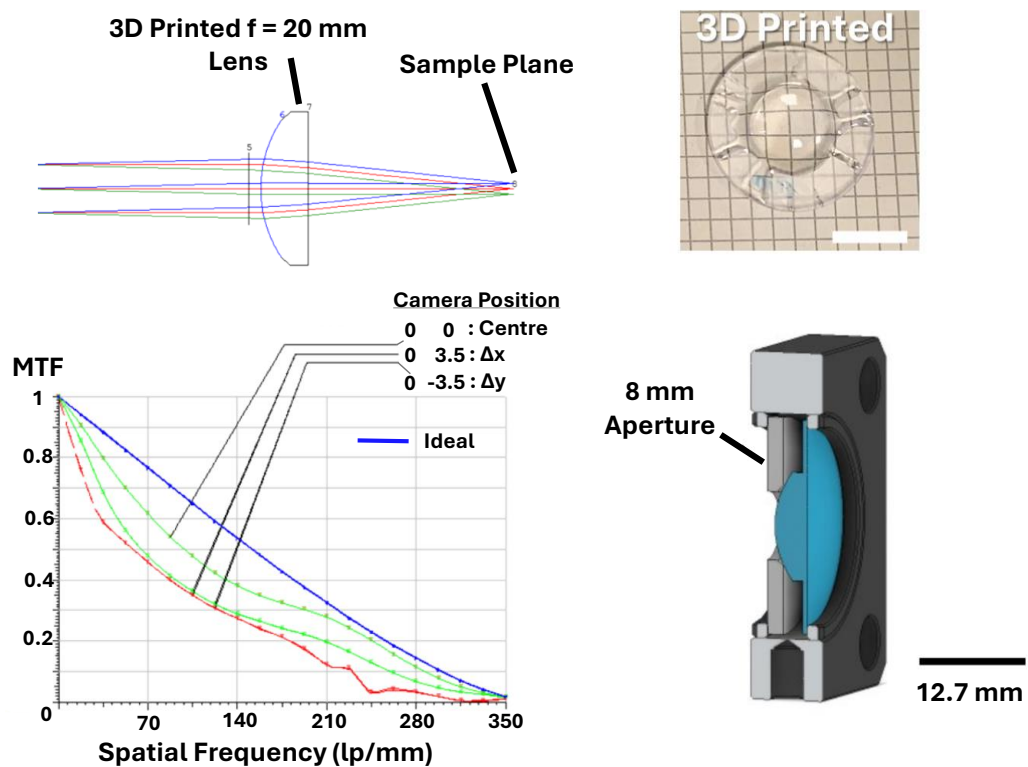


Figure 41. Raytrace diagram, photograph of single lens, modulation transfer function (MTF) and 3D assembly schematics for single lens objective. Single lens objective with entrance aperture of 8 mm diameter at 1 mm distance from the plano-convex lens; Photograph showing 3D printed single lens objective; the MTF shows clear image deterioration due to the basic spherical lens design; the 3D assembly shows the 3D printed support to house the lens in a 25.4 mm cage plate

Chapter 4. Imaging using 3D Printed Objectives

focused objective under test (green). As expected in the laterally displaced case, where the ± 3.5 mm results are shown as additional green lines which match so closely they overlap in the figure, there is a slightly deteriorated optical performance at 210 lp/mm. These results still match well with the theoretical maximum however.

To show the potential and influence of incorporating multiple 3D printed elements into the imaging arm of a microscope, a 4-lens objective geometry was additionally designed based on 6 mm diameter singlet element lenses (see Figure 36B). The geometry consists of an $f = 6$ mm aspheric front lens (1, Thorlabs APL0606), a $f = 10$ mm plano-convex secondary lens (2, Thorlabs LA1116), a $f = -6$ mm plano-concave compensation lens (3, Thorlabs LC2969) and a final $f = 15$ mm plano-convex lens (4, Thorlabs LA1222). Element spacings were optimised using Optalix, with a theoretical minimum optics limited imaging resolution of $1 \mu\text{m}$. Using Optalix, the theoretical objective was characterised using the geometrical analysis (Figure 42) and the resulting MTF, with the cross-sectional schematic also shown. The resulting geometric ray tracing analysis shown as the MTF features an obtained spatial frequency of $\approx 715 - 750$ lp/mm for both the theoretical maximum and the 3D printed objective for centrally focused and laterally displaced illumination. As expected, in contrast to the 8x objective, this objective obtains a significantly higher resolution through the combination of additional optics. Also to

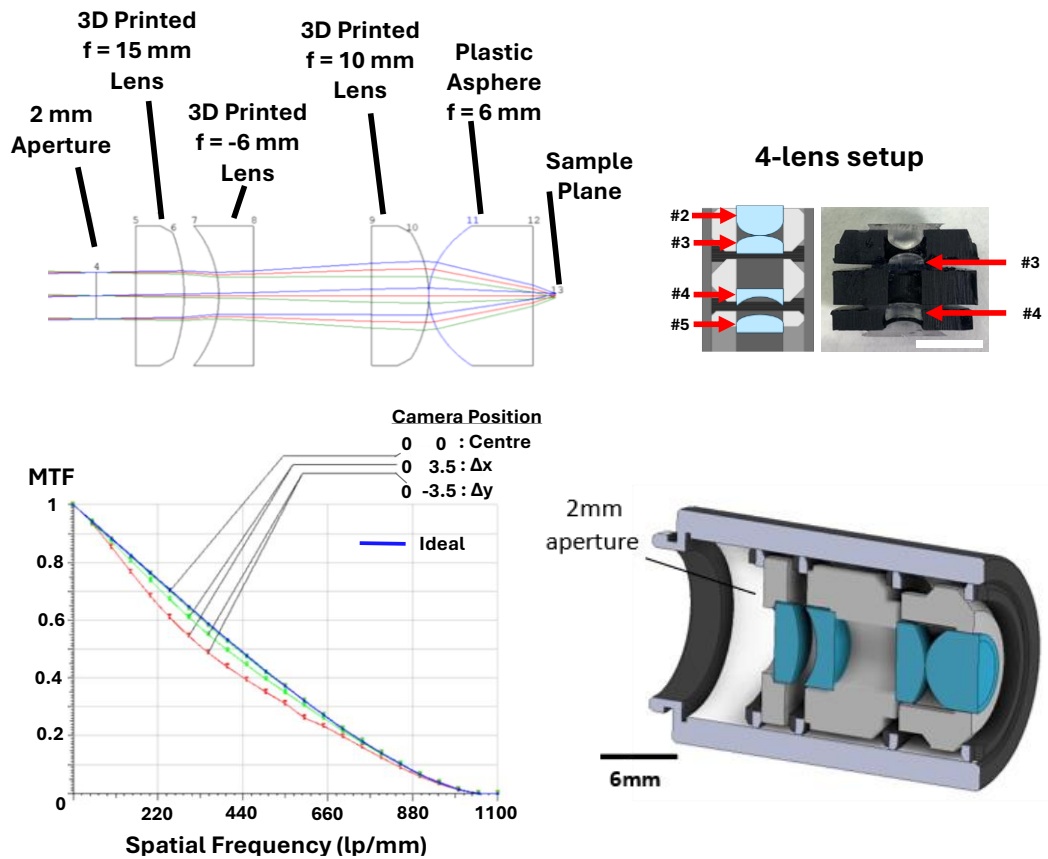


Figure 42. Raytrace diagram, schematic and photograph of multi-lens objective, modulation transfer function (MTF) and 3D assembly schematics for the multi-lens objective. Multi-lens objective with two plano-convex, one plano-concave and one aspheric lens and entrance aperture of 2 mm diameter at 1 mm distance from the proximal end lens; schematic and photograph of multi-lens objective; the MTF shows an almost diffraction limited performance; the 3D assembly highlights the multiple spacers for axial alignment of the lenses.

note, the deviations away from the centre have minimised impact on the optics in comparison to the larger diameter optic as per Figure 41 previously.

The lens geometry designs for the single and multi-lens objectives were taken from the stock lens catalogue on the Thorlabs website, allowing the use of commercial glass lenses as direct comparison to the generated 3D printed versions. Each lens geometry was available as a STEP file that could be converted to an STL file for printing and transferred to the free slicing software Chitubox for print preparation. As the multi-lens geometry was designed to mimic a 50x objective it has been labelled as such in each relevant figure, despite some practical deviation away from this modelled value.

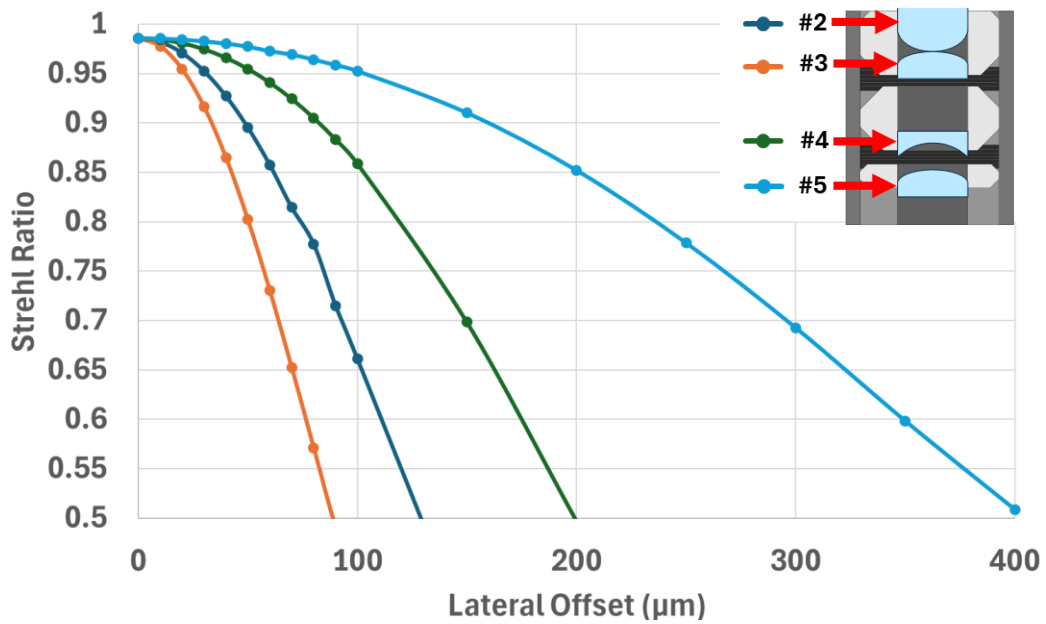


Figure 43. Strehl ratio plot against lateral offset of individual lenses with respect to the optical axis, with supporting lens figure as plot legend.

Both the 3D printed and commercial 12.7 mm diameter single element lens objectives were housed in a 30 mm cage plate fixed in a telecentric arrangement in the imaging system, with an 8 mm diameter aperture placed on their convex face to act as aperture stop. The commercial and 3D printed 6 mm diameter lenses of the 4-lens objectives were housed in a 12.7 mm lens tube with custom 3D printed spacers with chamfered edges and retaining rings which all help to minimise lateral offsets between the lenses and ensures the distance between each lens matched closely the objective design parameters. A 2 mm diameter stop aperture was integrated into the 3D printed lens holder design and positioned 1 mm after the final lens. The minimisation of lateral offset errors was essential as the ray trace simulations indicated that for some optics in the objective, deviations from the optical axis less than 100 μm in the lateral directions significantly reduced the achievable image quality, as shown in Figure 43.

By evaluating the Strehl ratio, one method of measuring the quality of optical image formation, against the lateral offsets of each individual optic, an understanding of how each optic impacted the image quality was obtained. In general, aberrations which move the Strehl ratio below 0.8 are below the diffraction limited ideal design. Lens #5 in the objective appears to have the least impact on optical quality as a function of lateral displacement, with diffraction-limited impacts only occurring after an $\approx 250 \mu\text{m}$ lateral displacement within the objective

Chapter 4. Imaging using 3D Printed Objectives

lens. Comparing this to lenses #3 or #4 for example, the resulting aberrations are significantly more impactful for lateral displacements lower than 100 μm . These results therefore confirm that whether evaluating 3D printed optics or commercial optics within this objective configuration, many of the aberrations which may be observed in imaging could be corrected for by efficiently centring each lens in respect to the optical axis.

4.2 Brightfield Imaging using a Single 3D Printed Lens

4.2.1 Sample Preparation

For brightfield imaging a 1951 USAF resolution target was used (Thorlabs R3L1S4P) along with a sample of variegated *Hosta* (*Hosta Undulata*), a freshwater cyanobacteria sample, and an onion cell sample. The USAF resolution target required no further sample preparation, but the biological/plant specimen required the following extra steps.

For the variegated *Hosta* sample the leaf cuticle was removed with a scalpel. This sample was then rinsed with deionized water to remove any debris that occurred during membrane removal. A small section (5 mm by 5mm) was placed onto a #1.5 coverslip with a small amount of deionized water and sealed with a glass microscope slide.

To mount the cyanobacteria, the specimen was washed with deionized water to remove detritus and the cyanobacteria were spread apart using tweezers on a #1.5 coverslip before being sealed onto a glass microscope slide using nail varnish.

The onion cells were prepared by dissecting a 5 mm x 5 mm section of the abaxial epidermis from a brown onion and mounting the membrane (5 mm x 5 mm) onto a #1.5 coverslip with 100 μl of neat Lugol's iodine solution (62650; Merck, Germany) to produce a stained specimen. This is so that the iodine can bind to the starch to give a blue-black colour to the epidermal cells, providing higher contrast for imaging of the cell walls and nuclei.

4.2.2 USAF Target Imaging

Using the microscope setup shown in Figure 36A with the Köhler brightfield transmission illumination and with the single 20 mm focal length lens as the 8x objective, the 1951 USAF Target shows comparable contrast between the commercial and 3D printed lenses (Figure 44A and B respectively) over their 1.4 mm by 0.9 mm field of views. For the 3D printed implementation, a small reflection shadow is visible, which is attributed to diffraction effects due to voxel patterns within the 3D printed optics. A small degradation in the image quality is additionally visible, with a zoom-in on groups 6 and 7 of the resolution target showing that for the 3D printed lens implementation group 6-6 can be clearly identified, leading to a resolution of approximately $6\ \mu\text{m}$, while the commercial lens implementation can resolve down to group 7-1, leading to a resolution of approximately $4.5\ \mu\text{m}$. In the digitally zoomed region of interest, the commercial line profile shows slightly higher contrast compared to the 3D printed lens with mean contrast values of $99 \pm 0.3\%$ and $95 \pm 2\%$ respectively, which will be due to slight blurring due to the scattering through the 3D printed objective. However, it is clear from these chrome lithography target results that comparable resolution and image clarity are obtainable using a single 3D printed lens as objective. The obtained resolution shows that the resolution

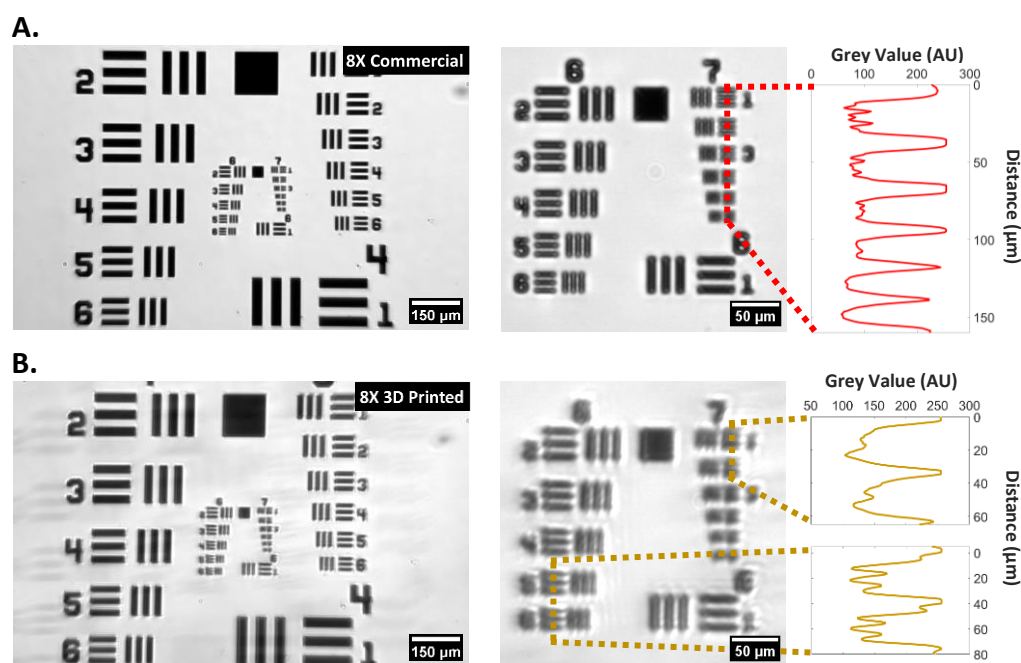


Figure 44. Brightfield USAF Target images using lens #1 as a single-lens 8x objective. (A) left - Full FOV 1951 USAF target using commercial lens #1 as objective; middle – central cropped ROI from commercial lens image on left; right – line graph taken through group 7 elements 1-6; (B) left – Full FOV 1951 USAF target using 3D printed lens #1 as objective; middle - central cropped ROI from 3D printed lens image on left; right - line graph taken through group 6 elements 5-6 and group 7 elements 1-2

of the 3D printed objective in this setup is sub-cellular, though it is vital to consider that this assumes a sample with minimal scattering and a thin axial-section.

4.2.3 Variegated *Hosta* Imaging

Brightfield transmission images using the 8x objective configurations of variegated *Hosta* (Figure 45) show clearly resolvable stomata (see arrows in Figure 45 A and B) and cell structure for both commercial and 3D printed imaging configurations. Stomata are microscopic pores responsible for gas exchange within the epidermis of the plant leaf and are made up of guard cells with auto-fluorescent chlorophyll containing chloroplasts. Each stoma, which itself is a pair of guard cells, is approximately 45 μm long, and 25 μm wide, and with a sub-cellular resolution we should expect to see individual chloroplasts in brightfield illumination within the guard cells. However, scattering within the tightly packed guard cells

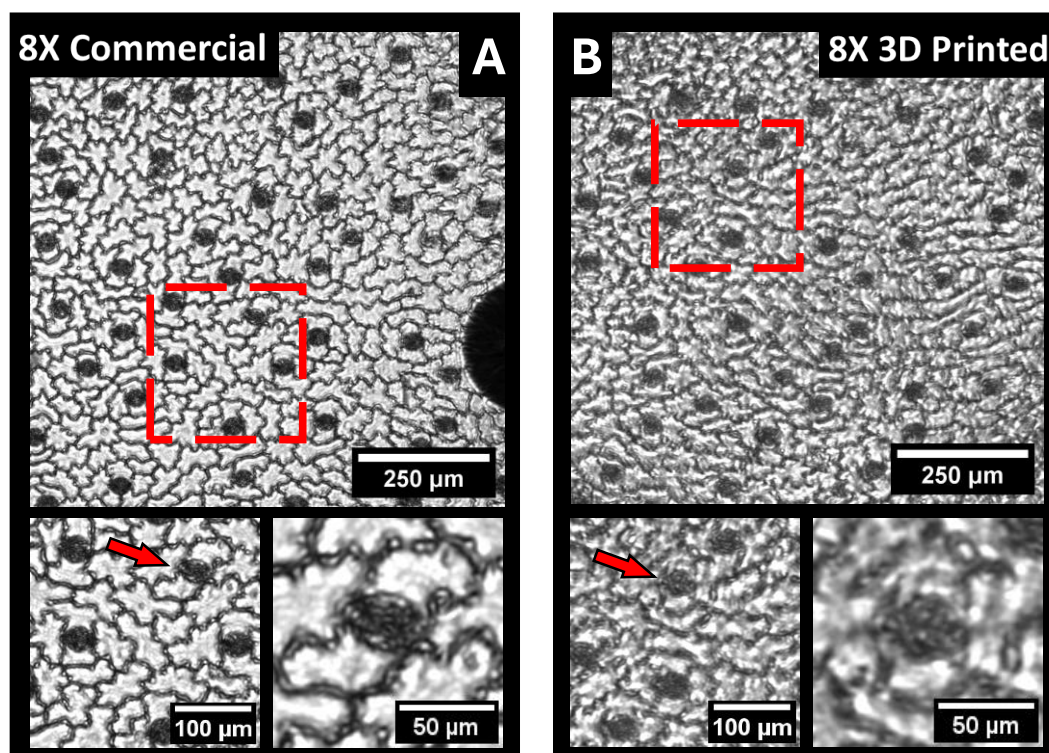


Figure 45. Brightfield variegated *Hosta* images using lens #1 as an 8x objective. (A) Top – Full FOV of the *Hosta* cellular network and stomata using the commercial 8x objective. Bottom Left – Digitally zoomed ROI showing multiple cells and stomata. Bottom Right – Digitally zoomed ROI of a single stoma surrounded by plant cells. (B) Top – Full FOV of the *Hosta* cellular network and stomata using the 3D printed 8x objective. Bottom Left – Digitally zoomed ROI showing multiple cells and stomata. Bottom Right – Digitally zoomed ROI of a single stoma surrounded by plant cells.

has rendered each stoma difficult to unpick and identify the individual guard cells for both the commercial and the 3D printed objectives at this magnification and NA. The slightly reduced resolution of the 3D printed lens shows extra blurring around the cell walls in the variegated *Hosta* images compared to the commercial lens images, and the cells themselves, though well defined, also exhibit less uniform illumination across the cell surface with visible saturation in many of the cells in the 3D printed objective image. As fluorescence microscopy will ignore bulk structure not excited at chlorophyll A or B's wavelengths, the expectation from this brightfield dataset is that the chloroplasts within the guard cells will be distinctly resolvable in comparison to the images of the brightfield dataset.

4.2.4 Cyanobacteria Imaging

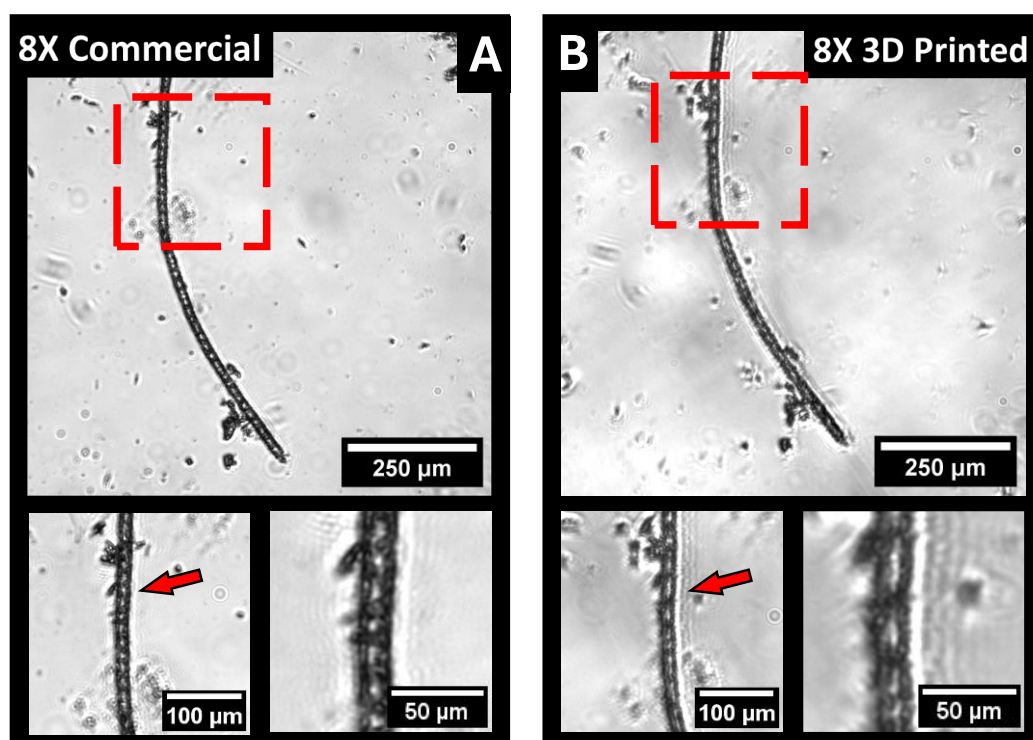


Figure 46. Brightfield cyanobacteria images using lens #1 as an 8x objective. (A) Top – Full FOV of an individual cyanobacteria filament using the commercial 8x objective. Bottom Left – Digitally zoomed ROI showing multiple cells within the filament. Bottom Right – Digitally zoomed ROI of the chloroplast containing cells. (B) Top – Full FOV of an individual cyanobacteria filament using the 3D printed 8x objective. Bottom Left – Digitally zoomed ROI showing multiple cells within the filament. Bottom Right – Digitally zoomed ROI of the chloroplast containing cells.

Chapter 4. Imaging using 3D Printed Objectives

Figure 46 shows brightfield images of filamentous cyanobacteria using the two 8x objectives, where individual cells in the cyanobacteria filament are clearly resolvable in both commercial and 3D printed imaging configurations. Cyanobacteria are aquatic photosynthetic bacteria which are abundant within algal environments, though as prokaryotes they are distinctly different to algal plant samples. As a broad range of cyanobacteria exist, their cellular structure varies in size from sub-micron scales to scales as high as 100 μm . The images obtained in Figure 46A and B clearly show the morphology of the overall cyanobacteria, with the shape of the individual cells within the filament distinguishably rectangular with an average size of $34 \pm 2 \mu\text{m}$ by $15 \pm 0.8 \mu\text{m}$ in the commercial case and $35 \pm 2 \mu\text{m}$ by $14 \pm 0.6 \mu\text{m}$ in the 3D printed case. The difference between the mean values is within the standard deviation of the measurements meaning the 3D printed optic complies well with the measured morphology from the commercial optic. Shown through Figure 46B is that the 3D printed objective has high enough resolution to determine whether or not the cyanobacteria sample features heterocytes and akinetes, which are specialised cell types with distinct morphology to their corresponding filament cells. Therefore, the overall level of detail obtained using a 3D printed objective exemplifies enough morphological data to allow biologists to distinguish which family of cyanobacteria this is.

As with the *Hosta* sample, again observed is the extra blurring around the edges of the biological structure for the 3D printed objective. Additionally, with empty background visible in the sample image, a hint of diagonal parallel lines are visible in the 3D printed case, which is assumed to be the same voxel patterning within the bulk optic resulting from the LCD 3D printing as previously described. This indicates that with further development in 3D desktop printing resolution, there may be potential for imaging using an 8x 3D printed objective without the observed patterning and with like-for-like optical clarity to the commercial lens used here as comparison.

4.2.5 Iodine-stained Onion Imaging

Using both 8x objectives on the iodine-stained onion sample, clearly defined cell walls and nuclei within the onion cells are evident in Figure 47. The contrast between the images obtained from the commercial and 3D printed 8x objectives is relatively similar with this sample, with both showing clearly distinguishable features across both objective images. Specifically, the contrast measurements from the commercial case are $58 \pm 2 \%$ compared to $71 \pm 4 \%$ in the 3D printed case. This result at first appears abnormal, though the justification

Chapter 4. Imaging using 3D Printed Objectives

for the measurements are that through the mostly transparent sample, the commercial optic is transmitting light better than the 3D printed optic, which is scattering further and therefore contributing to a higher contrast. While higher contrast may initially be perceived to be an improvement, in this case of a mostly transparent sample it is more of an indication of higher scattering as a result of the used objective. The cells themselves are large-scale, on the order of hundreds of micrometres long, though the nuclei, evident due to the iodine stain, are on the order of tens of micrometre in scale, visible using either of the objectives (Figure 47A and B bottom-right). Though intracellular detail is achievable using the resolution obtained through the USAF target, the nucleus of the onion cell contains sub-micron structures which are unresolvable at this NA using either of the 8x objectives. Additionally, the blurring around the edges of the cell walls in particular is still prominent within the 3D printed objective, though this is within the expectation as has been discussed previously.

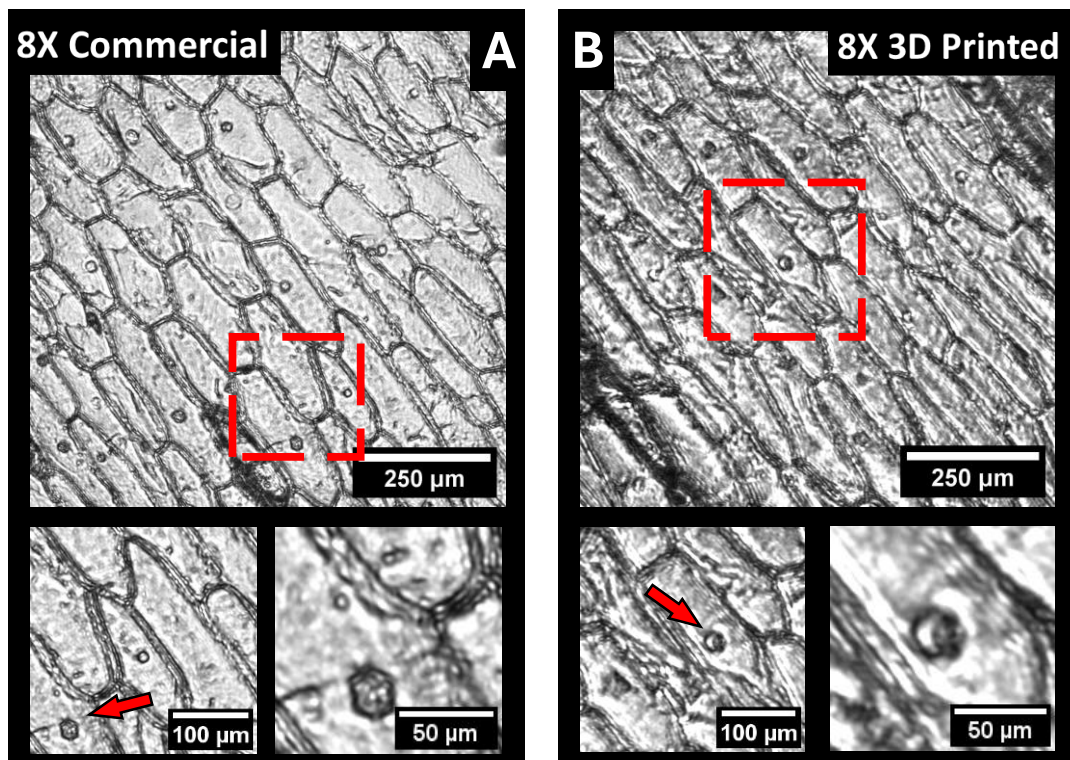


Figure 47. Brightfield onion images using lens #1 as an 8x objective. (A) Top – Full FOV of the iodine-stained onion cells using the commercial 8x objective. Bottom Left – Digitally zoomed ROI showing multiple cells and nuclei. Bottom Right – Digitally zoomed ROI of the onion nuclei. (B) Top – Full FOV of the iodine-stained onion cells using the 3D printed 8x objective. Bottom Left – Digitally zoomed ROI showing multiple cells and nuclei. Bottom Right – Digitally zoomed ROI of the onion nuclei.

4.3 Brightfield Imaging using Multiple 3D Printed Lenses

4.3.1 USAF Target Imaging

To evaluate the impact of using multiple 3D-printed lenses, the same microscope setup as shown in Figure 36A is used, but with the multi-lens objective configuration shown in Figure 36B instead of the single 20 mm lens. Multiple 3D printed 6 mm diameter lenses were used to sequentially replace one or more commercial glass elements within the multi-lens objective to get an experimental understanding if image degradation through 3D printed lenses is linearly or nonlinearly increasing when using multiple 3D printed elements in succession in a custom microscope objective. The baseline for comparison is a 4-lens configuration with only commercial lens element counterparts, which is used for imaging the 1951 USAF target to examine resolution and contrast as shown in Figure 48A. Each of the 4-lens objectives with different number of 3D printed elements is housed within a 3D printed holder, designed as per section 4.1.3. The magnification for the all-commercial implementation is measured to be approximately 48x, which is kept consistent when replacing lens 2 (Figure 48B) with a 3D printed element. However, replacing both lens 2 and lens 3 with 3D printed elements drastically decreases the magnification to 42x, and with lenses 2, 3 and 4 replaced with 3D printed lenses the magnification is shifted back toward 46x. These shifts in magnification are

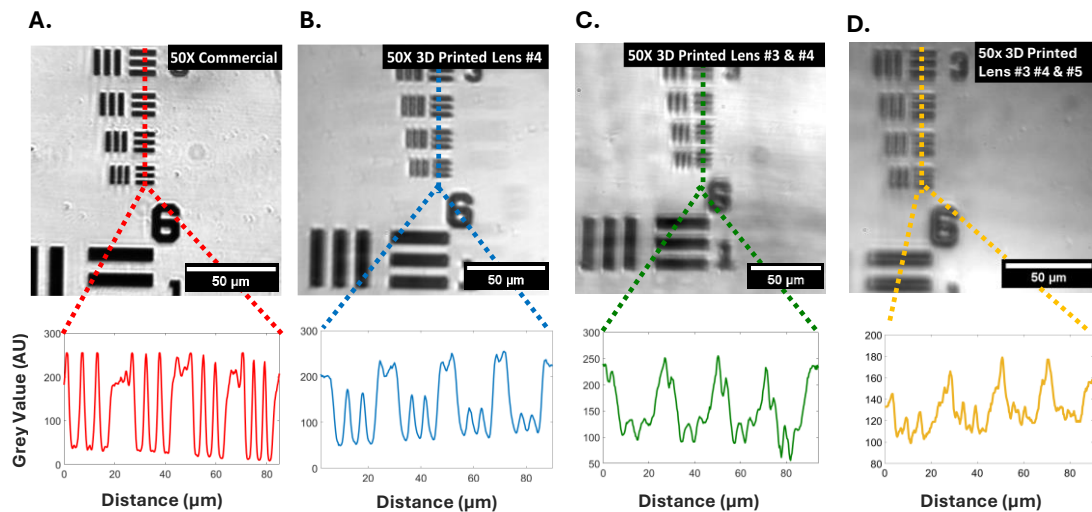


Figure 48. Brightfield images using the 4-lens objective. (A-D) 1951 USAF Group 7 target images with line plot profiles underneath using commercial 4-lens objective configuration. (A) Fully commercial 4-lens objective; (B) lens #4 replaced with a 3D printed version; (C) lenses #3 and #4 replaced with 3D printed versions; (D) lenses #3, #4 and #5 replaced with 3D printed versions

Chapter 4. Imaging using 3D Printed Objectives

more likely a result of sub-millimetre-scale axial displacements of single or multiple lenses in the 3D printed 4-lens setup which, at the high magnification, compounds into the shown differences in magnification. Additionally, diffraction effects are again evident in the 3D printed lens images, shown by faint replicate areas of the target laterally displaced across the FOV. Overall, the use of one or more 3D printed lens elements at the higher magnification allows resolving of the smallest line-pairs on the resolution target (group 7-6), indicating an imaging resolution of $< 2 \mu\text{m}$ and allowing sub-cellular details to be resolved using 3D printed optical elements. In addition to the sub-cellular resolution, the FOV is $75 \mu\text{m}$ by $75 \mu\text{m}$, which can allow for complete cell imaging of biological samples with the different internal structures resolvable as shown later. With a higher number of 3D printed lenses used in the 4-lens objective, an increased blurring and reduction in resolution is visible, originating from manufacturing tolerances and potential minor internal scattering within the volume of the 3D printed elements, though these issues were expected from the low-cost manufacturing method. As with the 8x configuration, sub-cellular resolution is obtained using multiple 3D printed lenses here, however the expectation is again that biological samples with higher scattering will deteriorate this resolution further. Finally, the contrast in the commercial implementation has a mean value of $92 \pm 5 \%$ and is comparable with the results of one or two 3D printed optics added into the objective with contrast values of $91 \pm 4 \%$ and $90 \pm 9 \%$ respectively. However, when adding a third 3D printed optic the contrast drops to $51 \pm 2 \%$ which is likely due to higher absorption as well as the higher probability of lateral and axial misalignments between each 3D printed optic within the 4-lens objective.

Chapter 4. Imaging using 3D Printed Objectives

To show the repeatability of optimally inserting different 3D printed optics into the objective can have on the obtained resolution and contrast, three replicates of the 3D printed lens #3 were used in imaging the 1951 USAF target. Though the lenses were identically processed, some deviation in the obtained quality of coating is clear as shown by the loss of homogenous clarity from Figure 49A compared to Figure 49B or C. Specifically, there is more significant blurring surrounding the USAF target lines in Figure 49C compared to Figure 49A or B which have sharper edges. Additionally, the shadowing of target areas around each part of the USAF target appears to increase in Figure 49C compared to Figure 49B, for example. This could be due to inhomogeneities across the spin-coated surface resulting in laterally offset phantom images. Despite this, the resolution still appears to be roughly similar across all three lenses based off of the finest points in the target with its respective contrast in grey value ranging from $77 \pm 3 \%$ to $92 \pm 3 \%$. The effects shown as a result of the variation in lenses are to be expected as the spin-coating process is more prone to minor faults due to human-error in the coating process itself, whether noticeable or not when processing the lens, compared to a more robust method such as a direct moulding techniques (assuming the master-mould itself is of

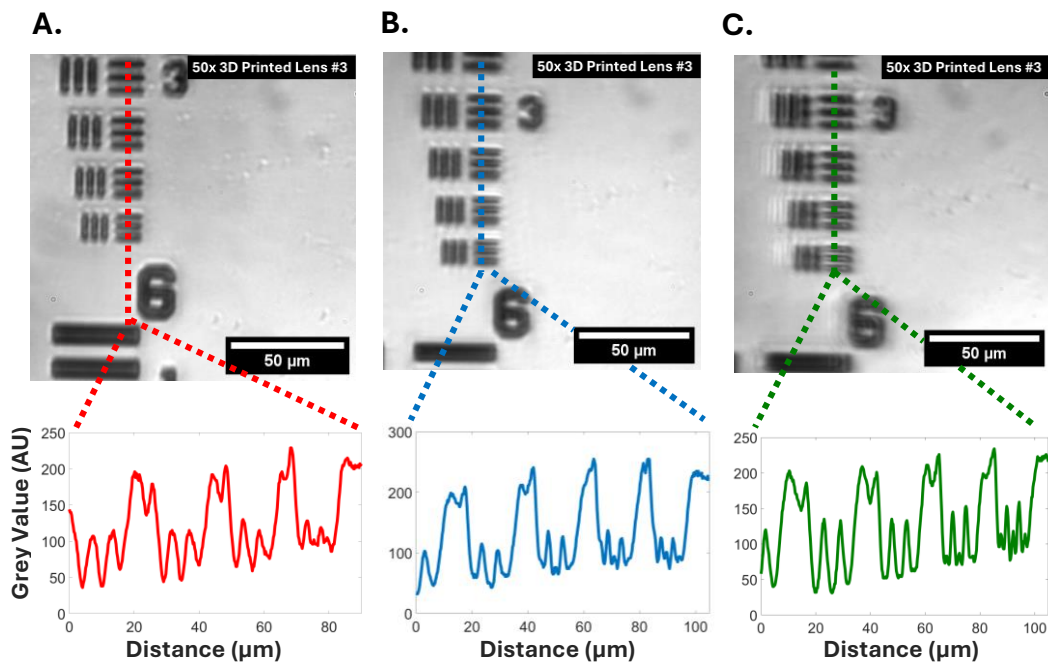


Figure 49. Brightfield images using three identically processed lenses of 3D printed lens #3 in the 4-lens objective configuration. (A-C) 1951 USAF Group 7 target images with line plot profiles underneath using commercial 4-lens objective configuration.

high quality). Equally, minor misalignments when assembling the different 4-lens objectives may also be contributing to the discrepancies between the image homogeneities shown.

4.3.2 Variegated *Hosta* Imaging

Figure 50A and B show the application of the 4-lens custom objectives with the same variegated *Hosta* biological sample as previously shown in section 4.2.2. In this case, the images from the 4-lens commercial and 3D printed versions have been scaled to remove the magnification mismatch and allow direct comparison of contrast and image quality. Figure 50A has a direct comparison between an all-commercial implementation and one that replaces a single lens element with a 3D printed version, with similar contrast visible between both, though with minor extra shadowing around the cell membranes likely due to the diffraction effects of the 3D printed lens. Still, cell nuclei, e.g. in the guard cells of the *Hosta* stoma, and membranes (see Figure 50 arrows) are clearly visible and distinguishable. This is due to the increase in achievable resolution obtained by the increased NA compared to the 8x objective configuration.

When adding a second 3D printed lens (Figure 50B) the imaging results show further blurring and potential multiple diffractive effects, which are specifically visible at the edges of the cell

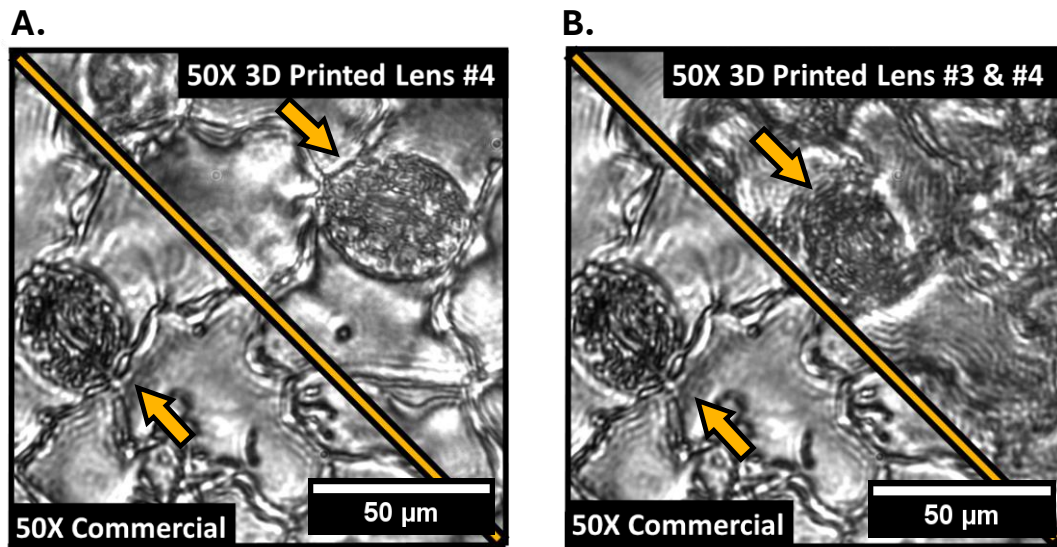


Figure 50. Brightfield variegated *Hosta* images using the 4-lens objective. (A) Commercial (left) and 3D printed (right) lens #4 objective images of the *Hosta* cells and stoma, with nuclei visible within the guard cells. (B) Commercial (left) and 3D printed (right) lens #3 and #4 objective images of the *Hosta* cells and stoma, with nuclei visible within the guard cells.

membranes. Due to the diffractive effects, the guard cells themselves lose overall clarity, in that they cannot be individually distinguished as easily in this configuration, though intracellular details are still obtained as individual nuclei can be resolved, as shown in Figure 50B at the arrow location. Overall, this dataset shows promise for e.g. field diagnosis with red blood cell samples as hundreds of blood cells could be distinguished from one another, leading to low-cost diagnosis with custom 3D printed objective design highly possible. Though a third 3D printed lens was integrated into the objective design for USAF target imaging, biological specimens were not imaged as the low contrast from the USAF target results exemplified that biological specimen image would lack contrast between sample features.

4.3.3 Cyanobacteria Imaging

Figure 51A and B show the same variety of configurations of the 4-lens objectives, imaging the cyanobacteria filament in this case. In the all commercial configuration (Figure 51A) the objective resolves clearly distinct individual compartments of the cyanobacteria, with some internal cellular structure observable. Alongside this is the same objective in which only a single 3D printed element was swapped, and though higher scattering can be seen we again can resolve the individual cells within the filament, with slightly less internal structure distinguishable compared to the commercial version.

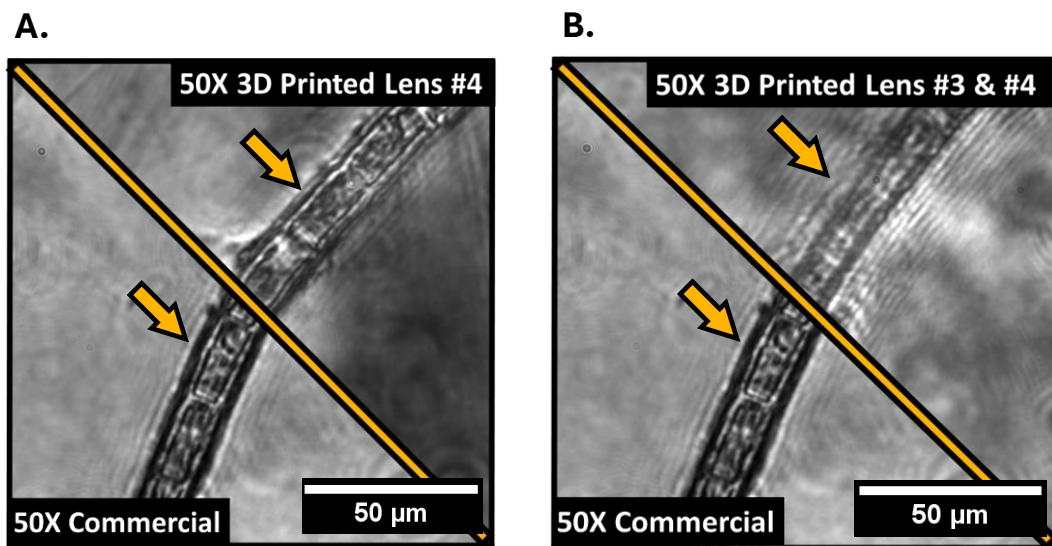


Figure 51. Brightfield cyanobacteria images using the 4-lens objective. (A) Commercial (left) and 3D printed (right) lens #4 objective images of the cyanobacteria filament with individual cells distinct from one another. (B) Commercial (left) and 3D printed (right) lens #3 and #4 objective images of the cyanobacteria filament.

Further blurring around the cell membrane and filament edge is specifically visible when adding a second 3D printed optic lens into the objective (Figure 51B), with multiple diffractive orders around this edge clearly visible and an overall thinning of the filament sample. This thinning is likely a result of the diffractive effects from the printed optics on the filament sample, and the loss in compartment resolution is expected in this configuration for the single cyanobacteria filament. In addition, it can be seen from sections 4.3.1 to 4.3.3 that with each 3D printed optic added into the objective, the Köhler illumination uniformity is reduced while imaging the sample, showing that the homogeneity of the images is affected by the 3D printed lens combinations.

4.3.4 Iodine-stained Onion Imaging

Figure 52A and B shows the 4-lens, 50x magnification objective configuration results from the iodine-stained onion sample. The commercial setup includes little information from the cytoplasm as is expected, though the nuclear membrane is distinct from the rest of the cell. At this higher resolution and magnification, the nucleolus which in this sample is approximately 5 μm can be identified in both the commercial configuration and the configuration including a single 3D printed lens, with their location shown in Figure 52A using the arrows. With multiple 3D printed lenses within the 50x objective the obtained detail within the nucleus is

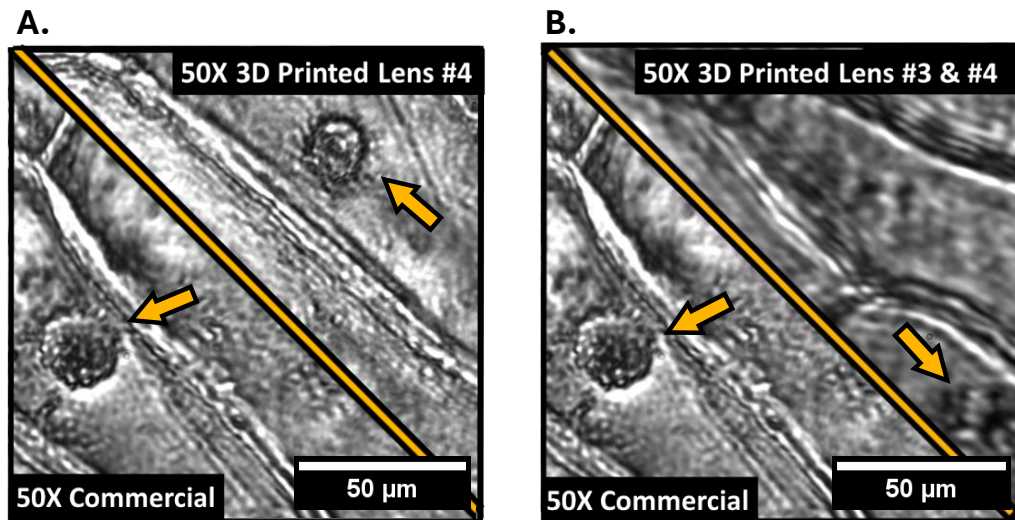


Figure 52. Brightfield onion images using the 4-lens objective. (A) Commercial (left) and 3D printed (right) lens #4 objective images of the onion cells and nucleus. (B) Commercial (left) and 3D printed (right) lens #3 and #4 objective images of the onion cells and nucleus.

Chapter 4. Imaging using 3D Printed Objectives

lost, and increased scattering is seen at both the cell membrane locations as well as within the cytoplasm itself.

Overall, the comparison of replacing one or more glass lenses in a custom objective with 3D printed equivalents shows the influence of inhomogeneities in the prints on specifically extra shadowing artefacts appearing, which degrade the image quality in dense biological samples. The assumed origin of these artefacts is a potential lens internal structuring of the refractive index originating from non-uniform illumination intensities in the print layers due to the LCD screen pixelation.

4.4 Fluorescence Imaging using a Single 3D Printed Lens

4.4.1 Sample Preparation

To show, to the author's knowledge, for the first time the performance of using 3D printed lens elements in an epi-fluorescence microscope system, images were captured using the earlier described 488 nm multi-mode laser excitation, with illumination and fluorescence collection through the objectives consisting of 3D printed elements. For all samples, a laser excitation power of 500 μ W was measured at the sample for the single lens, 8x magnification objective consisting of a 20 mm focal length commercial or 3D printed lens, and a maximum excitation power of 5 mW at the sample for the 4-lens, approximately 50x magnification objectives with multiple 3D printed lens elements. The increased power was necessary to compensate for variations in the SNR between the single-lens objective fluorescence response and the 4-lens objective fluorescence response.

For fluorescence imaging the same *Hosta* and cyanobacteria samples already introduced earlier were used, making use of the autofluorescence of chlorophyll in the chloroplasts for contrast. Chlorophyll A and B will be excited using 488 nm illumination, though at extremely low efficiencies compared to an illumination source that would be at a nearer-UV wavelength. The 488nm source was used despite the lower efficiency of chlorophyll excitation as nearer-UV excitation sources would contribute significantly higher absorbance within the objectives as the photopolymerising resin used for lens fabrication cures at wavelengths \approx 400 nm, which therefore would have significantly impacted the illumination of the sample. For point spread function evaluation a sample of 500 nm diameter microbeads (Thermo Scientific Fluoro-Max green G500) was used. Five microliters of the aqueous bead solution was placed on a #1.5 coverslip before being air dried, sealed with nail varnish on a microscope slide and imaged.

Chapter 4. Imaging using 3D Printed Objectives

To evaluate the illumination homogeneity through each imaging objective, a uniformly fluorescent commercial slide (Thorlabs FSK2) was used as an additional sample.

4.4.2 Uniform Fluorescent Slide Imaging

In order to understand how the fluorescence imaging will be affected by the 3D printed optics, a Thorlabs fluorescent slide was used as a uniform sample (Figure 53). The commercial single-lens, 8x objective, shown in Figure 53A, exhibits a homogenous Gaussian excitation captured fluorescence, as is expected from the multimode laser intensity distribution. Compared to the commercial objective, the 3D printed lens in Figure 53B shows less uniformity in the collected fluorescence across the full FOV, as supported by the line-plot beneath the figure as well. Greyscale variations of intensity $\approx 16\%$ are visible through a $500\ \mu\text{m}$ range in the central region of the commercial excitation, though this is an intensity variation which is approximately radially symmetric across this ROI. Compared to this, intensity variations

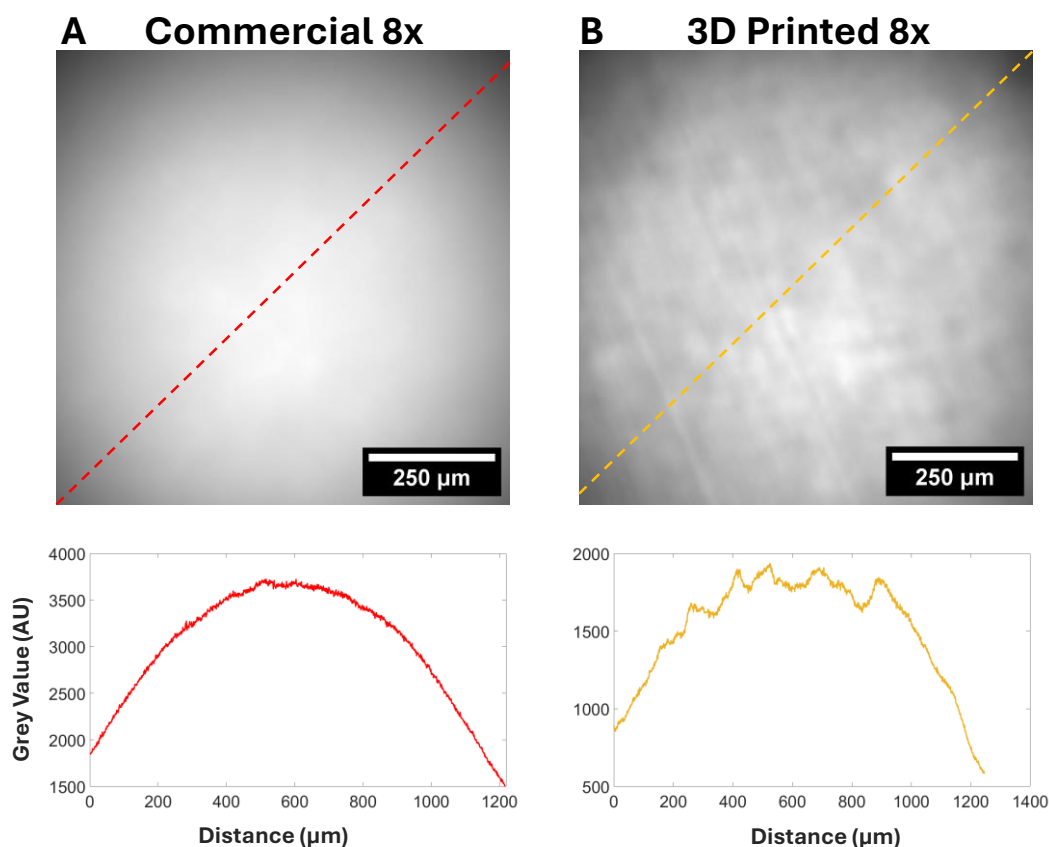


Figure 53. Fluorescent slide images taken using commercial and 3D printed 8x objectives. (A) Thorlabs fluorescent slide imaged with the commercial 8X objective. (B) Thorlabs fluorescent slide imaged with the 3D printed 8x objective.

across the same ROI in the 3D printed case are $\approx 18\%$ though the intensity changes with less symmetry across this ROI than in the commercial case. Nonetheless, the homogeneity still matches the commercial optics well enough to obtain quantitative biological information from more complex samples without concern over illumination artefacts.

4.3.3 Sub-resolution Beads

To determine the resolution using the fluorescence imaging system, as well as to evaluate the homogeneity of the captured fluorescence through a 3D printed optics element, the 8x single lens objective was used on a sub-resolution bead sample. Using the commercial 8x objective to excite and collect the fluorescence from the diffraction-limited bead (Figure 54A), the bead intensity distribution and therefore the PSF shows a radially homogenous spot with limited

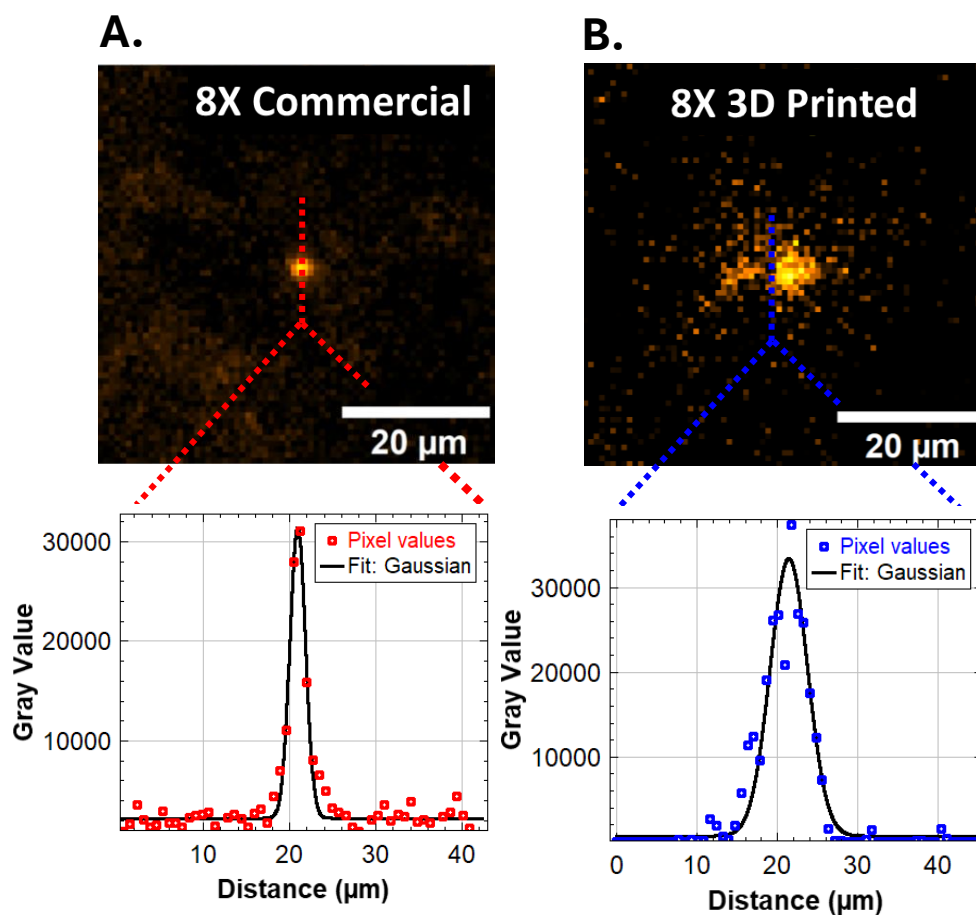


Figure 54. Fluorescent bead images taken using commercial and 3D printed 8x objectives. (A) 500 nm fluorescent bead imaged with the 8x commercial objective. (B) 500 nm fluorescent bead imaged with the 8x 3D printed objective.

Chapter 4. Imaging using 3D Printed Objectives

evidence of optical aberrations affecting the symmetry of the imaged sample. The PSF itself is Gaussian in profile, as shown by the graph in Figure 54A, with a mean measured FWHM resolution of $2.1 \pm 0.15 \mu\text{m}$ across five beads. Switching to the 3D printed lens, significant scattering can be observed from the PSF as the radial homogeneity is worse than the commercial lens objective in Figure 54A. This results in a loss in resolution, which again was obtained through the PSF FWHM and measured to be $6.6 \pm 0.86 \mu\text{m}$. The resolution obtained from each of these sub-resolution beads matches well with the expected outcome for the commercial lens, with a slightly higher resolution in the fluorescence calculated likely due to improved signal to noise compared to the brightfield case. However, for the 3D printed optic, the resolutions more closely match one another, which may indicate higher absorption or scattering within the 3D printed lens version in fluorescence imaging.

4.4.4 Variegated *Hosta* Imaging

To show the biologically relevant application of the 3D printed single lens, 8x objective, the variegated *Hosta* sample was imaged (Figure 55). Comparing the commercial lens and 3D printed lens for the 8x configuration shows good image contrast and the *Hosta* stomata remain easily resolved as can be seen from their characteristic shape and distinctly fluorescent chloroplasts. Additionally, the central pore responsible for gas exchange is distinct using both 8x lenses, visible as the larger region of non-fluorescing space between the chloroplasts within the guard cells. As chloroplasts within plant cells are generally $< 6 \mu\text{m}$ at their smallest, we can assume that each fluorescent spot is itself an individual chloroplast in the commercial case, given the obtained FWHM resolution from the sub-resolution beads in 4.4.3. However, for the 3D printed case each fluorescent spot may not be an individual chloroplast as per the resolution obtained from the PSFs in that same section, meaning we cannot distinguish an aggregation of chloroplasts from an individual chloroplast.

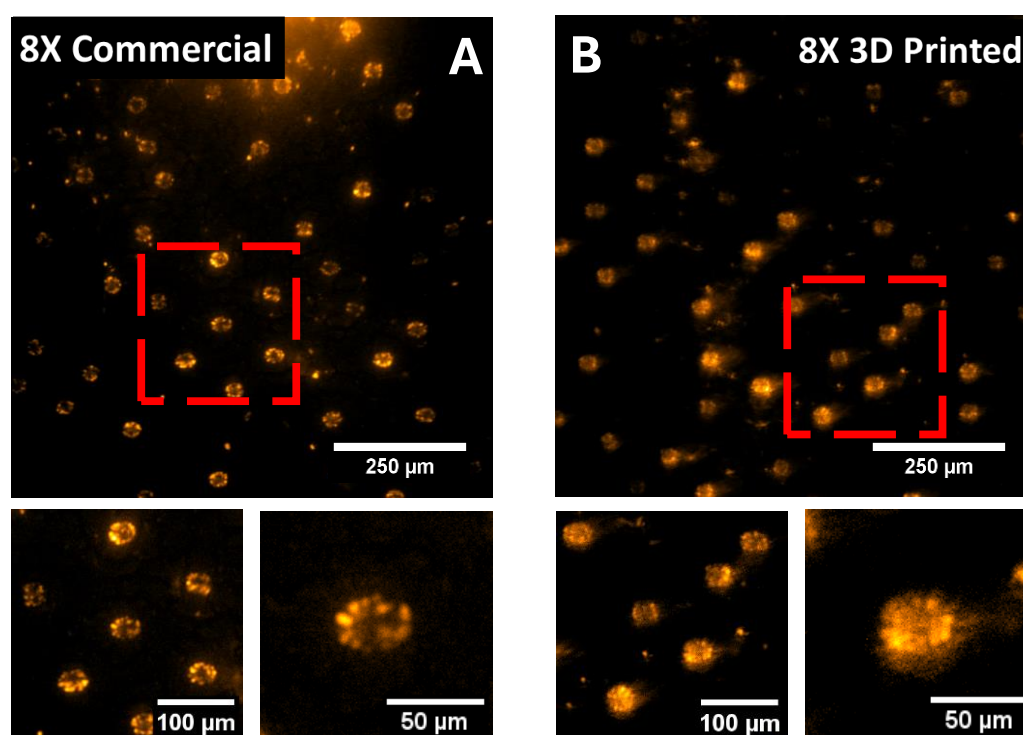


Figure 55. Fluorescence variegated *Hosta* images using lens #1 as an 8x objective. (A) Top – Full FOV of the fluorescing *Hosta* nuclei within the stomata guard cells using the commercial 8x objective. Bottom Left – Digitally zoomed ROI showing stomata nuclei. Bottom Right – Digitally zoomed ROI of a single stoma showing individually fluorescing nuclei. (B) Top – Full FOV of the fluorescing *Hosta* nuclei within the stomata guard cells using the commercial 8x objective. Bottom Left – Digitally zoomed ROI showing stomata nuclei. Bottom Right – Digitally zoomed ROI of a single stoma showing individually fluorescing nuclei.

4.4.5 Cyanobacteria Imaging

Shown in Figure 56 is the commercial and 3D printed single-lens 8x magnification objective configuration applied to auto-fluorescent cyanobacteria filament. The filament itself shows excellent contrast between the distinct fluorescing cells in both the commercial and 3D printed case. As the cells are distinct due to the non-fluorescent dark gaps between cells, the cells were measured to be $33 \pm 2 \mu\text{m}$ by $17 \pm 0.68 \mu\text{m}$, which corroborates the results from the brightfield images. In the 3D printed 8x image, additional blurring along the edge of the full filament is observable, though this is to be expected and matches the behaviour shown in the brightfield imaging experiments. However, this additional blurring make the edges more difficult to distinguish and the length and width therefore widen to measure at $35 \pm 2 \mu\text{m}$ by $20 \pm 2 \mu\text{m}$ respectively. Intracellular details within the cells of the cyanobacteria are also too close together to be able to distinguish as individual components within the cylindrical cells for both single-lens 8x objective cases.

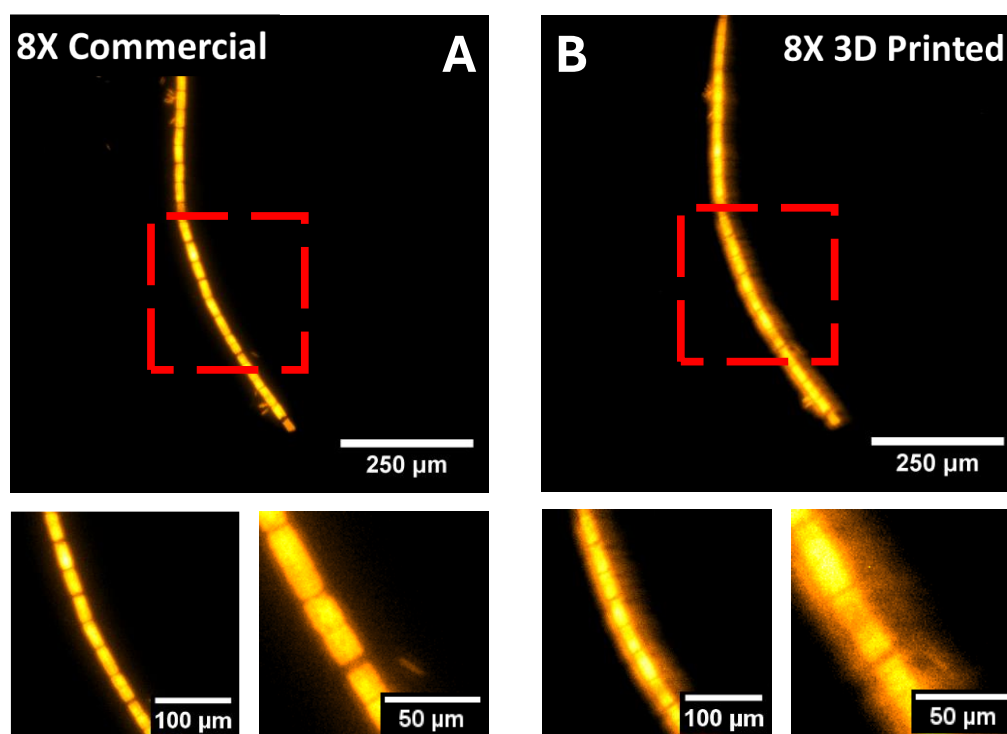


Figure 56. Fluorescent cyanobacteria images using lens #1 as an 8x objective. (A) Top – Full FOV of an individual fluorescing cyanobacteria filament using the commercial 8x objective. Bottom Left – Digitally zoomed ROI showing multiple cells within the filament. Bottom Right – Digitally zoomed ROI of the chloroplast containing cells. (B) Top – Full FOV of an individual fluorescent cyanobacteria filament using the 3D printed 8x objective. Bottom Left – Digitally zoomed ROI showing multiple cells within the filament. Bottom Right – Digitally zoomed ROI of the chloroplast containing cells.

4.5 Fluorescence Imaging using Multiple 3D Printed Lenses

4.5.1 Uniform Fluorescent Slide Imaging

Using the 4-lens 50x magnification objective configurations, images were taken of the excited fluorescence of the same Thorlabs fluorescent slide (Figure 57A-C) as with section 4.4.1. The commercial objective configuration (Figure 57A) shows the expected smooth light illumination profile across the FOV, aside from the vignetting at the edges of the illumination, though this is to be expected due to the laser illumination beam profile. In comparison to this data, Figure 57B shows a single 3D printed lens in the ~50x objective, and the homogeneity of the captured fluorescence is very similar to the commercial version with some minor differences in the overall homogeneity. Adding another lens into the objective (Figure 57C), however, shows some additional patterning onto the fluorescent sample which is originating from the illumination, due to compounding effects from the spin-coating process of the spherical surfaces. Comparing the intensity differences across a 100 μm ROI for all three objectives gives differences of 12 % in the commercial case, 10 % in the single printed optic case and 6 % in the double 3D printed case. This result seems counterintuitive as the data

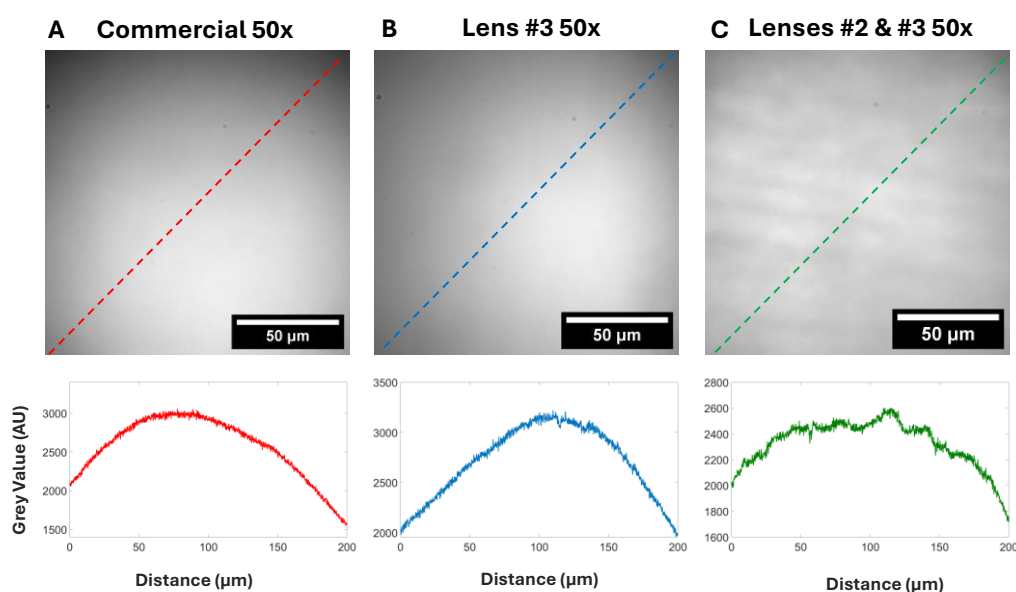


Figure 57. Uniform fluorescent target images captured using 4-lens commercial and 3D printed lens combinations with respective line plots underneath. (A) – Fluorescent slide captured using the commercial objective. (B) – Fluorescent slide captured using the lens #3 combination of the 3D printed objective. (C) – Fluorescent slide captured using lenses #2 and #3 in the 3D printed objective.

suggests that there are less major intensity variations across the FOV of the 3D printed objectives, and while viewing Figure C in comparison to A or B may support that the contrast is more homogenous due to the lack of a Gaussian-style intensity distribution, there are evident patterning aberrations in the image, exemplifying that the intensity variations do not tell the complete story. However, the data from the uniform slide still suggests that across the FOV larger samples may be minimally affected in comparison to samples with micron-scale fine structural detail.

4.5.2 Sub-resolution Beads

To show the aberrations generated through 3D printed optics within the 4-lens objective, fluorescent diffraction-limited beads were again used. As expected, the 50x commercial PSF (Figure 58A) shows radial symmetry with minimal optical aberrations recognised in the image. This resulted in a Gaussian PSF which across five beads measured a mean FWHM resolution of $1.23 \pm 0.03 \mu\text{m}$. Compared to this result, when using a single 3D printed lens within the 50x objective (Figure 58B), significant astigmatism is evident. This in turn reduces the radial

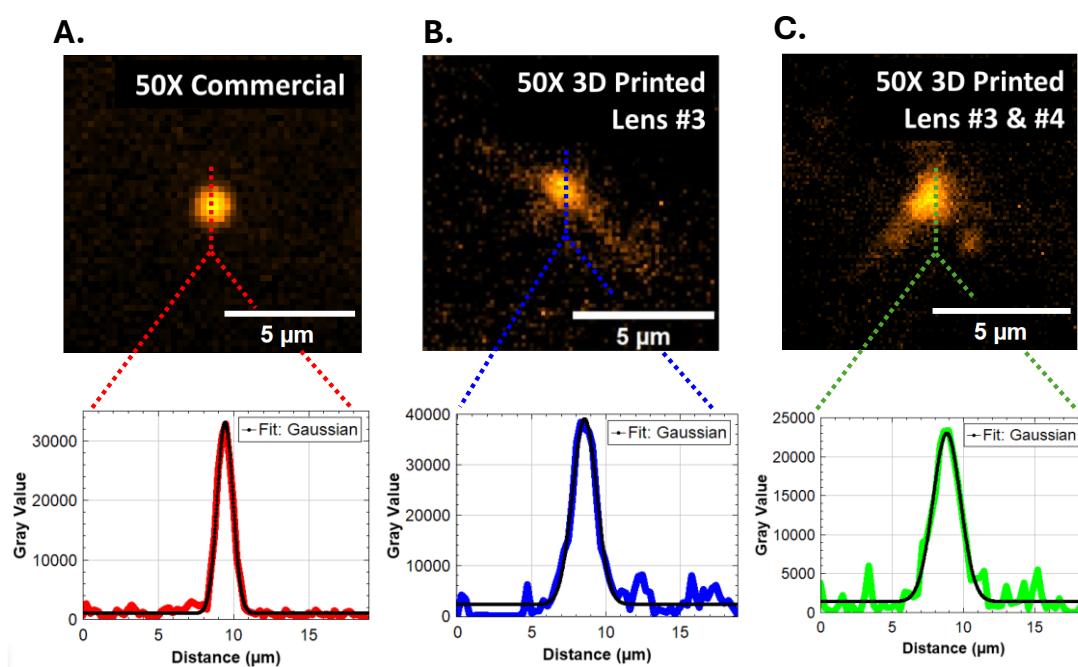


Figure 58. Fluorescent bead images taken using commercial and 3D printed 4-lens objectives. (A) 500 nm fluorescent bead imaged with the 4-lens commercial objective. (B) 500 nm fluorescent bead imaged with the 4-lens objective with 3D printed lens #3. (C) 500 nm fluorescent bead imaged with the 4-lens objective with 3D printed lens #3 and #4.

Chapter 4. Imaging using 3D Printed Objectives

symmetry of the PSF, and therefore impacts the resolution measured, which was found to be $1.95 \pm 0.26 \mu\text{m}$. Similarly, each additional 3D printed optic within this objective configuration deteriorates the obtainable fluorescence resolution, where the PSF using the configuration from Figure 58C resulted in a FWHM of $2.43 \pm 0.32 \mu\text{m}$. This signifies that the increased absorption and/or scattering through the 3D printed optics of the fluorescence response minimises the sub-cellular imaging success of the objectives with relatively high resolution of 50x.

4.5.3 Variegated *Hosta* Imaging

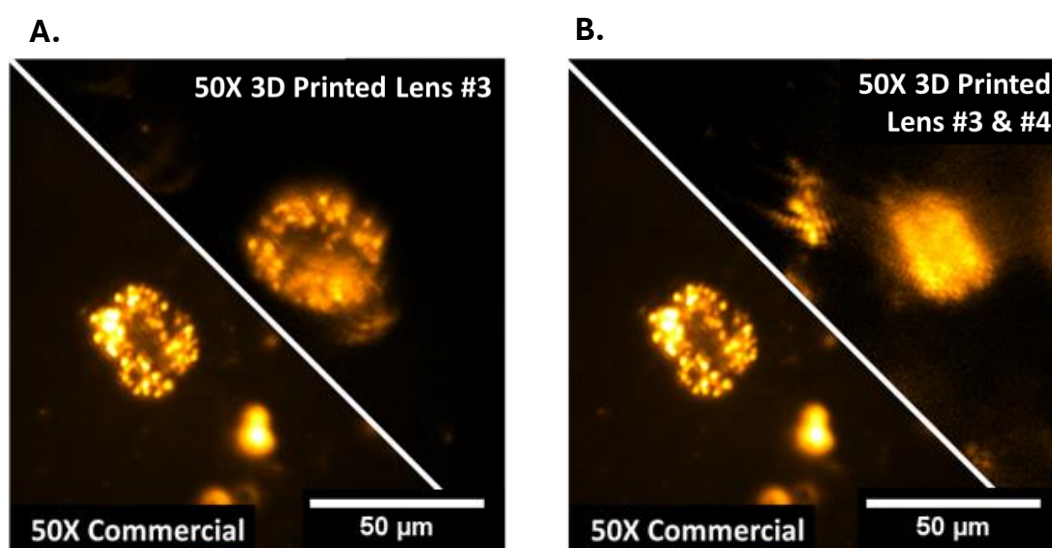


Figure 59. Fluorescent variegated *Hosta* images using the 4-lens objective. (A) Commercial (left) and 3D printed (right) lens #4 objective images of the *Hosta* stoma, with fluorescing nuclei visible within the guard cells. (B) Commercial (left) and 3D printed (right) lens #3 and #4 objective images of the *Hosta* stoma, featuring significant blurring in the 3D printed case.

Shown in Figure 59 is the 4-lens, 50x objective configurations applied to the variegated *Hosta* sample. Figure 59A exemplifies the achieved sub-cellular resolution, with individual chloroplasts visible in the guard cells of the stoma in both the commercial and 3D printed optic cases. Both configurations show excellent contrast and stoma morphology, though blurring around the stoma chloroplasts is seen in the 3D printed optic version compared to the commercial optics. When adding an additional 3D printed lens into the objective however (Figure 59B) the detail in distinguishing individual chloroplasts is lost and the entire stoma is blurred. This is not unexpected when comparing this result with both the FWHM resolution from section 4.5.2 as well as with the same brightfield result of the individual stoma, where

Chapter 4. Imaging using 3D Printed Objectives

the guard cells themselves lost visibility in section 4.3.2. Part of the reason for the loss in resolution could be due to the axial and/or lateral displacement of individual lenses within the 3D printed objective housing, meaning other 3D printed objectives using multiple lenses may exhibit more minor losses compared to this result. Through the conclusion it is still evident however that additional 3D printed optics within the imaging arm results in further degradation in the final image.

4.5.4 Cyanobacteria Imaging

The fluorescent cyanobacteria sample, shown in Figure 60, was imaged using the 4-lens 50x objective configurations as described previously. When using a single 3D printed lens within the 50x objective (Figure 60A), the differences between the commercial and 3D printed versions of the objective in imaging a fluorescent cyanobacteria sample are minor. Overall, there is increased blur across the entire 3D printed optic image, however the individual fluorescent cells are still explicitly distinct and resolvable, with some additional fluorescent detail within each cell perhaps obtainable in the commercial optic version. In comparison to the objective featuring multiple 3D printed elements (Figure 60B), there are less well-defined edges of each cell membrane compared to the commercial or single printed optic objective, which is an expected loss in detail suggested through the brightfield versions of the cyanobacteria. Still, the cyanobacteria cells are distinctly resolvable from one another using

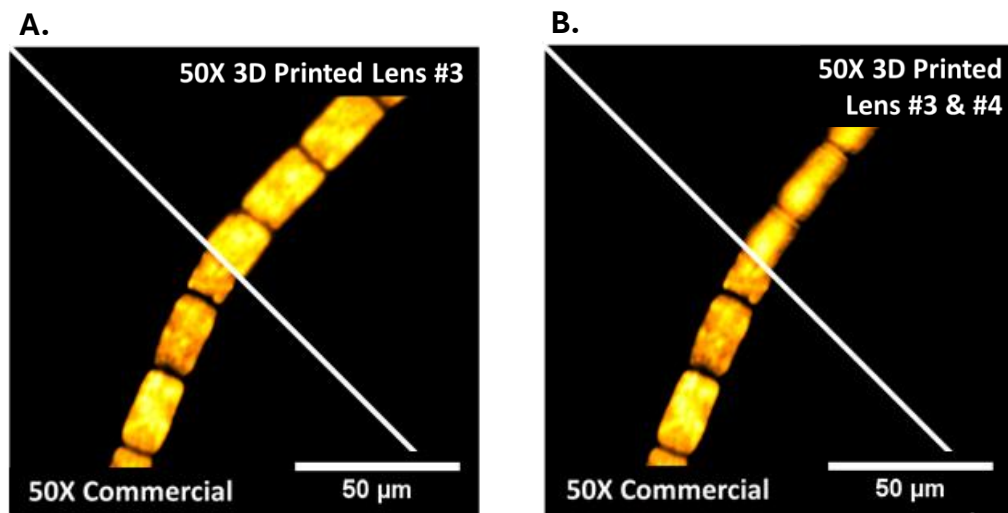


Figure 60. Fluorescent cyanobacteria images using the 4-lens 4-lens objective. (A) Commercial (left) and 3D printed (right) lens #4 objective images of the individually fluorescing cyanobacteria cells. (B) Commercial (left) and 3D printed (right) lens #3 and #4 objective images of the individually fluorescing cyanobacteria cells.

Chapter 4. Imaging using 3D Printed Objectives

multiple 3D printed elements, exemplifying the extent of which multiple 3D printed optics together can be utilised in fluorescence biology using this design of objective.

4.6 Discussion

Exemplified in this chapter is the application of 3D printed optics within optical microscopy. Collimated, focused and defocused illumination through 3D printed optical elements was shown to evaluate the best-suited illumination for microscopy. The optical elements were designed as microscope objectives within Optalix, which showed an 8x MTF upper limit of 245 lp/mm compared to ~ 715 lp/mm for the 4-lens objective design. Additionally, the relationship between lateral alignment within the $\sim 50x$ objective and the Strehl ratio was shown which exemplified lateral offsets between 50 and 300 μm in the optics can reduce the resolution of the objective significantly. The 3D printed optical elements were used in imaging a 1951 USAF target in brightfield modality with contrast values of $95 \pm 2\%$ compared to $99 \pm 0.3\%$ in the commercial 8x implementation. The USAF target also allowed the resolution to be obtained which was found to be 6 μm in the 3D printed 8x objective compared to 4.5 μm in the commercial implementation. It has also been shown that 3D printed objectives can identify sub-cellular biological features in brightfield microscopy by imaging *Hosta* stomata, cyanobacteria and iodine-stained onion cells. In brightfield specifically, the cyanobacteria cells were found to be approximately $34 \pm 2 \mu\text{m}$ by $15 \pm 0.8 \mu\text{m}$ in the commercial case and $35 \pm 2 \mu\text{m}$ by $14 \pm 0.6 \mu\text{m}$ in the 3D printed case. For brightfield microscopy using the $\sim 50x$ objective, it was shown from the USAF target that axial alignment of each lens within the objective itself could impact the magnification, with the lens varying from 48x to 42x across the 3D printed lens implementations. This implies that rigorous objective housing design can be critical in the successful imaging of a sample. Despite this, the results from the USAF target showed $< 2 \mu\text{m}$ resolution values for 1-3 lenses substituted for 3D printed versions. Additionally, contrast was shown to be similar across objectives including 0, 1 or 2 3D printed lenses with contrast values of $92 \pm 5\%$, $91 \pm 4\%$ and $90 \pm 9\%$ respectively, compared to a dramatic drop in contrast to $51 \pm 2\%$ when including an additional 3D printed lens. This also suggests that the chosen lens to be substituted for a 3D printed version could also have drastic effects on the obtained contrast obtained by the objective, not dissimilar to the Strehl ratio lateral offset results. Equally, the similarity between three identical 3D printed lenses supports that the contrast can vary depending on the repeatability of both processing the lenses and housing them within an objective, where across three identical lenses it was shown that the contrast can vary from $77 \pm 3\%$ up to $92 \pm 3\%$. Despite this, the objectives showed that sub-

Chapter 4. Imaging using 3D Printed Objectives

cellular details could be obtained from the biological samples with higher detail obtained in comparison to the 8x objective, as expected.

For both objective configurations, the fluorescence excitation and response was captured from a uniformly fluorescing slide to evaluate homogeneity across the surface. The 8x objective, in its commercial and 3D printed implementations, had deviations approximately equal at 16 % and 18 % respectively. Similarly, for the ~50x configuration, the fluorescence uniformity was found to have 12 %, 10 % and 6 % intensity fluctuations across the FOVs of the commercial, single 3D printed and dual 3D printed objectives. The resolution for the objectives was obtained using diffraction-limited beads, where in the 8x objective the commercial lens featured a $2.1 \pm 0.15 \mu\text{m}$ resolution limit compared to $6.6 \pm 0.86 \mu\text{m}$ in the 3D printed case. The lower resolution is expected in the 3D printed case, and the fluorescent bead results concur in the 3D printed case, though they are improved in the fluorescence detection. In the higher magnification objective, the PSF measurements found FWHM resolutions of $1.23 \pm 0.03 \mu\text{m}$, $1.95 \pm 0.26 \mu\text{m}$, and $2.43 \pm 0.32 \mu\text{m}$ in the commercial, 3D printed lens #3 and 3D printed lens #3 and #4 cases respectively. The objectives were subsequently tested on the same biological samples as in brightfield though now relying on the fluorescence response of Chlorophyll, where for the 8x magnification objective showed blurring of the individual chloroplasts in the 3D printed optic in comparison to the commercial lens, though with the structure of the stomata still discernible. When imaging the cyanobacteria sample, the size of the cells could be seen to be approximately $33 \pm 2 \mu\text{m}$ by $17 \pm 0.68 \mu\text{m}$ in the commercial 8x objective and $35 \pm 2 \mu\text{m}$ by $20 \pm 0.68 \mu\text{m}$ 3D printed 8x objective, though intracellular details were indistinguishable in the fluorescence imaging modality. The ~50x objective showed impressive results when resolving individual chloroplasts in the *Hosta* stomata for the 3D printed lens #3 especially, though when combining this with another 3D printed lens the aberrations blurred the fluorescence severely. However, the cyanobacteria sample showed more distinct cells at the higher magnification in the commercial and 3D printed implementations compared to the 8x objective.

These results hold significant potential for both the next evolution of 3D printers, which at their low costs still increase their printing accuracy, as well as for the use of custom design in-house fabricated optical elements for biological and super-resolution microscopy. In-house designed and fabricated plastic optics have been proven in this chapter to be capable of delivering at least $10 \mu\text{m}$ scale resolution across multiple biological specimens. This supports the case that 3D printed optics could be well positioned to offer rapid, low-cost, on the ground diagnostics in healthcare, especially within low-resource settings. The work shown here has

Chapter 4. Imaging using 3D Printed Objectives

therefore shown the current potential for 3D printed optics within imaging applications, though independent investigation of 3D printed optical elements has not yet been shown during the sample excitation. This therefore provides the opportunity for excitation evaluation of 3D printed optics within biological research, as well as their impact within super-resolution optical microscopy.

Chapter 5. Multifocal Image Scanning Microscopy using 3D Printed Optics

As introduced in Chapter 2, image scanning microscopy falls into the category of structured illumination based super-resolution techniques and uses focused point illumination combined with pixel re-assignment (either digitally or optically) to create a resolution enhancement. Pixelated detectors, such as small arrays of SPAD detectors or full sCMOS camera chips, have their individual pixels act as de-facto pinholes and allow re-assignment of collected fluorescence signals towards the illumination spot centre, leading to a $\sqrt{2}$ lateral resolution improvement. By laterally scanning the excitation, full images of the fluorescing samples can be created. Through image deconvolution, a further lateral resolution improvement is integrated into most processing pipelines and allows an up to 2x lateral resolution improvement compared to the diffraction-limited resolution of the microscope. Like approaches in confocal microscopy, multiple focused spots can be used to increase the speed and efficiency of the full image creation process through raster-scanning, resulting in imaging speed improvements with update rates of up to 24 kHz recently²³³ while maintaining sub-diffraction limited resolution. However, to create the illumination focal spot arrays, micrometre or sub-micrometre precision pinhole arrays and/or microlens arrays are required, with stringent requirements on glass microlens array spacing, lens shapes and surface homogeneity to enable tightly spaced fluorescent spots across the field of view. This requirement leads to significant costs for the optical elements and decreases in general the economic efficiency of the overall microscopy technique. While low-cost 3D printing techniques cannot obtain the same minimum microlens feature size and spacing precision of commercial glass microlens arrays, a custom designed sparser lenslet array with tailored spacing and curvatures can be manufactured to optical quality, allowing for the possibility of custom designed illumination patterns, and therefore the increased potential for democratised access to image scanning super-resolution approaches.

This chapter presents 3D printed microlens array elements and their implementation in a small footprint and affordable multifocal image scanning microscope (mISM) concept. The microscope utilises a single 2D MEMS micromirror to scan the excitation pattern, with multifocal patterned illumination created using a custom 3D printed optical quality lenslet

array. The chapter first introduces the design and optical performance of the 3D printed microlens array in comparison to a commercially available glass microlens array, followed by the demonstration of their use in a custom-built mISM setup. The mISM setup will additionally be described in detail and its performance evaluated comparing both microlens approaches for multifocal illumination generation.

5.1 Lenslet Arrays

5.1.1 Lenslet Array Design

Commercial microlens arrays are manufactured with such high precision through droplet techniques that individual lenslets can be on the order of 100 μm in diameter (and/or *pitch*) while maintaining smooth spherical geometries for a range of focal lengths (commonly 5-15 mm). These small diameter lenslets can be arranged in different patterns, e.g. rectangular or hexagonally patterned arrays, which provide fill factors commonly in the range of $> 95\%$. Specifically, the fill factor is the ratio of the areas covered by individual microlens unit cells within the array relative to the total area of the microlens array. In comparison, low-cost 3D printed microlenses with identical lenslet geometries and hundred-micrometre diameters are not achievable with the current generation of commercial desktop LCD printers. Modifying the printer itself by oscillating the printing base as shown by Yuan *et al.*²¹⁴ leads to more homogeneous print surfaces and lower obtainable pitches of 500 μm , though pixel resolution still limits achieving smaller microlens diameters. The inability of desktop 3D printers to produce commercial level microlens array geometries is due to the lateral and axial resolutions of a single-photon based LCD printer being limited to $> 10\ \mu\text{m}$ voxel dimensions. This therefore limits the achievable microlens pitch and curvature and therefore the overall spherical geometry of the designed array.

Higher resolution manufacturing methods such as 2PP, previously introduced in Chapter 2, provide sub-micron feature details and would be a worthy alternative to desktop printing microlens arrays (MLAs), however the costs of 2PP printing systems (in the range of £100k-£500k) limit the accessibility of the technique. The work in this chapter therefore focuses on evaluating the limits of desktop 3D printer for microlens array fabrication. As a commercial reference element, a polymer-on-glass MLA with 250 μm pitch and 7.5 mm focal length (Viavi MLA-S250-f30) was chosen, with the pitch and focal length balancing the anticipated requirements for minimising the number of lateral scan steps to get a full field image while minimising crosstalk between the individual microlenses where possible.

Chapter 5. Multifocal Image Scanning Microscopy using 3D Printed Optics

When attempting to obtain identical geometries to commercial or high-resolution MLAs using the current generation of low-cost commercial LCD printers, the resulting lenslets will have too few layers to allow creation of a reliable spherical surface geometry even with the developed spin-coating post-process approach. However, by increasing the pitch and/or decreasing each individual lenslets focal length, the spherical geometry of the lenses can be better preserved. Additionally, by printing a lenslet array at an angle or perpendicular to the 3D printer z-axis, full advantage of in-plane anti-aliasing can be used to reduce the impact of the limited lateral and axial pixel resolutions. These design constraints lead to a balance between print accuracy, achievable minimum focal length and the minimum pitch of 3D printed MLAs. In this work, the minimum array pitch was set ultimately to 1.6 mm and the maximum radius of curvature was set to 3 mm, based on initial experimental print tests.

The 3D printed lenslet arrays were designed in Autodesk Inventor 2023 using both a ‘honeycomb’ pattern and a square pattern (see Figure 61), where each lenslet has a 1.6 mm diameter and 3 mm radius of curvature. Each lenslet was designed to be 1200 μm centre to centre from its nearest neighbour to maximise the fill factor obtained when using larger diameter lenslets. As the manufacturing methodology from Chapter 3 section 3.1.6 was followed for lenslet array moulding, the 3D printed master copy included a well-type design with 32 mm diameter and 13 mm height to ensure the silicone moulding mixture could completely fill the cavity with a 3 mm thick wall and base to ensure the mould stays dimensionally stable. In addition, a 3D printed stop mask was designed as well with an identical layout to the lenslets. It consisted of a 1000 μm diameter pinhole at each lenslet centre location and was printed in non-transparent, black resin (Elegoo Mars 2 with Anycubic ABS-like Black resin) including an additional paint post-process step with black acrylic paint to reduce any residual light transmission. The mask was placed onto the lenslet face so each pinhole was concentrically aligned with the corresponding lenslet to minimize background illumination further. The difference between input and output power as a result of the 3D printed absorptive mask is $16 \pm 0.12 \mu\text{W}$ and $74 \pm 1.1 \mu\text{W}$ respectively, which means $\sim 80\%$ of the input power is removed from using the absorptive mask, though this is to be expected.

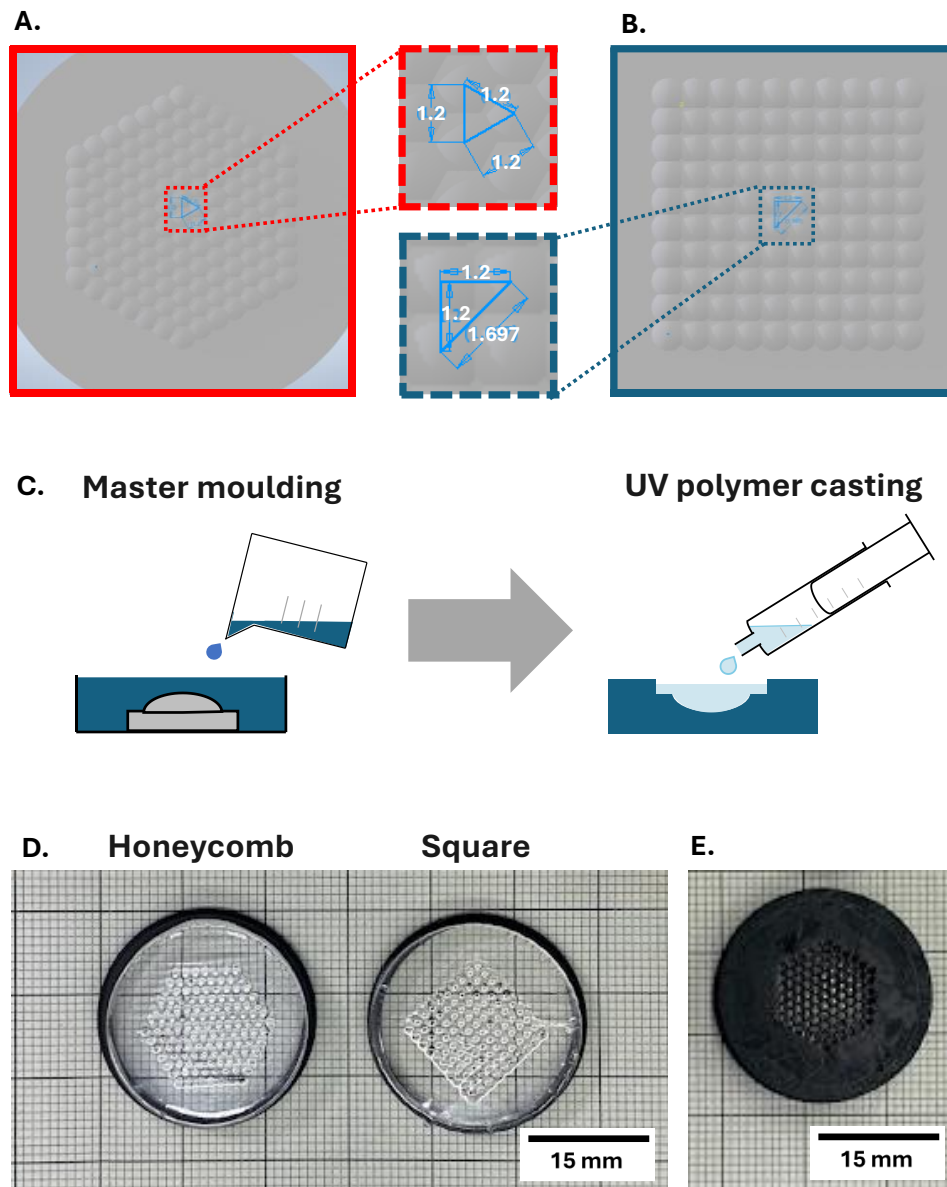


Figure 61. – Designs of lenslet arrays showing two different geometries and the corresponding lenslet pitch. (A) – Honeycomb design showing minimised pitch displacement. (B) – Square lenslet array design showing a higher pitch displacement. (C) – Moulding fabrication schematic showing silicone moulding and UV resin casting. (D) – Moulded versions of each design. (E) The absorptive honeycomb mask.

One of the main advantages of using a 3D printing approach is the design flexibility and adaptability, allowing the designing of custom MLAs with the illumination pattern directly adaptable to the intended application. For example, a honeycomb pattern was used for the mISM

Chapter 5. Multifocal Image Scanning Microscopy using 3D Printed Optics

research in this chapter to minimise the distance between fluorescence excitation spots opposed to a square design. This allows packing of more illuminated spots per unit area compared to a square array design, which helps to reduce the number of raster-scan points needed to build a complete image of the sample. Each focused point across the full scan must still move fully from its original position to the origin of its lateral neighbour in both x and y directions. The displacement between these neighbouring spots is however decreased in sample space from 39 ± 0.73 airy units (AU) in the xy-combined directions in the square lattice to 34 ± 0.66 AU in a honeycomb pattern as supported diagrammatically in Figure 61A and B. This helps to reduce the number of images required for ISM processing, and therefore imaging time and raw image stack size too. Figure 61C shows the schematic for moulding the shown MLA optics. Also shown in Figure 61D are the fabricated versions of each lenslet array type, with the matching absorptive honeycomb mask beside them in Figure 61E. Each array is manufactured on a 25.4 mm diameter base, with an overall horizontal microlens array size of 16 mm and 100 microlenses in the square geometry and 127 microlenses in the hexagonal geometry.

5.1.2 Lenslet and Pinhole Array Fabrication

As previously stated, the fabrication of the lenslet arrays follows the moulding approach detailed in Chapter 3 section 3.1.6. The essential steps are that a mould master copy is 3D printed and spin-coated to obtain an optically smooth lenslet array surface. After some outgassing period, a silicone mixture can be used to create a mould from the optically smooth master copy. Once the silicone mould had been produced, the final moulded optic could be created using Vida-Rosa UV curing resin, with a spin-coated glass slide gently pressed onto the planar surface to obtain an optical quality moulded MLA. The pinhole array matching the respective 3D printed lenslet geometry was fabricated using the same printer as the microlens array with black ABS-like resin. The print orientation for both the lenslet mould and pinhole array was at 90° to the print base to allow for better circularity of the individual pinholes as shown in Figure 62A and B, with the print including supports on the mould and pinhole array to avoid overprinting at the initial print layers. Following fabrication, the lenslet arrays could then be utilized in the ISM setup where the MLA component was either a commercial glass microlens array (Viavi MLA-S250-f30) or our home-produced 3D printed lenslet array.

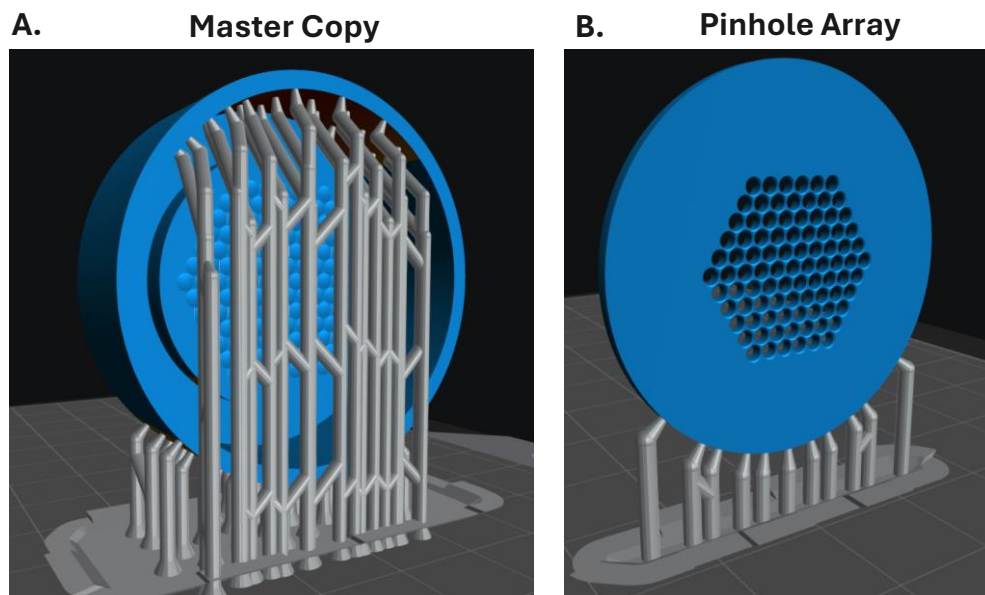


Figure 62. – Chitubox figure showing master copy (A) and pinhole array (B) at 90° to the build plate with supporting features.

5.2 Application in Multifocal Image Scanning Microscopy

Multifocal image scanning microscopy approaches following all-optical or computational approaches have been shown previously. While the pixel reassignment can be completed in-situ and significantly faster in an all-optical implementation, for simplicity of evaluating the impact of a single 3D printed optic within the excitation beam path, the more common computational implementation of multifocal ISM will be used with digital pixel reassignment.

5.2.1 Microscope Overview and Schematic

A custom microscope setup, shown in Figure 63, was created on an optical table for the multifocal ISM implementation, focusing on minimising optical elements where possible.

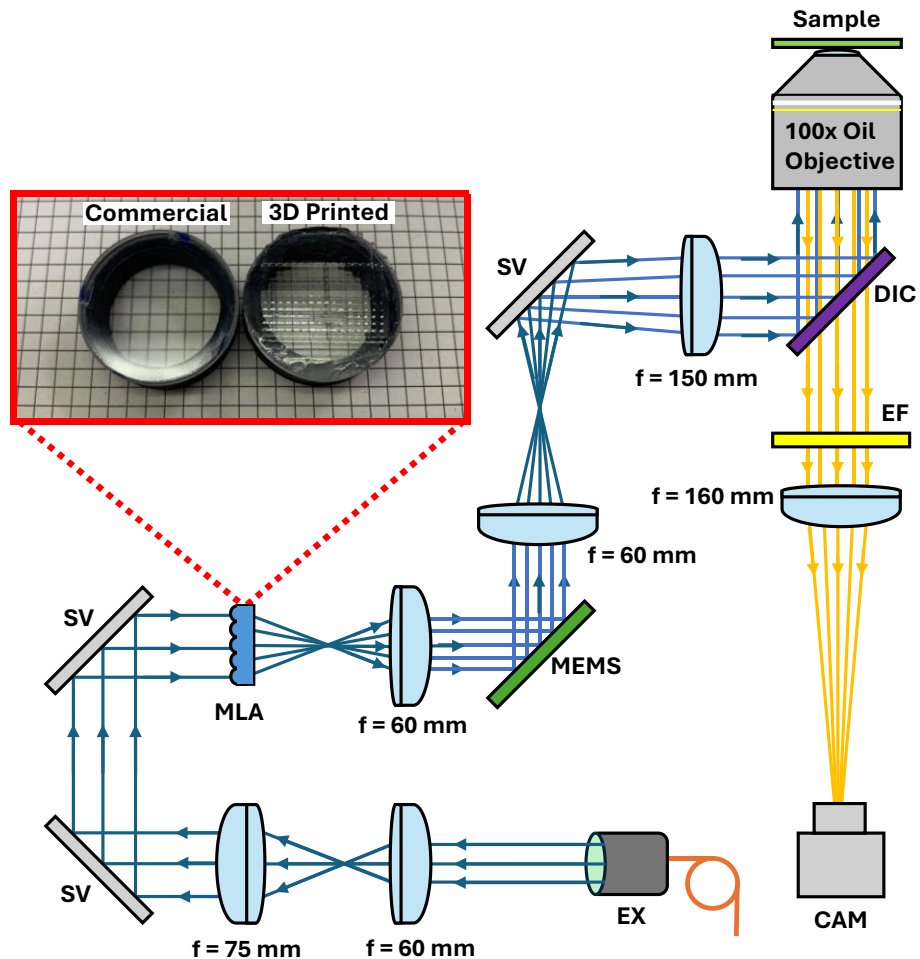


Figure 63. Microscope setup for multifocal ISM comparison of 3D printed and commercial lenslet arrays. EX – 488 nm single-mode fibre-coupled excitation. SV – silver mirror. MLA – lenslet array under investigation, either the commercial microlens array or the 3D printed lenslet array. MEMS – 2 mm diameter 2D MEMS micromirror. DIC - dichroic mirror; EF – emission filter. CM – IDS-3060 CMOS camera.

Chapter 5. Multifocal Image Scanning Microscopy using 3D Printed Optics

Affordability was an additional key consideration in the design, and therefore cost-effective laser sources, lenses & objectives, scanners, stages and cameras were all utilised. To show the proof-of-concept of a 3D printed optical element within a super-resolution system, a single excitation wavelength was used which was a 488 nm laser module (Odicforce OFL-488) that was mode-filtered through a single-mode fibre (Thorlabs FT030-Y). The fibre output was collimated to a 10 mm diameter using a fixed focus collimator (Thorlabs F810FC-543). The beam-diameter was then further expanded using a telescope consisting of a $f = 60$ mm achromatic lens (Thorlabs AC254-060-A) and an $f = 75$ mm achromatic lens (Thorlabs AC254-075-A) to ensure overfilling of the lenslet array. The output from the lenslet array was part of a 4f configuration in combination with a further $f=60$ mm achromatic lens to collimate each individual lenslet beam such that they overlap on the 2 mm diameter 2D scanning MEMS micromirror (Mirrorcle A7M20.2-2000AL). The reflected beams of the MEMS are guided through a further 4f configuration using a third $f=60$ mm achromatic lens and a $f=150$ mm achromatic lens (Thorlabs AC254-150-A) to conjugate the MEMS surface with the back-focal plane of a Zeiss 100x 1.25 NA oil immersion objective (Zeiss A-Plan 100x/1.25 Oil M27). The chosen 2.5x magnification of the 4f setup allows overfilling of the objective back aperture. Prior to the objective the excitation beams were reflected by a multi-band dichroic mirror (Chroma ZT405/488/561/640). The objective focused the lenslet beams onto the sample, with lateral scanning in the sample plane provided by the MEMS. The micromirror angular positioning can be adjusted with enough sensitivity to provide lateral movement of the focused illumination with sub-camera pixel accuracy. It was found that 5 DAC units moved the excitation by 1 pixel (without binning), and as 1 pixel is 62.5 nm we can infer that a single DAC unit has ≈ 12.5 nm movement positioning accuracy in the MEMS for our imaging pixel size. This allowed for raster-scanning at a Nyquist sampled 250 nm steps. Samples were microscope slide mounted and positioned with a manual x-y stage (Thorlabs MT1A/M) and a combined 5 mm manual / 20 μm piezo z-stage (Thorlabs NFL5DP20/M). A low-cost industrial CMOS camera (IDS U3-3060CP) was used to capture the observed fluorescence, with an emission filter (FELH0500) and 160 mm tube lens (Thorlabs AC254-160-A) completing the imaging arm. The camera was used with 2x2 binning to capture the raw images of the fluorescent samples with 125 nm binned pixel size.

5.2.2 Microscope Control

The excitation lenslet spots were laterally scanned across the sample using the 2D MEMS mirror controlled by an Arduino Uno through the Arduino software (Arduino 11.8.13). The

Chapter 5. Multifocal Image Scanning Microscopy using 3D Printed Optics

Arduino was connected through SPI to an 8-channel DAC board (Texas Instruments BOOST-DAC8568) with 4 DAC outputs controlling the four channels of the MEMS tip/tilt actuators. The DAC outputs are independently amplified using a 4 channel 68.3x voltage amplifier (Microchip HV56264) to provide the low power but high voltage (180V max) actuation required for the MEMS. Using the Arduino the electronics allow precise angular tip/tilt control of the mirror at an angle proportionate to the input voltage step, with the script used for this shown in Appendix D. Images were captured using an industrial grade CMOS camera (IDS U3-3060CP) and its native imaging software (IDS-Cockpit), with a trigger input provided by the Arduino. The acquisition was set to a rising-edge trigger so an image could be captured at each new laterally displaced excitation location and saved as an image stack at the end. By capturing an image at each raster scanned position, the generated image stack can then be pre-processed in ImageJ ready for computational ISM resolution improvements using a custom python script. The focus of the microscope was adjusted using a Thorlabs piezo controller (KPZ101) which allows for nanometre scale adjustments using the Thorlabs Kinesis software.

5.2.3 Image Processing

Each raw image acquired to create an image stack was pre-processed in Image J to remove hot pixels. The presence of hot pixels can affect the success of ISM processing as the hot pixels can be mistaken for fluorescence signals and therefore used as the centre for an individual illumination spot which will be processed into the finished image. By denoising the image stack through outlier removal, which in Image J used a pixel radius of 1 pixel with a threshold value of 1, the resulting input image stack minimises processing of ‘false’ signals. To obtain ISM images, Python was used for image processing, as shown in Figure 64, due to it being an open-source language with relatively easy to use GPU acceleration plugins. The developed ISM processing Python script is available in Appendix E. The mISM dataset consisted of 396 images for the commercial microlens implementation and 7199 images for the 3D printed microlens implementation. Each image was loaded sequentially into Python, where the locations of each maximum intensity were found using the python function `peak_local_max` from the `skimage.feature` plugin and their respective x and y coordinates assigned into an array for each image. Each of these coordinates referenced an image location where the focused excitation of the lenslet array could be found. By using these coordinate points and extracting a 7 x 7-pixel area around each maximum, the excited fluorescent points can then be processed for ISM improvements. To computationally process the full raw image stacks for ISM improvement GPU enhancement has been integrated to allow faster parallel processing using

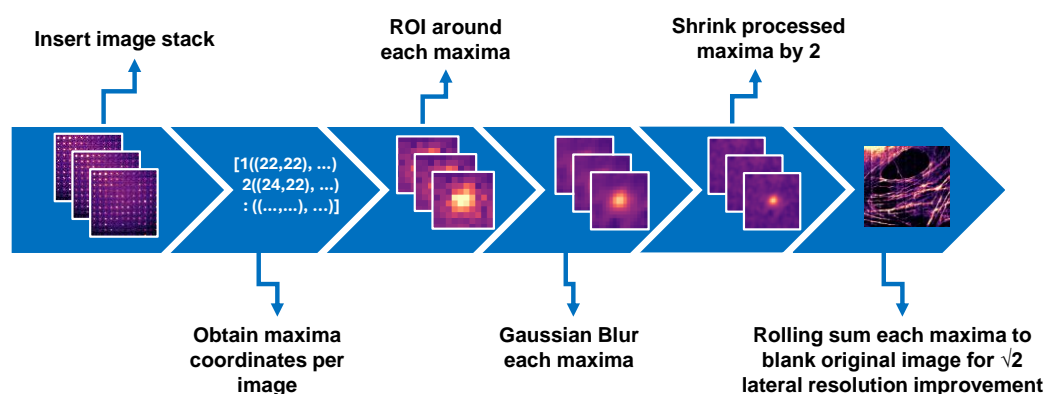


Figure 64. Schematic for the ISM processing script in Python. (Left to Right) – Image stack is loaded into Python; each maximum intensity coordinate location is saved as a variable; each maxima at each coordinate location is cropped to an ROI; each of the cropped maxima are individually convolved with a Gaussian Blur; each convolved maxima is shrunk to by a factor of two by doubling the spatial region around the maxima information; each resulting maxima is added into one image with original spatial dimensions but double the lateral pixel numbers.

a NVIDIA GeForce GTX 1650 SUPER card. The use of GPU enhancement in python through PyOpenCL was necessary as the code for ISM processing found up to ~ 440 maximum intensity coordinates and ~ 25 maximum intensity coordinates in the commercial and 3D printed implementations respectively per image. This means that the number of maxima coordinates in Python can easily enter the tens or hundreds of thousands per pre-processed image stack. Without GPU acceleration the biggest constraint for processing these datasets is the amount of memory (specifically RAM) available to run complete datasets without crashing the non-optimised code.

Once the maxima search and ROI extraction for the full pre-processed image stack was complete, each ROI was filtered with a Gaussian blur to mimic a physical pinhole, with the σ value of the python Gaussian filter function equal to 1.2 (see Appendix E). The chosen value of σ is discussed in more detail in section 5.3.2. There are two methods of pixel reassignment which could be used: the first is that each processed maxima ROI can be shrunk with interpolation, which can be affected by rounding errors. The second option, opted for here, is that a blank image can be created in e.g. Python with twice the number of pixels as the original image used to extract the maxima, and by re-assigning each processed maxima to double its original xy coordinates, the effect is an image with processed fluorescent spots half their original scale. As this was the chosen method, after the Gaussian filtering step each processed ROI was reassigned as stated. For example, if a 7×7 maxima ROI had original xy coordinates

Chapter 5. Multifocal Image Scanning Microscopy using 3D Printed Optics

of $x = 50$ pixels, $y = 50$ pixels on a 1000×1000 -pixel image, then the pixel reassignment on that same maxima after Gaussian processing would be at $x = 100$, $y = 100$ onto a 2000×2000 -pixel image. As such, the centre of each maxima position matches its previous location before ISM processing and scaling, though each fluorescent maxima now has ‘shrunk’ by a factor of 2. By following this process for each processed maxima, the result is a stack of images with the same pixel scale as the raw images though with the fluorescent spots half their original size and Gaussian filtered. Additionally, this pixel reassignment process means that going from a 1000×1000 -pixel to a 2000×2000 -pixel keeps the same spatial dimensions, as the pixel size is halved from e.g. 125 nm to 62.5 nm , therefore both images would be across a $125 \times 125 \mu\text{m}$ FOV, for example. When each maxima-reassigned complete 2D image of the ISM processed stack is additively combined through image summation, a resulting image is formed with up to $\sqrt{2}$ resolution improvement compared to the original image without pixel re-assignment. To obtain a 2-fold resolution improvement, a deconvolution step can be utilised on the processed image, however for initial comparisons of the 3D printed and commercial microlens illumination approaches this was omitted.

5.2.4 Imaging Test Samples

Three types of fluorescent samples were used for system and image processing evaluation: a homogeneously stained fluorescent slide, a sparse nanobead sample and a fixed biological tissue slide.

To evaluate the point spread function and therefore achievable resolution of the microscope setup pre- and post-ISM processing, commercial sub-resolution nano-beads (175 nm yellow-green beads, Invitrogen PS-Speck Microscope Point Source Kit P7220) were used. The 175 nm beads were vortexed in deionised water at a ratio of 1:10 per volume, and immediately pipetted ($100 \mu\text{l}$) onto a #1.5 glass coverslip with $98 \times 76 \text{ mm}$ size and left to air dry. The coverslip was then fixed onto a microscope slide and sealed using clear nail varnish.

To evaluate the homogeneity and shape of all multifocal illumination spots across a homogenous surface, a Thorlabs fluorescent slide (Thorlabs FSK2) was used. This is a full stained plastic microscope slide which fluoresces under the 488 nm excitation. This slide provides useful information on the lateral homogeneity of the excited fluorescence, though due to its thick staining axial information is poor due to out-of-focus light contributions.

For biological quantification of ISM using the 3D printed optics microlens array, commercially fixed and stained BPAE slides (Invitrogen Fluocells #1 BPAE) were additionally used. These

slides allow for microscope image performance quantification through analysis of the size and shape of their mitochondria or actin filaments.

5.3 Image Scanning Microscopy Results

5.3.1 Microscope & Lenslet Characterisation

To evaluate the performance of each type of lenslet array, a uniformly labelled fluorescence slide was used. A single raw resulting illumination image when using the commercial lenslet

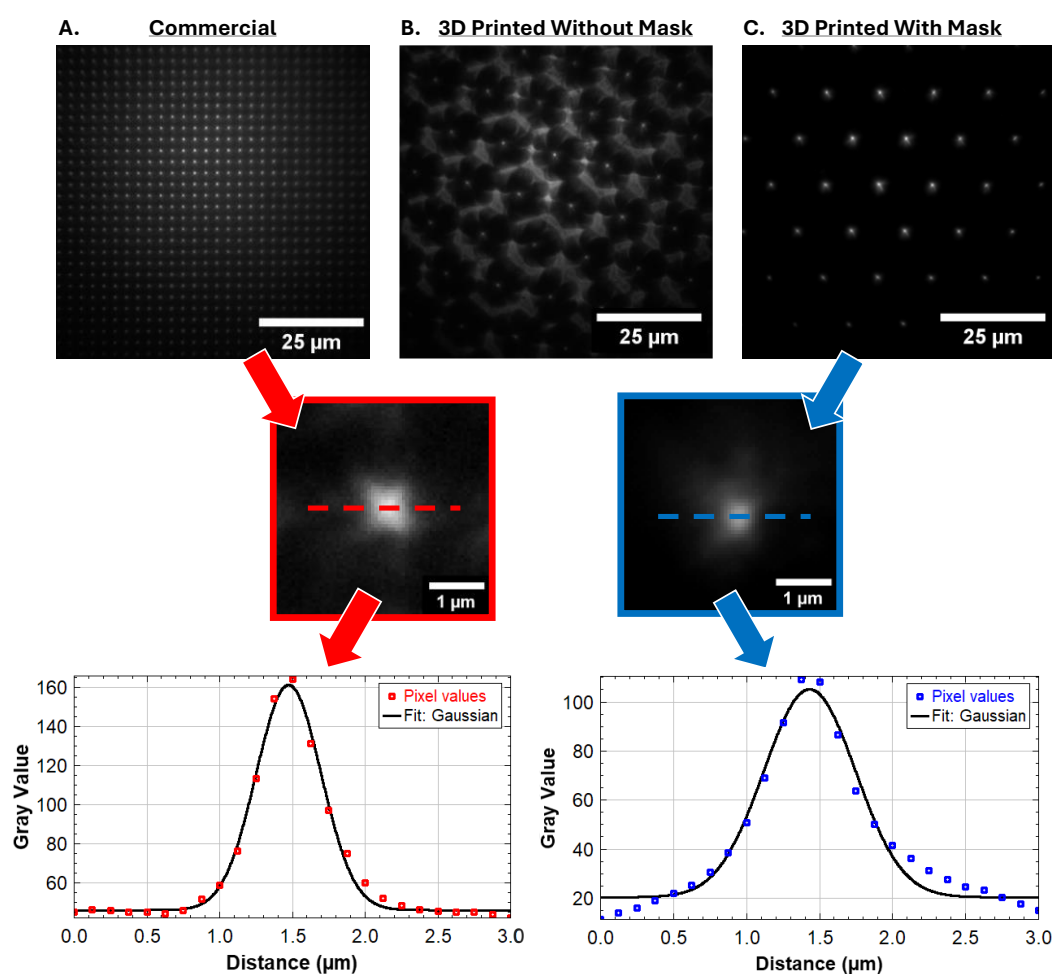


Figure 65. Fluorescence excitation on a uniform slide from the commercial and 3D printed lenslet arrays with individual spot line profiled below. (A) – Commercial microlens array with associated digitally zoomed in lenslet excitation ROI and line profile. (B) – 3D Printed lenslet array without background removing mask. (C) – 3D Printed lenslet array using background removing mask with associated digitally zoomed in lenslet excitation ROI and line profile.

Chapter 5. Multifocal Image Scanning Microscopy using 3D Printed Optics

array or the 3D printed lenslet array can be seen in Figure 65. For the commercial array (Figure 65A) a Gaussian homogeneity across the illuminated spots can be seen. This is to be expected from the non-flat fielded illumination source, and each individually excited spot in the commercial optic should exhibit approximately radially Gaussian profiles (see digitally zoomed ROI from Figure 65A), though across the full FOV the excitation from one microlens is evidently not equal to other microlens spots across the FOV. As such the power distribution across the full FOV is also expected to differ. The circumference of each 3D printed lenslet passed through scattered saturating illumination (see Figure 65B), which was mitigated using a 3D printed absorptive mask (Figure 65C). The transmission at the circumference locations is due to the overlapping areas of the lenslets themselves. Though the commercial optic also shows background absorption, it is not featured as clearly around the circumference of the lenslets as in the 3D printed case. Depending on the used ISM code, this may provide marginal detrimental or even no detrimental effects in the final image reconstruction, especially if each centrally focused spot location within the resulting image is predetermined as an ROI in the ISM code itself. By using the previously mentioned 3D printed mask, however, the computational steps around mapping the excitation spots to lateral pixel locations were not required. An additional benefit of using a mask over the lenslet array is that the illumination is pinholed to remove signal from the lenslet boundaries and overlaps, which results in tighter fluorescence excitation due to removing potential focal variations at the edges of each lenslet.

To show the obtained quality of the excitation spots in the sample plane of the commercial and 3D printed lenslet setup, line profiles were taken (Figure 65A and C) from each optic's respective focused excitation. As expected, the commercial optic shows more radial symmetry in its excitation per excited focal spot than the 3D printed optic. The commercial shows tight packing of the lenslet excitation with spacing between each illumination spots of 8.3 ± 0.15 AU, with enough SNR between the background and fluorescent regions to provide Gaussian intensity beam profiles with a mean diameter of 1.4 ± 0.05 AU at FWHM. The commercial optic does still exhibit some inhomogeneity in each fluorescent spot, which could be due to minor axial or angular misalignment of the MLA itself. However, given that ISM will focus only on the excitation spots themselves and process them with Gaussian symmetry, the inhomogeneities at the edges of the excitation should not be detrimental to the result of the ISM process.

Due to the limitations of 3D printing fine structural details with the developed low-cost technique, each lenslet contributes a more unique illumination profile in the 3D printed optic case. The 3D printed optic in Figure 65C shows significantly less dense excited fluorescent

Chapter 5. Multifocal Image Scanning Microscopy using 3D Printed Optics

spots than in the commercial case, with 34 ± 0.66 AU distance between each, though the excitation still exhibits a relatively Gaussian profile across each spot with a measured mean FWHM of 3.2 ± 0.3 AU. Though more images are therefore required to build up a complete 2D image through raster-scanning, the crosstalk between individual lenslets will be lower than the crosstalk from the tightly packed commercial array. As with the commercial case, the edges of the spots' illumination should not impede the quality of the resulting ISM processing, and the spots themselves should further match a Gaussian profile when convolved with a Gaussian blur, leading to a more ideal effective excitation in ISM.

An additional use of the uniform fluorescent slide as initial calibration sample is the lenslet intensities can be normalised to one another to compensate for any inhomogeneity from their production, which is a calibration step which can be done once and used as a baseline for successive imaging experiments. This was not performed for the results within this chapter as the most elementary case was taken as a benchmark. Nonetheless, the effect of inhomogeneous illumination intensities on the resulting ISM image should be relatively minor in the form of mismatching intensity tiles after image summation of the laterally scanned points. This means no extra detail might be lost from the differing illumination, though the image itself may have a 'mosaic' illumination tiling, making deductions about biological structures less trivial and prevent quantitative evaluations.

5.3.2 ISM Imaging Using Fluorescent Nanobeads

To process the lateral scans of all focal spots into a final ISM image, two variables had to be optimised: the ROI size around each focal excitation spot of the fluorescence signal to be processed; and the severity of the standard deviation value σ in the Gaussian Filter function in Python which is a proxy for the digital pinhole size. Using 175 nm fluorescent beads as the target (Figure 66A), shown is a processed ROI around each fluorescing bead (Figure 66 B-C) with the pixel value of the cropped region varying from 5x5 pixel to 9x9 pixel. Shown in Figure 66(D-F) is the use of the Gaussian filter function from Python with the standard deviation varying from 0.6 to 1.8. To contextualise the results from this figure, the diffraction-limited cases are evaluated shown in Figure 67. The widefield results shown in Figure 67A, which were obtained using regular widefield illumination, and the laser-scanned results in Figure 67B are created by the summation of the scanned raw image stack without any pixel re-assignment. Each of these cases have similar resolutions of 331 ± 13 nm and 324 ± 13 nm respectively, averaged over five identical beads from the FWHM of their respective line-plots. To calibrate the Python code to obtain an optimal ROI and standard deviation value, different values were compared as per Figure 66.

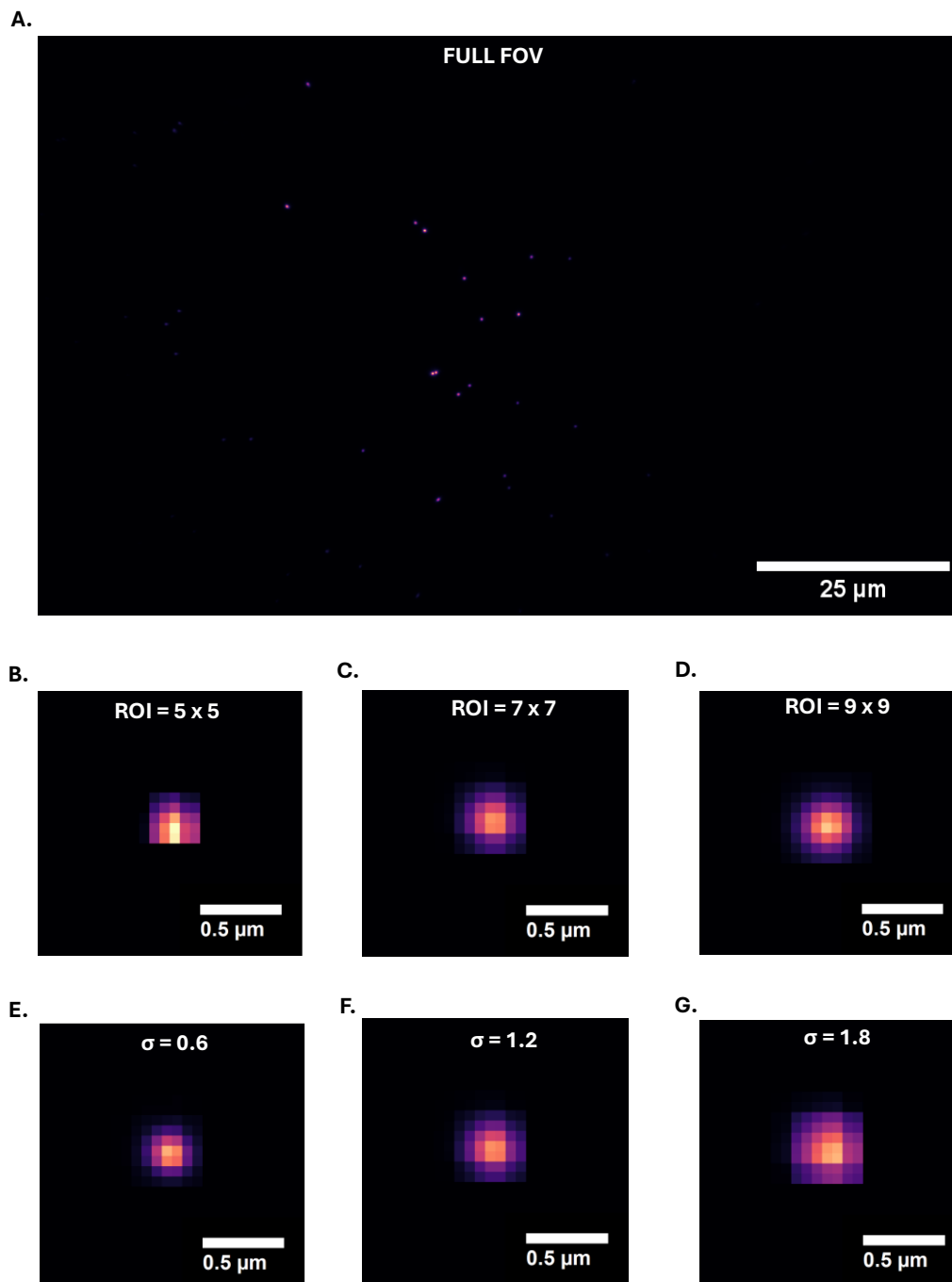


Figure 66. Analysis of processing ROI and Gaussian Blur on resulting 175 nm bead, with widefield FOV for bead reference. (A) – Summed laser-scanning image showing each fluorescent bead in the dataset. (B-D) – Different results of ISM processing from pixel ROI windows of the fluorescent maxima. (E-G) – Different results of ISM processing from Gaussian Blur standard deviation values from a 7x7 fluorescence maxima ROI.

From Figure 66B it is evident that an ROI of 5x5 pixels crops signal from the resulting bead image, and this is additionally quantified through bead resolution measurements of 205 ± 20

Chapter 5. Multifocal Image Scanning Microscopy using 3D Printed Optics

nm compared to both the 7x7 and 9x9-pixel ROI results which were 245 ± 9 nm and 250 ± 7 nm respectively. From these results the 7x7 ROI was chosen as the results were on average 96 % comparable in intensity values to the 9x9 window. As such, the wider window was discounted in favour of minimised computational resources e.g. processing time and RAM memory required. Additionally, the effect of σ , which is the standard deviation value in the Gaussian Filter step of ISM processing, was evaluated on its effect on the fluorescence signal. The results were evaluated using a 7x7 ROI and Figure 66E and G show values toward the extremes of the optimal σ value. For a standard deviation of 0.6 in the Gaussian filtering step, the resulting bead has only been slightly blurred, with the two-times pixel reassignment dominating the result as the resolution of the bead artificially becomes 190 ± 7 nm. Without the Gaussian filtering, the bead would have been simply half the laser-scanned resolution (i.e. 162 nm) showing that the filter has convolved the fluorescent signal slightly. However, though

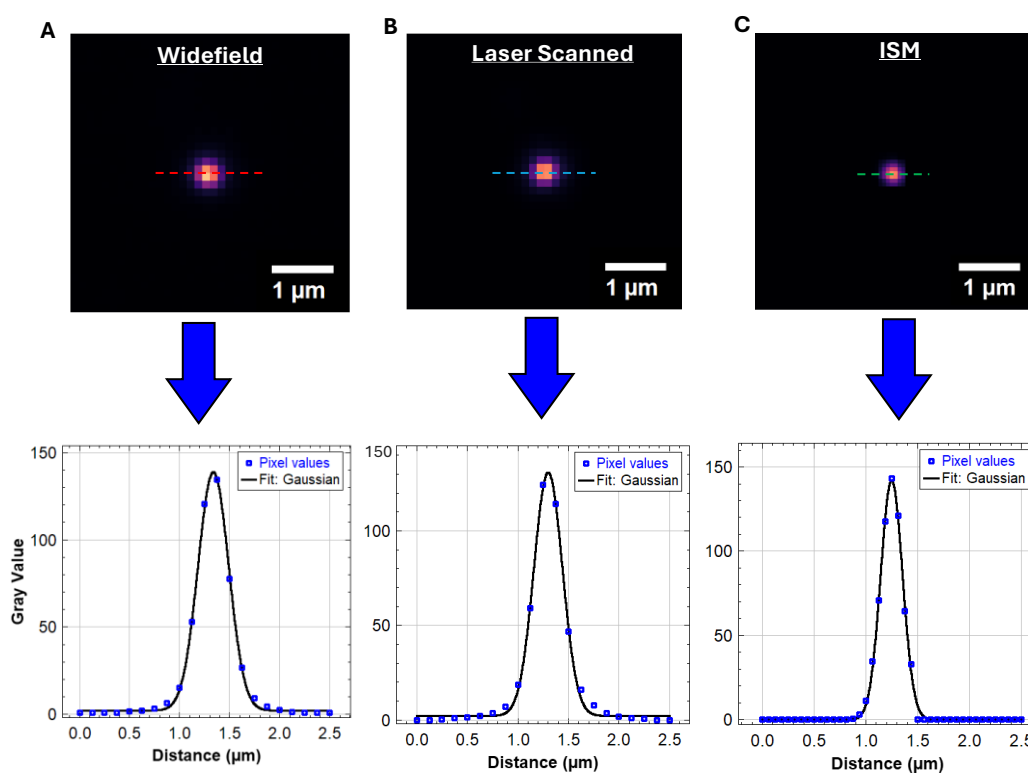


Figure 67. Resolution measurements from diffraction-limited and ISM configurations using 175 nm beads. (A) – Widefield image of 175 nm bead with resulting line-plot below. (B) – Summated image from the commercial MLA multifocal laser scanned implementation with respective line-plot below. (C) – optimised ISM on the 175 nm bead sample with respective line-plot below.

the result appears to be impressively resolution enhanced, the resolution improvement is beyond the $\sqrt{2}$ expected from ISM. It can therefore be inferred that the resolution enhancement is not strictly or quantifiably true regarding the ISM processing method. Equally, with a standard deviation value of $\sigma=1.8$, the fluorescence response from the bead is visually over-convolved with a resulting resolution of 292 ± 15 nm which is a resolution enhancement on the bead from both widefield and laser-scanning, though only a 1.1x improvement compared to the 1.4 to be expected. As such, a combination of the sigma value of 1.2 and an ROI of 7x7 gave the results keeping in-line with ISM expectations. For the optimised ISM process shown in Figure 67C, with $\sigma = 1.2$ and a ROI of 7x7 pixels around each captured fluorescent spot, the FWHM resolution is 245 ± 9 nm, which corresponds to a 1.34x resolution improvement, which is in line with ISM expectations. As such, these variables were utilised in all subsequent image processing steps for analysing more complex and less sparsely labelled fluorescent biological samples, with structural comparisons able to be quantitatively compared between diffraction-limited and commercial and 3D printed ISM results.

5.3.3 Widefield Imaging BPAE Mitochondria

To position the sample with a cell in the centre of the imaging field-of-view a widefield image was first captured of a fixed BPAE cell slide, with distinct mitochondrial structures visible. To do this, the MLA was bypassed in the microscope setup shown in the schematic in Figure 63 of section 5.2.1. This therefore creates collimated illumination onto the fluorescent sample, which allows for a conventional widefield fluorescence image of the BPAE sample for comparison and validation of the ISM improvements. The interval between imaging in widefield and imaging with the MLA integrated is less than 1min, so lateral drifts are not prominent and axial refocusing of the excitation is simple as the imaging plane has not shifted outside of a fluorescence excitation response. For the cell slide specifically, the labelling should have actin with Alexa488, however due to potential cross-labelling and intensity drops over time the nominally mitotracker red labelled mitochondria are prevalent in their fluorescence response compared to the actin network.

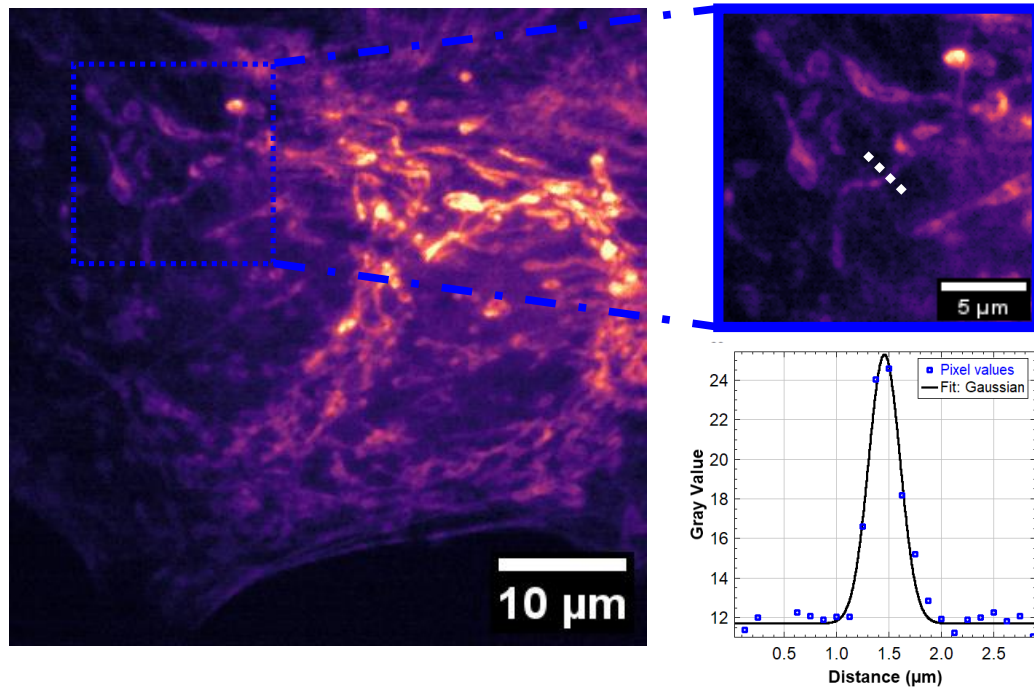


Figure 68. Widefield image of BPAE cell with fluorescent labelled mitochondria, including a digital zoom in of a ROI and cross-section through a mitochondria strand.

Shown in Figure 68 is the full FOV of the BPAE cell used for ISM and a digitally zoomed ROI, where notably background noise is present through the sample which diminishes the identification of structural details due to poor contrast in more dense parts of the sample. For example, in the thicker central region of the sample the contrast is $58 \pm 5\%$ compared to $69 \pm 3\%$ toward the edge of the sample. This is an issue which should be largely removable using ISM as background is mitigated as a by-product of the focused illumination spots and digital pinholing, similar to optical processing steps in a confocal microscope. Mitochondria are still distinguishable from the background with an average FWHM of 376 ± 13 nm for the selected cross-section shown in the zoomed-in region, showing that the results are in line with the diffraction limited 175 nm bead results.

5.3.4 ISM Imaging BPAE Mitochondria

Due to the higher density of fluorescence illumination spots, the commercial dataset for ISM features significantly less laterally scanned images and therefore significantly less time is needed to obtain a complete dataset. The commercial and 3D printed scans for ISM featured lateral steps of 250 nm which helped in both cases to ensure Nyquist sampling. Overall, the

Chapter 5. Multifocal Image Scanning Microscopy using 3D Printed Optics

commercial scan lasted approximately 30 seconds to obtain 396 2D images. In comparison, the 3D printed optic scan requires ~ 5-minute imaging timescales to obtain 7199 2D images. In part, the scan period is due to the 10 ms wait time required for the MEMS mirror to stabilise to its newly appointed angle without capturing distortions induced by the mirror vibration.

The difference in acquisition time between the commercial and 3D printed lenslet arrays is overall significant, where the number of images required for the sparser lenslet array is a factor of 18x greater. The difference in lenslet spacing between the commercial and printed optic additionally creates or increases several non-trivial challenges, including:

- the time taken to obtain a complete dataset of a single FOV (~ 5 minutes, > 10x longer than the commercial case)
- the axial and lateral stability of the sample stage throughout this imaging period
- the allocated memory for the pre-ISM dataset (~ 1.2 GB for the 3D printed optic vs 80 MB for the commercial optic, due to the increased quantity of images)
- and the required RAM to process the greater number of images.

It should be noted, however, that though more images are required to obtain the completed dataset, per image there are fewer fluorescent spots to process and resample at once compared with the commercial lenslet dataset, which balances the memory requirements for the post-processing steps per image.

Once the raster scans had been completed for identical locations on the BPAE cells, each 2D RAW image within the stack of RAW images was pre-processed in ImageJ. This included some basic hot pixel reduction to maximise the accuracy of the local maximum finding plugin within the ISM Python script. Additionally, a reduced ROI with 400 by 400 pixels (equivocal to 50 x 50 μm compared to the 120 x 75 μm full camera FOV) at the centre of the dataset was taken to focus on observing the outcomes of the ISM code on the stained mitochondria as well as to minimise the processing power necessary to compute the ISM image. The pre-processed images were then ready to be fed into the previously detailed Python script for ISM image processing. For comparison to the ISM images, the stack of pre-processed images was summated into a single image in ImageJ as shown in Figure 69 for the commercial and 3D printed optic versions. This creates a laser-scanned sample image with qualities not unlike a widefield image. When comparing the commercial laser-scanned image to the widefield image

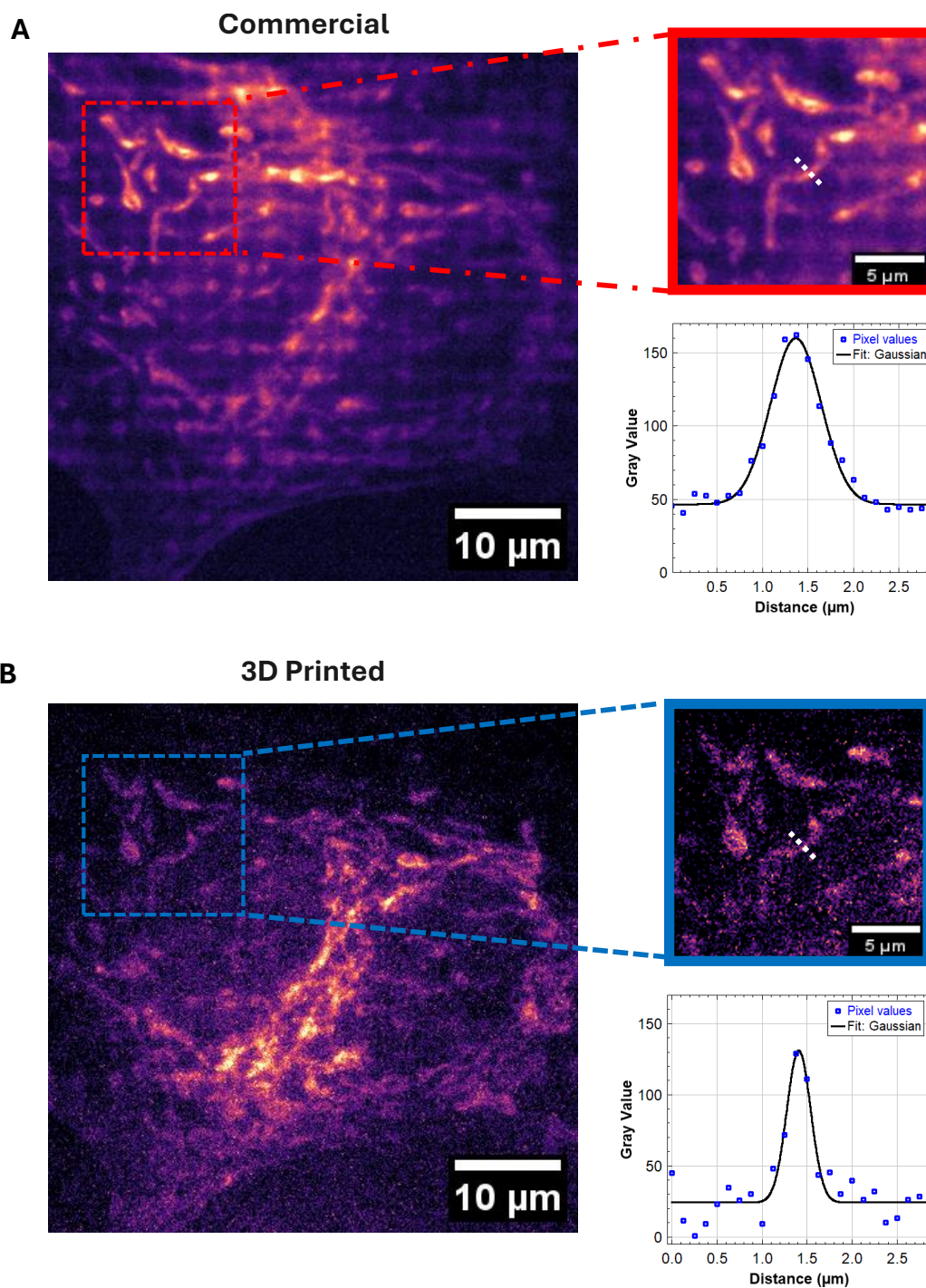


Figure 69. Laser scanned summed images from the commercial and 3D printed lenslet arrays without pixel re-assignment. (A) – The mitochondria in a BPAC cell with corresponding digital zoomed ROI and respective ROI line plot for a mitochondria structure using the commercial lenslet array. (B) – The same BPAC cell with labelled mitochondria with corresponding digital zoomed ROI and respective ROI line plot for the mitochondria structure cross-section using the 3D printed lenslet array.

from Figure 68, a higher grey value intensity is obtained through an identical cross-section of

Chapter 5. Multifocal Image Scanning Microscopy using 3D Printed Optics

mitochondria though the commercial laser-scanned image itself is prone to oversampling after the image summation step. This can be seen from the grid-like patterning in Figure 69A, and this could be reduced by either minimising the oversampling at the edges of each axes maximum lateral step, or by summing the images through maximum intensity or standard deviation methods. The former option was not opted for to ensure enough lateral steps were obtained for the pixel reassignment step of the ISM processing within this benchmark test of the microscope system. The latter option was also not preferred over simple summation as there was uncertainty over the impact of any induced filtering of pixels within the proposed alternative summation methods, which may have impacted the quantification of 3D printed optics within this benchmark dataset. Additionally, the commercial laser-scanned image does show worse contrast than the widefield image, with contrast values of $33 \pm 2 \%$ in thick sample regions and $48 \pm 3 \%$ in thinner sample sections. This lower contrast, contrary to expectation from widefield, is due to lower exposure times compared to the dataset as the microlens array excitation spots exhibited inhomogeneous excitation across the full FOV. Therefore, to ensure the fluorescence response did not saturate the final image the captured images had to have their intensity balanced toward the central most intensely fluorescing region, resulting in a generally lower contrast image.

This is equally true for the 3D printed optic image from Figure 69B, where contrast values as low as $15 \pm 1 \%$ in dense regions and $9 \pm 0.9 \%$ in sparse regions were measured. The inverse problem to the commercial optic exists here however, as more fluorescence was captured in the central region compared to the thinner sections of the sample, making the contrast balanced better toward the centrally imaged section of the sample. This difference between the commercial and 3D printed implementations is likely due to the application of the absorbing mask in the 3D printed MLA setup as well as the sparsity of the lenslet excitation itself, minimising crosstalk. By including the mask, the background excitation will have been largely eliminated from exciting fluorescence, tightening the signal received. Though the advantage of the commercial optic features tighter illumination spacing, no background illumination or illumination at the lenslet edges can be completely removed, resulting in lower contrast compared to the 3D printed optic. The commercial and 3D printed optic laser-scanned images from Figure 69 show mitochondria details across the measured region of $574 \pm 13 \text{ nm}$ and $446 \pm 82 \text{ nm}$ respectively, obtained from the FWHM of the Gaussian profile like taken as shown. The loss in resolution compared to the widefield dataset is likely due to the reduced SNR in the laser-scanned datasets, as inhomogeneous excitation through the lenslet array meant some areas fluoresced more than others, meaning the excitation intensities were lower than in the

widefield case. This equally explains the higher standard deviation uncertainty in the average FWHM taken for the 3D printed dataset, as low SNR noise contributed more uncertainties than in the commercial MLA or widefield cases.

To obtain the resolution enhanced image, the image stacks were then processed through the ISM Python code to convolve and reassign the pixels, which is shown in Figure 70 for both the commercial and 3D printed lenslet array implementations. As expected from ISM processing, the contrast is dramatically improved in comparison to the original laser-scanned images, with thicker regions in the commercial optic dataset containing contrast values of $93 \pm 3 \%$ and thinner sample sections containing $95 \pm 1 \%$ contrast values. At the same ROI for the diffraction-limited results, the obtained details from the mitochondria show for the commercial optic in Figure 70A that the mitochondria width decreases to $390 \pm 19 \text{ nm}$, which is as expected a $\sqrt{2}$ improvement on the laser-scanned resolution. Similarly, for the 3D printed optic, thicker regions have corresponding high contrast values of $94 \pm 2 \%$ and in thinner regions of the sample the contrast is $97 \pm 2 \%$.

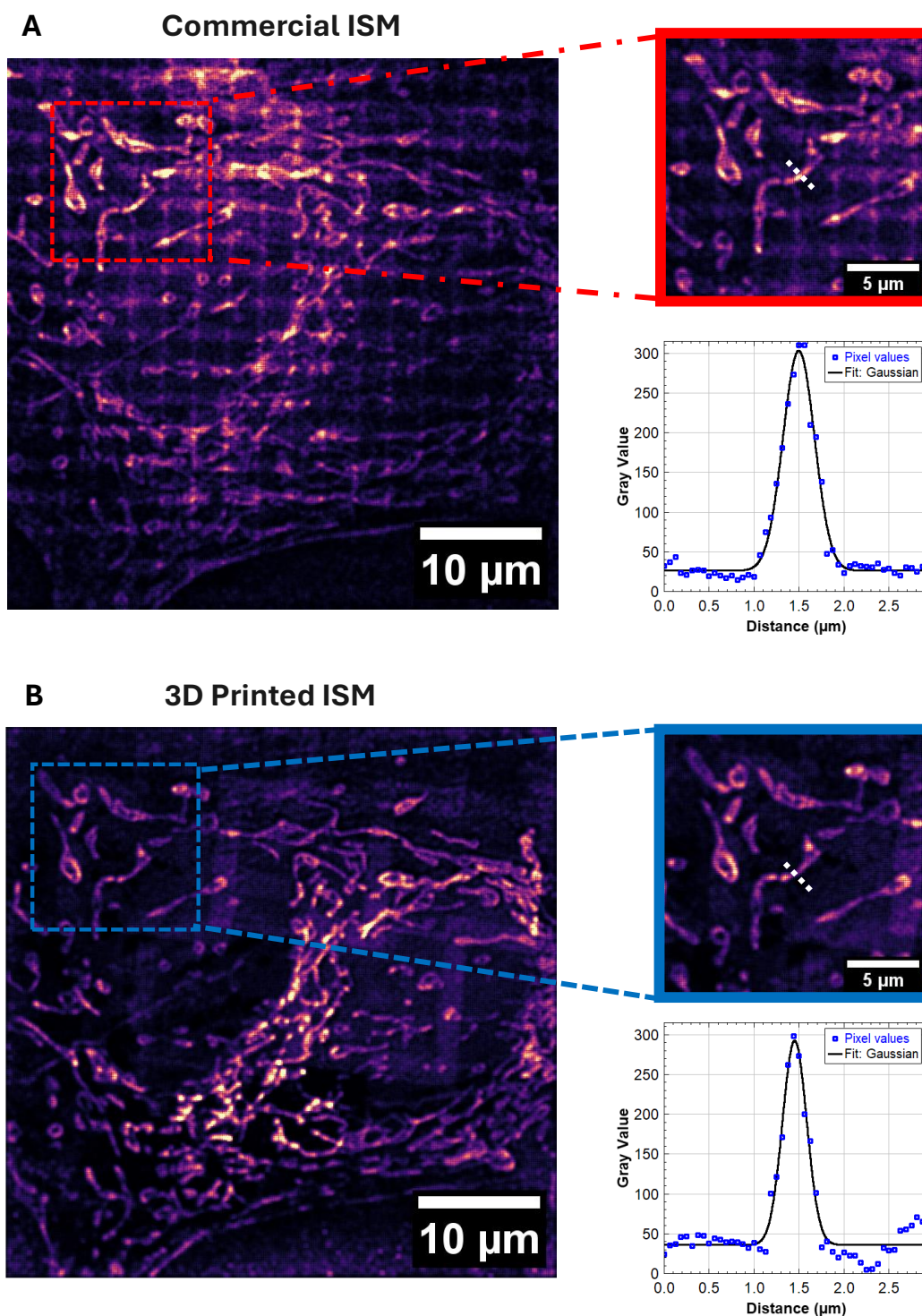


Figure 70. Commercial and 3D Printed ISM results. (A) – Commercial microlens array ISM processed image, with corresponding digital zoomed ROI and respective line profile to show the cross section of a mitochondria structure. (B) – 3D Printed lenslet array ISM processed image, with corresponding digital zoomed ROI and respective line profile to show identical mitochondria structure cross section.

As such, the resolution improvement obtained from the ISM image in Figure 70B is calculated

Chapter 5. Multifocal Image Scanning Microscopy using 3D Printed Optics

to be 335 ± 21 nm at FWHM, which is also in-line with a $\sqrt{2}$ improvement. Both datasets show significant improvement to contrast in comparison to both their respective results in Figure 69 and in comparison to the widefield results from section 5.3.3. Though comparable to the results from the widefield mitochondria dataset, these results have significant impact for bio-imaging as this benchmark data suggests that 3D printed optics can be utilised in obtaining super-resolution microscopy results. As ISM offers 2-fold improvements on the diffraction limited-results, it has been shown in this section the benchmarked potential for custom 3D printed lenslet arrays in resolving features beyond the optical diffraction limit.

5.4 Discussion

This chapter has shown the application of 3D printed optics in a particular implementation of super-resolution microscopy. The application of 3D printed lenses in setups for imaging sub-micron biological features shows that the current performance of low-cost desktop 3D printing is beyond what could have been anticipated for low-cost additive manufacturing only 5 years ago. In-house designed and fabricated plastic optics have been shown in this chapter to be capable of delivering the $\sim\sqrt{2}$ resolution improvement through ISM as shown in the resolution improved diffraction-limited beads with 245 ± 9 nm resolution compared to 324 ± 13 nm from the laser-scanned approach. It should be noted that ISM has a comparatively higher tolerance to the impact of in-plane optical aberrations of the sample compared to other super-resolution methods such as more classical 2D SIM, due to the virtual pinholing of the captured fluorescence and the reassignment step. This property makes ISM therefore enormously complimentary to the use of 3D printed optics within the designed optical system, as though extra aberrations may be apparent when using 3D printed spin-coated lenses in imaging, a final image can be constructed with similar quality to a commercial glass lenslet array.

The developed ISM processing Python script was evaluated in terms of the Gaussian Filter standard deviation and pixel ROI around fluorescent signals. This evaluation was performed to both evaluate minimum pixel-windows required to capture fluorescence without removing signal arbitrarily. Additionally, the standard deviation value was investigated to establish results in-line with the current published ISM work featuring maximal $\sqrt{2}$ improvements without deconvolution. Though the code utilises a maxima finding function, this method is not optimised as more rigorous fluorescence excitation examining methods could feature similar results without the requirement of absorptive masks, for example. In the current experimental setup, many things can be improved upon. For example, the next steps of the processing code

Chapter 5. Multifocal Image Scanning Microscopy using 3D Printed Optics

can include a quantitative conversion of the Gaussian filter standard deviation into spatial coordinates, such as a translation of σ into a value 1.5x the image pixel size. Additionally, including a fixed ROI through which fluorescence signals can be found would remove the dependency on the current dynamic maximum intensity pixel locating function which is prone to hot pixels. For the 3D printed optic in particular, the time for datasets to be acquired could also be improved upon by investigating lenslet array-spacing minimisation further. Despite these improvements, the absorptive mask did minimise crosstalk of fluorophores in comparison to the commercial lenslet array and in its custom design also minimised the distance from one excited ROI to another excited ROI through the honeycomb design with 39 ± 0.73 AU in the xy-combined directions compared to the square lattice with 34 ± 0.66 AU

Confirmation that the ISM processing did not arbitrarily remove information to obtain the resolution enhancement was shown in the comparison of BPAE data. The widefield illumination resolved mitochondria better than the diffraction-limited laser-scanned approaches, with mitochondria found to be 376 ± 13 nm in widefield compared to 574 ± 13 nm in the commercial MLA and 446 ± 82 nm in the 3D printed optic due to poor contrast from the scanned imaging setup. As the ISM processed code resolved the mitochondria to a similar scale as the widefield image, with the ISM result being 335 ± 21 nm, the ISM is resolving the structure with similar accuracy to the widefield dataset. As such, the 3D printed optic can be capable of being multiple orders of magnitude lower in cost (without factoring in 3D printing equipment costs) in comparison to the commercial glass optic used, which holds unique potential for custom lenslet arrays within the all-optical implementation of the method, for example, which utilises two MLAs¹¹¹. This outcome opens 3D printed optics up to having the potential of being at the forefront of novel instrument development for biological and biomedical research, as well as offering rapid, low-cost, on the ground diagnostics in healthcare.

Chapter 6. Conclusion

The aim of the work within this thesis was to exemplify the current stage of low-cost desktop 3D printing technology in its application into optical microscopy. This was through the development and characterisation of the designed 3D printed optical components in comparison to commercial equivalent optics, which were possible to be used in the excitation and capture of brightfield and fluorescence information. This final chapter discusses the main results achieved through each of the previous data chapters.

6.1 Research Achievements

An analysis of the current literature in Chapter 2 of 3D printed components showed a current missing link between desktop 3D printed optical components and their application within biological optical microscopy. As such, after detailing the required background in optical microscopy and imaging methods, the low-cost optical 3D printing methods could be developed with the intention of evaluating biological samples in optical and super-resolution microscopy. The results within Chapter 3 characterised the printed and commercial optics using similar methods to those from Chapter 2's literature. Different 3D printing resins and printers were first evaluated to determine the optimal technology and materials at different stages of the PhD. Specific printers and resins were chosen for characterisation based on their release dates in respect of the PhD research timeline. A spin-coating method was developed for optical quality post-processing of the 3D printed parts due to the replicability of the method across multiple planar and non-planar surfaces. The planar surfaces of 3D printed optics were made optically transparent by spin-coating a glass microscope slide with clear resin and combining the planar surface with the microscope slide. By vacuuming bubbles from this combination, the 3D printed surface became optically clear without the influence of bubbles. To quantify this, non-contact methods were used to evaluate the form and roughness of the processed surface using the Veeco White Light Interferometer. The results from this showed sub-wavelength flatness in both form across the measured surface area and in the roughness of the part as well. With this method characterised, non-planar surfaces could then be evaluated for their developed methodologies adherence to commercially similar optics. To create optical clarity in the non-planar surfaces of a 3D printed lens, the staircase effect was smoothed by spin-coating the surface with clear resin. The spin-coating speed required honing for lenses

Chapter 6. Conclusion

with different prescriptions and geometries, which was developed through contact characterisation approaches. The Tencor Alpha-Step stylus profiler was used to obtain 1-dimensional information about the roughness of the lens surface. By inputting the data into a circle-fitting function in MATLAB, the radius of curvature of the lens, closely related to the focal length, can be extracted with comparisons drawn to an ideal circular fit. It was found that by combining this script with the data from the stylus profiler that for a single lens design different radii of curvature could be extracted across changes in the hundreds of RPM spin-speed. This therefore allows each lens geometry to be honed to an optimal spin-speed for the spin-coating post-processing methodology. As the intention of 3D printed optics within this research was finally for super-resolution microscopy integration, a modified manufacturing technique for custom optical quality components had to be developed. This was primarily due to the requirement of an array of custom millimetre-scale lenses which required higher manufacturing resolution than the larger lenses designed previously. As such, at the time of developing this manufacturing method a 3D printed with higher lateral printing resolution (Phrozen Sonic Mini 8K S) became available. This printer allowed the creation of a moulding methodology for the super-resolution microscopy method from Chapter 5.

The moulding method required a master copy to be created, where a lenslet array designed with < 2 mm lenslet diameters was printed. By spin-coating the lenslet array surface with clear resin and UV curing, an optical quality smooth surface was created which was then outgassed and filled with silicone to create a master mould. By creating a master mould, optical elements could be mould manufactured at a fraction of the costs of commercial microlens arrays, with a glass slide placed onto the open surface of the mould to create optical quality flat surfaces. The moulded optic was also then characterised using the same contact and non-contact methods previously, with some mismatch from the design apparent showing further improvements are possible on the manufacturing of custom lenslet arrays. Despite this, the optical components showed surface profiles with promising optical characteristics for optical microscopy. With quantified methods of optical quality 3D printing developed, the manufactured optics themselves required characterisation regarding their wavelength dependant transmissivity. Cuboids of different thicknesses were printed and processed to characterise the two resins used in the post-processing methods (Formlabs Clear and Vida-Rosa transparent resins) transmissivity. The results showed transmissions above 90% for many of the processed components across a range of optical thicknesses and wavelengths. Moulding methods showed better performance for optical transmission compared to the direct printing method due to the volume non-uniformity effects originating from pixel illumination

Chapter 6. Conclusion

inhomogeneities. With the 3D printed optics characterised fully, the parts could therefore be utilised within brightfield and fluorescence imaging of biological samples for the first time, to the authors knowledge, as shown in Chapter 4.

To quantify the observations of biological samples using 3D printed lenses, objectives were designed using Optalix for comparison to commercial optics. By using the direct printing methods of lens manufacture from Chapter 3, 8x and ~50x objectives were made using single or multiple 3D printed lenses in conjunction with one another. The objectives were used for brightfield sample collection as well as in epifluorescence where the 3D printed objectives could be used to both excite and collect fluorescence from a sample. The results of the 3D printed optical elements in brightfield were first characterised by imaging a 1951 USAF target. Contrast values of $95 \pm 2 \%$ were observed from the 8x 3D printed objective and $99 \pm 0.3 \%$ in the commercial 8x implementation. A measure of the resolution was also obtained using the USAF target which was $6 \mu\text{m}$ in the 3D printed 8x objective compared to $4.5 \mu\text{m}$ in the commercial implementation. Additionally, the 8x 3D printed objectives were able to identify sub-cellular biological features in brightfield microscopy by imaging *Hosta* stomata, cyanobacteria and iodine-stained onion cells. The 3D printed optic images featured more aberrations than the commercial optic, though intracellular details were still observable. The cyanobacteria cells morphology were found to be approximately $34 \pm 2 \mu\text{m}$ by $15 \pm 0.8 \mu\text{m}$ in the commercial case and $35 \pm 2 \mu\text{m}$ by $14 \pm 0.6 \mu\text{m}$ in the 3D printed case. Using the ~50x objective the USAF target exemplified $< 2 \mu\text{m}$ resolution values for commercial and 1-3 3D printed lenses substituted into the objective. Additionally, contrast was shown to be similar across objectives including 0, 1 or 2 3D printed lenses with contrast values of $92 \pm 5 \%$, $91 \pm 4 \%$ and $90 \pm 9 \%$ respectively. The 3D printed 4-lens objectives were also capable of showing that sub-cellular details could be obtained from the biological samples, specifically from within the guard cells of the *Hosta* stomata.

For both objective configurations, the fluorescence homogeneity was captured from a uniformly fluorescing slide and showed intensity deviations of 16 % and 18 % from the commercial and 3D printed objectives respectively. For the commercial, single 3D printed and dual 3D printed ~50x objectives, the fluorescence uniformity had 12 %, 10 % and 6 % intensity fluctuations across the $100 \mu\text{m}$ FOV respectively. The resolution for the objectives was obtained using 175 nm fluorescent beads, with FWHM resolution limits of $2.1 \pm 0.15 \mu\text{m}$ and $6.6 \pm 0.86 \mu\text{m}$ were shown for the 8x commercial and 3D printed objectives respectively. For the ~50x objective, resolution limits of $1.23 \pm 0.03 \mu\text{m}$, $1.95 \pm 0.26 \mu\text{m}$, and $2.43 \pm 0.32 \mu\text{m}$

Chapter 6. Conclusion

in the commercial, 3D printed lens #3 and 3D printed lens #3 and #4 cases were observed respectively. When evaluating the *Variiegated Hosta* and cyanobacteria sample in fluorescence, the 8x magnification objective showed blurring of the individual chloroplasts in the 3D printed optic in comparison to the commercial lens, though with the structure of the stomata still discernible. In comparison to brightfield, the size of the cyanobacteria cells were approximately measured to be $33 \pm 2 \mu\text{m}$ by $17 \pm 0.68 \mu\text{m}$ in the commercial 8x objective and $35 \pm 2 \mu\text{m}$ by $20 \pm 0.68 \mu\text{m}$ in the 3D printed 8x objective. The $\sim 50\times$ objective resolved individual fluorescent chloroplasts in the *Hosta* stomata with the 3D printed lens #3 though this was not equally observed when using multiple 3D printed optics in the 4-lens configuration. Despite this, the cyanobacteria sample showed more distinct cells at the higher magnification in the commercial and 3D printed implementations compared to the 8x objective. Chapter 4's resulting data therefore opens the research and applications of 3D printed optics into exciting areas within biology, optical design, and healthcare.

Especially promising is the capability of custom optical design with 3D printed optics within biological microscopy, where Chapter 5 exemplified the current state of low-cost 3D printed lenslet arrays. An ISM processing Python script was created to evaluate the potential for 3D printed optics within super-resolution microscopy. The manufactured lenslets were characterised regarding their illumination spacing in comparison to a commercial microlens array, as well as their illumination homogeneity across the entire lenslet excitation within the image plane. By designing the lenslet arrays into a honeycomb pattern instead of a square pattern, the scan length was able to be ~ 5 AU shorter in one axis. This results in an image difference of ~ 165 images per image in the fully scanned axis, which reduces the number of total images for a complete RAW stack and therefore the time and size of data acquisition. The manufactured optic was also shown to deliver the $\sim\sqrt{2}$ resolution improvement through ISM using diffraction-limited beads with 245 ± 9 nm resolution compared to 324 ± 13 nm from the laser-scanned approach. Of significance are the image scanning microscopy images acquired of mitochondria within a fixed BPAE sample using an optically clear manufactured custom lenslet array. The diffraction-limited mitochondrial structure results of 376 ± 13 nm in widefield concurred with the ISM results of 335 ± 21 nm which therefore holds promise to resolve structures accurately beyond the diffraction limit using a custom designed moulded optic. This result acts as a first-principal marker that super-resolution optical microscopy could be possible using 3D print assisted optics, which therefore holds unique potential to a variety of other optical super-resolution methods.

6.2 Future Work

Through the demonstrated application of 3D printed optics shown in this thesis, there is a clear and vast potential for 3D printed optics integration into multiple different imaging modalities. Directly leading on from this work is the direct follow-on work for the use of 3D printed optics in further image scanning microscopy setups, allowing imaging of sample structures well beyond the diffraction limit. One exciting advancement of this could be within the use of two matched lens arrays to create an all-optical configuration as per iSIM methods, therefore mitigating the computational limitations shown described in Chapter 5 and providing significant speed improvements to the imaging setup compared to the setup shown in Chapter 5. This will exemplify beyond doubt the role of 3D printed optics within biomedical optical imaging, especially in comparison to super-resolution methods that use expensive OEM elements or optical components. Next to this direct follow-on approach, there is a significant possibility for 3D printed custom optics to be integrated into other super-resolution microscopy methods, and with further 3D printer development the quality of the optics themselves hold significant potential within custom optics development. For example, 3D printed optics could be useful for prism manufacturing for total internal reflection fluorescence microscopy to generate evanescent fields, or for half-ball lenses useful for the resolution-enhancing solid-immersion lens imaging technique. And for improved optical sectioning, a 3D printed cylindrical lens can be designed and manufactured for light-sheet applications in the interest of improving a system's axial resolution. Equally, custom lenslet arrays could be manufactured to match the pitch of LED arrays, the issue in optical microscopy of illumination field homogeneity which can be difficult to obtain from LED arrays. Considering the diffractive effects shown in Chapter 4, there is also the potential for this feature from directly printed optics to be leveraged as a benefit within diffractive optic imaging, making the usability of a freeform printed optic of even higher potential. Of key interest is also the area of active optics, where control of the optics geometry and free-form shape potential could be leveraged to manufacture adaptive focal length optical elements, for example. Outside of the direct work includes applications in photon detection, where light simply needs to be detected compared to the higher restrictions of high-quality imaging within microscopy. There are therefore the potential areas of oceanography for 3D printed optic integration in the detection of light emitted from bioluminescent phytoplankton to study species population statistics, as well as within quantum detection technologies and beyond these into space technology. The application of 3D printed optics also has further potential in healthcare, with low-cost imaging methods at the cellular level or above always required. Included in this is the foreseeable

Chapter 6. Conclusion

inclusion of 3D printed optics into low-cost optomechanical microscopy methods, such as the OpenFlexure microscope, to leverage the benefits of custom fully 3D printable systems. Also worth consideration is the creation of new optical design toolboxes due to the significant degrees of freedom in customising a 3D printed optic in contrast to glass manufacturing methods. It can therefore be observed from the work shown within this thesis that 3D printed optical components have only begun to show their vast potential within healthcare and research contexts so far.

References

- [1] Vaidya, N., and Solgaard, O., “3D printed optics with nanometer scale surface roughness,” *Microsystems and Nanoengineering* 4(1), (2018).
- [2] Berglund, G.D., and Tkaczyk, T.S., “Fabrication of optical components using a consumer-grade lithographic printer,” *Optics Express* 27(21), 30405 (2019).
- [3] Hooke, R., [Micrographia, or, Some Physiological Descriptions of Minute Bodies Made by Magnifying Glasses :With Observations and Inquiries Thereupon] (1664).
- [4] Van Leewenhoek, A., [Concerning little Animals by him in Rain- Well- Sea- and Snow water; as also in water wherein Pepper had lain infused] (1675).
- [5] Ramón-Azcón, J., Lopez-Muñoz, G., and Rydosz, A., [Fundamentals] , in *Human Organs-On-a-chip*, Elsevier, 105–135 (2024).
- [6] Wang, G., and Fang, N., [Detecting and tracking nonfluorescent nanoparticle probes in live cells] , 1st ed., in *Methods Enzymol* 504, 1st ed., Elsevier Inc., 83–108 (2012).
- [7] Abbe, E., “Beiträge zur Theorie des Mikroskops und der mikroskopischen Wahrnehmung: II. Die dioptrischen Bedingungen der Leistung des Mikroskops,” *Archiv für mikroskopische Anatomie* 9(1), 418–440 (1873).
- [8] Abbe, E., “The Relation of Aperture and Power in the Microscope,” *Transaction of the Society* 460–473 (1882).
- [9] Rayleigh, Lord, “On the theory of optical images, with special reference to the microscope,” *The London, Edinburgh, and Dublin Philosophical Magazine and Journal of Science* 42(255), 167–195 (1896).
- [10] Airy, G.B., “On the diffraction of an object-glass with circular aperture:,” *Transactions of the Cambridge Philosophical Society* 5, 283–291 (1835).
- [11] Smolyaninov, I.I., “Optical microscopy beyond the diffraction limit,” *HFSP Journal* 2(3), 129–131 (2008).
- [12] Wong, A.M.H., and Eleftheriades, G. V., “An optical super-microscope for far-field, real-time imaging beyond the diffraction limit,” *Scientific Reports* 3, 1–6 (2013).
- [13] Liu, S., and Jang, B., “H-LEACH: A high energy-efficient routing protocol for wireless sensor networks,” *Far East Journal of Electronics and Communications* 13(2), 99–106 (2014).
- [14] Palounek, D., Vala, M., Bujak, Ł., Kopal, I., Jiříková, K., Shaidiuk, Y., and Piliarik, M., “Surpassing the Diffraction Limit in Label-Free Optical Microscopy,” *ACS Photonics* (2024).
- [15] Lew, M., Lew*, M.D., von Diezmann*, A.R.S., and Moerner, W.E., “Easy-DHPSF open-source software for three-dimensional localization of single molecules with precision beyond the optical diffraction limit,” *Protocol Exchange* 1–18 (2013).
- [16] Moerner, W.E., “Microscopy beyond the diffraction limit using actively controlled single molecules,” *Journal of Microscopy* 246(3), 213–220 (2012).
- [17] Tinning, P.W., Franssen, A.J.P.M., Hridi, S.U., Bushell, T.J., and McConnell,

References

- G., "A 340/380 nm light-emitting diode illuminator for Fura-2 AM ratiometric Ca²⁺ imaging of live cells with better than 5 nM precision," *Journal of Microscopy* 269(3), 212–220 (2018).
- [18] Veledar, O., Byrne, P.O., Danaher, S., Allen, J.I.H., Thompson, L.F., and McMillan, J.E., "Simple techniques for generating nanosecond blue light pulses from light emitting diodes," *Measurement Science and Technology* 18(1), 131–137 (2007).
- [19] Tapley, A., Switz, N., Reber, C., Davis, J.L., Miller, C., Matovu, J.B., Worodria, W., Huang, L., Fletcher, D.A., et al., "Mobile digital fluorescence microscopy for diagnosis of tuberculosis," *Journal of Clinical Microbiology* 51(6), 1774–1778 (2013).
- [20] Hart, S.J., and JiJi, R.D., "Light emitting diode excitation emission matrix fluorescence spectroscopy," *Analyst* 127(12), 1693–1699 (2002).
- [21] Beach, J.M., "A LED light calibration source for dual-wavelength microscopy," *Cell Calcium* 21(1), 63–68 (1997).
- [22] Tinning, P., Donnachie, M., Christopher, J., Uttamchandani, D., and Bauer, R., "Miniaturized structured illumination microscopy using two 3-axis MEMS micromirrors," *Biomedical Optics Express* 13(12), 6443 (2022).
- [23] Christopher, J.L., Tinning, P.W., Uttamchandani, D., and Bauer, R., "3D printing optical components for microscopy using a desktop 3D printer," *Proceedings Volume 12013, MOEMS and Miniaturized Systems XXI; 120130F22* (2022).
- [24] Strathman, M., Liu, Y., Li, X., and Lin, L.Y., "Dynamic focus-tracking MEMS scanning micromirror with low actuation voltages for endoscopic imaging," *Optics Express* 21(20), 23934 (2013).
- [25] Qi, B., Himmer, A.P., Gordon, L.M., Yang, X.D.V., Dickensheets, L.D., and Vitkin, I.A., "Dynamic focus control in high-speed optical coherence tomography based on a microelectromechanical mirror," *Optics Communications* 232(1–6), 123–128 (2004).
- [26] Carlson, K., Shin, H.J., Ra, H., Lee, D., Solgaard, O., and Richards-Kortum, R., "Single fiber confocal microscope using a two-axis microscanner for cellular imaging," *Conference on Lasers and Electro-Optics and 2006 Quantum Electronics and Laser Science Conference, CLEO/QELS 2006* 14(19), 275–277 (2006).
- [27] Jung, W., McCormick, D.T., Zhang, J., Wang, L., Tien, N.C., and Chen, Z., "Three-dimensional endoscopic optical coherence tomography by use of a two-axis microelectromechanical scanning mirror," *Applied Physics Letters* 88(16), (2006).
- [28] Singh, J., Teo, J.H.S., Xu, Y., Premachandran, C.S., Chen, N., Kotlanka, R., Olivo, M., and Sheppard, C.J.R., "A two axes scanning SOI MEMS micromirror for endoscopic bioimaging," *Journal of Micromechanics and Microengineering* 18(2), (2008).
- [29] Liu, J.T.C., Mandella, M.J., Ra, H., Wong, L.K., Solgaard, O., Kino, G.S., Piyawattanametha, W., Contag, C.H., and Wang, T.D., "Miniature near-infrared dual-axes confocal microscope utilizing a two-dimensional

References

- microelectromechanical systems scanner,” *Optics Letters* 32(3), 256 (2007).
- [30] Wang, T.D., Mandella, M.J., Contag, C.H., and Kino, G.S., “Dual-axis confocal microscope for high-resolution in vivo imaging,” *Optics Letters* 28(6), 414 (2003).
- [31] Chen, S.-L., Xie, Z., Ling, T., Jay Guo, L., Wei, X., and Wang, X., “Miniaturized all-optical photoacoustic microscopy based on microelectromechanical systems mirror scanning,” *Optics Letters* 37(20), 4263 (2012).
- [32] Liu, T., Rajadhyaksha, M., and Dickensheets, D.L., “MEMS-in-the-lens architecture for a miniature high-NA laser scanning microscope,” *Light: Science and Applications* 8(1), (2019).
- [33] Ra, H., Piyawattanametha, W., Taguchi, Y., Lee, D., Mandella, M.J., and Solgaard, O., “Two-dimensional MEMS scanner for dual-axes confocal microscopy,” *Journal of Microelectromechanical Systems* 16(4), 969–976 (2007).
- [34] Arrasmith, C.L., Dickensheets, D.L., and Mahadevan-Jansen, A., “MEMS-based handheld confocal microscope for in-vivo skin imaging,” *Optics Express* 18(4), 3805 (2010).
- [35] Liu, L., Wang, E., Zhang, X., Liang, W., Li, X., and Xie, H., “MEMS-based 3D confocal scanning microendoscope using MEMS scanners for both lateral and axial scan,” *Sensors and Actuators, A: Physical* 215, 89–95 (2014).
- [36] Piyawattanametha, W., Ra, H., Mandella, M.J., Loewke, K., Wang, T.D., Kino, G.S., Solgaard, O., and Contag, C.H., “3-D near-infrared fluorescence imaging using an MEMS-based miniature dual-axis confocal microscope,” *IEEE Journal on Selected Topics in Quantum Electronics* 15(5), 1344–1350 (2009).
- [37] Piyawattanametha, W., Ra, H., Loewke, K.E., Mandella, M.J., Contag, C.H., Qiu, Z., Wang, T.D., Friedland, S., Liu, J.T., et al., “In vivo near-infrared dual-axis confocal microendoscopy in the human lower gastrointestinal tract,” *Journal of Biomedical Optics* 17(02), 1 (2012).
- [38] Kim, K.H., Park, B.H., Maguluri, G.N., Lee, T.W., Rogomentich, F.J., Bancu, M.G., Bouma, B.E., de Boer, J.F., and Bernstein, J.J., “Two-axis magnetically-driven MEMS scanning catheter for endoscopic high-speed optical coherence tomography,” *Optics Express* 15(26), 18130 (2007).
- [39] Strathman, M., Liu, Y., Keeler, E.G., Song, M., Baran, U., Xi, J., Sun, M.-T., Wang, R., Li, X., et al., “MEMS scanning micromirror for optical coherence tomography,” *Biomedical Optics Express* 6(1), 211 (2015).
- [40] Jung, W., Zhang, J., Wang, L., Wilder-Smith, P., Chen, Z., McCormick, D.T., and Tien, N.C., “Three-dimensional optical coherence tomography employing a 2-axis microelectromechanical scanning mirror,” *IEEE Journal on Selected Topics in Quantum Electronics* 11(4), 806–809 (2005).
- [41] Aguirre, A.D., Hertz, P.R., Chen, Y., Fujimoto, J.G., Piyawattanametha, W., Fan, L., and Wu, M.C., “Two-axis MEMS Scanning Catheter for Ultrahigh Resolution Three-dimensional and En Face Imaging,” *Optics Express* 15(5), 2445 (2007).
- [42] Piyawattanametha, W., Barretto, R.P.J., Ko, T.H., Flusberg, B.A., Cocker,

References

- E.D., Ra, H., Lee, D., Solgaard, O., and Schnitzer, M.J., “Fast-scanning two-photon fluorescence imaging based on a microelectromechanical systems two-dimensional scanning mirror,” *Optics Letters* 31(13), 2018 (2006).
- [43] Millett-sikking, A., Dean, K.M., Fiolka, R., Fardad, A., Whitehead, L., and York, G., “High NA single-objective light-sheet,” [10.5281/zenodo.3244420](https://doi.org/10.5281/zenodo.3244420).
- [44] Bishop, K.W., Glaser, A.K., and Liu, J.T.C., “Performance tradeoffs for single- and dual-objective open-top light-sheet microscope designs: a simulation-based analysis,” *Biomedical Optics Express* 11(8), 4627 (2020).
- [45] Betzig, E., Patterson, G.H., Sougrat, R., Lindwasser, O.W., Olenych, S., Bonifacino, J.S., Davidson, M.W., Lippincott-Schwartz, J., and Hess, H.F., “Imaging intracellular fluorescent proteins at nanometer resolution,” *Science* 313(5793), 1642–1645 (2006).
- [46] Biteen, J., Thompson, M., Tselentis, N. et al., “Super-resolution imaging in live *Caulobacter crescentus* cells using photoswitchable EYFP,” *Nat Methods* 5, 947–949 (2008).
- [47] Hess, S.T., Girirajan, T.P.K., and Mason, M.D., “Ultra-high resolution imaging by fluorescence photoactivation localization microscopy,” *Biophysical Journal* 91(11), 4258–4272 (2006).
- [48] Rust, M., Bates, M. & Zhuang, X., “Sub-diffraction-limit imaging by stochastic optical reconstruction microscopy (STORM),” *Nat Methods* 3, 793–796 (2006).
- [49] Heilemann, M., Van de Linde, S., Schuttpelz, M., Kasper, R., Seefeldt, B., Mukherjee, A., Tinnefeld, P., and Sauer, M., “Subdiffraction-Resolution Fluorescence Imaging with Conventional Fluorescent Probes,” *Angew. Chem. Int. Ed.* 2008, 47, 6172–6176.
- [50] Ober, R.J., Ram, S., and Ward, E.S., “Localization Accuracy in Single-Molecule Microscopy,” *Biophysical Journal* 86(2), 1185–1200 (2004).
- [51] Wombacher, R., Heidbreder, M., van de Linde, S. et al., “Live-cell super-resolution imaging with trimethoprim conjugates,” *Nat Methods* 7, 717–719 (2010).
- [52] Siddig, S., Aufmkolk, S., Doose, S., Jobin, M.L., Werner, C., Sauer, M., and Calebiro, D., “Super-resolution imaging reveals the nanoscale organization of metabotropic glutamate receptors at presynaptic active zones,” *Science Advances* 6(16), 1–12 (2020).
- [53] Sharonov, A., and Hochstrasser, R.M., “Wide-field subdiffraction imaging by accumulated binding of diffusing probes,” *Proceedings of the National Academy of Sciences of the United States of America* 103(50), 18911–18916 (2006).
- [54] Schnitzbauer, J., Strauss, M.T., Schlichthaerle, T., Schueder, F., and Jungmann, R., “Super-resolution microscopy with DNA-PAINT,” *Nature Protocols* 12(6), 1198–1228 (2017).
- [55] Mashanov, G.I., Tacon, D., Knight, A.E., Peckham, M., and Molloy, J.E., “Visualizing single molecules inside living cells using total internal reflection fluorescence microscopy,” *Methods* 29(2), 142–152 (2003).
- [56] Tokunaga, M., Imamoto, N. & Sakata-Sogawa, K., “Highly inclined thin

References

- illumination enables clear single-molecule imaging in cells.," *Nat Methods* 5, 159–161 (2008).
- [57] Lin, Y., Long, J.J., Huang, F., Duim, W.C., Kirschbaum, S., Zhang, Y., Schroeder, L.K., Rebane, A.A., Velasco, M.G.M., et al., "Quantifying and optimizing single-molecule switching nanoscopy at high speeds," *PLoS ONE* 10(5), 1–20 (2015).
- [58] Filius, M., Cui, T.J., Ananth, A.N., Docter, M.W., Hegge, J.W., Van Der Oost, J., and Joo, C., "High-Speed Super-Resolution Imaging Using Protein-Assisted DNA-PAINT," *Nano Letters* 20(4), 2264–2270 (2020).
- [59] Schueder, F., Stein, J., Stehr, F., Auer, A., Sperl, B., Strauss, M.T., Schwille, P., and Jungmann, R., "An order of magnitude faster DNA-PAINT imaging by optimized sequence design and buffer conditions," *Nature Methods* 16(11), 1101–1104 (2019).
- [60] Lee, J., Park, S., and Hohng, S., "Accelerated FRET-PAINT microscopy," *Molecular Brain* 11(1), 3–9 (2018).
- [61] Auer, A., Strauss, M.T., Schlichthaerle, T., and Jungmann, R., "Fast, Background-Free DNA-PAINT Imaging Using FRET-Based Probes," *Nano Letters* 17(10), 6428–6434 (2017).
- [62] Barentine, A.E.S., Lin, Y., Courvan, E.M., Kidd, P., Liu, M., Balduf, L., Phan, T., Rivera-Molina, F., Grace, M.R., et al., "An integrated platform for high-throughput nanoscopy," *Nature Biotechnology* 41(11), 1549–1556 (2023).
- [63] Heintzmann, R., and Huser, T., "Super-Resolution Structured Illumination Microscopy," *Chemical Reviews* 117(23), 13890–13908 (2017).
- [64] Markwirth, A., Lachetta, M., Mönkemöller, V., Heintzmann, R., Hübner, W., Huser, T., and Müller, M., "Video-rate multi-color structured illumination microscopy with simultaneous real-time reconstruction," *Nature Communications* 10(1), 1–11 (2019).
- [65] Hell, S.W., and Wichmann, J., "Breaking the diffraction resolution limit by stimulated emission: stimulated-emission-depletion fluorescence microscopy," *Optics Letters* 19(11), 780 (1994).
- [66] Hell, S., Willig, K., and Dyba, M., "Nanoscale resolution with focused light: STED and other RESOLFT microscopy concepts," *Handbook of Biological Confocal Microscopy*(May 2015), 571–579 (2006).
- [67] Keller, J., Schönle, A., and Hell, S.W., "Efficient fluorescence inhibition patterns for RESOLFT microscopy," *Optics Express* 15(6), 3361 (2007).
- [68] Schwentker, M.A. et al., "Wide-field subdiffraction RESOLFT microscopy using fluorescent protein," *Microsc. Res. Tech.*, 70: 269-280. (2007).
- [69] Waldchen, S., Lehmann, J., Klein, T., Van De Linde, S., and Sauer, M., "Light-induced cell damage in live-cell super-resolution microscopy," *Scientific Reports* 5, 1–12 (2015).
- [70] Strack, R., "Imaging: Death by super-resolution imaging," *Nature Methods* 12(12), 1111 (2015).
- [71] Laissue, P.P., Alghamdi, R.A., Tomancak, P., Reynaud, E.G., and Shroff, H., "Assessing phototoxicity in live fluorescence imaging," *Nature Methods* 14(7), 657–661 (2017).

References

- [72] Lukinavičius, G., Blaukopf, C., Pershagen, E., Schena, A., Reymond, L., Derivery, E., Gonzalez-Gaitan, M., D'Este, E., Hell, S.W., et al., "SiR-Hoechst is a far-red DNA stain for live-cell nanoscopy," *Nature Communications* 6, 1–7 (2015).
- [73] Hein, B., Willig, K.I., and Hell, S.W., "Stimulated emission depletion (STED) nanoscopy of a fluorescent protein-labeled organelle inside a living cell," *Proceedings of the National Academy of Sciences of the United States of America* 105(38), 14271–14276 (2008).
- [74] Lukinavičius, G., Umezawa, K., Olivier, N., Honigmann, A., Yang, G., Plass, T., Mueller, V., Reymond, L., Corrêa, I.R., et al., "A near-infrared fluorophore for live-cell super-resolution microscopy of cellular proteins," *Nature Chemistry* 5(2), 132–139 (2013).
- [75] Schermelleh, L., Heintzmann, R., and Leonhardt, H., "A guide to super-resolution fluorescence microscopy," *Journal of Cell Biology* 190(2), 165–175 (2010).
- [76] Lukinavičius, G., Reymond, L., D'Este, E. et al., "Fluorogenic probes for live-cell imaging of the cytoskeleton," *Nat Methods* 11, 731–733 (2104).
- [77] Butkevich, A. et al., "Fluorescent Rhodamines and Fluorogenic Carbopyronines for Super-Resolution STED," *Angew.Chem.Int. Ed.* 2016, 55,3290 –3294 (2016).
- [78] Reuss, M., Engelhardt, J., and Hell, S.W., "Birefringent device converts a standard scanning microscope into a STED microscope that also maps molecular orientation," *Optics Express* 18(2), 1049 (2010).
- [79] Yan, L., Gregg, P., Karimi, E., Rubano, A., Marrucci, L., Boyd, R., and Ramachandran, S., "Q-plate enabled spectrally diverse orbital-angular-momentum conversion for stimulated emission depletion microscopy," *Optica* 2(10), 900 (2015).
- [80] Gould, T.J., Kromann, E.B., Burke, D., Booth, M.J., and Bewersdorf, J., "Auto-aligning stimulated emission depletion microscope using adaptive optics," *Optics Letters* 38(11), 1860 (2013).
- [81] Rankin, B.R., Kellner, R.R., and Hell, S.W., "Stimulated-emission-depletion microscopy with a multicolor stimulated-Raman-scattering light source," *Optics Letters* 33(21), 2491 (2008).
- [82] Göttfert, F., Wurm, C.A., Mueller, V., Berning, S., Cordes, V.C., Honigmann, A., and Hell, S.W., "Coaligned dual-channel STED nanoscopy and molecular diffusion analysis at 20 nm resolution," *Biophysical Journal* 105(1), 6–8 (2013).
- [83] Bottanelli, F., Kromann, E.B., Allgeyer, E.S., Erdmann, R.S., Baguley, S.W., Sirinakis, G., Schepartz, A., Baddeley, D., Toomre, D.K., et al., "Two-colour live-cell nanoscale imaging of intracellular targets," *Nature Communications* 7(May 2015), 1–5 (2016).
- [84] Vicidomini, G., Schönle, A., Ta, H., Han, K.Y., Moneron, G., Eggeling, C., and Hell, S.W., "STED Nanoscopy with Time-Gated Detection: Theoretical and Experimental Aspects," *PLoS ONE* 8(1), (2013).
- [85] Westphal, V., Blanca, C.M., Dyba, M., Kastrup, L., and Hell, S.W., "Laser-

References

- diode-stimulated emission depletion microscopy,” *Applied Physics Letters* 82(18), 3125–3127 (2003).
- [86] Vicidomini, G., Moneron, G., Han, K. et al., “Sharper low-power STED nanoscopy by time gating,” *Nat Methods* 8, 571–573 (2011).
- [87] Staudt, T., Engler, A., Rittweger, E., Harke, B., Engelhardt, J., and Hell, S.W., “Far-field optical nanoscopy with reduced number of state transition cycles,” *Optics Express* 19(6), 5644 (2011).
- [88] Göttfert, F., Pleiner, T., Heine, J., Westphal, V., Görlich, D., Sahl, S.J., and Hell, S.W., “Strong signal increase in STED fluorescence microscopy by imaging regions of subdiffraction extent,” *Proceedings of the National Academy of Sciences of the United States of America* 114(9), 2125–2130 (2017).
- [89] Heine, J., Reuss, M., Harke, B., D’Este, E., Sahl, S.J., and Hell, S.W., “Adaptive-illumination STED nanoscopy,” *Proceedings of the National Academy of Sciences of the United States of America* 114(37), 9797–9802 (2017).
- [90] Gonzalez Pisfil, M., Nadelson, I., Bergner, B., Rottmeier, S., Thoma, A.W., and Dietzel, S., “Stimulated emission depletion microscopy with a single depletion laser using five fluorochromes and fluorescence lifetime phasor separation,” *Scientific Reports* 12(1), 1–15 (2022).
- [91] Gustafsson, M.G.L., Agard, D.A., and Sedat, J.W., “I5M: 3D widefield light microscopy with better than 100 nm axial resolution,” *Journal of Microscopy* 195(1), 10–16 (1999).
- [92] Gustafsson, M.G.L., “Surpassing the lateral resolution limit by a factor of two using structured illumination microscopy,” *Journal of Microscopy* 198(2), 82–87 (2000).
- [93] Gustafsson, M.G., “Extended resolution fluorescence microscopy,” *Current Opinion in Structural Biology* 9(5), 627–628 (1999).
- [94] Lukosz, W., and Marchand, M., “Optischen Abbildung Unter Überschreitung der Beugungsbedingten Auflösungsgrenze,” *Optica Acta: International Journal of Optics* 10(3), 241–255 (1963).
- [95] Shao, L., Isaac, B., Uzawa, S., Agard, D.A., Sedat, J.W., and Gustafsson, M.G.L., “I5S: Wide-field light microscopy with 100-nm-scale resolution in three dimensions,” *Biophysical Journal* 94(12), 4971–4983 (2008).
- [96] Gustafsson, M.G.L., Shao, L., Carlton, P.M., Wang, C.J.R., Golubovskaya, I.N., Cande, W.Z., Agard, D.A., and Sedat, J.W., “Three-dimensional resolution doubling in wide-field fluorescence microscopy by structured illumination,” *Biophysical Journal* 94(12), 4957–4970 (2008).
- [97] Rego, E.H., Shao, L., Macklin, J.J., Winoto, L., Johansson, G.A., Kamps-Hughes, N., Davidson, M.W., and Gustafsson, M.G.L., “Nonlinear structured-illumination microscopy with a photoswitchable protein reveals cellular structures at 50-nm resolution,” *Proceedings of the National Academy of Sciences of the United States of America* 109(3), (2012).
- [98] Gustafsson, M.G.L., “Nonlinear structured-illumination microscopy: Wide-field fluorescence imaging with theoretically unlimited resolution,”

References

- Proceedings of the National Academy of Sciences of the United States of America 102(37), 13081–13086 (2005).
- [99] Heintzmann, R., Jovin, T.M., and Cremer, C., “Saturated patterned excitation microscopy—a concept for optical resolution improvement,” *Journal of the Optical Society of America A* 19(8), 1599 (2002).
- [100] Wei, F., and Liu, Z., “Plasmonic structured illumination microscopy,” *Nano Letters* 10(7), 2531–2536 (2010).
- [101] Li, D., Shao, L., Chen, B.C., Zhang, X., Zhang, M., Moses, B., Milkie, D.E., Beach, J.R., Hammer, J.A., et al., “Extended-resolution structured illumination imaging of endocytic and cytoskeletal dynamics,” *Science* 349(6251), (2015).
- [102] Müller, C.B., and Enderlein, J., “Image scanning microscopy,” *Physical Review Letters* 104(19), 1–4 (2010).
- [103] Sheppard, C.J.R., “Super-resolution in confocal imaging,” *Optik (Jena)* 80(2), 53–54 (1988).
- [104] Sheppard, C.J.R., Castello, M., Tortarolo, G., Vicidomini, G., and Diaspro, A., “Image formation in image scanning microscopy, including the case of two-photon excitation,” *Journal of the Optical Society of America A* 34(8), 1339 (2017).
- [105] Bertero, M., and Pike, E.R., “Resolution in diffraction-limited imaging, a singular value analysis i. The case of coherent illumination,” *Optica Acta* 29(6), 727–746 (1982).
- [106] Gregor, I., and Enderlein, J., “Image scanning microscopy,” *Current Opinion in Chemical Biology* 51, 74–83 (2019).
- [107] Castello, M., Sheppard, C.J.R., Diaspro, A., and Vicidomini, G., “Image scanning microscopy with a quadrant detector,” *Optics Letters* 40(22), 5355 (2015).
- [108] Koho, S. V., Slenders, E., Tortarolo, G., Castello, M., Buttafava, M., Villa, F., Tcarenkova, E., Ameloot, M., Bianchini, P., et al., “Two-photon image-scanning microscopy with SPAD array and blind image reconstruction,” *Biomedical Optics Express* 11(6), 2905 (2020).
- [109] Schulz, O., Pieper, C., Clever, M., Pfaff, J., Ruhlandt, A., Kehlenbach, R.H., Wouters, F.S., Großhans, J., Bunt, G., et al., “Resolution doubling in fluorescence microscopy with confocal spinning-disk image scanning microscopy,” *Proceedings of the National Academy of Sciences of the United States of America* 110(52), 21000–21005 (2013).
- [110] York, A.G. et al., Parekh, S.H., Dalle Nogare, D., Fischer, R.S., Temprine, K., Mione, M., Chitnis, A.B., Combs, C.A., and Shroff, H., “Resolution doubling in live, multicellular organisms via multifocal structured illumination microscopy,” *Articles nAture methods |* 9(7), 749 (2012).
- [111] York, A., Chandris, P., and Nogare, D. et al., “Instant super-resolution imaging in live cells and embryos via analog image processing,” *Nat Methods* 10, 1122–1126 (2013).
- [112] Ingaramo, M., York, A.G., Wawrzusin, P., Milberg, O., Hong, A., Weigert, R., Shroff, H., and Patterson, G.H., “Two-photon excitation improves multifocal

References

- structured illumination microscopy in thick scattering tissue,” *Proceedings of the National Academy of Sciences of the United States of America* 111(14), 5254–5259 (2014).
- [113] Gregor, I., Spiecker, M., Petrovsky, R., Großhans, J., Ros, R., and Enderlein, J., “Rapid nonlinear image scanning microscopy,” *Nature Methods* 14(11), 1087–1089 (2017).
- [114] Zang, O.M.E.R.T., Eldkhun, D.A.N.F., Grawal, A.N.A., and Esacher, A.L.J., “Two-photon PSF-engineered image scanning microscopy” 44(4), 3–6 (2019).
- [115] De Luca, G.M.R., Breedijk, R.M.P., Brandt, R.A.J., Zeelenberg, C.H.C., de Jong, B.E., Timmermans, W., Azar, L.N., Hoebe, R.A., Stallinga, S., et al., “Rescan confocal microscopy: scanning twice for better resolution,” *Biomedical Optics Express* 4(11), 2644 (2013).
- [116] Breedijk, R.M.P., Wen, J., Krishnaswami, V., Bernas, T., Manders, E.M.M., Setlow, P., Vischer, N.O.E., and Brul, S., “A live-cell super-resolution technique demonstrated by imaging germinosomes in wild-type bacterial spores,” *Scientific Reports* 10(1), 1–12 (2020).
- [117] Roth, S., Sheppard, C.J.R., and Heintzmann, R., “Superconcentration of light: circumventing the classical limit to achievable irradiance,” *Optics Letters* 41(9), 2109 (2016).
- [118] Velu, R., Calais, T., Jayakumar, A., and Raspall, F., “A comprehensive review on bio-nanomaterials for medical implants and feasibility studies on fabrication of such implants by additive manufacturing technique,” *Materials* 13(1), 92 (2020).
- [119] Chen, Q., Mangadlao, J.D., Wallat, J., De Leon, A., Pokorski, J.K., and Advincula, R.C., “3D printing biocompatible polyurethane/poly(lactic acid)/graphene oxide nanocomposites: Anisotropic properties,” *ACS Applied Materials and Interfaces* 9(4), 4015–4023 (2017).
- [120] Auricchio, F., and Marconi, S., “3D printing: Clinical applications in orthopaedics and traumatology,” *EFORT Open Reviews* 1(5), 121–127 (2016).
- [121] Chae, M.P., Rozen, W.M., McMenamin, P.G., Findlay, M.W., Spychal, R.T., and Hunter-Smith, D.J., “Emerging Applications of Bedside 3D Printing in Plastic Surgery,” *Frontiers in Surgery* 2(June), 1–14 (2015).
- [122] Cornejo, J., Cornejo-Aguilar, J.A., Vargas, M., Helguero, C.G., Milanezi De Andrade, R., Torres-Montoya, S., Asensio-Salazar, J., Rivero Calle, A., Martínez Santos, J., et al., “Anatomical Engineering and 3D Printing for Surgery and Medical Devices: International Review and Future Exponential Innovations,” *BioMed Research International* 2022, (2022).
- [123] Manapat, J.Z., Chen, Q., Ye, P., and Advincula, R.C., “3D Printing of Polymer Nanocomposites via Stereolithography,” *Macromolecular Materials and Engineering* 302(9), 1–13 (2017).
- [124] Giannatsis, J., and Dedoussis, V., “Decision support tool for selecting fabrication parameters in stereolithography,” *International Journal of Advanced Manufacturing Technology* 33(7–8), 706–718 (2007).
- [125] Lan, P.T., Chou, S.Y., Chen, L.L., and Gemmill, D., “Determining fabrication orientations for rapid prototyping with stereolithography apparatus,” *CAD*

References

- Computer Aided Design 29(1), 53–62 (1997).
- [126] Huang, Y.M., Kuriyama, S., and Jiang, C.P., “Fundamental study and theoretical analysis in a constrained-surface stereolithography system,” *International Journal of Advanced Manufacturing Technology* 24(5–6), 361–369 (2004).
- [127] Pham, D.T., and Ji, C., “A study of recoating in stereolithography,” *Proceedings of the Institution of Mechanical Engineers, Part C: Journal of Mechanical Engineering Science* 217(1), 105–118 (2003).
- [128] Pham, D.T., Dimov, S.S., and Gault, R.S., “Part orientation in stereolithography,” *International Journal of Advanced Manufacturing Technology* 15(9), 674–682 (1999).
- [129] Chockalingam, K., Jawahar, N., Chandrasekar, U., and Ramanathan, K.N., “Establishment of process model for part strength in stereolithography,” *Journal of Materials Processing Technology* 208(1–3), 348–365 (2008).
- [130] Maruo, S., Ikuta, K., and Korogi, H., “Remote light-driven micromachines fabricated by 200 nm microstereolithography,” *Proceedings of the IEEE Conference on Nanotechnology 2001-Janua*, 507–512 (2001).
- [131] Bertsch, A., Jézéquel, J.Y., and André, J.C., “Study of the spatial resolution of a new 3D microfabrication process: The microstereophotolithography using a dynamic mask-generator technique,” *Journal of Photochemistry and Photobiology A: Chemistry* 107(1–3), 275–281 (1997).
- [132] Takagi, T., and Nakajim, N., “Photoforming Applied to Fine Forming,” *Transactions of the Japan Society of Mechanical Engineers Series C* 59(560), 1255–1260 (1993).
- [133] Yoshimoto, T., Miyaki, I., Yaze, H., Maruka, Y., Ri, N., Teramoto, T., Morohoshi, K., and Koyagi, Y., “Micro-stereo-lithography system,” *Emerging Lithographic Technologies X* 6151(2006), 61513I (2006).
- [134] Microstereolithography, H.T., “Light-Driven Mems Made By,” *Technical Digest. MEMS 2001. 14th IEEE International Conference on Micro Electro Mechanical Systems (Cat. No.01CH37090)* 594–597 (2001).
- [135] Ikuta, K., and Hirowatari, K., “Real three dimensional micro fabrication using stereo lithography and metal molding,” *IEEE Micro Electro Mechanical Systems* 42–47 (1993).
- [136] Schmidt, J., Altun, A.A., Schwentenwein, M., and Colombo, P., “Complex mullite structures fabricated via digital light processing of a preceramic polysiloxane with active alumina fillers,” *Journal of the European Ceramic Society* 39(4), 1336–1343 (2019).
- [137] Hornbeck, L.J., Incorporated, T.I., and Box, P.O., “Digital Light Processing1M for High-Brightness, High-Resolution Applications,” *SPIE Vol. 3013 • 0277-786X/97/\$10.00* 3013, 27–40.
- [138] Liu, Z., Liang, H., Shi, T., Xie, D., Chen, R., Han, X., Shen, L., Wang, C., and Tian, Z., “Additive manufacturing of hydroxyapatite bone scaffolds via digital light processing and in vitro compatibility,” *Ceramics International* 45(8), 11079–11086 (2019).
- [139] Huang, R.J., Jiang, Q.G., Wu, H.D., Li, Y.H., Liu, W.Y., Lu, X.X., and Wu,

References

- S.H., "Fabrication of complex shaped ceramic parts with surface-oxidized Si₃N₄ powder via digital light processing based stereolithography method," *Ceramics International* 45(4), 5158–5162 (2019).
- [140] He, R., Liu, W., Wu, Z., An, D., Huang, M., Wu, H., Jiang, Q., Ji, X., Wu, S., et al., "Fabrication of complex-shaped zirconia ceramic parts via a DLP-stereolithography-based 3D printing method," *Ceramics International* 44(3), 3412–3416 (2018).
- [141] Reinhardt, C., Passinger, S., Chichkov, B.N., Marquart, C., Radko, I.P., and Bozhevolnyi, S.I., "Laser-fabricated dielectric optical components for surface plasmon polaritons," *Optics Letters* 31(9), 1307 (2006).
- [142] Doraiswamy, A., Jin, C., Narayan, R.J., Mageswaran, P., Mente, P., Modi, R., Auyeung, R., Chrisey, D.B., Ovsianikov, A., et al., "Two photon induced polymerization of organic-inorganic hybrid biomaterials for microstructured medical devices," *Acta Biomaterialia* 2(3), 267–275 (2006).
- [143] Sun, H.-B., Kawakami, T., Xu, Y., Ye, J.-Y., Matuso, S., Misawa, H., Miwa, M., and Kaneko, R., "Real three-dimensional microstructures fabricated by photopolymerization of resins through two-photon absorption," *Optics Letters* 25(15), 1110 (2000).
- [144] Maruo, S., Nakamura, O., and Kawata, S., "Three-dimensional microfabrication with two-photon-absorbed photopolymerization," *OPTICS LETTERS / Vol. 22, No. 2* 22(2), 132–134 (1997).
- [145] Yokoyama, S., Nakahama, T., Miki, H., and Mashiko, S., "Two-photon-induced polymerization in a laser gain medium for optical microstructure," *Applied Physics Letters* 82(19), 3221–3223 (2003).
- [146] Watanabe, T. et al., "Photoresponsive Hydrogel Microstructure Fabricated by Two-Photon Initiated Polymerization," *Adv. Funct. Mater.* 2002, 12, No. 9, September (2002).
- [147] Cumpston, B.H., Ananthavel, S.P., Barlow, S., Dyer, D.L., Ehrlich, J.E., Erskine, L.L., Heikal, A.A., Kuebler, S.M., Lee, I.S., et al., "Two-photon polymerization initiators for three-dimensional optical data storage and microfabrication," *NATURE* 398(March), 51–54 (1999).
- [148] Wu, S., Serbin, J., and Gu, M., "Two-photon polymerisation for three-dimensional micro-fabrication," *Journal of Photochemistry and Photobiology A: Chemistry* 181(1), 1–11 (2006).
- [149] He, X., Li, T., Zhang, J., and Wang, Z., "STED direct laser writing of 45 nm Width Nanowire," *Micromachines* 10(11), (2019).
- [150] Juodkasis, S., Mizeikis, V., Seet, K.K., Miwa, M., and Misawa, H., "Two-photon lithography of nanorods in SU-8 photoresist," *Nanotechnology* 16(6), 846–849 (2005).
- [151] Gan, Z., Cao, Y., Evans, R.A., and Gu, M., "Three-dimensional deep sub-diffraction optical beam lithography with 9 nm feature size," *Nature Communications* 4(May), 1–7 (2013).
- [152] Zhang, L., Wang, C., Zhang, C., Xue, Y., Ye, Z., Xu, L., Hu, Y., Li, J., Chu, J., et al., "High-Throughput Two-Photon 3D Printing Enabled by Holographic Multi-Foci High-Speed Scanning," *Nano Letters* 24(8), 2671–2679 (2024).

References

- [153] Pisanello, M., Zheng, D., Balena, A., Pisano, F., De Vittorio, M., and Pisanello, F., “An open source three-mirror laser scanning holographic two-photon lithography system,” *PLoS ONE* 17(4 April), 1–13 (2022).
- [154] Balena, A., Bianco, M., Pisanello, F., and De Vittorio, M., “Recent Advances on High-Speed and Holographic Two-Photon Direct Laser Writing,” *Adv. Funct. Mater.* 2023, 33, 2211773 (2023).
- [155] Chagas, A.M., Prieto-Godina, L.L., Arrenberg, A.B., and Baden, T., “The €100 lab: A 3D-printable open-source platform for fluorescence microscopy, optogenetics, and accurate temperature control during behaviour of zebrafish, *Drosophila*, and *Caenorhabditis elegans*,” *PLoS Biol* 15(7): e2002702 (2017).
- [156] Sharkey, J.P., Foo, D.C.W., Kabla, A., Baumberg, J.J., and Bowman, R.W., “A one-piece 3D printed flexure translation stage for open-source microscopy,” *Review of Scientific Instruments* 87(2), (2016).
- [157] Meng, Q., Harrington, K., Stirling, J., and Bowman, R., “The OpenFlexure Block Stage: sub-100 nm fibre alignment with a monolithic plastic flexure stage,” *Optics Express* 28(4), 4763 (2020).
- [158] Knapper, J., Whiteford, F., Rosen, D., Wadsworth, W., Stirling, J., Mkindi, C., Mduda, J., Sanga, V.L., Nyakyi, P.T., et al., “Developing the OpenFlexure Microscope towards medical use: Technical and social challenges of developing globally accessible hardware for healthcare,” *Philosophical Transactions of the Royal Society A: Mathematical, Physical and Engineering Sciences* 382(2274), (2024).
- [159] McDermott, S., Ayazi, F., Collins, J., Knapper, J., Stirling, J., Bowman, R., and Cicutta, P., “Multi-modal microscopy imaging with the OpenFlexure Delta Stage,” *Optics Express* 30(15), 26377 (2022).
- [160] Rosen, D.G., de Mello, E.S., Dhingra, S., Dawsey, S.M., Knapper, J., Bowman, R., and Anandasabapathy, S., “Utility of a low-cost 3-D printed microscope for evaluating esophageal biopsies,” *Annals of 3D Printed Medicine* 13(June 2023), 100145 (2024).
- [161] Knapper, J., Collins, J.T., Stirling, J., McDermott, S., Wadsworth, W., and Bowman, R.W., “Fast high-precision autofocus on a motorised microscope: Automating blood sample imaging on the OpenFlexure Microscope,” *J. Microsc.* 2022;285:29–39. (2021).
- [162] Lu, M.Y., Williamson, D.F.K., Chen, T.Y., Chen, R.J., Barbieri, M., and Mahmood, F., “Data-efficient and weakly supervised computational pathology on whole-slide images,” *Nature Biomedical Engineering* 5(6), 555–570 (2021).
- [163] Grant, S.D., Richford, K., Burdett, H.L., McKee, D., and Patton, B.R., “Low-cost, open-access quantitative phase imaging of algal cells using the transport of intensity equation,” *Royal Society Open Science* 7(1), (2020).
- [164] Cabello, M.K.E., and De Guzman, J.E., “Utilization of accessible resources in the fabrication of an affordable, portable, high-resolution, 3D printed, digital microscope for Philippine diagnostic applications,” *PLOS Global Public Health* 3(11), (2023).
- [165] Diep, T.T., Needs, S.H., Bizley, S., and Edwards, A.D., “Rapid Bacterial

References

- Motility Monitoring Using Inexpensive 3D-Printed OpenFlexure Microscopy Allows Microfluidic Antibiotic Susceptibility Testing,” *Micromachines* 13(11), (2022).
- [166] Patton, B.R., Grant, S.D., Cairns, G.S., and Wistuba, J., “Adapting the 3D-printed Openflexure microscope enables computational super-resolution imaging,” *F1000Research* 8, 1–13 (2019).
- [167] Matsui, T., and Fujiwara, D., “Optical sectioning robotic microscopy for everyone: the structured illumination microscope with the OpenFlexure stages,” *Optics Express* 30(13), 23208 (2022).
- [168] Tristan-Landin, S.B., Gonzalez-Suarez, A.M., Jimenez-Valdes, R.J., and Garcia-Cordero, J.L., “Facile assembly of an affordable miniature multicolor fluorescence microscope made of 3D-printed parts enables detection of single cells,” *PLoS ONE* 14(10), 1–17 (2019).
- [169] Brown, J.W.P., Bauer, A., Polinkovsky, M.E., Bhumkar, A., Hunter, D.J.B., Gaus, K., Sierrecki, E., and Gambin, Y., “Single-molecule detection on a portable 3D-printed microscope,” *Nature Communications* 10(1), 1–7 (2019).
- [170] Martens, K.J.A., van Beljouw, S.P.B., van der Els, S., Vink, J.N.A., Baas, S., Vogelaar, G.A., Brouns, S.J.J., van Baarlen, P., Kleerebezem, M., et al., “Visualisation of dCas9 target search in vivo using an open-microscopy framework,” *Nature Communications* 10(1), 1–11 (2019).
- [171] Amann, S., Witzleben, M. von, and Breuer, S., “3D-printable portable open-source platform for low-cost lens-less holographic cellular imaging,” *Scientific reports* 9(1), 11260 (2019).
- [172] MacDonald, N.P., Zhu, F., Hall, C.J., Reboud, J., Crosier, P.S., Patton, E.E., Wlodkovic, D., and Cooper, J.M., “Assessment of biocompatibility of 3D printed photopolymers using zebrafish embryo toxicity assays,” *Lab on a Chip* 16(2), 291–297 (2016).
- [173] Diederich, B., Lachmann, R., Carlstedt, S., Marsikova, B., Wang, H., Uwurukundo, X., Mosig, A.S., and Heintzmann, R., “A versatile and customizable low-cost 3D-printed open standard for microscopic imaging,” *Nature Communications* 11(1), 5979 (2020).
- [174] Cairns, G.S., and Patton, B.R., “An open-source alignment method for multichannel infinite-conjugate microscopes using a ray transfer matrix analysis model,” *Philosophical Transactions of the Royal Society A: Mathematical, Physical and Engineering Sciences* 382(2274), (2024).
- [175] Brinksmeier, E., Mutlugünes, Y., Klocke, F., Aurich, J.C., Shore, P., and Ohmori, H., “Ultra-precision grinding,” *CIRP Annals - Manufacturing Technology* 59(2), 652–671 (2010).
- [176] Komanduri, R., Lucca, D.A., and Tani, Y., “Technological advances in fine abrasive processes,” *CIRP Annals - Manufacturing Technology* 46(2), 545–596 (1997).
- [177] Tan, N.Y.J., Zhang, X., Neo, D.W.K., Huang, R., Liu, K., and Senthil Kumar, A., “A review of recent advances in fabrication of optical Fresnel lenses,” *Journal of Manufacturing Processes* 71(April), 113–133 (2021).
- [178] Spina, R., Walach, P., Schild, J., and Hopmann, C., “Analysis of lens

References

- manufacturing with injection molding,” *International Journal of Precision Engineering and Manufacturing* 13(11), 2087–2095 (2012).
- [179] Falahati, M., Zhou, W., Yi, A., and Li, L., “Fabrication of polymeric lenses using magnetic liquid molds,” *Applied Physics Letters* 114(20), (2019).
- [180] Li, L., Raasch, T.W., Sieber, I., Beckert, E., Steinkopf, R., Gengenbach, U., and Yi, A.Y., “Fabrication of microinjection-molded miniature freeform Alvarez lenses,” *APPLIED OPTICS / Vol. 53, No. 19* (2014).
- [181] Feng, Z., Huang, L., Gong, M., and Jin, G., “Beam shaping system design using double freeform optical surfaces,” *Optics Express* 21(12), 14728 (2013).
- [182] Wu, R., Feng, Z., Zheng, Z., Liang, R., Benítez, P., Miñano, J.C., and Duerr, F., “Design of Freeform Illumination Optics,” *Laser and Photonics Reviews* 12(7), 1–18 (2018).
- [183] Li, J., Thiele, S., Quirk, B.C., Kirk, R.W., Verjans, J.W., Akers, E., Bursill, C.A., Nicholls, S.J., Herkommer, A.M., et al., “Ultrathin monolithic 3D printed optical coherence tomography endoscopy for preclinical and clinical use,” *Light: Science and Applications* 9(1), (2020).
- [184] Acikgoz, H., Arya, R.K., and Mittra, R., “Statistical analysis of 3D-printed flat GRIN lenses,” *2016 IEEE Antennas and Propagation Society International Symposium, APSURSI 2016 - Proceedings*(November 2017), 473–474 (2016).
- [185] Squires, A.D., Constable, E., and Lewis, R.A., “3D printing of aspherical terahertz lenses and diffraction gratings,” *International Conference on Infrared, Millimeter, and Terahertz Waves, IRMMW-THz1–2* (2014).
- [186] Zhang, S., “Design and fabrication of 3D-printed planar Fresnel zone plate lens,” *Electronics Letters* 52(10), 833–835 (2016).
- [187] Zhang, S., Arya, R.K., Pandey, S., Vardaxoglou, Y., Whittow, W., and Mittra, R., “3D-printed planar graded index lenses,” *IET Microw. Antennas Propag.*, 2016, Vol. 10, Iss. 13, pp. 1411–1419 (2015).
- [188] Squires, A.D., Constable, E., and Lewis, R.A., “3D Printed Terahertz Diffraction Gratings And Lenses,” *Journal of Infrared, Millimeter, and Terahertz Waves* 36(1), 72–80 (2015).
- [189] Suszek, J., Sypek, M., Makowski, M., Garet, F., Ducin, I., Kakarenko, K., Bomba, J., and Coutaz, J.-L., “Evaluation of the shadow effect in terahertz kinoform gratings,” *Optics Letters* 38(9), 1464 (2013).
- [190] Sun, J., and Hu, F., “Three-dimensional printing technologies for terahertz applications : A review,” *Int J RF Microw Comput Aided Eng.* 2020;30:e21983 (2020).
- [191] Canning, J., Hossain, M.A., Han, C., Chartier, L., Cook, K., and Athanaze, T., “Drawing optical fibers from three-dimensional printers,” *Optics Letters* 41(23), 5551 (2016).
- [192] Cook, K., Balle, G., Canning, J., Chartier, L., Athanaze, T., Hossain, M.A., Han, C., Comatti, J.-E., Luo, Y., et al., “Step-index optical fiber drawn from 3D printed preforms,” *Optics Letters* 41(19), 4554 (2016).
- [193] Zhao, Q., Tian, F., Yang, X., Li, S., Zhang, J., Zhu, X., Yang, J., Liu, Z., Zhang, Y., et al., “Optical fibers with special shaped cores drawn from 3D printed preforms,” *Optik* 133, 60–65 (2017).

References

- [194] Cook, K., Canning, J., Leon-Saval, S., Reid, Z., Hossain, M.A., Comatti, J.-E., Luo, Y., and Peng, G.-D., "Air-structured optical fiber drawn from a 3D-printed preform," *Optics Letters* 40(17), 3966 (2015).
- [195] Gissibl, T., Schmid, M., and Giessen, H., "Spatial beam intensity shaping using phase masks on single-mode optical fibers fabricated by femtosecond direct laser writing," *Optica* 3(4), 448 (2016).
- [196] Kowalczyk, M., Haberko, J., and Wasylczyk, P., "Microstructured gradient-index antireflective coating fabricated on a fiber tip with direct laser writing," *Optics Express* 22(10), 12545 (2014).
- [197] Bianchi, S., Rajamanickam, V.P., Ferrara, L., Di Fabrizio, E., Liberale, C., and Di Leonardo, R., "Focusing and imaging with increased numerical apertures through multimode fibers with micro-fabricated optics," *Optics Letters* 38(23), 4935 (2013).
- [198] Gissibl, T., Thiele, S., Herkommer, A., and Giessen, H., "Two-photon direct laser writing of ultracompact multi-lens objectives," *Nature Photonics* 10(8), 554–560 (2016).
- [199] Weiss, I., and Marom, D.M., "Direct 3D nano-printing on optical fiber tip," International Conference on Optical MEMS and Nanophotonics 02-05-Aug, 1–2 (2015).
- [200] Guo, R., Xiao, S., Zhai, X., Li, J., Xia, A., and Huang, W., "Micro lens fabrication by means of femtosecond two photon photopolymerization," *Optics Express* 14(2), 810 (2006).
- [201] Osipov, V., Doskolovich, L.L., Bezus, E.A., Cheng, W., Gaidukeviciute, A., and Chichkov, B., "Fabrication of three-focal diffractive lenses by two-photon polymerization technique," *Applied Physics A: Materials Science and Processing* 107(3), 525–529 (2012).
- [202] Schumann, M., Bückmann, T., Gruhler, N., Wegener, M., and Pernice, W., "Hybrid 2D-3D optical devices for integrated optics by direct laser writing," *Light: Science and Applications* 3(December 2013), 1–9 (2014).
- [203] Hu, Y., Chen, Y., Ma, J., Li, J., Huang, W., and Chu, J., "High-efficiency fabrication of aspheric microlens arrays by holographic femtosecond laser-induced photopolymerization," *Applied Physics Letters* 103(14), (2013).
- [204] Lightman, S., Hurvitz, G., Gvishi, R., and Arie, A., "Miniature wide-spectrum mode sorter for vortex beams produced by 3D laser printing," *Optica* 4(6), 605 (2017).
- [205] Chen, Q.D., Wu, D., Niu, L.G., Wang, J., Lin, X.F., Xia, H., and Sun, H.B., "Phase lenses and mirrors created by laser micronanofabrication via two-photon photopolymerization," *Applied Physics Letters* 91(17), 1–4 (2007).
- [206] Malinauskas, M., Žukauskas, A., Purlys, V., Belazaras, K., Momot, A., Paipulas, D., Gadonas, R., Piskarskas, A., Gilbergs, H., et al., "Femtosecond laser polymerization of hybrid/integrated micro-optical elements and their characterization," *Journal of Optics* 12(12), (2010).
- [207] Lightman, S., Hurvitz, G., Gvishi, R., and Arie, A., "Tailoring lens functionality by 3D laser printing," *Applied Optics* 56(32), 9038 (2017).
- [208] Shan, Y., Krishnakumar, A., Qin, Z., and Mao, H., "Reducing lateral stair-

References

- stepping defects in liquid crystal display-based vat photopolymerization by defocusing the image pattern,” *Additive Manufacturing* 52(January), 102653 (2022).
- [209] Xu, Y., Huang, P., To, S., Zhu, L.-M., and Zhu, Z., “Low-Cost Volumetric 3D Printing of High-Precision Miniature Lenses in Seconds,” *Adv. Optical Mater.* 2022, 10, 2200488 (2022).
- [210] Heinrich, A., [3D Printing of Optical Components] , Springer (2021).
- [211] Rodriguez, D., Fernandez, J., Quiroga, J., and Vazquez, D., “Smoothing of 3D Printed Lenses,” *US 10 , 086 , 575 B2*, United States (2018).
- [212] Rooney, L.M., Christopher, J., Watson, B., Kumar, Y.S., Copeland, L., Walker, L.D., Foylan, S., Amos, W.B., Bauer, R., et al., “Printing, Characterizing, and Assessing Transparent 3D Printed Lenses for Optical Imaging,” *Advanced Materials Technologies* 9(15), (2024).
- [213] Vallejo-Melgarejo, L.D., Reifenberger, R.G., Newell, B.A., Narváez-Tovar, C.A., and Garcia-Bravo, J.M., “Characterization of 3D-printed lenses and diffraction gratings made by DLP additive manufacturing,” *Rapid Prototyping Journal* 25(10), 1684–1694 (2019).
- [214] Yuan, C., Kowsari, K., Panjwani, S., Chen, Z., Wang, D., Zhang, B., Ng, C.J.X., Alvarado, P.V.Y., and Ge, Q., “Ultrafast Three-Dimensional Printing of Optically Smooth Microlens Arrays by Oscillation-Assisted Digital Light Processing,” *ACS Applied Materials and Interfaces* 11(43), 40662–40668 (2019).
- [215] Ge, Q., Li, Z., Wang, Z., Kowsari, K., Zhang, W., He, X., Zhou, J., and Fang, N.X., “Projection micro stereolithography based 3D printing and its applications,” *International Journal of Extreme Manufacturing* 2(2), (2020).
- [216] Zheng, X., Lee, H., Weisgraber, T.H., Shusteff, M., DeOtte, J., Duoss, E.B., Kuntz, J.D., Biener, M.M., Ge, Q., et al., “Ultralight, ultrastiff mechanical metamaterials,” *Science* 344(6190), 1373–1377 (2014).
- [217] Zheng, X., Smith, W., Jackson, J., Moran, B., Cui, H., Chen, D., Ye, J., Fang, N., Rodriguez, N., et al., “Multiscale metallic metamaterials,” *Nature Materials* 15(10), 1100–1106 (2016).
- [218] Walker, D.A., Hedrick, J.L., and Mirkin, C.A., “Using a Mobile Liquid Interface,” *Science* 366, 360–364 (2019) 18 364(October), 360–364 (2019).
- [219] Lipkowitz, G., Samuelsen, T., Hsiao, K., Lee, B., Dulay, M.T., Coates, I., Lin, H., Pan, W., Toth, G., et al., “Injection continuous liquid interface production of 3D objects,” *Science Advances* 8(39), 1349–1352 (2022).
- [220] Elgarisi, M., Frumkin, V., Luria, O., and Bercovici, M., “Fabrication of freeform optical components by fluidic shaping,” *Optica* 8(11), 1501 (2021).
- [221] Assefa, B.I.G.A., Pekkarinen, M.A.P., Partanen, H.E.P., Iskop, J.O.B., Urunen, J.A.R.I.T., and Aarinen, J.Y.S., “Imaging-quality 3D-printed centimeter-scale lens” 27(9), 12630–12637 (2019).
- [222] Gawedzinski, J., Pawlowski, M.E., and Tkaczyk, T.S., “Quantitative evaluation of performance of three-dimensional printed lenses,” *Optical Engineering* 56(08), 1 (2017).
- [223] Chen, X., Liu, W., Dong, B., Lee, J., Ware, H.O.T., Zhang, H.F., and Sun, C.,

References

- “High-Speed 3D Printing of Millimeter-Size Customized Aspheric Imaging Lenses with Sub 7 nm Surface Roughness,” *Advanced Materials* 30(18), 1–8 (2018).
- [224] Liberale, C., Cojoc, G., Candeloro, P., Das, G., Gentile, F., De Angelis, F., and Di Fabrizio, E., “Micro-optics fabrication on top of optical fibers using two-photon lithography,” *IEEE Photonics Technology Letters* 22(7), 474–476 (2010).
- [225] Gissibl, T., Thiele, S., Herkommer, A., and Giessen, H., “Sub-micrometre accurate free-form optics by three-dimensional printing on single-mode fibres,” *Nature Communications* 7, 1–9 (2016).
- [226] Thiele, S., Arzenbacher, K., Gissibl, T., Giessen, H., and Herkommer, A.M., “3D-printed eagle eye: Compound microlens system for foveated imaging,” *Science Advances* 3(2), 1–7 (2017).
- [227] Toulouse, A., Thiele, S., Giessen, H., and Herkommer, A.M., “Alignment-free integration of apertures and nontransparent hulls into 3D-printed micro-optics,” *Optics Letters* 43(21), 5283 (2018).
- [228] Thiele, S., Pruss, C., Herkommer, A.M., and Giessen, H., “3D printed stacked diffractive microlenses,” *Optics Express* 27(24), 35621 (2019).
- [229] Asadollahbaik, A., Thiele, S., Weber, K., Kumar, A., Drozella, J., Sterl, F., Herkommer, A.M., Giessen, H., and Fick, J., “Highly Efficient Dual-Fiber Optical Trapping with 3D Printed Diffractive Fresnel Lenses,” *ACS Photonics* (2019).
- [230] Gonzalez-Hernandez, D., Varapnickas, S., Merkininkaitė, G., Čiburys, A., Gailevičius, D., Šakirzanovas, S., Juodkasis, S., and Malinauskas, M., “Laser 3d printing of inorganic free-form micro-optics,” *Photonics* 8(12), 1–12 (2021).
- [231] Reynoso, M., Gauli, I., and Measor, P., “Refractive index and dispersion of transparent 3D printing photoresins,” *Optical Materials Express* 11(10), 3392 (2021).
- [232] Xu, Y., Huang, P., To, S., Zhu, L.M., and Zhu, Z., “Low-Cost Volumetric 3D Printing of High-Precision Miniature Lenses in Seconds,” in *Adv Opt Mater* 10(17) (2022).
- [233] Ta, D.-M., Aguilar, A., and Bon, P., “Label-free image scanning microscopy for kHz super-resolution imaging and single particle tracking,” *Optics Express* 31(22), 36420 (2023).
- [234] “Main differences between confocal and widefield microscopy,” *Axiom Optics*, <<https://www.axiomoptics.com/blog/main-differences-between-confocal-and-widefield-microscopy/>> (2 October 2024).
- [235] Kaderuppan, S.S., Wong, E.W.L., Sharma, A., and Woo, W.L., “Smart Nanoscopy: A Review of Computational Approaches to Achieve Super-Resolved Optical Microscopy,” *IEEE Access* 8(December), 214801–214831 (2020).
- [236] Chiu, S.W., and Leake, M.C., “Functioning nanomachines seen in real-time in living bacteria using single-molecule and super-resolution fluorescence imaging,” *International journal of molecular sciences* 12(4), 2518–2542

References

- (2011).
- [237] Göorlitz, F., Hoyer, P., Falk, H.J., Kastrop, L., Engelhardt, J., and Hell, S.W., “A STED microscope designed for routine biomedical applications,” *Progress in Electromagnetics Research* 147(April), 57–68 (2014).
- [238] Zhao, T., Wang, Z., Chen, T., Lei, M., Yao, B., and Bianco, P.R., “Advances in High-Speed Structured Illumination Microscopy,” *Frontiers in Physics* 9(May), 1–12 (2021).
- [239] Ward, E.N., and Pal, R., “Image scanning microscopy: an overview,” *Journal of Microscopy* 266(2), 221–228 (2017).
- [240] York, A.G. et al., “Resolution_doubling_in_live_mu.PDF.pdf,” *Nat Methods* 9, 749–754 (2012).
- [241] Ristok, S., Erkommer, M.H., and Iessen, H.A.G., “Stitching-free 3D printing of millimeter-sized highly transparent spherical and aspherical optical components,” Vol. 10, No. 10 / 1 October 2020 / *Optical Materials Express* 2370 10(10), 2370–2378 (2020).
- [242] Li, B., Liao, C., Cai, Z., Zhou, J., Zhao, C., and Jing, L., “Femtosecond laser 3D printed micro objective lens for ultrathin fiber endoscope,” *Fundamental Research* 4 (2024) 123–130 Contents 4, 123–130 (2024).
- [243] Ali, M., Alam, F., Vahdati, N., and Butt, H., “Printed Holographic Fresnel Lenses,” *Adv. Eng. Mater.* 2022, 24, 2101641 (2022).
- [244] Alam, F., Ali, M., Elsherif, M., Salih, A.E., El-atab, N., and Butt, H., “3D printed intraocular lens for managing the color blindness,” *Additive Manufacturing Letters* 5(September 2022), 100129 (2023).
- [245] Hisham, M., Salih, A.E., and Butt, H., “3D Printing of Multimaterial Contact Lenses,” *ACS Biomater. Sci. Eng.* 2023, 9, 4381–4391 (2023).

Appendix A

3D Printer including Specifications	Printing Resin	Printed Lens	Base Exposure Time	Layer Exposure Time	Spin-coating Speed	Spin-coating Time	Coating Resin and Quantity
Elegoo Mars 2 • 10 μm layers • 49 μm lateral resolution	Formlabs Clear	12.7 mm diameter 20 mm focal length	50 s	9 s	1800 RPM	12 s	120 mg VidaRosa
Elegoo Mars 2 • 10 μm layers • 49 μm lateral resolution	Formlabs Clear	6 mm diameter 10 mm focal length	50 s	9 s	2600 RPM	15 s	4 mg VidaRosa
Elegoo Mars 2 • 10 μm layers • 49 μm lateral resolution	Formlabs Clear	6 mm diameter 15 mm focal length	50 s	9 s	2800 RPM	15 s	4 mg VidaRosa
Elegoo Mars 2 • 10 μm layers • 49 μm lateral resolution	Formlabs Clear	6 mm diameter -6 mm focal length	50 s	9 s	4000 RPM	10 s	4 mg VidaRosa
Phrozen Sonic Mini S • 10 μm layers • 23 μm lateral resolution	Anycubic High Clear	1.2 mm pitch 5 mm focal length	40 s	3 s	6000 RPM	10 s	100 mg VidaRosa

Table 3. Printing and processing overview required for the resins and printers used within the thesis.

Appendix B

```

%Created by Jay L.C. 220414
% This script utilises the function circfit.m, this is a revival of 13 year old code
% Input x & y data as column vectors
% Output is centre point (yc,xc), radius R and coefficients a & b

%% % Rename & shrink x & y data if necessary

% x=xA;
% y=yA;

plot(x,y,'-'), title(' measured points') % plot input data

%% % reconstruct theoretical circle from data
[xc,yc,Re,a] = circfit(x,y);

yt = -(a(2)/2) + sqrt((-x.^2)-(a(1)*x)-(a(3)) + ((a(2)/2)^2)); %convex form
% yt = (a(2)/2) + sqrt((-x.^2)-(a(1)*x)-(a(3)) + ((a(2)/2)^2)); %concave form
error = ((y-yt))*1000;%convex form, coeffiecient of 1000 for scale
% error = ((y+yt))*1000;%concave form

%%
figure
subplot(2,1,1)
plot(x,y,'-',x,yt,'. '), %convex form
% plot(x,y,'-',x,-yt,'. '), %concave form
legend('Measured','Fitted')
% xlabel 'Measurement Distance (mm)', ylabel 'Measurement Height (mm)'

subplot(2,1,2)
bar(x,error)
% xlabel 'Measurement Distance (mm)', ylabel 'Form Residuals (\mum)'

function [xc,yc,R,a] = circfit(x,y)

```

Appendices

```
%  
% [xc yx R] = circfit(x,y)  
%  
% fits a circle in x,y plane in a more accurate  
% (less prone to ill condition )  
% procedure than circfit2 but using more memory  
% x,y are column vector where (x(i),y(i)) is a measured point  
%  
% result is center point (yc,xc) and radius R  
% an optional output is the vector of coefficient a  
% describing the circle's equation  
%  
%  $x^2+y^2+a(1)*x+a(2)*y+a(3)=0$   
%  
% By: Izhak bucher 25/oct /1991,  
% x=x(:); y=y(:);  
% c=1/3;  
% h = ((x.^2)+(y.^2));  
% k = -0.5267;  
% A = 0.13119e-3;  
% B = 0.40187e-5;  
% C = -0.14129e-6;  
% a=[x y ones(size(x))]\(-(a(2)/2) + sqrt((-x.^2)-(a(1)*x)-(a(3)) + ((a(2)/2)^2)));  
% xc = -.5*a(1);  
% yc = -.5*a(2);  
% R = sqrt((a(1)^2+a(2)^2)/4-a(3));  
  
x=x(:); y=y(:);  
a=[x y ones(size(x))]\(-(x.^2+y.^2));  
xc = -.5*a(1);  
yc = -.5*a(2);  
R = sqrt((a(1)^2+a(2)^2)/4-a(3));
```

Appendix C

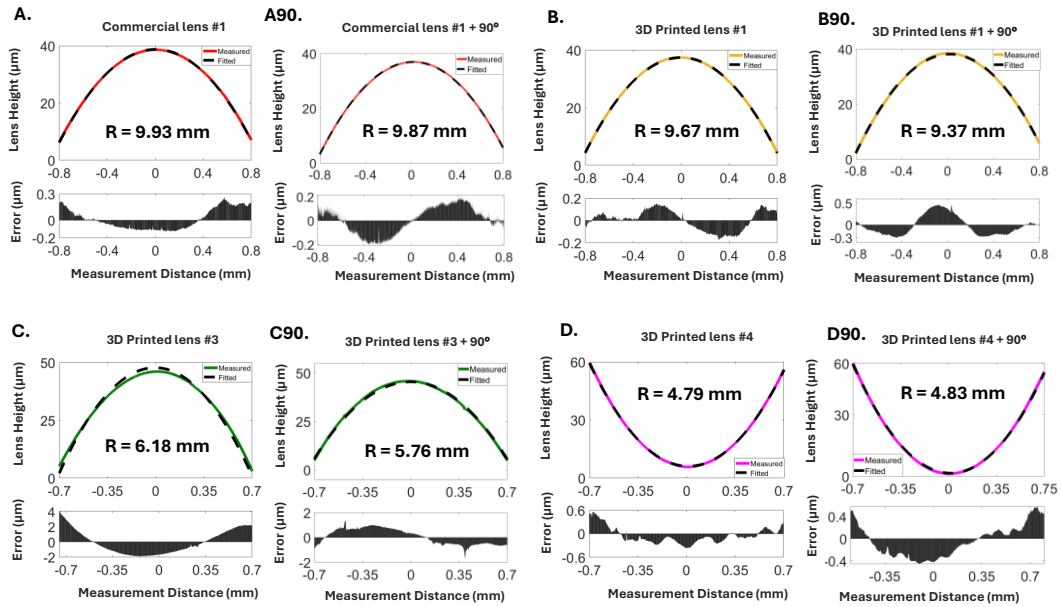


Figure 71. Geometrical characteristics of the lenses within section 3.x.x with 90° rotational variants in the measurement axis. (A) Surface profile of a commercial 20 mm focal length, 12.7 mm diameter lens; (A90) Surface profile of A rotated by 90°; (B) Surface profile of a 3D printed version of a 20 mm focal length, 12.7 mm diameter lens; (B90) Surface profile of B rotated by 90°; (C) Surface profile of a 3D printed 10 mm focal length, 6 mm diameter lens; (C90) Surface profile of C rotated by 90°; (D) Surface profile of a 3D printed plano-concave lens with a -6 mm focal length and 6 mm diameter; (D90) Surface profile of D rotated by 90°;

Appendix D

```
//Arduino controlled 8-channel DAC for 2 full MEMS chip control (although using only 1!!)
//8-channel DAC used is BOOST-DAC8568 board, which connects via SPI and chip having 32-bit
data input
//4 prefix bits (0000), 4 control bits (0011), 4 address bits (0000-0111), 16 data bits, 4 feature bits
(0000) for all 8 channels (max value 65535)
//for simultaneously updating all 8-channels, first write new data for channel 1-7 (or 1-3) and then do
a write+updateAll on channel 8 (or 4)
//Write new data without update for ch 1-3: (0000),(0000),(0000)-(0010),(16 data bits),(0000)
//Write new data with update ALL on channel 4: (0000),(0010),(0011), (16 data bits), (0000)
//serial input form LabView/python, for 1 mirror movement: 23 characters for single mirror change
instruction, example "<30000,30000,30000,30000>"

//serial input from python, for raster scan: start position, x step size, x steps, y step size, y steps,
exposure time, step wait time
//example: 51 characters excluding brackets
"<20000,40000,30000,30000,00050,020,00050,020,050,010>"
// 3DP range <20000,40000,30000,20000,00050,060,00050,060,050,010>
// comm range <20000,40000,30000,30000,00050,018,00050,022,050,010>
//include <Wire.h>
#include <SPI.h>
#define CS 10 //digital pin 10 as chip select for SPI
#define trigger_o 5 //trigger output on pin 5
#define RSET 7 //digital pin 7 as reset

//SPI pins: 13 SCK, 12 MISO, 11 MOSI, 10 SS

SPISettings settingsA(10000000, MSBFIRST, SPI_MODE1);

const uint16_t numChars = 445; //max length of serial read
char receivedChars[numChars];

uint16_t expTime = 0; //exposure time per image/grab
uint16_t waitTime = 0; //wait time between step initiated and completed
uint16_t frameNo = 0;
uint16_t step4Delay = 00; //time for steps in 4 step position change in microseconds - overall 3*this
time value for full pos change
uint16_t Pos1[8]= {30000,30000,30000,30000,0,0,0,0}; //integers to write to DAC
uint16_t CurrentPos[8] = {0,0,0,0,0,0,0,0}; //initialise previous channel values to 0
uint16_t nextPos[8] = {0,0,0,0,0,0,0,0}; //initialise next position to 0
uint16_t receivedNo = 0;
uint16_t xSteps = 0;
uint16_t ySteps = 0;
uint16_t xStepSize = 0;
uint16_t yStepSize = 0;

boolean newData = false;

//=====

void setup() {
  Serial.begin(115200);
  Serial.println("8-channel DAC8568 - Confocal");
}
```

Appendices

```
pinMode(CS, OUTPUT);
SPI.begin();
SPI.setBitOrder(MSBFIRST);
digitalWrite(CS, HIGH);

pinMode(RSET, OUTPUT);
digitalWrite(RSET, HIGH);

//set all outputs to 0V
SPI.beginTransaction(settingsA);
digitalWrite(CS, LOW);
SPI.transfer(0x06);
SPI.transfer(0x00);
SPI.transfer(0xff);
SPI.transfer(0xff);
digitalWrite(CS, HIGH);
digitalWrite(CS, LOW);
SPI.transfer(0x04);
SPI.transfer(0x00);
SPI.transfer(0x00);
SPI.transfer(0xff);
digitalWrite(CS, HIGH);
digitalWrite(CS, LOW);
SPI.transfer(0x08);
SPI.transfer(0x00);
SPI.transfer(0x00);
SPI.transfer(0x01);
digitalWrite(CS, HIGH);

pinMode(trigger_o, OUTPUT);
digitalWrite(trigger_o, LOW);

//Serial.println(SERIAL_BUFFER_SIZE);

}

//=====

void loop() {
  // serial read to get commandline input or input from Python
  receivedNo = receivedWithMarkers();

  if (receivedNo == 23 && newData == true) //check if sent instructions are for just MEMS position
  change
  {
    //Code for moving MEMS to new position
    char * strtokIndx; //used by strtok as index
    strtokIndx = strtok(receivedChars, ","); Pos1[0] = atoi(strtokIndx);
    strtokIndx = strtok(NULL, ","); Pos1[1] = atoi(strtokIndx);
    strtokIndx = strtok(NULL, ","); Pos1[2] = atoi(strtokIndx);
    strtokIndx = strtok(NULL, ","); Pos1[3] = atoi(strtokIndx);
    //order of Pos1 allocation might need changed to map physical output channels on MEMS correctly
    Pos1[4]=0;Pos1[5]=0;Pos1[6]=0;Pos1[7]=0;

    Serial.println("Mirror move to");
    writeToDAC(Pos1);
    Serial.println((String)Pos1[0]+","+Pos1[1]+","+Pos1[2]+","+Pos1[3]);
  }
}
```

Appendices

```
}

if (receivedNo == 51 && newData == true) //check if sent instructions are for raster scan
{
    //code for running raster scan
    char * strtokIdx; //used by strtok as index
    strtokIdx = strtok(receivedChars, ","); Pos1[0] = atoi(strtokIdx);
    strtokIdx = strtok(NULL, ","); Pos1[1] = atoi(strtokIdx);
    strtokIdx = strtok(NULL, ","); Pos1[2] = atoi(strtokIdx);
    strtokIdx = strtok(NULL, ","); Pos1[3] = atoi(strtokIdx);
    strtokIdx = strtok(NULL, ","); xStepSize = atoi(strtokIdx);
    strtokIdx = strtok(NULL, ","); xSteps = atoi(strtokIdx);
    strtokIdx = strtok(NULL, ","); yStepSize = atoi(strtokIdx);
    strtokIdx = strtok(NULL, ","); ySteps = atoi(strtokIdx);
    strtokIdx = strtok(NULL, ","); expTime = atoi(strtokIdx);
    strtokIdx = strtok(NULL, ","); waitTime = atoi(strtokIdx);

    Serial.println("Raster scan " + String(xSteps) + " by " + String(ySteps));

    writeToDAC(Pos1);
    for (int i=0; i < ySteps; i++)
    {
        Serial.println("Line" + String(i));
        for (int k=0; k < xSteps; k++)
        {
            nextPos[0] = Pos1[0] + k*xStepSize;
            nextPos[1] = Pos1[1] - k*xStepSize;
            nextPos[2] = Pos1[2] + i*yStepSize;
            nextPos[3] = Pos1[3] - i*yStepSize;
            Serial.println((String)nextPos[0]+","+nextPos[1]+","+nextPos[2]+","+nextPos[3]);
            writeToDAC(nextPos);
            delay(waitTime);
            digitalWrite(trigger_o, HIGH);
            delay(1);
            digitalWrite(trigger_o, LOW);
            delay(expTime);
        }
    }

}

memset(receivedChars, 0, sizeof(receivedChars));
newData = false;
receivedNo = 0;
}

//=====
uint16_t receivedWithMarkers() {
    static boolean recvInProgress = false;
    static uint16_t ndx = 0;
    char startMarker = '<';
    char endMarker = '>';
    char rc;

    ndx = 0;
    while (Serial.available() > 0 && newData == false) {
        rc = Serial.read();
```

Appendices

```
if (recvInProgress == true) {
    if (rc != endMarker) {
        receivedChars[ndx] = rc;
        ndx++;
        // Serial.print(rc);
        if (ndx >= numChars) {
            ndx = numChars - 1;
        }
    }
    else {
        receivedChars[ndx] = '\0'; // terminate the string
        recvInProgress = false;
        newData = true;
        // Serial.println();
        // Serial.println(ndx);
        return ndx;
    }
}
else if (rc == startMarker) {
    recvInProgress = true;
}
delay(5);
}
}

//=====
void writeToDAC(uint16_t posData[8]) {
    uint8_t cmdByte[8] = {0x00,0x10,0x20,0x30,0x40,0x50,0x60,0x70}; //command of 0011 to write
    to DAC channel n, with 0000 to 0011 being the channels
    uint8_t addrByte[8] = {0x00,0x00,0x00,0x00,0x00,0x00,0x00,0x02}; //control bit with 0000 to
    write to DAC buffer only and 0010 to write to DAC buffer+update all channels
    uint16_t prevPos[8];
    uint16_t posWrite;

    float a[20] = {0.025, 0.05, 0.075, 0.1, 0.15, 0.2, 0.25, 0.3, 0.4, 0.5, 0.6, 0.7, 0.75, 0.8, 0.85, 0.9,
    0.925, 0.95, 0.975, 1};
    float b[20] = {0.975, 0.95, 0.925, 0.9, 0.85, 0.8, 0.75, 0.7, 0.6, 0.5, 0.4, 0.3, 0.25, 0.2, 0.15, 0.1,
    0.075, 0.05, 0.025, 0};
    //float a[30] = {0.05, 0.5, 0.95, 1};

    for (int u=0;u<8;u++)
    {
        prevPos[u] = CurrentPos[u];
    }

    //Wire.beginTransmission(ad5676_address);
    SPI.beginTransaction(settingsA);

    //NEW WRITE FUNCTION
    for (int m=0;m<20;m++)
    {
        for (int j=0;j<8;j++)
        {
            if (posData[j] != CurrentPos[j] && posData[j] < 65536)
            {
                if (posData[j]>prevPos[j])

```

Appendices

```
{
  posWrite = (uint16_t) (((posData[j]-prevPos[j])*a[m]) + prevPos[j]);
}
else
{
  posWrite = (uint16_t) (((prevPos[j]-posData[j])*b[m]) + posData[j]);
}
digitalWrite(CS, LOW);
SPI.transfer(addrByte[j]);
SPI.transfer(cmdByte[j]|((posWrite >>12) & 0xFF));
SPI.transfer((posWrite >> 4) & 0xFF);
SPI.transfer((posWrite << 4) & 0xFF);
digitalWrite(CS, HIGH);
CurrentPos[j] = posWrite;
//Serial.println(CurrentPos[j]);
}
}
//delayMicroseconds(step4Delay);
}

//Wire.endTransmission();
}
```

Appendix E

```
# -*- coding: utf-8 -*-  
"""
```

```
Created on Mon Apr 15 17:18:31 2024
```

```
@author: Jay Christopher  
"""
```

```
import os  
import numpy as np  
import skimage  
import skimage.io  
import matplotlib.pyplot as plt  
from tkinter import filedialog  
from scipy.ndimage import gaussian_filter  
import imageio  
import pyopencl as cl  
import pyopencl.array as cl_array  
import time  
from skimage.feature import peak_local_max  
  
### GPU Setup  
platform = cl.get_platforms()[1]  
device = platform.get_devices()[0]  
context = cl.Context([device])  
queue = cl.CommandQueue(context)  
ctx = context  
  
### Load Images  
  
image_stack = skimage.io.imread(os.path.normpath(filedialog.askopenfilename(  
    title="Select either an individual tiff or tiff stack"),  
    filetypes=[('Tiff', '.tif')],  
    defaultextension='.tif',  
    initialdir=os.getcwd()  
)))  
  
### Prep Image stack  
  
sq_length = image_stack.shape[1] # square image  
  
image_centre_x = image_stack.shape[1]/2  
image_centre_y = image_stack.shape[2]/2  
  
image_sq = image_stack[:,int((image_centre_x)-sq_length/2):int((image_centre_x)+sq_length/2),  
    int((image_centre_y)-sq_length/2):int((image_centre_y)+sq_length/2)].copy()  
  
plt.imshow(image_sq[0],cmap='gray') #plot input image  
  
### Find Maxima
```

Appendices

```
maxima_found = np.empty(len(image_sq), dtype=object)

for n in range(len(image_sq)):

    # maxima_found[n] =
    peak_local_max(image_sq[n,:,:],min_distance=40,threshold_abs=0.0,threshold_rel=None,
    #                    exclude_border=20) # use if 3D printed honeycomb

    maxima_found[n] =
    peak_local_max(image_sq[n,:,:],min_distance=14,threshold_abs=0.0,threshold_rel=None,
    exclude_border=10) #use if commercial lenslet array

for t in range(len(maxima_found)-1):
    if t==0:
        num_maxima = 0
        num_maxima = len(maxima_found[t])+len(maxima_found[t+1])
    else:
        num_maxima = num_maxima +len(maxima_found[t+1])

fig, axes = plt.subplots(1, 2, figsize=(8, 3), sharex=True, sharey=True)
ax = axes.ravel()
ax[0].imshow(image_sq[1],cmap=plt.cm.gray)
ax[0].axis('off')
ax[0].set_title('Original')

ax[1].imshow(image_sq[1], cmap=plt.cm.gray)
ax[1].autoscale(False)
ax[1].plot(maxima_found[1][:,1], maxima_found[1][:,0], 'r.')
ax[1].axis('off')
ax[1].set_title('Peak local max')

### ISM Processing prep

sq_length = 7 # number of pixels for maxima ROI processing

h = maxima_found[1][:,0] #x coordinates of maxima
w = maxima_found[1][:,1] #y coordinates of maxima

t_begin = time.time()

roi_prep =
cl_array.empty(queue,[num_maxima,len(image_sq[1][:]),len(image_sq[1][:])],dtype=np.int32)
#multiple maxima per image

# roi_prep =
cl_array.empty(queue,[num_maxima,len(image_sq[0][:]),len(image_sq[0][:])],dtype=np.int32)
#single maximum in images

t_roi = time.time()

gpu_cropped_roi = roi_prep[:, int(h[1]-sq_length/2):int(h[1]+sq_length/2),
    int(w[1]-sq_length/2):int(w[1]+sq_length/2)] #multiple maxima per image

# gpu_cropped_roi = roi_prep[:, int(h[0]-sq_length/2):int(h[0]+sq_length/2),
```

Appendices

```
#          int(w[0]-sq_length/2):int(w[0]+sq_length/2)] #single maximum in images

t_gpu = time.time()

cropped_roi = np.zeros_like(gpu_cropped_roi,dtype=np.int32) #cropped windows around each
maxima

t_crop=time.time()

sigma = 1.2

processed_spot = gaussian_filter(cropped_roi,sigma) #processed maxima

t_proc = time.time()
t_end = time.time() # End time

print((t_roi - t_begin))
print((t_gpu - t_roi))
print((t_crop - t_gpu)/60)
print((t_proc - t_crop)/60)
print((t_end - t_begin)/60)

### ISM Processing of Data

k = 0
for j in range(len(maxima_found)):
    for l in range(len(maxima_found[j])):
        h = maxima_found[j][l,0]
        w = maxima_found[j][l,1]

        cropped_roi[k] = image_sq[[j],int(h-sq_length/2):int(h+sq_length/2),
            int(w-sq_length/2):int(w+sq_length/2)]

        processed_spot[k] = gaussian_filter(cropped_roi[k],sigma)

        k = k+1

fig, axes = plt.subplots(1, 2, figsize=(8, 3), sharex=True, sharey=True)
ax = axes.ravel()
ax[0].imshow(cropped_roi[0],cmap=plt.cm.gray)
ax[0].axis('off')
ax[0].set_title('Original Apertured')

ax[1].imshow(processed_spot[0], cmap=plt.cm.gray)
ax[1].autoscale(False)
ax[1].axis('off')
ax[1].set_title('Aperture + Gaussian')

### ISM Pixel reassignment

scale = len(image_sq[0][1])*2
```

Appendices

```
new_image_sq = np.full([len(maxima_found),scale,scale],0,dtype=np.uint8) # creates a blank image
2x size of input image
new_maxima_coords = maxima_found*2 # each maxima coordinate is remapped onto 2x image size
new_h = new_maxima_coords[1][:,0]
new_w = new_maxima_coords[1][:,1]

k=0
for i in range(len(maxima_found)):
    for m in range(len(maxima_found[i])):
        new_h = new_maxima_coords[i][m,0]
        new_w = new_maxima_coords[i][m,1]

        new_image_sq[[i,int(new_h-sq_length/2):int(new_h+sq_length/2),
            int(new_w-sq_length/2):int(new_w+sq_length/2)] = new_image_sq[[i,int(new_h-
sq_length/2):int(new_h+sq_length/2),
            int(new_w-sq_length/2):int(new_w+sq_length/2)]+processed_spot[k] # pixel reassignment of
processed maxima

        k = k+1

### Save Remapped Processed Spots

save_path = os.path.normpath(filedialog.askdirectory(title=("Select or create a folder to save
individual images")))

num=0

for i in range(len(new_image_sq)):
    imageio.imwrite(save_path + ('\\')+ str(num) + '.tif', new_image_sq[i])
    num = num+1
```